Synthesis and Characterisation of 2D Organic Materials

Zur Erlangung des akademischen Grades eines
Doktor der Naturwissenschaften Dr. rer. nat.

von der KIT-Fakultät für Chemie und Biowissenschaften des
Karlsruher Instituts für Technologie (KIT)

genehmigte

DISSERTATION
von

Concepción del Carmen Molina Jirón de Moreno
aus

Colón, Panamá

Präsident: Prof. Dr. Manfred Kappes

Referent: Prof. Dr. Mario Ruben
Korreferent: Priv.-Doz. Dr. Artur Böttcher
Prüfer: Priv.-Doz. Pavel Levkin
Prüfer: Prof. Dr. Patrick Théato

Tag der Prüfung: 16.10.2019

Contents

List of Figures

List of Schemes

Abstract

"***Synthesis and Characterisation of 2D Organic Materials***" is a dissertation submitted for the award of a Doctor in Natural Sciences at the Karlsruhe Institute of Technology (KIT), Faculty of Chemistry and Biosciences.

The discovery of graphene triggered an intense general research interest in various 2D materials due to their extraordinary properties. For more than a decade, the number of publications dealing with 2D materials has been steadily increasing, along with the development or discovery of other novel 2D structures. Despite all this, graphene is the most studied 2D material in the world due to its remarkable electronic and mechanical properties and is used in various practical applications. The wide range of applications for graphene requires, among other things, the development of new manufacturing methods. In particular, the Chemical Vapour Deposition (CVD) method has established itself for the growth of graphene layers, since this process makes it possible to produce very large graphene areas. In addition, the electronic properties of single-layer graphene, which cannot be tuned for certain applications, have led scientists to search for alternative graphene-like materials. One possible alternative is nanocrystalline graphene (NCG), the properties of which can be controlled during the growth process to allow fine tuning of the electronic band-gap and thus its integration into transistors or other electronic devices. In addition, recent research has also focused on new 2D carbon allotropes that could be used in technological applications. The necessary control in the manufacturing process is the motivation for the development of new methods for the synthesis of graphene and NCG, as well as a novel carbon-based 2D material, known as Graphdiyne (GDY).

In this PhD thesis, the first research project involves the synthesis of graphene using carbon dioxide (CO_2), an environmentally problematic gas source. Different metallic substrates were tested to investigate the possibility of CO_2 activation and reduction to graphene. The selected metals are copper (Cu), for its properties in graphene synthesis, and palladium (Pd), for its known catalytic activity. The synthesis was performed using an atmospheric pressure CVD reactor (APCVD) and hydrogen as reductant. Raman spectroscopy, Atomic Force Microscopy (AFM) and Transmission Electron Microscopy (TEM) confirm the formation of multilayer graphene. Furthermore, our study shows that CO_2 can be effectively converted to graphene when the concentration of the metal mixture contains more than 82at.% Cu.

In the second research project we try to synthesise nanocrystalline graphene (NCG) from an organic molecule. Common methods of NCG synthesis use either photoresists or polymers that require high temperatures, vacuum and long exposure times for successful graphitisation of the precur-

sor. The domain sizes achievable in these processes are typically 8-12 nm. With our process, using the organic molecule hexaethynyl benzene, we are able to produce large areas of NCG with larger crystal domains. These show the expected semiconducting properties in our conductivity studies.

The third research project deals with the synthesis of graphdiyne (GDY), a new carbon-based material. GDY was proposed as the most stable non-natural carbon allotrope with a band gap of 0.46 eV and high porosity. The band gap characteristic offers the possibility to integrate GDY in transistors and transistor-like devices and to use it for gas separation, catalysis, etc. To date, only two GDY precursors have been used for the synthesis of GDY, namely hex-ethynyl benzene and 1,3,5-trythynyl benzene. Due to the very interesting properties predicted for GDY, we are endeavouring to synthesise new GDY materials from various organic precursors such as hexaethynylbenzene, hexakis[4-(ethynyl)phenyl]benzene, 1,3,5-tris[4-(ethynyl)phenyl]benzene and 1,3,6,8- tetrakis(ethynyl)pyrene using an APCVD reactor and Cu foils as substrate. The structural and physical properties of the produced GDY layers were investigated using a variety of spectroscopic and surface characterisation techniques. TEM analyses show that the GDY layers obtained are mostly amorphous, while optical bandgap studies show an insulator character. Our results contrast strongly with theoretical predictions and other published reports.

In summary, the points listed below have been successfully implemented: (*i*) synthesis of graphene from an abundant and problematic carbon source (CO_2); (*ii*) growth of NCG with formation of large crystal domains from an organic molecule; and (*iii*) fabrication of GDY layers from three different precursors. The syntheses described here offer alternative methods for obtaining high quality 2D materials.

Zusammenfassung

"***Synthesis and Characterisation of 2D Organic Materials***" ist eine am Karlsruher Institut für Technologie (KIT), Fakultät für Chemie und Biowissenschaften, angefertigte Dissertation zur Erlangung des Doktorgrades in Naturwissenschaften.

Mit der Entdeckung von Graphen wurde ein großes Interesse an verschiedensten 2D-Materialien geweckt. Grund dafür sind die außergewöhnlichen Eigenschaften, die Graphen aufzeigt. Seit nunmehr als einem Jahrzehnt nimmt die Zahl der Publikationen, die sich mit 2D-Materialien befassen stetig zu. Der Zuwachs an Publikationen ist einhergehend mit der Entwicklung und Entdeckung neuer 2D-Materialien. Trotz alledem ist Graphen aufgrund seiner bemerkenswerten elektronischen und mechanischen Eigenschaften weltweit das bislang am meisten untersuchte und in verschiedenen praktischen Anwendungen verwendete 2D-Material. Die vielfältigen Einsatzmöglichkeiten von Graphen machen unter anderem auch die Entwicklung neuer Herstellungsmethoden erforderlich. Dabei hat sich insbesondere die Chemical-Vapour-Deposition (CVD)-Methode zum Wachstum von Graphen-Schichten etabliert. Bei diesem Prozess ist die Herstellung sehr großer Graphen-Flächen möglich. Die für bestimmte Anwendungen nicht abstimmbaren elektronischen Eigenschaften von einlagigem Graphen führen dazu, dass Wissenschaftler nach alternativen Graphen-ähnlichen Materialien forschen. Eine mögliche Alternative ist z.B. nanokristallines Graphen (NCG), dessen Eigenschaften beim Wachstumsprozess kontrolliert werden können. Damit ist eine Feinabstimmung der elektronischen Bandlücke und seine Integration in Transistoren oder andere elektronische Geräte möglich. Zudem beschäftigt sich die Forschung auch mit neuen 2D-Kohlenstoff-Allotropen, welche in technologischen Anwendungen eingesetzt werden könnten. Die erforderliche Kontrolle beim Herstellungsprozess ist Motivation für die Entwicklung neuer Methoden zur Synthese von Graphen und NCG, sowie einem neuartigen kohlenstoffbasierten 2D-Material namens Graphdiyne (GDY).

In dieser Doktorarbeit umfasst das erste Forschungsprojekt die Synthese von Graphen unter Verwendung von Kohlenstoffdioxid (CO_2), einem umweltproblematischen Gas. Hierzu wurden verschiedene metallische Substrate getestet, um die Möglichkeit der CO_2-Aktivierung und -Reduktion zu Graphen zu untersuchen. Die ausgewählten Metalle sind Kupfer (Cu) wegen seiner Eigenschaften bei der Graphen-Synthese und Palladium (Pd) wegen seiner bekannten katalytischen Wirkung. Die Synthese wurde unter Verwendung eines Atmosphärendruck-CVD-Reaktors (APCVD) und Wasserstoff als Reduktionsmittel durchgeführt. Ramanspektroskopie, Rasterkraftmikroskopie (AFM) und Transmissionselektronenmikroskopie (TEM) bestätigen die Bildung von mehrlagigem Graphen. Darüber hinaus zeigen unsere Ergebnisse, dass CO_2 effektiv zu Graphen reduziert werden kann, wenn die Konzentration des Metallgemischs mehr als 82 at.% Cu enthält.

Im zweiten Forschungsprojekt wird versucht, nanokristallines Graphen (NCG) aus organischen Molekülen zu synthetisieren. Gängige Methoden der NCG-Synthese verwenden entweder Photoresist oder Polymere. Hierbei sind für die erfolgreiche Graphitierung des Vorläufers hohe Temperaturen, Vakuum und lange Belichtungszeiten notwendig. Die bei diesen Prozessen erreichbaren Domaingrößen liegen typischerweise bei 5 nm. Mit dem von uns durchgeführten Prozess, unter Verwendung des organischen Moleküls Hexaethynylbenzol, sind wir in der Lage großflächige NCG-Schichten mit größeren Kristalldomänen herzustellen. Diese zeigen in unseren Leitfähigkeitstests die erwarteten halbleitenden Eigenschaften.

Das dritte Forschungsprojekt beschäftigt sich mit der Synthese von Graphdiyne (GDY), einem neuen Kohlenstoff-basierten Material. GDY wurde als das stabilste nichtnatürlich vorkommende Kohlenstoff-Allotrop mit einer Bandlücke von 0,46 eV und hoher Porosität vorgeschlagen. Die Bandlückeneigenschaften bieten die Möglichkeit, GDY in Transistoren und transistorähnlichen Vorrichtungen zu integrieren und für die Gastrennung, Katalyse usw. einzusetzen. Bis heute wurden nur zwei GDY-Vorläufer für die Synthese von GDY eingesetzt, Hexethynylbenzol und 1,3,5-Triethynylbenzol. Aufgrund der für GDY sehr interessanten vorhergesagten Eigenschaften, sind wir daran interessiert, neue GDY-Materialien aus verschiedenen organischen Vorläufern zu synthetisieren, wie Hexaethynylbenzol, Hexakis[4-(ethynyl)phenyl]benzol, 1,3,5-tris[4-(ethynyl)phenyl]benzol und 1,3,6,8- Tetrakis(ethynyl)pyren. Dabei wurde ein APCVD-Reaktor und Cu-Folie als Substrat verwendet Die strukturellen und physikalischen Eigenschaften der hergestellten GDY-Schichten wurden mit einer Vielzahl von spektroskopischen und Oberflächencharakterisierungstechniken untersucht. TEM-Analysen zeigen, dass die erhaltenen GDY-Schichten größtenteils amorph sind, während optische Bandlückentests Eigenschaften eines Isolators zeigen. Unsere Ergebnisse stehen in starkem Kontrast zu theoretischen Vorhersagen und anderen veröffentlichten Publikationen.

Zusammenfassend lässt sich sagen, dass die nachfolgend aufgelisteten Punkte erfolgreich umgesetzt wurden: (*i*) Synthese von Graphen aus einer reichlich vorhandenen und problematischen Kohlenstoffquelle (CO_2); (*ii*) Wachstum von NCG mit Ausbildung großer Kristalldomänen aus organischen Molekülen und (*iii*) Herstellung von GDY-Schichten aus drei verschiedenen Vorstufen. Die hier beschriebenen Synthesen bieten alternative Methoden zur Gewinnung hochwertiger 2D-Materialien.

Dedication

This PhD thesis is dedicated to the memory of my grandparents Salvadora Maltéz de Molina and Pastor Jirón. It is also dedicated to my family, specially to the three pillars of my life: my mother Sofía Jirón de Molina, Martín Molina Maltéz, and to my lovely husband Eufemio Moreno Pineda.

Esta tesis doctoral está dedicada a la memoria de mis abuelos Salvadora Maltéz de Molina y Pastor Jirón. También, está dedicada a los tres pilares de mi vida: mis padres Sofía Jirón de Molina y Martín Molina Maltéz, y a mi amado esposo Eufemio Moreno Pineda.

Declaration

I, Concepción del Carmen Molina Jirón de Moreno, declare that this thesis entitled *"Synthesis and Characterisation of 2D Organic Materials"* and the work presented in it are my own and are part of the work undertaken under the supervision of Prof. Dr. Mario Ruben at the Institute of Nanotechnology (INT), at the Karlsruhe Institute of Technology (KIT). I confirm that:

- This work was done wholly while in candidature for a research degree at KIT.
- The whole thesis was written by me and no other sources other than the specified were used.
- The rules for ensuring good scientific practice of the Karlsruhe Institute of Technology (KIT) have been used and the submission and archiving of the primary data, in accordance with section A(6) of the rules for ensuring good scientific practice of KIT, has been ensured.
- The electronic version of the work is consistent with the written version.
- Where I have consulted the published work of others, this is always clearly attributed.
- I have acknowledged all main sources of help.
- Where the thesis is based on work done by myself jointly with others, I have made clear exactly what was done by others and what I have contributed myself.
- Furthermore, I declare that I did not undertake any previous doctoral studies and that I am currently not enrolled in any other ongoing doctoral procedure.

Signature: ______________________________

Date: ______________________________

Deklaration

Ich, Concepción del Carmen Molina Jirón de Moreno, erkläre, dass diese Arbeit mit dem Titel "*Synthesis and Characterisation of 2D Organic Materials*" und die darin vorgestellten Ergebnisse meine eigenen. Die Arbeit wurde unter der Leitung von Prof. Dr. Mario Ruben am Institut für Nanotechnologie (INT), am Karlsruher Institut für Technologie (KIT) angefentigt. Ich bestätige dass:

- Diese Arbeit wurde vollständig während der Kandidatur für ein Forschungsstudium am KIT durchgeführt.
- Die gesamte Arbeit wurde von mir verfasst und es wurden keine anderen Quellen als die angegebenen verwendet.
- Es wurden Maßnahmen zur Sicherstellung einer guten wissenschaftlichen Praxis des Karlsruher Instituts für Technologie (KIT) angewendet und die Übermittlung und Archivierung der Primärdaten gemäß Abschnitt A(6) der Regeln zur Sicherstellung einer guten wissenschaftlichen Praxis des KIT sichergestellt.
- Die elektronische Fassung des Werkes entspricht der schriftlichen Fassung.
- Im Fall, dass ich die veröffentlichten Arbeiten anderer konsultiert habe, wird dies immer eindeutig zugeordnet.
- Ich habe alle wichtigen Hilfsquellen zur Kenntnis genommen.
- Wenn die Arbeit auf Arbeiten basiert, die ich gemeinsam mit anderen geleistet habe, habe ich kenntlich gemacht, was von anderen geleistet wurde und was ich selbst beigesteuert habe.
- Des Weiteren erkläre ich, dass ich kein vorheriges Promotionsstudium absolviert habe und mich derzeit nicht in einem anderen laufenden Promotionsverfahren befinde.

Unterschrift: ______________________________

Datum: ______________________________

Acknowledgement

First of all, I would like to thank to the Almighty Lord for always blessing me.

I would like to thank Prof. Ruben for giving me the opportunity to conduct this PhD work in his working group.

During these three years I have met several people that have contributed to my personal and academic development. I would like to give them the acknowledgement they deserve.

First, I have to start with the person that has given me all the support and guidance that I needed during this time, to Eufemio Moreno Pineda, who has taught me all the necessary to become a good scientist.

Now I would like to thank all my labmates for all the help and support that they have provided me with. To Nithin ”IPB” Suryadevara, Zhi Chen, Verónica Gómez-Piedrafríta, Shirin Shakouri, Tingting Ruan, Asato ”Shinobi” Mizuno, Ami Saito, Svetlana Klyaskaya, Senthil Kuppusamy, Li Yu, Liang Xu, Nico Balzer, Michal Valasek, Sören Schlittenhardt and others that have share with us in the chemistry labs. All of you guys became my family during this time.

I want to thank my collaborator, and friend, Mohamed Reda Chellali for all the effort that he put in the work of “CO_2 to graphene”, thanks for the help that I received from you.

I will also like to thank mi parcero Leonardo Velasco for transmitting me part of his knowledge of SEM and for being always willing to give me a good explanation about materials science.

I would like to thank the TEM group, specially to Shyam Chethala, who was always willing to help me and explain my all about TEM, even when I was a bit lost. Thanks a lot for being very patient with me.

Talking about patient, I have to acknowledge Rainer Kraft for his collaboration in the transport measurement and for all the physic knowledge that he has taught me. Also I would like to thank Prof. Krupke, Preeti Pandey, Romain Daneau and Mrs. Simone Dehm, for all their help in the realisation of the transport measurement.

I would like to thank Mr. Stefan Walheim for taught me how to use the AFM. I would like to thank Mr. Hagen Sparrengeberger for being always very helpful with all about the labs supplies.

I cannot finish without acknowledging the people that have been always there, not only in the scientific part but also in the personal life. I thank my parents, Sofia Jirón de Molina and Martín Molina Maltéz for all their support during my whole life.

Now, I would like to thank my husband, Eufemio, you are my everything and you have always push me to be a better person and scientist, thanks for your patience, support and company.

Concepción del Carmen Molina Jirón de Moreno

Chapter 1

Introduction

1.1 Two-Dimensional Materials

2D materials, also known as single layer materials, are crystalline systems comprising a single layer of atoms. The existence of 2D materials was a debated issue in the first decades of the 20^{th} century, since 2D materials were thought to be unstable at any finite temperature according to classical physics[1,2]. For many years, several materials presenting layered structures, have been employed in their bulk forms[3]; examples of these are graphite and molybdenum sulphide (MoS_2). The layered nature of the materials is a consequence of the strong bonds within the atoms in the same plane but weak interactions between the layers above and below by van der Waals interactions[4]. Note that the weak van der Waals forces make it possible to obtain one to few layers 2D systems from the bulks forms.

Since Novoselov and Geim obtained for the very first time an isolated 2D material, known as graphene, through mechanical exfoliation of bulk graphite[5], there has been a boost in research towards novel 2D materials, the main driving force being the unique electronic[6], mechanic and physical properties[7] exhibited by graphene. To this end, a lot of effort has been devoted to the investigation on new 2D structures, more particularly on the synthesis and characterisation of other carbon- and non-carbon-based 2D materials[8]. The 2D material family has grown considerably and up to date several other members have been obtained and studied, such as: graphene, silicene, germanene, hexagonal boron nitrile (*h*-BN), silicon carbide (SiC), metal transition chalconides (TMCs) and their derivatives[2,9]. The structure of some members of the family of 2D material is shown in Figure 1.1. Many of the reported 2D materials have exhibited features such as low thickness, high breaking strain and variable electronic properties, that make them useful in flexible electronics applications[10]. On one hand, the semi-conductor properties shown by some 2D material gives the possibility to use them as flexible transistors[11,120]; while on the other hand, pristine graphene can be used as electrode material due to its high conductivity[13] (*vide infra*).

Moreover, one of the advantages of the 2D materials, compared to others low dimensional materials, is that some of them have bulk counterparts, which signifies that they can be synthesised not only through bottom-up but

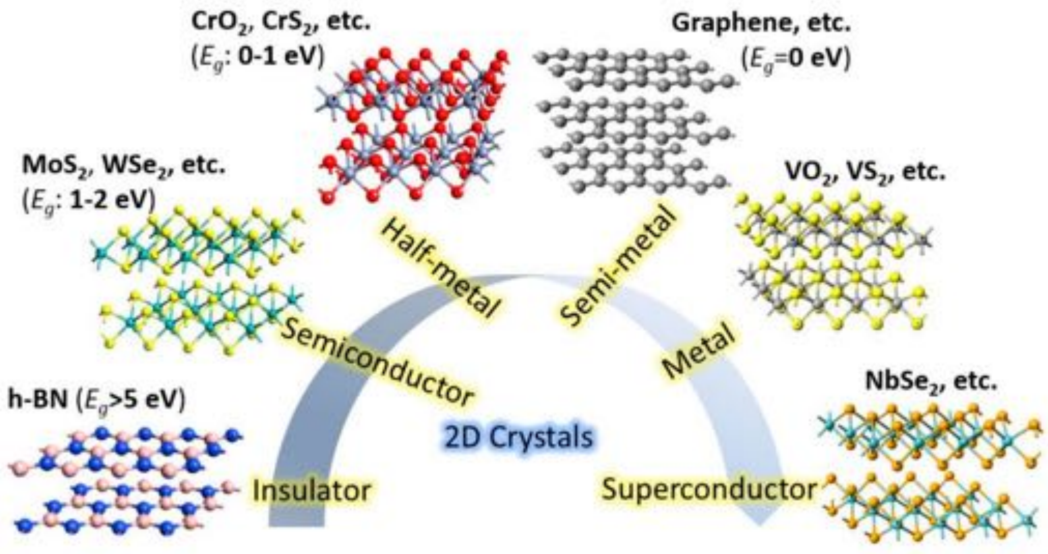

Figure 1.1: 2D Materials. Examples of 2D materials highly investigated in technological applications. Reproduced from Ref. [10]. Copyright 2014 Society of Photo-Optical Instrumentation Engineers (SPIE).

also by top-down approaches[14]. Additionally, 2D materials present layer-layer interactions, which entail unusual properties to the material allowing an excellent platform for the studies of fundamental physics[16]. The family of 2D materials has exhibited an wide spectrum of electronic properties including semimetals, metals, semiconductor with different band-gaps, and insulators[17,18]. Additionally, a sharp atomic interphase can be obtained by stacking or merging different 2D materials, creating a lateral or vertical hetero-structure, which can lead to new properties due to the layer-layer interaction, providing developments of new devices with different functions[19].

All the unique features of the 2D materials, make them potentially useful in many fields such as: optoelectronics, sensors, electronics, catalysis, sensors, flexible and wearable devices, among others[3,7]. The 2D materials properties are closely related to their structure, for example the number of layers, phases, doping, grain boundaries, defects, etc., have a vital influence in the electronics properties of the 2D material[3,20]. The materials, which present a high carrier mobility and low interface scattering, are commonly defect-free with few grain boundaries, and are considered high quality 2D materials. Large area and high-quality materials are required to develop devices with reproducible performance[21]. Nevertheless, to achieve such materials, it is important to understand the growth process to prepare a 2D system with controllable structure, quality, few grain boundaries, among other properties[22]. In this regard, different approaches have been developed for the synthesis of 2D materials such as: liquid exfoliation, mechanical exfoliation and vapour phase growth. The mechanical exfoliation was employed to delaminate bulk graphite using Scotch tape, which allowed to obtain for the first graphene. Unfortunately, this methodology presents some disadvantages such as its impossibility to obtain large area of 2D materials, as well as this methodology relies highly on the experience of the operator, due to the difficulties to control the number of layers, orientation and phase[8,23].

Undoubtedly, the properties of 2D materials, and the continuous technological advances force scientists worldwide to find (*i*) new 2D materials, which could also bring new properties to be exploited in several fields and (*ii*) the development of new synthetic methodologies too obtain higher quality 2D materials[23,24].

1.2 Characterisation of 2D materials

Several surface techniques have been employed for the characterisation of 2D materials, ranging from spectroscopic techniques up to microscopies[3,8,17]. The aim of this section is to introduce the basic concept of the most employed surface characterisation techniques used in this doctoral work.

1.2.1 Raman Spectroscopy

Raman spectroscopy is a technique based on the scattering of monochromatic light, typically from a laser source. During the scattering process, the energy of the light changes upon interaction with the material, process known as inelastic scattering[25]. During the scattering process a photon with energy $E_{Laser} = h\nu$ and momentum $p_{Laser} = p_s$ interacts with the sample and scatters producing a photon with an energy and momentum lower/larger than the initial energy, i.e. E_s and p_s, respectively. Due to energy conservation laws, the scattered photon has energy and momentum of the following form:

$$E_s = hv \pm E_q \quad \text{and} \quad p_s = p_s \pm i \tag{1.1}$$

where E_q and q are the energy and momentum of the photon that is annihilated or created during the scattering process. This change provides information about vibrational, rotational and other low energy transitions in materials[26].

The Raman effect results from molecular deformations in the electric field (E) determined by molecular polarisability (α). The laser beam, which can be considered as an oscillating electromagnetic wave with electrical vector E, induces an electric dipolar moment ($P = \alpha E$) upon interaction with the sample, resulting in the deformation of the sample. Due to the periodic deformation, the materials vibrate with an energy of the form E_q.

Raman spectroscopy is based on two photon scattering process, contrary to Infrared Spectroscopy (IR), which is a one photon process. Depending on the scattering process, three different processes can occur in Raman spectroscopy (see Fig. 1.2)[26,27]:

1. A material with no Raman-active mode absorbs a photon with energy $h\nu$ from a given vibrational state and the molecule returns back from the excited state to the same vibrational state. After de-excitation

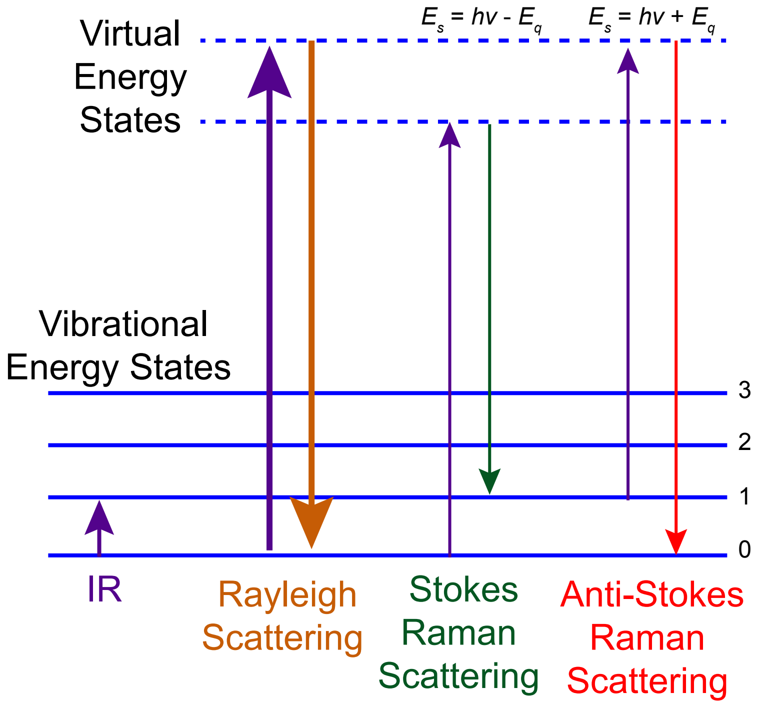

Figure 1.2: Raman Spectroscopy. Scheme of the energy transitions involved in Raman, i.e. Stokes, anti-Stokes and Rayleigh, the last two being two-photon process. Note that IR is a one-photon process.

a photon of energy $h\nu$ is emitted. This interaction, with no energy change, or elastic process, is termed as **Rayleigh scattering**.

2. A photon with energy $h\nu$ is absorbed by a Raman-active material, at the basic vibrational state. Certain amount of the energy of the photon is transferred to the Raman-active mode with energy E_q and the resulting energy of the scattered light is reduced to $E_s = h\nu\text{-}E_q$. The radiation scattered with a frequency lower than that of the incident laser energy ($E_s = h\nu\text{-}E_q$) is known as **Stokes radiation**.

3. A photon with energy $h\nu$ is absorbed by a Raman-active molecule, from an excited vibrational state. The energy excess of the excited Raman mode is released; hence, the molecule returns to the its basic vibrational state. The resulting frequency of scattered light increases an amount corresponding to the difference between the excited state at the time of the absorption and the ground state, i.e. ($E_s = h\nu+E_q$). That is, the difference in energy of the scattered photon corresponds to the difference in energy between the initial and final rotational and/or vibrational states. The scattered radiation has an energy larger than the incident energy ($E_s = h\nu+E_q$) of the laser is called **anti-Stokes**[25].

For carbon-based materials this technique is highly used, since it gives information regarding the type of carbon-based material under study, the thickness and the degree of defects present in the sample. Moreover, it is a non-destructive technique which can be used directly on the surface of the substrate, without requiring any complex sample preparation[28−30].

1.2.2 Atomic Force Microscopy (AFM)

AFM is a surface technique which provides information about the structural aspect of the material as well as the thickness of the material under study. This microscopy is based on the deflection of the laser beam system onto a position-sensitive detector. In AFM, a probing tip is attached to a cantilever and in response to the force between the cantilever, also called lever, and the sample, the laser light is deflected[31].

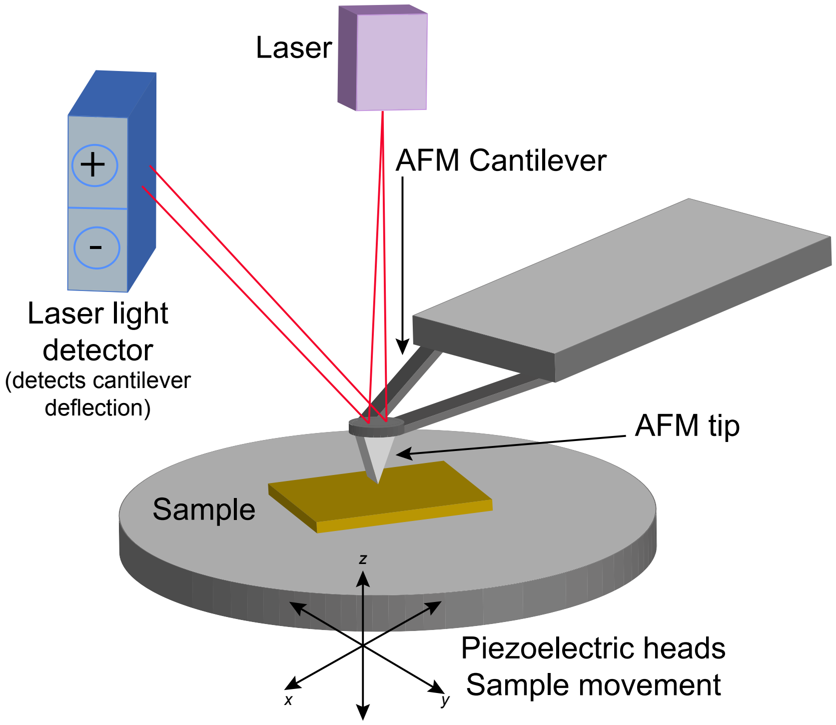

Figure 1.3: Atomic Force Microscope. Graphic representation of the AFM microscope and the detection mechanism involved.

In force microscopy the probing tip is attached to a cantilever-type spring. In response to the force between tip and sample the light on the lever is deflected. AFM images are recorded by scanning the sample relative to the probing tip and digitising the deflection of the light on the lever as a function of the lateral position x, y. AFM is based on the forces between the tip and the sample, hence, these forces allow the AFM imaging[32]. The force between the tip and the sample is not measured directly, but by measuring the deflection of the lever through Hooke's law[33]:

$$F = -kz \tag{1.2}$$

where F is the force and k is the stiffness constant of the lever and z is the position of the tip upon interaction with the sample.

A feedback loop, using the laser deflection, is employed to control the force and tip position. As observed in Fig. 1.3, the laser is reflected from the back of the cantilever of the AFM tip. As the tip interacts with the surface, the laser position on the photodetector is used in the feedback loop to track the surface for imaging and measuring[32,34].

The typical forces between probing tip and sample oscillate between 10^{-11} to 10^{-6} N allowing the non-destructive imaging. Two AFM modes are distinguished: contact and non-contact mode. In the non-contact mode, the tip-sample separations ranges from 10 to 100 nm, therefore, allows the sensing of forces such as van der Waals, electrostatic, magnetic or capillary forces, thus, providing information about surface topography, amongst others. When the probing tip is in contact with the sample, ionic repulsion forces permit the surface topography to be traced with high resolution[33–35].

1.2.3 Transmission Electron Microscopy (TEM)

The transmission electron microscope is an extremely powerful instrument for the characterisation of materials, since it provides not just morphological information at nanoscale level, but also give structural information through diffraction experiments. During the TEM experiment, a thin sample is irradiated with a high energy beam of electrons. During the process, the interactions between the electrons and the atoms can be used to observe characteristics of the materials such as the crystal structure, dislocations and grain boundaries, number of layers in multilayer system, etc. In addition, chemical analysis can also be performed through Electron Energy Loss Spectrometry (EELS). Furthermore, TEM can be employed for *in-situ* studies such as thermal treatments and reactions[36].

The basic principle of TEM is based on the same rules that the light microscope uses, but instead of employing light it uses electrons. The smaller wavelength of electrons than the wavelength of light, gives TEM a resolution order of magnitudes better than in conventional light microscopes. Due to the high resolution, TEM experiments can give access to fine details in materials up to atoms. Moreover, TEM can be carried out in two modes as follows[37]:

1. **Imaging:** in this mode, the electron beam is focused into a thinner beam by a condenser lens. High angle electrons are excluded by the condenser aperture. When the beam strikes the material under study, some part of the beam is transmitted, depending on the transparency and thickness of the sample. The transmitted portion of the beam is subsequently re-focused to a detector, typically a phosphor screen or a charge coupled device (CCD) camera. Enlargement of the image is achieved through sets of lenses. When the transmitted electron beam hits the detector, light is generated allowing the user to see an image of the specimen under study. The areas where the sample was hit with less electrons present a darker contrast than the areas where more electrons were transmitted (Fig. 1.4 (left)).

2. **Diffraction:** when the electrons pass through the sample, they are scattered by the interaction (electrostatic potential) between the beam and the atoms forming the sample. The scattered light then passes through an electromagnetic objective, which focusses the scattered electrons onto one point in the image plane. When the electrons are scattered in the same direction by the sample, they are collected in a single point,

leading to the formation of a diffraction pattern. The diffraction patter provides crystallographic information about the space group symmetries in the crystal, the orientation of the sample and, crystallographic constants (Fig. 1.4 (right)).

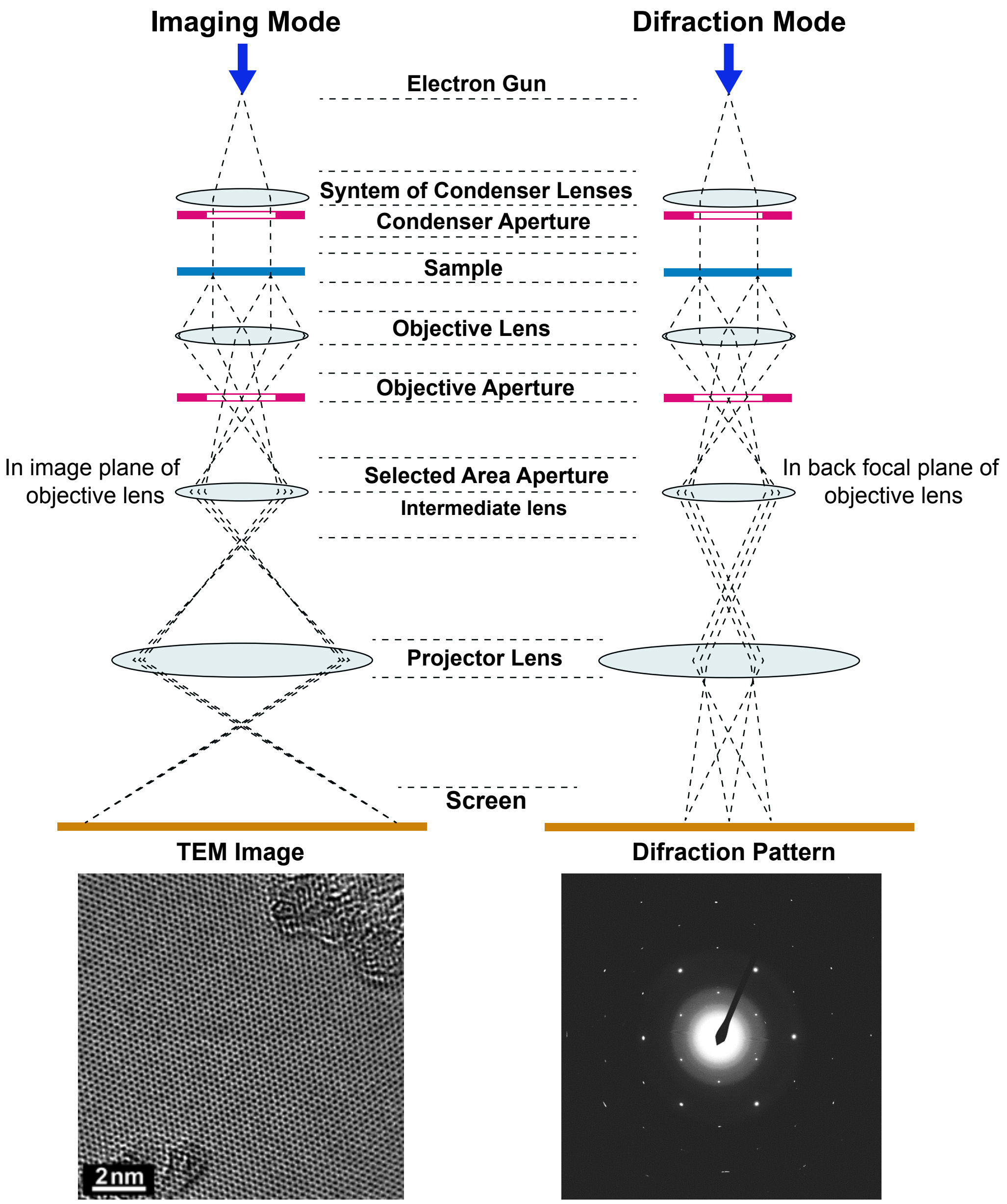

Figure 1.4: Transmission Electron Microscopy. Schematic view of the two operating modes of the TEM microscope. To the left side (top), the configuration for the imaging mode with an TEM image of graphene (bottom). To the right side (top), the diffraction configuration with the TEM diffraction pattern of a monolayer graphene (bottom).

1.3 Graphene

Many years ago, the existence of 2D materials were unimaginable, the arguments presented by Landau and Peierls was that a 2D material was thermodynamically unstable[1]. For several decades, scientist believed that obtaining an elemental atomic layer was impossible. The theory was experimentally supported by Mermin, who showed that at around a dozen of atomic layers, a 2D material became melted or destroyed[2]. It was until 2004, more than 50 years later, that Novoselov and Geim, utilising a very simple mechanical exfoliation method, employing scotch tape obtained a monolayer of graphite known as graphene[16,38]. This resulted in the isolation of an atomic monolayer with a honeycomb arrangement with highly crystalline structure. The two-dimensional sheet consists only in carbon atoms with sp^2 hybridisation. Moreover, graphene can be thought as the building block of all other carbon-based materials with different dimensionality[39]. For instance, graphene can be wrapped and become a 0D fullerene or stacked into graphite (3D) or rolled up to a 1D nanotube (Fig. 1.5).

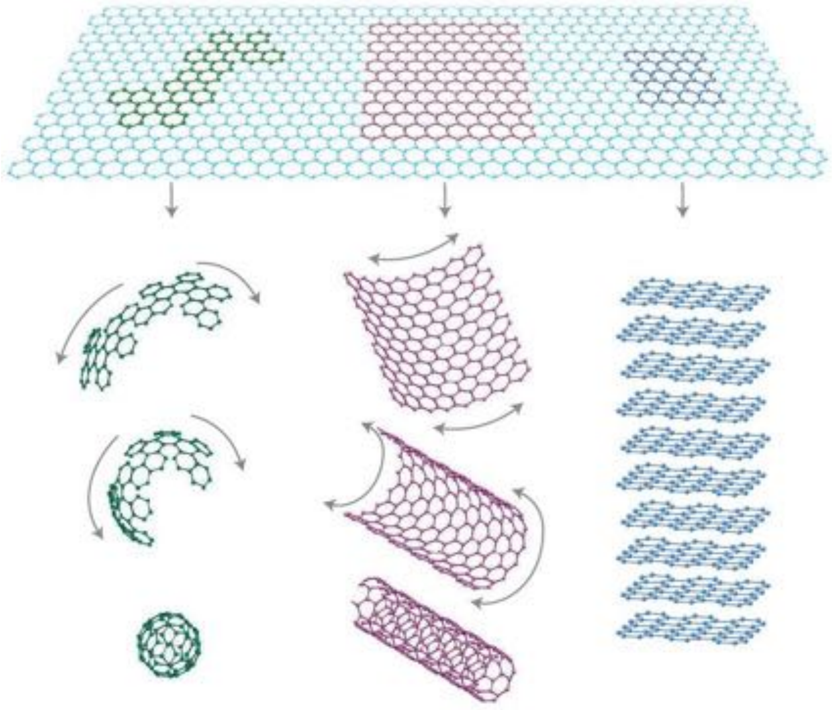

Figure 1.5: Graphene and Graphene-like Materials. Graphene as fundamental building block of all others carbon-based materials with different dimensionality. Reproduced from Ref. [1]. Copyright 2007 Springer Nature.

1.3.1 Graphene's Lattice

The elemental unit of graphene is carbon, being the responsible for the outstanding properties observed. The ground-state electronic configuration of C, the sixth element in the periodic table, is $1s^2 2s^2 2p_x{}^1 2p_y{}^1 2p_z{}^0$ (Fig. 1.6b). There are six electrons surrounding the nucleus of C, four of them are the valence electron (Fig.1.6a)[4]. Those electrons in the valence shell of C gives the possibility to form three hybridisations known sp, sp^2 and sp^3. The orbital $2p_z$ is shown empty for convenience, although the energy levels of the orbitals $2p_x$ and $2p_y$ are equivalent to the orbital $2p_z$[40].

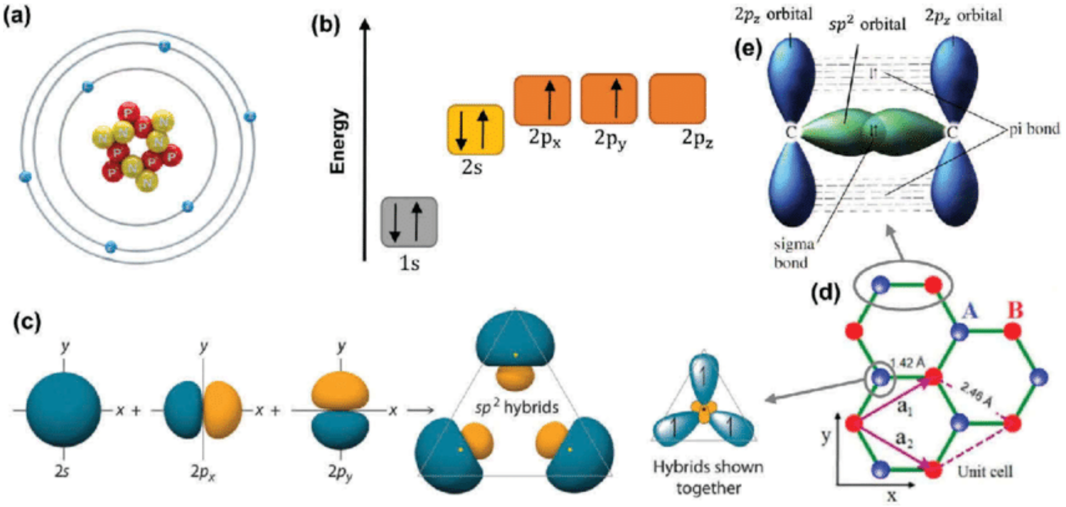

Figure 1.6: Schematic representation of the formation of graphene structure. (a) The atomic structure of Carbon; (b) Electronic configuration of C; (c) sp^2 hybridisation; (d) Crystal structure of graphene, unit cell and a_1 and a_2 are unit-cell vectors; (e) sp^2 hybridisation between to C atoms in graphene forming the π and σ bonds. Reproduced from Ref. [4]. Copyright 2018 G. Yang. et al. published by the National Institute for Materials in Science in partnership with Taylor & Francis Group.

The sp^2 hybridisation is formed by the interaction of the $2s$, $2p_x$ and $2p_y$ orbitals (Fig. 1.6c). In graphene, a honeycomb network of C with a planar structure is obtained when three neighbouring C atoms share the sp^2 electrons, yielding a monolayer[41]. The stability of the planar ring is a result of the resonance and delocalisation of the electron in the system. In graphene a normal sp^2 hybridisation of two atoms of C form an out-of-plane π orbitals which contain the $2p_z$ orbitals that are perpendicular to the planar structure. Moreover, an in-plane σ bond involves in the sp^2 hybridised orbitals $2s$, $2p_x$ and $2p_y$, resulting in a short inter-atomic length of 1.42 Å, that gives to graphene C-C bonds stronger than the C-C sp^3 bonds in diamond. This last point gives remarkable mechanical properties such as: strong Young's Modulus of 1TPa and intrinsic tensile strength of 130.5 GPa. Furthermore, the π orbitals between adjacent layers in graphene induce a weak Van der Waals interaction. The half-filled π band allows the free-moving electrons in graphene crystal structure, which triggers a zero band-gap between the conductance band and valance band. This results in graphene possessing an extraordinary electronic conductance[4,42].

As mentioned above, graphene cannot be described by a honeycomb lattice, due to the inequivalence between adjacent carbon atoms. In contrast, the hexagonal arrangement of graphene can be described by a triangular *Bravais lattice* composed of *two-atom basis*. Note that the distance between equivalents carbon atoms is 1.42 Å, which is the average distance between a σ bond (C–C) and a π-bond (C=C). The vectors connecting the inequivalent C atoms in the triangular Bravais lattice are then[4,41]:

$$\vec{a}_{1,2} = \frac{a}{2}(1, \pm\sqrt{3}) \tag{1.3}$$

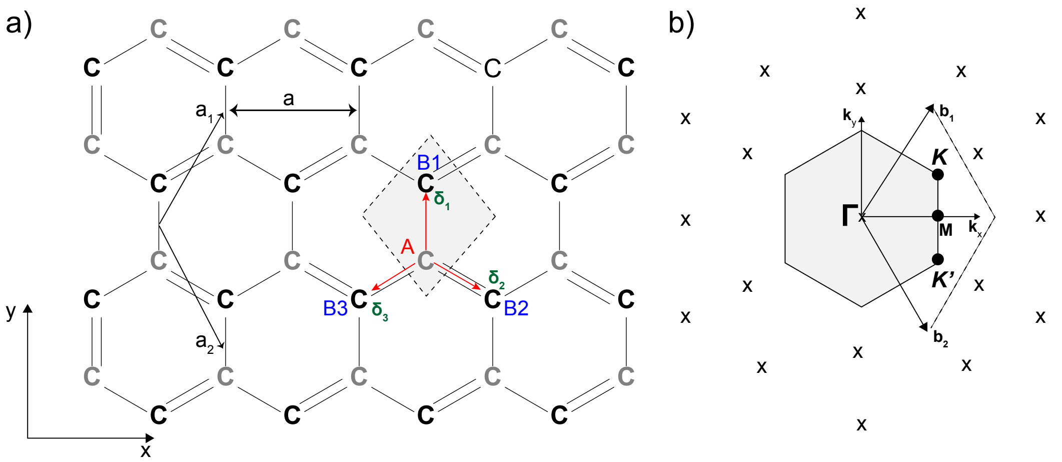

Figure 1.7: Graphene Crystal Structure.(a) Honeycomb lattice. The vectors δ_1, δ_2, and δ_3 connect the carbon atoms, separated by a distance $a = 1.42$ Å. The vectors a_1 and a_2 are basis vectors of the triangular Bravais lattice; (b) Reciprocal lattice of the triangular lattice. Its primitive lattice vectors are b_1 and b_2. The shaded region represents the first Brillouin zone (BZ), with its centre Γ and the two inequivalent corners K and K'.

The lattice spacing of the basis vectors is therefore, $a_0\sqrt{3}a = 2.46$ Å. The relative position of the vector of atoms B_l ($l = 1, 2, 3$) with respect to A_i is denoted as $\vec{\delta}_l$, and its three nearest neighbour vector (carbon atoms) are given by:

$$\vec{\delta}_1 = (0, \frac{a}{\sqrt{3}}), \quad \vec{\delta}_2 = (\frac{a}{2}, -\frac{a}{2\sqrt{3}}) \quad \text{and} \quad \vec{\delta}_3 = -\frac{a}{2}, -\frac{a}{2\sqrt{3}}) \tag{1.4}$$

The reciprocal lattice of a triangular arrangement can be defined by the Bravais lattice depicted in Fig. 1.7, with vectors of the form:

$$\vec{b}_{1,2} = (\frac{2\pi}{a}, \pm\frac{2\pi}{\sqrt{3}a}) \tag{1.5}$$

Physically, all sites of the reciprocal lattice represent equivalent vectors. Any propagating wave through the reciprocal lattice vector is a multiple of 2π, i.e. the vibrational excitation or quantum-mechanical wave packet. The first Brillouin Zone (BZ) in graphene is a set of inequivalent points in the reciprocal space, where long wavelength excitations are situated in the vicinity of the Γ point, in the middle of the first BZ. The six corners of the first BZ consist of the inequivalent points K and K' represented by the vectors[43]:

$$\pm K = \pm\frac{4\pi}{3\sqrt{3}a} \tag{1.6}$$

The four remaining corners (shown in grey in Fig. 1.7b) may indeed be linked to one of these points through translational symmetry by a reciprocal lattice vector. These crystallographic points play an essential role in the electronic properties of graphene since their low-energy excitations are centred around the points K and K'.

1.3.2 Applications of Graphene

Since the discovery of graphene thousands of publications have proposed its utilisation, leading to the investigation of new synthetic pathways for the growth of different types of graphene, e.g. monolayer, few-layer and multilayer graphene[44]. This aspect is of high importance, given that the physical properties of the obtained graphene can vary with the type of methodology employed for the growth of the material (Fig. 1.8). Therefore, the field in which graphene can be applied is contingent upon on the type of synthetic method employed. It has been shown a very wide range of technological application for graphene depending on the resistivity of this material. I will dedicate the following section to briefly describe some application in which graphene have been proposed as scaffold[45].

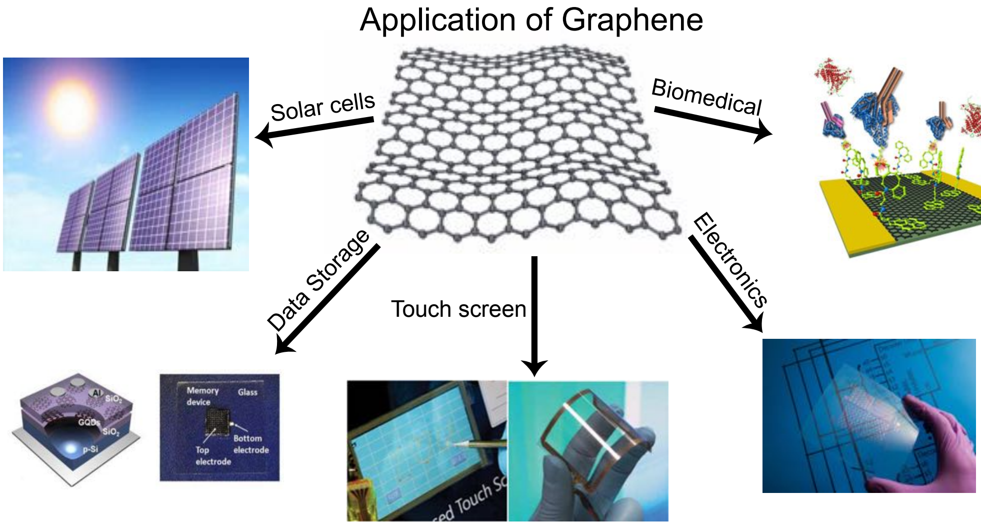

Figure 1.8: **Applications of Graphene.** Scheme of the diverse applications in which graphene could be integrated.

Data Storage: the continuous miniaturisation of technological devices pushes the technological industry to the nanometric limit. This, jointly with the reduction of size of storage device units, or the efforts to increment the capacity of the flash-drive, have driven the utilisation of graphene in data storage devices. The fabrication of flash memories from graphene is a field that has shown important findings. For example, graphene oxide, a chemically modified graphene containing oxygen groups, embedded in a modified indium electrode has shown write-read-erase-read-rewrite cycle for a non-volatile memory device. Additionally, graphene oxide has been utilised to design data storage devices yielding capacities of 0.2 Tbits cm^3, resulting in a capacity ten times higher than the current 16 GB USB flash drive. Moreover, Hong et al.[46] have created a prototype of graphene-based flash memories (GFM) material. By integrating graphene in a floating gate structure, the authors obtained a wide memory window and retention times longer than 10 years at room temperature[46]. Undoubtedly, these results highlight the advantages of graphene-based devices in storage technologies.

Electronics: due to the exceptional conductivity exhibited by monolayer graphene, it was proposed for the fabrication of high-speed electronics[47].

However, the electronic devices consist of semiconductor materials, which have a band-gap in their electronic structure that is required for ON and OFF states in the electronic devices. Conversely, graphene has exhibited a zero-band gap in its structure, therefore, scientist has turned their attention to few layer graphene. Currently, transistor application is only achieved in bilayers and when the electrical field is applied vertically it leads to an open band-gap. The control of the numbers of layers in electronic application is very important. In transparent electrode application, a low resistance, comparable to indium tin oxide (ITO) ($<100\ \Omega$/sheet), is required. In graphene this number is achieved only in 3-4 layers after doping. Moreover, the mechanical strength and flexibility of graphene gives some advantages over the ITO, which is inelastic and rigid. Furthermore, few-layer of CVD graphene has been employed as anode electrode in photovoltaic devices showing a power conversion efficiency (PCE) of 1.71%, which represents 55.2% PCE more of a device based on ITO.

Biotechnological Applications: graphene has also been used in biotechnological applications. An example of this in the utilisation of graphene as biosensors. The biosensors were prepared employing epitaxial graphene, grown of SiC, which was functionalised with antibodies to target the detection of the biomarker 8-hydroxydeoxyguanosine (8-OHdG). The 8-OHdG is an indicative in blood, saliva and urine of DNA damage, therefore, high levels of this biomarker are associated to increased risk of several cancer types[48]. The biosensor based on epitaxial graphene was commercialised one year after the first report (in 2016). Others studies have proposed graphene as replacement of the tungsten electrodes in the fabrication of electrodes for the body, due to the graphene flexibility, bio-compatibility and conductivity. Some investigations have also demonstrated that uncoated graphene can be employed as neuro-interface electrode without any alteration or damage in the signal strength or formation of scar tissue.

1.3.3 Synthesis of Graphene

The synthesis of graphene has become an important topic in the study of this 2D material owing to its outstanding properties, which have led scientist to find new ways to obtain larger areas with well-defined crystallinity. A controllable route is desirable since it will allow systematic control over graphene, hence, leading to a rational design of the particular properties for specific applications. There are two methodologies to prepare graphene, better known as (*i*) top-down approaches[47,49] and (*ii*) bottom-up[19,50]. Top-down processes consists on the de-lamination of the stacked layers of graphite. An example of this, is the first isolation of graphene achieved by mechanical exfoliation of graphite utilising scotch tape. Moreover, bottom-up approaches involve the synthesis of graphene from a carbon source such as organics molecules and gases (CH_4, C_2H_2, CO, etc.). Until now, there are few important challenges in the commercialisation of graphene, the most important is to produce a low-cost route to obtain large area, very crystalline and reproducible graphene. In this regard, many procedures have been developed over last decade (Fig. 1.9)[51]. In the following section a brief description of both methods is given.

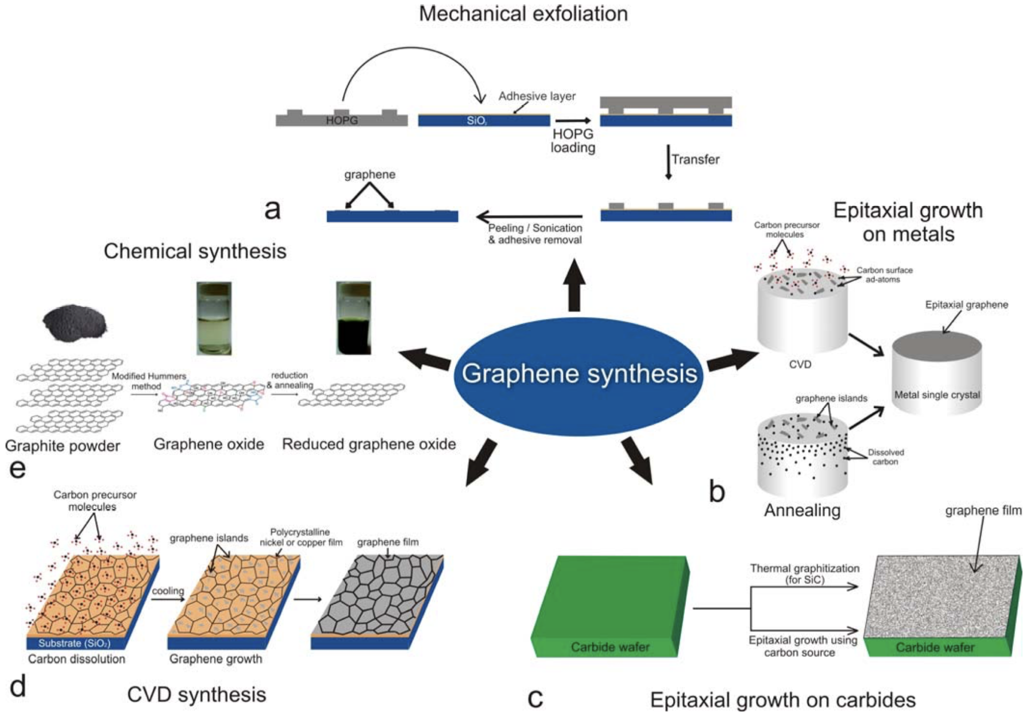

Figure 1.9: Synthesis of Graphene. The synthesis of Graphene has been accomplished using two different approaches: (*i*) Top-down and (*ii*) Bottom-up approaches. Reproduced from Ref. [51]. Copyright 2018 G. Yang. et al. published by the National Institute for Materials in Science in partnership with Taylor & Francis Group.

1.3.3.1 Top-down methodologies

Top-down approaches consist in the disassembling process of a system into its basic forms. Some of the common top-down approaches are described below.

Mechanical Exfoliation: The process of mechanical exfoliation involves the peeling layer by layer of a bulk material, in this case graphite. The Van der Waals attraction between adjacent flakes has to be overcome to complete the process. This mechanical issue can be overwhelmed through two different routes, i.e. lateral force and normal force. The normal force can be applied in the peeling of two layers of graphite with scotch tape, therefore, the Van der Waals forces are broken[39]. The motion between two layers can be promoted by applying lateral force through a graphite self-lubricating in lateral direction. These two routes are very well-used to yield a very high-quality graphene[52].

Liquid-phase Exfoliation: this methodology comprises the wet chemistry dispersion of graphite, following a sonication with the appropriate solvent. Surfactants can be employed during the liquid-phase exfoliation. A new methodology employing nanoparticles of Fe_3O_4 as “particle wedge”, for the assisted liquid-phase exfoliation of graphite has also been. described. This process offers some advantages such as: easy delamination, reduction of sonication time, thus, the arising structural defects from long-term sonication are also reduced. Lately, a green methodology has been reported that implies the exfoliation of graphite employing pure water free of surfactants or chemicals. Large areas of few-layers graphene were produced with this process. The strategy of this methodology involves the preparation of edge hydroxylated graphene with the assistance of vapour pre-treatment making the process of de-lamination easer[54].

Electrochemical exfoliation: The electrochemical exfoliation of graphite consists in the use of highly oriented pyrolytic graphite or graphite as electrodes in a solution (aqueous or non- aqueous). The electrochemical parameters such as applied bias current and the electrolyte concentration play an important role in the control of the thickness and the exfoliation/oxidation levels of graphene.

Chemical Reduction of Graphene Oxide (GO): The reduction of graphene by employing chemical reagents is a methodology used to produce large-scale of this material. The procedure presents few disadvantages due to the utilisation of toxic reductants (hydrazine or sodium borohydride), as well as the obtained reduced graphene tends to re-agglomerate. The new trend in this regard is to utilise green and environmentally friendly reagents[55,56]. There are many studies of the improvement of this methodology, since it can yield large-scale reduced graphene with the appropriates properties.

Although it is possible to obtain graphene from top-down methodologies, each methodology has some drawbacks. For instance, the mechanical electrochemical and exfoliation methods are capable of fabricating monolayers to few-layers of graphene, but the reproducibility of the obtained graphene flakes employing these methodologies is minimal. Moreover, fragmentation of graphite can occur as a result of the mechanical process, leading to small area of graphene[57]. In addition, graphene synthesised from reduced graphene oxides (RGOs) usually causes incomplete reduction of graphite oxide, resulting in the successive degradation of electrical properties depending on its degree of reduction.

1.3.3.2 Bottom-up approaches

Contrary to top-down approaches, a bottom up synthesis method consists in the synthesis of the nanostructures employing the basic units, therefore, directly building atom-by-atom the desired materials. In the following a brief description will be given for common bottom-up synthesis, with particular attention of Chemical Vapour deposition (CVD), synthetic method employed in this doctoral work[57].

Epitaxial Growth: epitaxial graphene has been obtained by thermal decomposition of SiC, it can be applied in graphene-based electrical devices without any transfer procedure. The process involves the desorption of Si at increased temperatures, leaving the carbon atoms behind to form few-layer graphene. The desorption of only Si atoms is due to their vapour pressure is small compared to C[58]. Additionally, this type of process requires high vacuum to avoid any contamination. Furthermore, Cu (111) and other transition metals, such as Pt(111), Ni(111), Ir(111) and Ru(111), have been used to obtain epitaxial graphene grown from a thermal decomposition of ethylene in an ultra-high vacuum chamber[59,ref]. One of the major disadvantages of this method is that there is no control over the thickness and homogeneity of the grown graphene and it is not possible to transfer the graphene onto any other substrate[60].

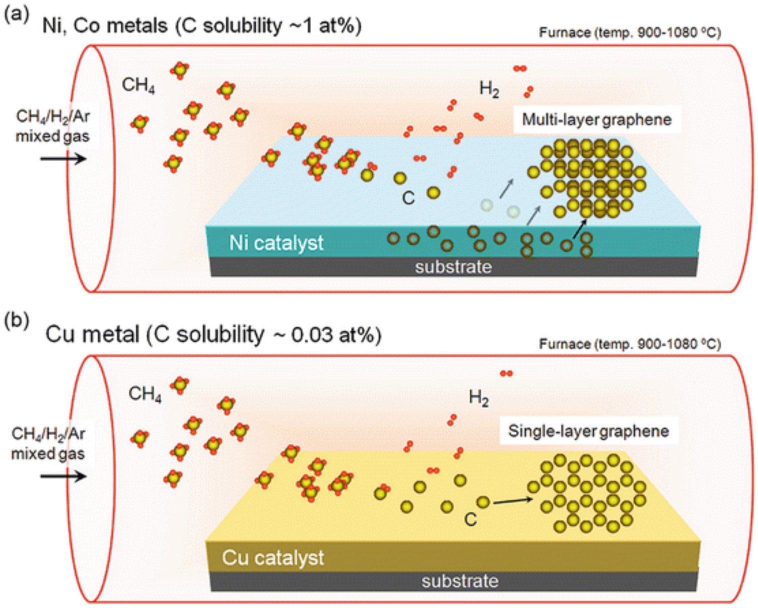

Figure 1.10: Synthesis of Graphene. Schematic representation of CVD growth of graphene employing metallic substrates. Reproduced from Ref. [62] with permission of Springer Japan.

Chemical Vapour Deposition: CVD has become the most employed methodology to grow graphene on metallic substrates at high temperatures (Fig. 1.10). Unlike the epitaxial growth that also involves a thermal treatment, the metallic substrates employed in CVD growth are normally polycrystalline thin foils, therefore, their grains are randomly oriented[61]. The first successful experiment on growing graphene employing a CVD reactor and CH_4, as the carbon source, was performed using Ni as the metallic substrate. Since then, many experiments were carried out to synthesise graphene on Ni, however, the process was not self-limited leading to high thickness. Additionally, the rate of the cooling played an important role in the formation of the graphene film. On one hand, it was observed that at very fast cooling rates, there was no graphene formation since most of the C was trapped within the Ni lattice, due to the high solubility of C in Ni. On the other hand, moderate cooling rates can lead to an appropriate formation of graphene, however, leading to thick graphene. The mechanism of graphene growth on Ni involves the dissolution of carbon on Ni in the solid state. This metal has a considerable solubility of C, which represented a problem in the growth of graphene, as reflected in the thickness. Lately, scientists turned their attention to the utilisation of Cu foil as substrate for graphene growth. Cu presented an important advantage over Ni: the solubility of C in Cu at the solid state is very low, therefore, the thickness of the grown graphene is limited to the Cu surface. Moreover, with Cu substrate it is possible to obtain from monolayer to few-layer graphene[62,63].

CVD methodology presents few disadvantages, for instance: the polycrystalline nature of the metallic substrates and the transference process, which might induce many defects, such as cracks in the film. Many efforts have been made in the improvement of the transference process, yielding several suitable approaches. It has to be highlighted that the CVD process offers the possibility of obtaining large-scale areas of monolayers to few-layer graphene. Lately, there are some attempts trying to grow graphene directly on di-electric substrates and on glass at much higher temperature for their direct use in electronic devices[11].

1.3.4 Characterisation of Graphene

Raman spectroscopy has been employed as the most valuable tool for the characterisation of graphitic materials. For graphene, it not just allows its characterisation, but also allows the determination of the number of layers, quantification of defects, doping level and the indirect assessment of the electronic properties *via* the study of the electron-phonon coupling. Moreover, Raman spectroscopy has proven to be the most popular technique for the characterisation of a wide range of carbon-based materials such as amorphous carbons, fullerenes, diamonds, carbon chains, polyconjugated molecules and carbon nanotubes[64].

The Raman spectra of a monolayer of crystalline graphene (MLG) shows two important peaks, corresponding to the different allowed vibrational modes of the systems. These vibrational modes have been coined as G ($\approx$1580 cm^{-1}) and 2D peaks (also often termed as G′ peak, occurring at $\approx$2700 cm^{-1}). The G peak is associated with the doubly degenerate (E_{2g} symmetry) longitudinal optical (LO) and in-plane transverse optical (TO) phonon mode at the centre of the Brillouin zone (Γ); while the 2D peak is the overtone of the TO phonon around the K points. Note that the G peak is position independent of the excitation energy of the laser (Fig. 1.11)[65].

1.4 Nanocrystalline Graphene

An ideal single layer of graphene, displays a zero band-gap, an elevated tensile strength and large thermal conductivity at room temperature. Unfortunately, in spite these extraordinary properties, the number of applications in which a single layer of graphene can be used are limited, hence, other materials must be incorporated or assembled, in order to be employed in several technological applications. Some of the desired characteristics of graphene might be improved during the assembling process, nevertheless, the amount of the disorder and defects introduced to the graphene sheet is not fully controllable. Furthermore, disorder can also be introduced into graphene during the synthetic process, such as topological defects, vacancies, sp^3 defects, among others[4].

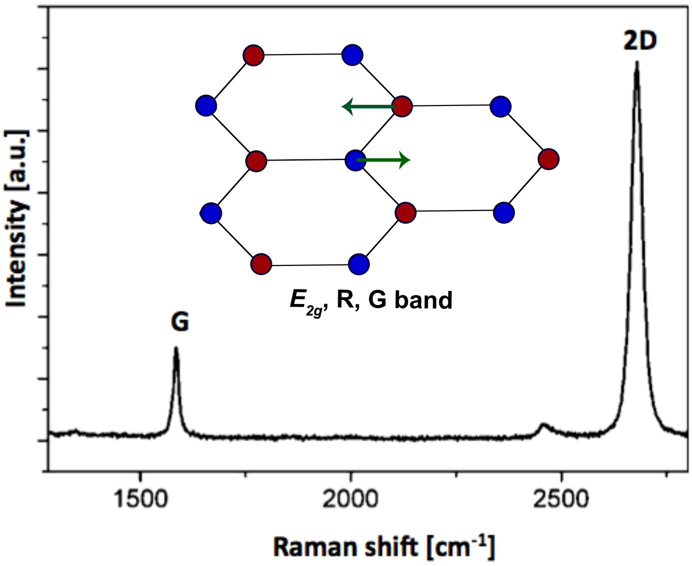

Figure 1.11: Raman of Graphene. Raman Spectrum of monolayer Graphene exhibiting the G and D modes and the vibrational modes of the G band (Inset).

Recently, it has been shown that graphene-like materials are also of technological importance[66]. It has been shown that graphene-like materials can be grown on different substrates in controllable forms and thicknesses *via* thermal graphitisation of the polymer films[24]. The thermal graphitisation of the polymer films can result in domain sizes of the order of a few nanometres; hence, these materials have been termed nanocrystalline graphene (NCG). Technologically, nanocrystalline graphene is of high importance, and has been studied in applications such as photonics, electronics, strain sensing or transparent conducting electrodes, are some examples[67,68].

Moreover, the investigation of NCG is just commencing, as evidenced by the number of publications of NCG compared to the large number of publications of graphene. Consequently, there is a large number of possible applications and synthetic methodologies to be investigated for NCG, making it an attractive material for the scientific community.

1.4.1 Synthesis of Nanocrystalline Graphene

Conventionally, nanocrystalline graphene is grown employing carbonaceous materials at high temperatures, yielding few nanometre size crystalline domains. Depending on the carbon source, the technique can be classified as follows:

Conversion of SAM: NCG can be fabricated by cross-linking of aromatic self-assembled monolayers (SAMs) *via* electron-radiation and posterior annealing at elevated temperatures (> 900 °C). The report presented by Turchanin et al. shows that graphitisation of the SAMs can be conducted in two ways: (*i*) the cross-linking of the SAMs is carried out on a gold substrate (Au), followed by the transference of the material to a SiO_2 substrate for the annealing step at high temperature; (*ii*) the functionalisation of SAMs on the Au substrate and direct annealing on the Au substrate. Afterwards, the obtained NCG is transferred to the desired insulator substrate. One disadvantage of this synthetic method is the number of defects and low mobility at room temperature[69].

Graphitisation of photoresist: NCG can also be obtained by direct growth of NCG on different substrates from photoresists by annealing it at 1000 °C in the presence of H_2 and Ar gas mixture. The thickness of the NCG can be controlled by the initial thickness of resist material. A drawback in this method is the prolongated heating treatment (up to 24 hours) and the relatively small size of the crystal domains ($<$5 nm)[67,70].

Growth of free-standing nanocrystalline graphene: It has been shown that NCG can also be obtained *in-situ* during TEM studies by heating of a free-standing polymer film. Between 600–1000 °C the growth of the crystalline domains of NCG occurs by the consumption of the residual amorphous carbon around the graphitic domains. The amorphous carbon is transformed in one of two alternative ways, either by catalyst free growth onto the graphitic layer or by attachment to the active edges of graphitic domains. This catalyst free transformation creates new small graphitic structures, some of which are highly mobile at higher temperatures and are attached to other edges, increasing the domain size. At temperatures between 1000–1200 °C, the growth proceeds by merging of the large domains, which become active at elevated temperatures. As can be inferred, the NCG grown by this technique is of very limited size, due to the inherent TEM characteristics[71,72].

1.4.2 Characterisation of NCG

The characterisation of the structural properties of NCG, such as grain size, and its effect on the electrical and thermal transport properties are of major interest for technological devices. Disorder-induced symmetry-breaking effects have an important effect on the properties of the materials, such as the relaxation of photo-excited carriers and transport properties. The sp^2 carbons, possessing a high symmetry, particularly are highly sensitive to symmetry-breaking disorder, which can be efficiently detected *via* spectroscopy, being contingent upon the symmetry of the material. Raman spectroscopy has been established as one of the most sensitive, and informative, technique for the characterisation of sp^2 carbon materials. The presence of disorder in NCG, mainly composed of sp^2 hybridised carbon, leads to a very rich and intriguing Raman spectra[65].

1.4.2.1 Raman of NCG

As described in earlier sections, the Raman spectrum of a monolayer of graphene exhibits solely two bands, i.e. G and 2D peaks, at 1580 cm^{-1} and 2700 cm^{-1}, respectively. These two arise due to the perfect crystalline structure and defect free character of the MLG. The G peak results from LO and TO phonon modes, arising from a three-step process in graphene. The 2D-band, which is an overtone (or second harmonic) of the D-band is a symmetry allowed second-order Raman process. This mode is accessed by a combination of two TO phonon around the K points (*vide supra*). This band is always observed, even in the absence of defects, and has a frequency twice the observed for the D peak. The D peak depends on the excitation wavelength of the laser and varies from 2640 to 2700 cm^{-1} for 633 to 488 nm. The 2D-band is very sensitive to foreign dopants and electrostatic gating; however, the primary use of the 2D-band spectrum has been to gain knowledge of the number of layers in bi to few layers' graphene, due to the sensitivity to the stacking order and to inter-layer interactions[73].

In contrast, upon increasing the level of disorder and number of defects, the symmetry of the system is lowered and further peaks arise. This is the case of another peak, known as D peak, which occurs at around 1300 cm^{-1}, and is a result of the lowering of symmetry of the perfect structure of graphene (Fig. 1.12). Note that the letter "D" denotes disorder-induced. This peak is a consequence of the double resonant Raman process and occurs in a four-step process: (*i*) absorption of photon, (*ii*) elastic defect scattering, (*iii*) inelastic scattering of electron-phonon, and (*iv*) electron/hole recombination plus photon emission. Furthermore, the D peak position varies with excitation energy, thus, a D phonon with larger momentum has a higher energy causing a larger red-shift for higher excitation energies. The D peak has been employed as the signature for the identification of nanocrystalline graphene. A pronounced D peak with respect to G peak denotes smaller grain size[16,74,75].

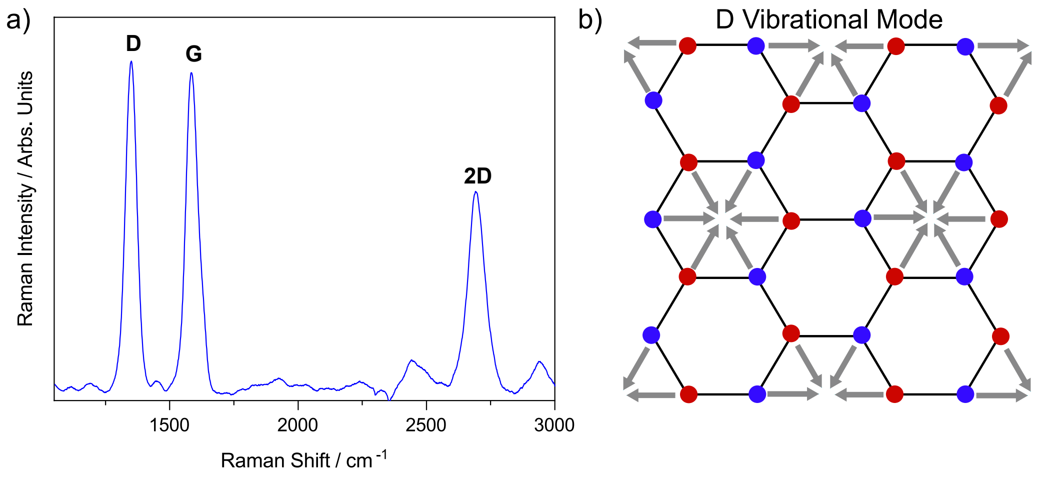

Figure 1.12: Raman Spectrum of NCG. (a) Raman Spectrum of nanocrystalline Graphene; (b) D vibrational mode, induced by the defects in NCG.

1.4.2.2 Determination of Crystal Size in Graphene

The determination of the crystal size in NCG is of high importance, as it is directly reflected on the physical properties of the graphitic material. Raman spectroscopy has proven to be also a valuable tool for the determination of the crystal size on nanocrystalline graphite, as described by pioneer works in the 1970 by Tuinstra and Koenig, who noted the relationship between the intensity ratios of the D and G peaks and the crystal size of the nanocrystalline graphite[76]. In their report, Tuinstra and Koenig highlighted that the crystal size L_a varies inversely with the intensity of the D and G peaks as follows[77]:

$$\frac{I_D}{I_G} = \frac{C(\lambda)}{L_a} \tag{1.7}$$

where C is a proportionality constant (515.5 nm) = 440 nm. This relationship is only valid for large crystal size or low defects. Upon increasing disorder, the I_D/I_G behaves in two different manners. In the first behaviour, the I_D/I_G increases due to the larger density of elastic scattering created by the higher number of defects. The increment of I_D/I_G will change and start decreasing as soon as the number of defects is too high, which indicates the formation of amorphous carbon, hence, attenuating the Raman peaks.

If the density of defects is larger than ~6 nm, then the size of the crystal domains can be obtained from:

$$\frac{I_D}{I_G} = \frac{C(\lambda)}{L_a^2} \tag{1.8}$$

where $C(\lambda)$ = 102 nm for 514 nm laser excitation.

The high defect regime was denoted by Ferrari et al. as NCG and mainly sp^2 amorphous carbon phases. In the high defect region, the I_D/I_G ratio is directly proportional to square of the crystallite size as follows:

$$\frac{I_D}{I_G} = C(\lambda)L_a^2 \tag{1.9}$$

The $C(\lambda)$ for eq (1.8). is 0.0055 at 514 nm laser excitation. Note that the low defect regime follows the original Tuinstra and Koenig relation. However, it has been found that the of I_D/I_G peak depends on the excitation energy of the laser. Cançado et al. generalised the formula of Tuinstra and Koenig to account for the energy or wavelength of the Raman laser line as[78]:

$$\frac{I_D}{I_G} = \frac{560}{(E_l^4)(L_a)} \tag{1.10}$$

$$\frac{I_D}{I_G} = \frac{2.4 \times^{-10} (\lambda)}{L_a} \tag{1.11}$$

Where L_a is given in nm scale, while the average integrated intensity area ratio is considered, instead of the peak intensity ratio of I_D/I_G. These two relationships are valid for crystal sizes larger than 10 nm. Later Cançado et al. showed that the full width at half maximum (FWHM) of all the three distinct peaks of NCG are independent of excitation laser energy, hence, formulating the equation as function of FWHM as[79]:

$$\Gamma_{FWHM} = A + B + L_a^{-1} \tag{1.12}$$

The values A and B are linear fit parameters and have been tabulated experimentally from X-ray diffraction and Scanning Tunnelling Microscopy (STM) data and are given in Table 1.1.

Table 1.1: Parameters A and B obtained for the D, G, and 2D bands.

Γ_{FWHM}	A / cm^{-1}	B / cm^{-1}
Γ_D	19	500
Γ_G	11	560
Γ_{2D}	26	1000

1.4.2.3 Amorphisation of Hybridised carbons

The signatures of graphitic materials in the Raman spectra is of utmost importance for the identification of the nature of the graphitic material, i.e. to distinguish between graphene to amorphous carbon with solely sp^3 carbons. The dependence on the physical properties on the sp^2 to sp^3 ratio offers a great versatility to carbon-based materials. Various degrees of graphitic ordering, ranging from nanocrystalline graphite to glassy carbon, exist deepening on the sp^2 bonded carbons[80].

It has been shown that graphite can be converted to NCG by thermal treatment. The evaluation of the amorphization trajectory, can similarly be estimated by Raman spectroscopy, where the several stages from ordered graphite to NCG to amorphous carbon and finally to sp^3 bonded tetrahedral amorphous carbon can be noted. By inspection of the peak position and the intensity ratio of I_D/I_G, the amorphization state of the carbon material can be easily deduced. For NCG the position of the G peak shifts from 1600cm^{-1} to 1580 cm^{-1}, as a result of amorphization of sp^2 carbons. Furthermore, the maximum of I_D/I_G changes with the carbon type on the material, resulting in a powerful tool for the determination of the degree of crystallinity and defects in NCG[73,75,77].

1.5 Graphdiyne

Besides graphene and its derivatives, several other 2D materials have been studied for their implementation in different fields. Amongst them, other carbon based 2D systems have also been envisaged as prospect materials for several applications[81,82]. An example of carbon based 2D systems are the Graphynes 2D materials, which are formed by the combination of sp- and sp^2-hybridised carbon atoms (Fig. 1.13)[83]. The presence of sp-hybridised carbons confers graphyne materials properties different to the observed for sp^2-containing carbon allotropes, i.e. graphene, NCG, carbon nanotubes, etc. For instance, the well distributed large pore structures and π-conjugation have been proposed in gas separation technologies, and energy related field[84,85].

The first proposal of graphdiyne (GYD) was reported in 1987 by R. H. Baughman et al.[86], however, the very reactive nature and flexibility of sp-carbons precluded its synthesis until 23 year later, when through an *in-situ* Glaser coupling reaction of the hexaethynylbenzene (HEB) molecule on a copper (Cu) substrate was obtained[87]. The report of the first GYD boosted the investigation of the synthetic pathways of GDY and the applicability of

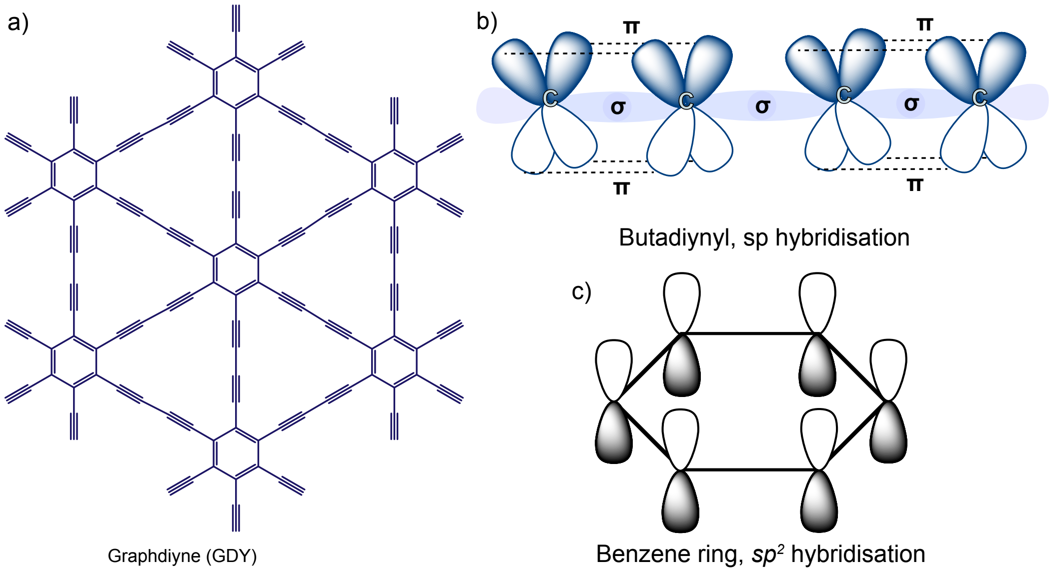

Figure 1.13: Graphdiyne. Schematic represenation of GDY from hexaethynylbenzene and *sp* hybridisation of carbon in the network

these materials in many applications[83].

GDY comprises a 2D planar network composed of diacetylenic bonds between benzene rings. GDY is the most stable non-natural carbon allotrope encompassing diacetylene bonds and theoretical reports have predicted a direct band-gap of 0.46 eV and large carrier mobilities (10^4-10^5 cm^2 V^{-1} s^{-1}) at room temperature[88], hence, GDY has been proposed as highly promising 2D material for nanoelectronics. Since the first report of GDY, several related systems with different morphologies have been reported, e.g. films, nanowires, powders and nanowalls. These have been obtained employing various synthetic methodologies, such as wet and dry, and have been proposed in many different areas ranging from catalysis to water remediation[83,89].

Despite being known for already almost 10 years, GDY films are far from the ideal single atom films, solely composed of *sp* and sp^2-carbons. Instead, GDY are often few to multilayer systems with low crystallinity, highlighting the difficulties faced during the growth process. In the following sections I will revised the most important aspect of this prospect carbon-based 2D material.

1.5.1 Structural Aspects

Graphynes is the generic name to refer to a class of carbon-based structures where two adjacent sp^2-hybridised carbon atoms are connected by acetylene groups. The 2D structure of Graphynes is reminiscent of that of graphene, however, in contrast to graphene, the carbons are covalently bound by *sp*- and sp^2 carbon atoms. The classification of these materials is, therefore, achieved by the number of -C≡C- present between two adjacent sp^2-carbons in the 2D network (Fig. 1.14)[90].

Conversely to graphene and NCG, four types of carbon-carbon bonds can be observed in graphynes, i.e. (*i*) sp^2-sp^2 carbon bonds of the benzene rings; (*ii*) the sp^2-sp carbons bonds between neighbouring C=C double and C≡C triple bonds; (*iii*) sp-sp triple carbon bonds; and (*iv*) the sp-sp single carbon bonds linking adjacent C≡C bonds. Commonly, the predicted bond lengths for the four different bonds of graphynes are 1.48-1.50 Å (aromatic bonds), 1.18-1.19 Å (triple bonds), and 1.46-1.48 Å (single bonds).

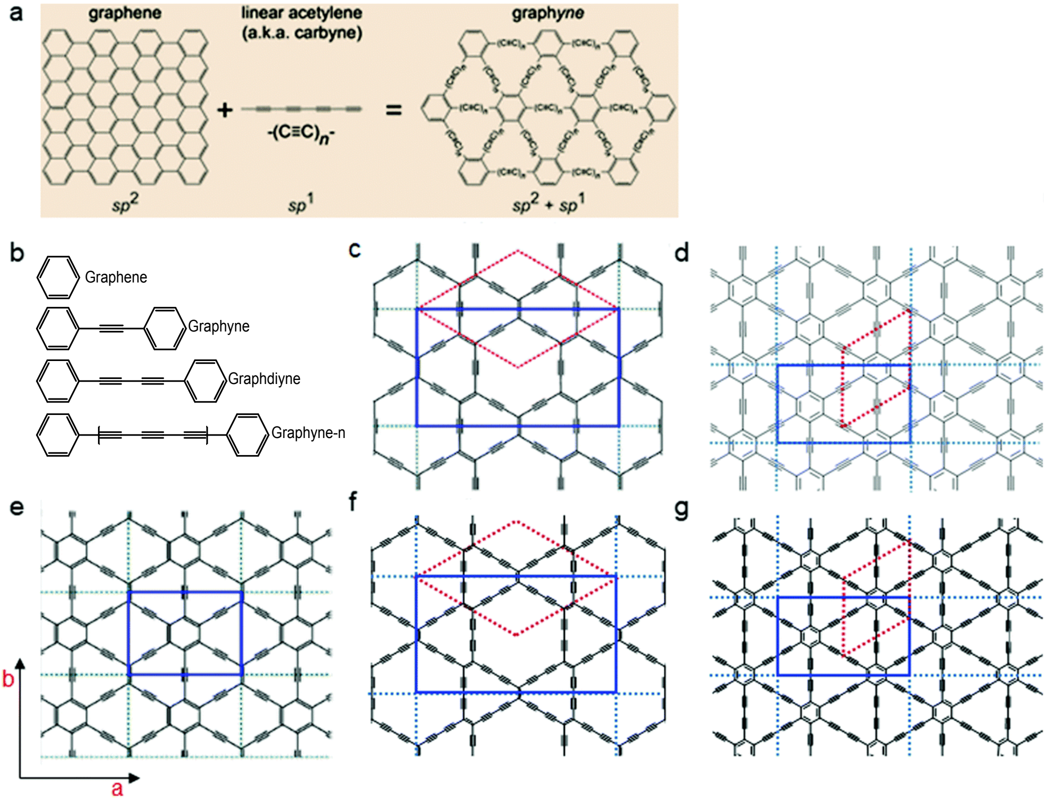

Figure 1.14: Graphynes Family. (a) schematic representation of the structure of graphene and GDY; (b) Graphyne units; (c) β-graphyne; (d) γ-graphyne; (e) 6,6,12-graphyne; (f) β-graphdiyne; and (g) GDY. The red dotted line in (b–d); (f) and (g) show the primitive cell, indicating the smallest repeating unit for constituting graphyne. Modified from Ref. [83] with permission of Royal Society of Chemistry 2019.

The structural aspects of graphynes, i.e. crystal structure and symmetry, are contingent upon the arrangement of the *sp*- and sp^2-hybridised carbons (Table 1.2). The majority of graphynes have hexagonal symmetry, such as graphene, with the exception being for 6,6,12-graphyne, which possesses a rectangular symmetry. In table 1.2 are given the lattice constants for some graphynes structures and are compared to graphene, with no *sp*-carbon. Among the several graphynes structure proposed, GDY has been predicted as the more stable carbon allotrope containing butadiynyl -C≡C-C≡C- bonds[91].

The bond lengths in GDY are 1.41 Å for the sp^2-sp^2 carbon bonds in benzene rings, 1.40 Å for the sp^2-sp carbon bonds in-between neighbouring C=C double and C≡C triple bonds, 1.24 Å for the triple sp-sp carbon bonds, and 1.33 Å for the single sp-sp bonds connecting two adjacent C≡C bonds. The

Table 1.2: Parameters **A** and **B** obtained for the D, G, and 2D bands.

Carbon allotropes	Lattice constant / Å	Acetylenic linkages / %
β-Graphyne	9.5004	66.67
γ-Graphyne	6.8826	33.33
6,6,12,-Graphyne	$a = 9.44$; $b = 6.90$	41.67
γ-Graphdiyne	9.48	50
Graphene	2.47	0

sp-sp bonds connecting two adjacent C≡C bonds has some character of double bonds through the effect of conjugation.

One of the most employed technique to investigate the structural aspects of GDY is Transmission Electron Microscopy. Calculation of molecular dynamics simulation (VASP) method of GDY has predicted the optimised lattice constant to be 9.48 Å. As graphene, the GDY lattice also belongs to the hexagonal unit cell with the P_6/mmm space group. To calculate the d-spacing of the hexagonal system the following formula holds:

$$\frac{1}{d^2} = \frac{3}{4}\left(\frac{h^2 + hk + k^2}{a^2}\right) + \frac{l^2}{c^2} \qquad (1.13)$$

which results in the d-spacings of the (100) being 0.821 nm, while for the (110) plane is 0.474 nm.

In addition, there are three possible and highly symmetric different stacking modes of few-layer GDY, defined as AA-, AB- and ABC-stacking modes (see Fig. 1.15). These stacking modes belong to the $P6/mmm$, $P6_3/mmc$, and $R\bar{3}m$ point symmetries, respectively. Experimentally, Luo and Lu et al. have obtained the Selected Area Electron Diffraction (SAED) pattern and high-resolution TEM (HRTEM) image of a six-layer GDY sheet[93], while Zhang and Liu et al. were able to obtain a trilayer GDY film and investigated it HRTEM image and the SAED pattern. These results provide evidence of the existence of single layer GDY. The optimised crystal parameters a, b, c, and ϑ of the energy-minimised GDY structure are 9.38 Å, 9.38 Å, 3.63 Å, and 120°, respectively, with an interlayer distance of GDY layers is 3.7 Å[93].

1.5.2 Synthesis

The diverse carbon allotropes that could in principle be created have propitiated a large number of investigations in the past twenty years. The main goal of the different research efforts is to find new methodologies to synthesise novel carbon-based materials, exploiting the numerous possible structural combinations of the different hybridisation forms of carbon, i.e. sp, sp^2 and sp^3. The active investigations have afforded materials such as graphene, carbon nanotubes, fullerene, amongst others. Note that several of these new materials have shown very interesting properties[82].

In spite the reports of novel forms of carbon 2D materials, the synthesis of systems with well-defined structures and properties is still a challenge. In this regard, GDY has been predicted as a stable non-natural allotrope,

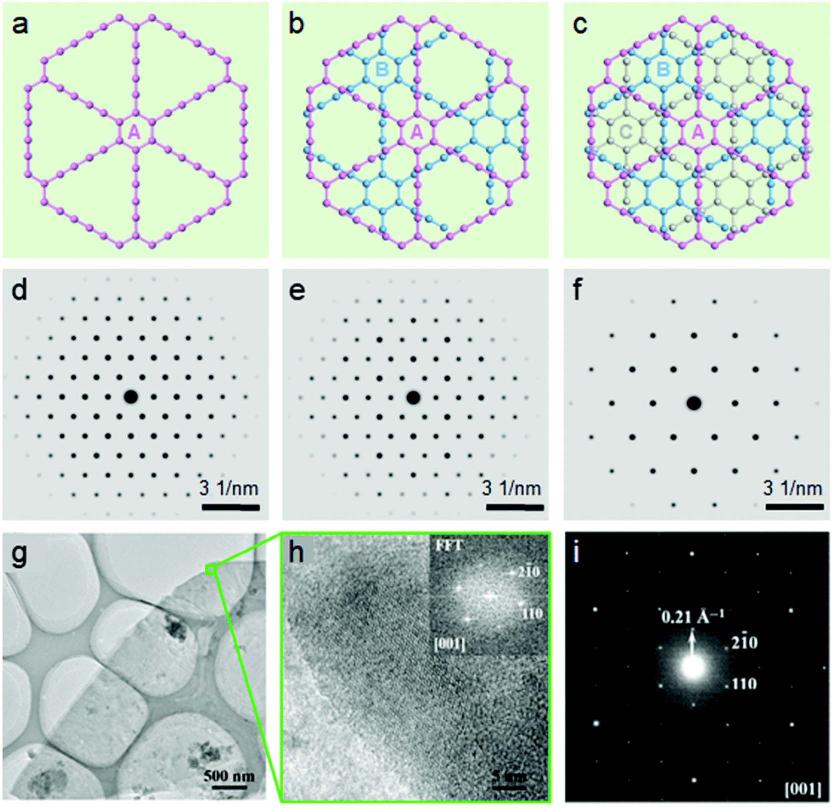

Figure 1.15: TEM images of SAED pattern and HRTEM of few-layer GDY. (a–f) The possible stacking structures of the corresponding TEM/SAED simulation patterns of GDY. (a) AA stacking, (b) AB stacking, and (c) ABC stacking. Panels (d), (e) and (f) are the simulated diffraction patterns for AA, AB and ABC stackings, respectively; (g) Low-magnification TEM image of six-layer GDY nanosheets; (h) HRTEM image of the circled area in (g); Inset is the fast Fourier transform (FFT) pattern of the HRTEM image; (i) SAED pattern of GDY nanosheets. Modified from Ref. [92]. Copyright Tsinghua University Press and Springer-Verlag GmbH Germany 2018.

boosting numerous investigations on the synthesis of this material. Structurally different GDY systems can be synthesised depending on: (*i*) the dimensionality (1D or 2D) and (*ii*) size and morphology of the nanostructure (2D nanofilms, 2D nanowalls, 1D nanowires and 1D nanotubes). The synthesis of the latter usually involves high temperatures, and other methods such as, chemical vapour deposition, vapour solid-liquid (VLS), among others. In the following section the synthesis and characterisation of the different graphdiyne nanostructures will be briefly described[90].

1.5.2.1 Graphdiyne Films

In 2010 Li et al. reported for the first time the synthesis of GDY on copper foil, where a cross-coupling reaction of hexaethynylbenzene is catalysed by the copper foil. The reaction was carried out in a pyridine solution, for a period of 72 h at 60 °C under an inert atmosphere of argon. Li and co-workers were able to obtain a large area GDY material ($\sim$ 3.6 cm^2), with the Cu foil acting both as catalyst and substrate. In addition, the large surface area of copper allows the directional growth of the GDY film[87].

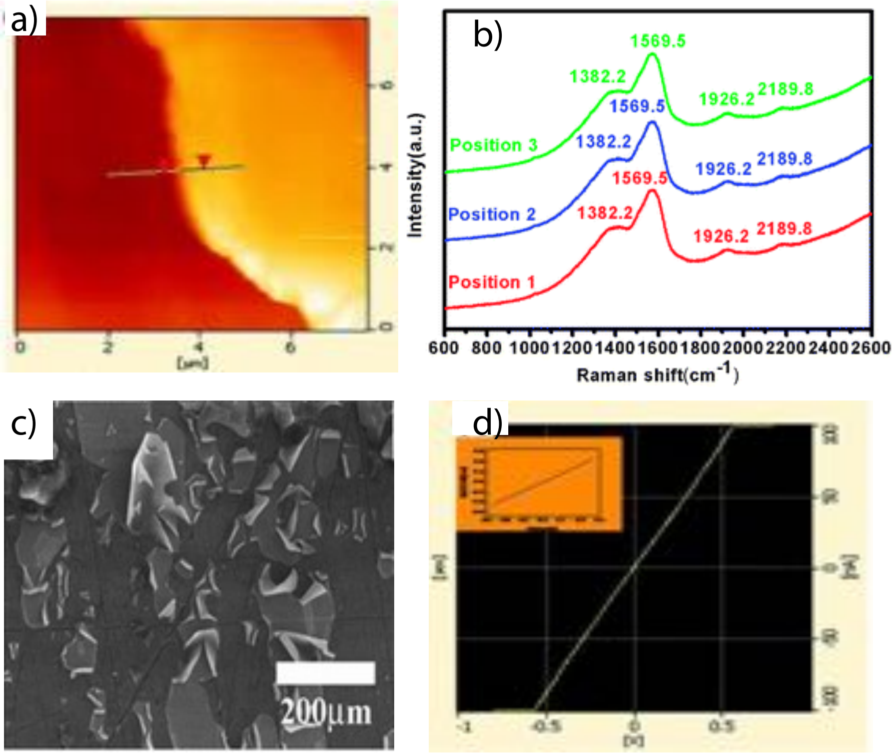

Figure 1.16: Graphdiyne Films. (a) AFM image of the grown GDY, (b) Raman spectra, (c) SEM and (d) *I-V* curve of the grown GDY. Modified from Ref. [87] with permission of Royal Society of Chemistry 2019.

The characterisation of the film was carried out through Raman spectroscopy, atomic force microscopy, scanning electron microscopy (SEM) and transmission electron microscopy after the transference of the film two a silicon substrate. AFM studies allowed the determination of the thickness of the films resulting in a thickness of 970 nm, denoting the formation of a multilayer GDY film (Fig. 1.16a).

The GDY quality and uniformity on copper surface were estimated using Raman spectroscopy. To gain insight in the homogeneity of the film, Raman measurement was performed in different positions on the film as shown in Fig. 1.16b. All the spectra exhibit four main peaks at: 1382.2, 1569.5, 1926.2 and 2189.8 cm^{-1}. The breathing vibration mode of sp^2 carbon in aromatic rings is observed at 1382.2 cm^{-1}, which shows a hypsochromic shift compared with graphite D band. Furthermore, the first-order scattering E_{2g} mode correspond in the Raman spectrum to the band at 1569.5 cm^{-1}. This mode is assigned to in-phase stretching vibration sp^2 carbon domains in aromatic rings. The E_{2g} mode shifts towards lower wavelength when compared to graphite G band (1575 cm^{-1}). The vibration of the conjugated butadiyne links (-C≡C-C≡C-) is observed at 2189.8 and 1926.2 cm^{-1}. The intensity of the ratio between the stretching vibration sp^2 carbon domains and the breathing vibration of sp^2 carbon domains, both in aromatic rings, are a measure of the order and number defects in the graphdiyne film.

Moreover, in Fig. Fig. 1.16c it can be seen the SEM of the split GDY film, denoting some curling of the GDY films on the edges. This clearly signals the flexibility of the GDY film. In addition, High Resolution Transmission Electron Microscopy (HRTEM) was utilised to obtain images from the multilayer GDY film, resulting in lattice fringes of 4.19 Å and a film without defects or dislocation. Additionally, the ratio intensity exhibited a value of 0.729 indicating that the film has a high order and low defects, in agreement with HRTEM.

The electrical properties of the film were additionally probed through AFM measurements employing a conductive cantilever directly in contact with the film under application of a bias voltage. Fig. 1.16d shows I-V curve for the GDY film, exhibiting a linear behaviour consistent with an Ohmic behaviour. The conductivity obtained was 2.516×10^{-4} S m^{-1}, demonstrating that the GDY film has excellent semiconducting properties when compared to silicon and graphene.

More recently, Qian et al. reported a new synthetic method to grow GDY nanofilms[94]. The obtained nanofilms are continuous layers that grow on a substrate with a thickness of nanometric scale. The methodology consists in the synthesis of GDY films on ZnO nanorod arrays as substrate, GDY powder as starting material, under vapour-liquid-solid conditions (VLS). The GDY powder was obtained using the *in-situ* cross-coupling reaction conditions (*vide supra*). This mechanism involves a combination of reduction and self-catalysed VLS growth process, where the low weigh GDY contained in the powder is evaporated in a furnace at 700 °C, and transported by an inert gas to the low temperature zone (620 °C) of the furnace, where the growth is achieved (Fig. 1.17a). The ZnO is reduced to elemental Zn which works as catalyst in the VLS growth process.

Moreover, the authors demonstrated that the amount of GDY powder placed in the VLS process has a significant influence in the thickness of the film, i.e. when the amount of GDY powder was decreased to a third, the thickness of the film was reduced 24 folds. For example, when 20 mg of GDY powder were employed, the average thickness was around 540 nm, whilst when 3 mg were used the determined thickness was ca. 22 nm. The decrease in the nanofilm thickness was detected by optical microscopy, as a measure of high transparency of the nanofilm (Fig. 1.17b). Furthermore, through SEM it was found a large continuous GDY area, greater than 4.8 mm^2, with a very smooth structure (Fig. 1.17c). The nanofilm of GDY a thickness of 22 nm showed very weak contrast with the substrate and high transparency, indicating the formation of a GDY films of approximately 30 layers.

Raman spectroscopy was further employed for the characterisation of the GDY film. Four characteristic GDY peaks of conjugated diyne groups were found in the Raman spectrum. Intriguingly, a strong shift in the Raman vibration was observed for three different samples with different thickness, exhibiting shorter wavenumber upon decreased film thickness (Fig. 1.17d). The highly ordered and defectless film was inferred by the intensity ration (D/E_{2g}) value of 0.96. The stacked pairs distance in the film was found to be

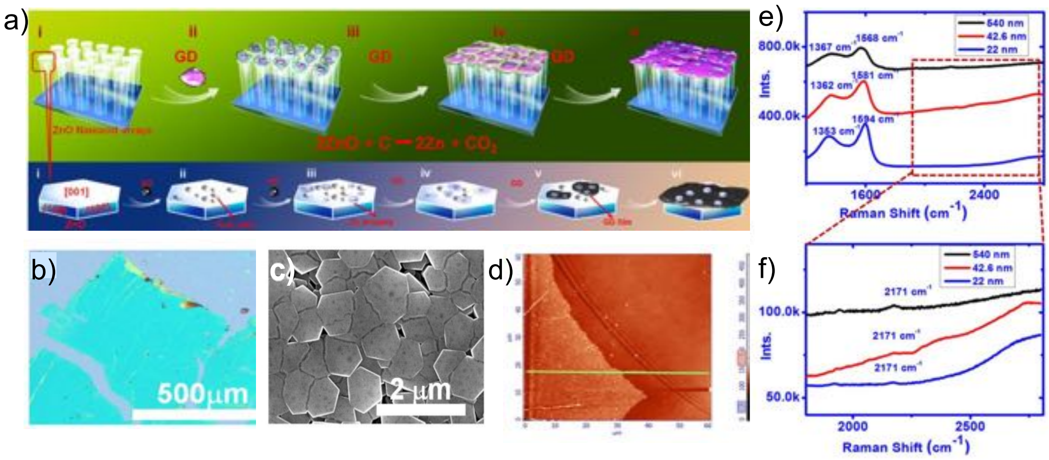

Figure 1.17: Graphdiyne Films Obtained through vapour-liquid-solid (VLS) method. (a) schematic representation of the methodology used to grow GDY employing VLS and ZnO; (b) optical image of the obtained GDY film; (c) SEM image of the GDY Film ; (d) AFM of the grown GDY film; (e) Raman spectrum of the grown GDY; (f) Zoom-in at the di-acetilene linkage. Modified from Ref. [94] Tsinghua University Press and Springer-Verlag GmbH Germany 2018.

0.365 nm *via* HRTEM.

The electrical properties of the GDY film was probed *via* a bottom-gate film transistor (TFT) on OTs/SiO_2/Si, where Au electrodes were evaporated directly on the GDY film transistor. The electrical performance was measured in over 100 devices resulting in an average mobility of 30 $cm^2\ V^{-1}\ s^{-1}$, resulting in very high average mobilities up to 2800 S cm^{-1}. The electrical proprieties of GDY displayed not saturated output curves of GDY, indicating that GDY film has itself high conductivity. Although the values of field-effect mobility found in the film studied by Qian and co-workers are slightly lower than the theoretically calculated for GDY monolayer, the work pave the way to the study of GDY -based materials towards electronic devices.

It is worth mentioning that GDY films have also been reported by on surface synthesis employing Scanning Tunnelling Microscopy (STM). Klappenberger et al. have studied the homo-coupling reaction of alkyl terminal compound on-surface synthesis *via* STM[95]. In 2012, they achieved the synthesis of covalent nanostructures employing a STM apparatus with high vacuum and compounds with alkyl terminal groups as precursors[96,95]. Two tripodic compounds were employed for the on-suface homo-coupling reaction on Ag (111). The organic precursors were evaporated on the metallic substrate and the self-assembling process took placed at low temperature. Afterwards, a selective homo-coupling was induced by the thermal treatment performed to the layers formed by the organic precursor, leading to the formation of covalent dimers. The authors have observed that when the temperature is increased, some reticulated covalent networks is produced such as hexagonal pores, although long-range order is missing along the formed network[96,95]. Moreover, experiments using Au(111) and the same organic precursor on

Ag(111) and a thermal treatment, resulted in a cyclotrimerisation reaction. This observation has suggested that the homo-coupling type of the terminal alkyl can be steered by the chemical nature of the substrate. The works are very important for the understanding of the homo-coupling reaction on-surface of the terminal alkyl compound and for the formation of an ordered and high quality carbon-based network[95,97].

1.5.2.2 Graphdiyne Nanowalls

In 2015, Zhou and co-workers described the synthesis of a GDY nanowalls obtained through a modified Glaser-Hay coupling reaction (Fig. 1.18a)[98]. The nanowalls are interconnected nanosheets vertically standing on the substrate. The modified Glaser-Hay coupling reaction was performed employing copper plates as well as an adjusted ratio of N,N,N',N'-tetramethyethylenediamine (TMEDA), acetone and pyridine. As the metallic cooper can be swiftly oxidised to copper ions in the presence of a base, the copper ions act as catalyst in the reaction. The modification improved upon several aspects of the original reaction as: (*i*) the rate of the coupling reaction (by performing the reaction in a non-alkaline solution as acetone); (*ii*) enhancement of the yield due to the solubility of the reagents is enhanced and the small acidity of the solution enhances the stability of the precursor, making it more stable than in the pyridine solution. Additionally, the authors showed that GDY nanowalls could be growth uniformly by adapting the N ligands quantity.

SEM studies reveal the morphology of nanowalls, resulting in a continuous matrix of vertical constructed nanowalls with large voids (Fig. 1.18b). The cross-section suggests that the nanowalls are extraordinary uniform, around a hundred nanometers high on the whole surface. Moreover, AFM of a mechanically exfoliated nanowall films transferred to a silicon substrate shows a thickness of 15.5 nm (Fig. 1.18c). HRTM also reveals crystalline areas of the GDY nanowall, with lattice fringes of 0.466 nm being in agreement with theoretical reports. Additionally, TEM revealed another crystal form is present in the film suggesting curved GDY sheets, as evidenced by lattice parameter (0.365 nm). The lattice parameter of the GDY nanowall is slightly larger than the one from graphene, indicating that more delocalisation on the nanowall than in graphene.

Four important peaks were observed in the GDY nanowall, i.e. 1383.7, 1568.7, 1939.8 and 2181.1 cm^{-1}. The D band peak in aromatic rings is presented at 1383.7 cm^{-1}, and the band G appears in aromatic rings at 1568.7 cm^{-1}. However, the peak at 1939.8 cm^{-1} remained without clear theoretical assignment, and it has been associated with vibration related to carbon-carbon triple bond.

The field-emission performance of GDY nanowalls reveals, in a typical plot of emission density versus the applied electric field, values of E_{to} (turn-on-field) about 6.6 V/μm and a E_{thr} (threshold field) of 10.7 V/µm. The obtained values are lower than the observed for vertically aligned graphene sheets, however, in general the field emission properties of GDY nanowalls are consistent with Flowler-Nordheim (F–N) theory, which has shown that

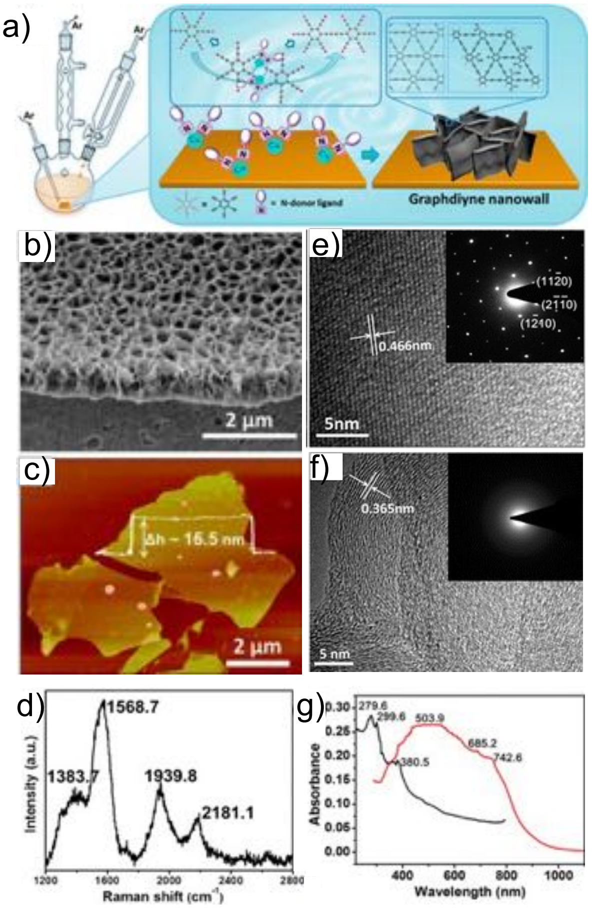

Figure 1.18: Graphdiyne Nanowalls. (a) Scheme of the experimental setup for the Glaser-Hay coupling reaction; (b) SEM image of a cross-section of graphdiyne nanowalls on Cu substrate; (c) AFM image of Nanowalls on Si/SiO$_2$, with a thickness of 15.5 nm; (d) Raman spectra of GDY nanowalls; (e) HRTEM images of GDY nanowalls with an inset showing the SAED patterns with high crystallinity and the lattice fringe; (f) HRTEM images of GDY nanowalls showing a SAED pattern of the interlayer space and a curved stacks of 0.365 nm; (g) UV-vis spectrum of the nanowalls. Modified from Ref. [98]. Copyrights 2015, American Chemical Society.

the electron emission from nanowalls is a result of tunnelling.

1.5.2.3 Graphdiyne Nanowires

The use of vapor-liquid-solid (VLS) growth process offers several advantages to synthesise high ordered, crystalline and almost defect-free nanomaterials. It allows a controllable manner to produce nanomaterials. This methodology has been coupled to surface techniques such as coating with metals such as Au, Fe, Ni, etc., acting as catalyst. Keeping this in mind, Qian et al. have reported the synthesis of graphdyine nanowires (GDNWs). Nanowires are defined as 1D nanostructures, commonly having diameters of the order of tens of nanometers, with unconstrained length scales. The authors obtained a well-defined 1D surface with a very high quality (defect-free) using VLS growth process to deposit GDY on a silicon surface coated with ZnO nanorod as a substrate[99].

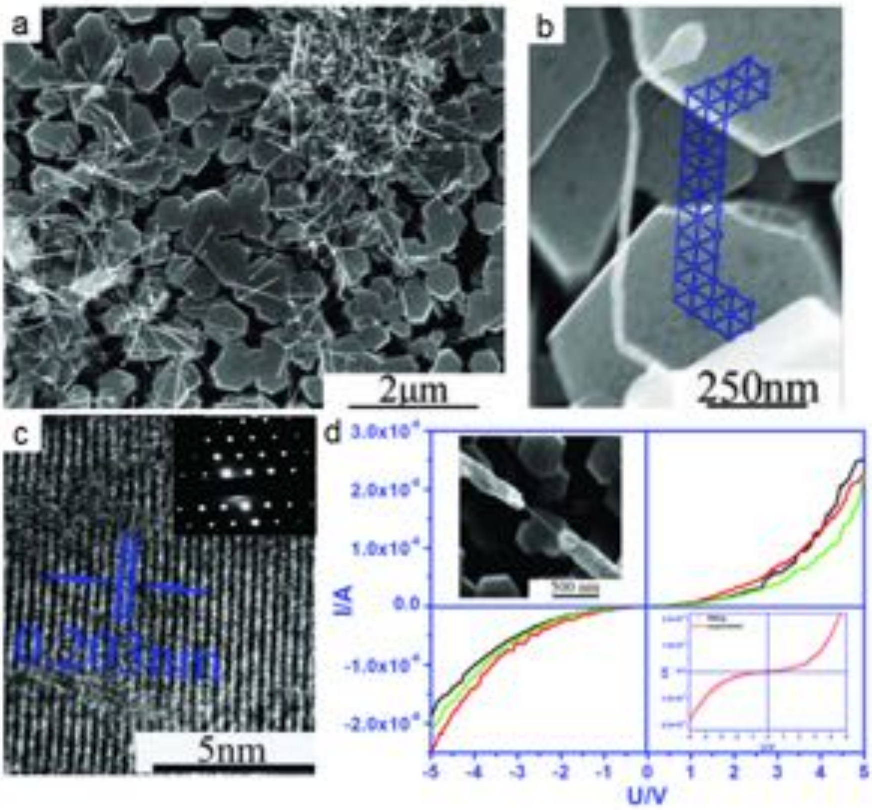

Figure 1.19: Graphdiyne Nanowires. (a,b) SEM image of GDNWs grown on ZnO nanorod. (c) HRTEM image of a GDNW, and inset is the corresponding SAED pattern. (d) typical current-voltage (*I*–*V*) curves of GDNWs. Top inset: high magnification SEM image of the measurement circuit. Bottom inset: an experimental *I*–*V* curve and a theoretical fitting curve. Modified from Ref. [99] by Royal Society of Chemistry.

An amount of GDY powder was placed in the centre of the furnace (750 °C) and the low weigh GDY was evaporated and carried out by an inert gas followed by its deposition on the substrate in the low temperature area for 30 min. One of the advantages of utilising ZnO is that it can be easily reduced to its elemental form, which can be used as catalyst in this process to grow GDY. It also offers the possibility of controlled growth and can, moreover, induce an ordered nanostructure (*vide supra*).

Important results have also been found regarding the morphology and architecture of the GDNWs by SEM. Most of the wire-like GDY has grown on the edge of the ZnO nanorod array on the silicon surface. It seems that the major density of GDNW is accumulated on the margins of the surface, whilst on the centre the quantity of aggregate GDNW is minor (Fig. 1.19a).

Several nanowires with different lengths and diameters were obtained, for example Fig. 1.19b shows a nanowire with a length around 1070 nm and a diameter of 20 nm. The same nanowire was analysed by HRTEM and it displayed clear lattice fringes without defect and dislocations of 0.203 nm (Fig. 1.19c). The electric properties of GDNWs were analysed by common *I*-*V* curves exhibiting average resistances of about 3.01×10^5, 2.58×10^5, 4.3×10^5 Ω. The average conductivity was around 1.9×10^3 S M^{-1} and the mobility was ca. 7.1×10^5 cm^2 V^{-1} s^{-1} at room temperature, which has an equal order of magnitude than the observed in graphene (Fig. 1.19d). These measurements indicate that GDNWs are promising prospect to be employed as semiconductors similarly to carbon nanotubes and graphene.

In addition, Klappenberger et al. have studied the synthesis of GDY nanowires through Scanning Tunnelling Microscopy (STM)[100,101]. The authors were able to obtain 30 nm length of GDY nanowires on a Ag(877) vicinal surface, which interestingly improved the chemoselectivity of the homo-coupling process and allowed the control of synthesis of the GDY nanowires. Moreover, the same authors have been able to synthesise GDY nanowires on a flat Ag (111) surface, however, the authors observed a variety of side-reactions that led to irregular branched networks[100]. More recently, Klappenberger and co-workers have presented GDY nanowires functionalised with carbinitrile groups on a Ag(455) surface[101]. The authors demonstrated that the CN moieties funcionalised in the backbones of terphenylene with extended alkyl terminal, can improve the selectivity of the alkyl homo-coupling to form polymers strands. Through this approach, it was possible to obtain 40 nm long semi-conductor nanowires by using the templating effect of the vicinal Ag(455) surface.

1.5.2.4 Graphdiyne Nanotubes

On the quest of new GDY nanostructures applicable in the nanoelectronic field led to the synthesis of a different 1D form of GDY, known as GDY nanotubes (GDNT). The GDY nanotubes are structure with a tube-like morphology and with nanometric scale. These GDNT are reminiscent to nanowires, but unlike wires, tubes are hollow and, as carbon nanotubes, might be single-walled or multi-walled. In this regard, Li et al. have obtained GDY nanotubes employing the well-known cross-coupling reaction on an anodic Al_2O_3 template, which one side was fixed to the Cu foil (Fig. 1.20a)[102]. Afterwards, an annealing process was performed at high temperature (650 °C) for 6 h.

Li and co-workers studied the annealing effect on the GDNT morphology. HRTEM image of GDNT film before annealing showed amorphous nanotubes morphology with thickness of about 40 nm, 200 nm of diameter and 40 μm length. After the annealing process at 650 °C the GDNT film became thinner with a thickness about 15 nm, more compact and ordered with no change in length and diameter (Fig. 1.20b-c). Additionally, GDNT exhibited a smooth surface and uniform wall thickness, with weak polycrystalline rings, signifying a partially crystalline GDNT nature (Fig. 1.20d).

Moreover, the authors conducted field emission (FE) measurements of GDNT and GDY films, in order to compare their FE characteristics. The field emission characteristics of GDNT were achieved for both, not annealed GDNTs and for annealed GDNTs (Fig. 1.20e). The not annealed GDNTs exhibit a turn-on field (E_{to}) and threshold field (E_{htr}) of 5.75 and 12.66 V/µm, respectively and the maximum current density was around 1.5 mA/cm^2.

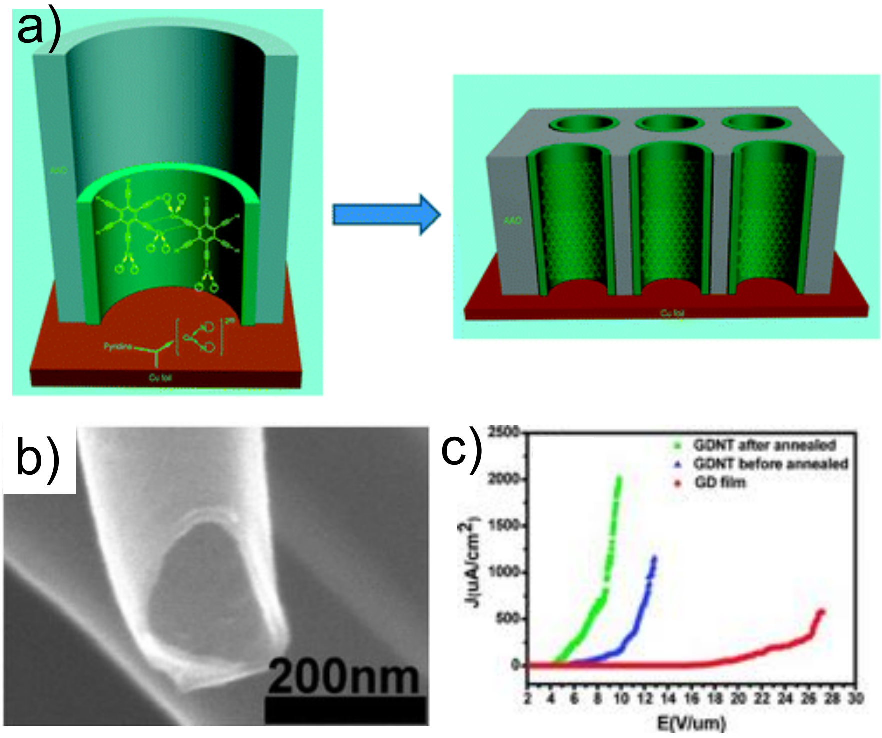

Figure 1.20: Synthesis of GDY nanotubes (GDNTs). (a) scheme of the mechanism used to fabricate GDNT arrays; (b) SEM images of GDNTs after being annealed. (e) F-N plot of GDNT array comparing the GDNTs before annealing (blue), after annealing (green), and the graphdiyne film (red). Modified from Ref. [102]. Copyrights 2011, American Chemical Society.

Nonetheless, when the annealing as performed the turn-on field and the threshold field decreased to 4.20 and 8.83 V/µm, respectively and the maximum current density of GDNT increased to 2 mA/cm^2. The E_{to} and E_{htr} for all of the field emission analysis realised by Li et al., are the electronic fields required to produce a current density of 10 mA/cm^2 and 1 mA/cm^2 respectively. The measurements corroborated that when the annealing process was performed in GDY nanotube, the GDNT emission properties improved. The wall thickness is a key factor for the field emission of nanotubes; this is consistent with the enhancement of the GDNTs emission properties, when the thickness became lower due to the annealing process. The measurements of E_{to} and E_{htr} of GDY films shown values about 17.18 and 30.01 V/µm, respectively. The GDY films exhibited a lower current density (0.6 mA/cm^2), compare to GDNTs. The results indicate that they have morphology-dependent field emission properties. The stability of the field emission was assessed observing the current density during 4800 s, showing that a degradation of the current density was not sensed during that period of time, which has demonstrated the high stability of field emission of GDNTs.

1.5.2.5 Graphdiyne Nanosheets

An alternative approach for the synthesis of GDY films was presented by Sakamoto, Nishihara, and co-workers, leading to the formation of GDY crystalline nanosheets at the liquid/liquid or gas/liquid interface of employing HEB as a precursor (Fig. 1.21)[103]. For this, Cu(II) acetate and pyridine were used to catalysed the reaction. During the synthetic process, the precursor was dissolved in the lower layer using dichloromethane as a solvent, while the catalysts were maintained in the upper layer. At the interface of the two solutions, it was possible to grow GDY nanosheets with crystalline characteristics, resulting in hexagonal domains.

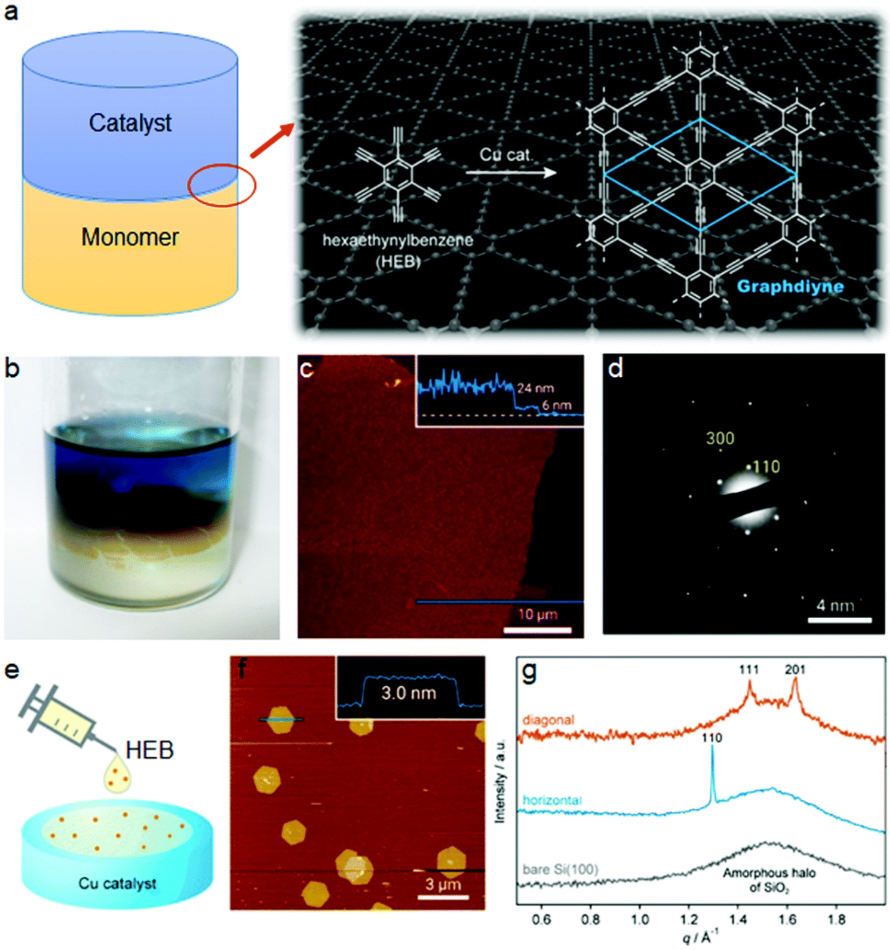

Figure 1.21: Interface-assisted GDY growth. (a) Interface methodology; (b) Picture of the experimental setup of liquid-liquid method; (c) SEM hexagonal pattern obtained in the GDY film; (d) TEM image of GDY film in (c); (e) The TEM SAED pattern of GDY showing high crystallinity; (f) AFM image of GDY film with thickness of 3 nm; (g) Low angle XRD of GDY. Modified from Ref. [103]. Copyrights 2011, American Chemical Society.

Moreover, the as prepared GDY nanosheets possess a side size of 1.5 μm and a uniform thickness of ca. 3.0 nm. In a similar procedure, hexaethynyltriphenylene precursor was also coupled to form free-standing films. The liquid-liquid interfacial synthetic strategy was also employed to synthesise ultrathin films of nitrogen substituted GDY, with thickness of approximately $\sim$ 4 nm, corresponding to approximately 12 GDY layers.

1.5.2.6 Graphdiyne *via* CVD

More recently, a synthetic approach employing Chemical Vapour Deposition reactor, HEB as monomer and Ag foil as substrate, have been developed[104]. Intriguingly, the author found the synthesis of GDY to be possible employing solely the surface of the Ag foils, leading to an amorphous GDY film with a thickness of maximum 1.4 nm. The CVD method provides another simple method for the preparation of GDY films of few-layer thickness. The as-prepared film exhibited conductivity of 6.72 S cm^{-1}, which is characteristic of semiconductors. The GDY film can be used as a substrate to suppress the fluorescence and enhance Raman signals of attached molecules Fig. 1.22.

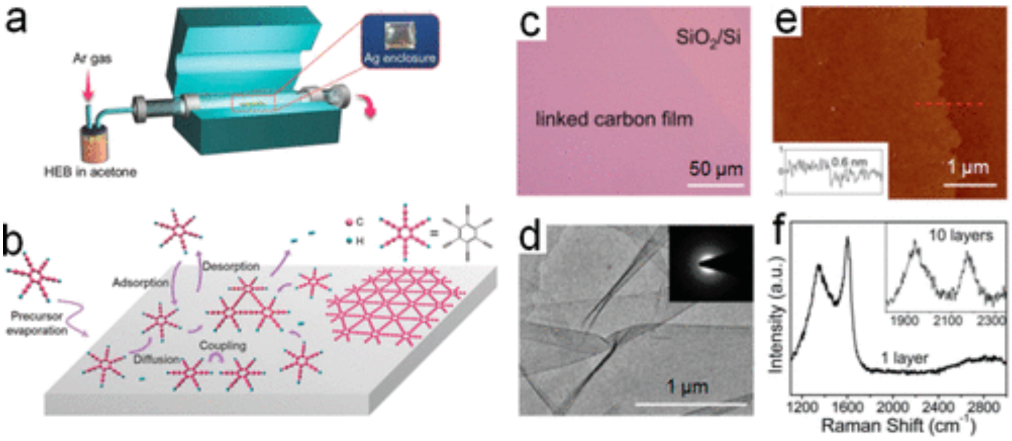

Figure 1.22: CVD synthesis of GDY film on Ag foil. (a) Scheme of the CVD setup; (b) schematic mechanism of the formation of the GDY network on Ag; (c) Optical Image of the grown GDY film transferred to a SiO_2/Si substrate; (d) TEM image of the GDY film with an inset that correspond to the SAED pattern of the film; (e) Raman spectrum of the obtained GDY on Ag foil. Modified from Ref. [102]. Copyrights 2017, Wiley-VCH Verlag GmbH &. KGaA Weinheim.

1.6 Graphdiyne Applications

Based on the structure and properties that Graphdiyne has shown and the ones that have been predicted, GDY has been proposed for many technological applications, such as: energy[105], catalysis[87], sensors[106], optoelectronics[107], separation membrane[108] among others[109]. GDY has been proposed in energy application due to two important characteristics, e.g. its 2D planar structure, as graphene, and the larger pores. These two characters give GDY the possibility of be integrated in energy storage and conversion, since the porosity of GDY can be used as channels to organise larger numbers of lithium ions and small molecules as H_2. Moreover, some approaches have demonstrated that integrating GDY-based LIBs in lithium storage devices, can improve the electrochemical properties such as high stable capacity and the rate of performance[110].

In catalysis, GDY has been proposed as an excellent non-metallic oxygen reduction electro-catalyst. It has been suggested that GDY could catalyse the oxidation of CO at low temperatures, as suggested by density functional theory calculations (DFT). Furthermore, by atomic doping, the nature of GDY can be tuned. Zhang group demonstrated that by doping GDY with nitrogen atoms, an excellent electrocatalyst for Oxygen Reduction Reaction (ORR) can be obtained[111]. The electro-catalytic activity of such material competes with commercial Pt/C catalysts. More importantly, N-doped GDY possesses a better stability than Pt/C catalysts. GDY has also been proposed as component of optoelectronic devices, owing to the zero-energy band-gap predicted by first principle calculations. Likewise, it has been proposed in photovoltaic applications. The planar and rigid arrangement of GDY and the uniform porous size of GDY have also been considered for storage and separation of molecules. As a matter of fact, Jiao group explored the hydrogen, carbon monoxide, and methane diffusion through GDY resulting in good hydrogen separation[112].

In summary, GDY has been proposed for several important and potential application prospects in optoelectronics, electronics, as semiconductor, separation and energy storage materials, amongst others. Experimental and theoretical results have shown peculiar properties for this material, thus, GDY gaining considerable attention from the scientific community[113].

Aims of the Thesis

Since the first report on graphene, studies of two dimensional (2D) materials have been boosted, owing to the remarkable properties shown by graphene and others. The main driving force for the intensive investigation of 2D systems are the unique electronic, mechanic and physical properties exhibited by these systems and their applicability in diverse technological fields. Many of the reported 2D materials exhibit interesting properties such as low thickness, high breaking strain and variable electronic properties, that make them useful in flexible electronics applications. All the before mentioned properties are of utmost importance for the development of faster and smaller devices, as required by Moore's law. Considering these aspects, the aims of this thesis are focused on synthesis and characterisation of different 2D carbon-based materials through three main projects as follows:

1. **"Direct Conversion of CO_2 to Graphene: Merging Two Fields":** in this chapter I will explore the possible implementation of CO_2, a very stable and environmentally problematic molecule, as carbon source for the synthesis of a technologically important material as it is graphene. For these, we study a series of metallic substrates employing copper (Cu), palladium (Pd) and their mixtures for the possible activation and reduction of the carbon in CO_2 as the building block for graphene *via* Atmospheric Pressure Chemical Vapour Deposition reactor (APCVD). The main goal of the metallic substrates is to study the catalytic power of the metals in the reduction of CO_2 using H_2 as the reductant. Through this methodology, we propose a green-chemistry concept to create Graphene from the abundant CO_2 molecule.

2. **"Nanocrystalline Graphene from an Organic Molecule":** in this chapter we try to explore a new synthetic methodology where an organic molecule is employed for the synthesis of nanocrystalline graphene (NCG). The main goal of this project is to achieve NCG with milder conditions than the already employed methods, as well as to obtain larger domain size of NCG. Current methods for the synthesis of NCG rely on the graphitisation of the organic materials at very high temperatures for long exposure times and high vacuums. In contrast, our exploitation of an organic molecule for the synthesis of NCG relies on relatively lower temperatures as well as very short exposure times, leading to large domain size of NCG. For this project, I also make use of an APCVD reactor for the synthesis of the material. As growth substrate, we make use of copper foil, due to the nice characteristics exhibited by this metal for the growth of graphene and graphene-like materials.

3. **"CVD Synthesis of Graphdiyne from Organic Molecules":** in the quest for new carbon-based 2D materials in this chapter we explore the synthesis, structural and physical characterisation of new graphdiyne (GDY) materials. These 2D materials have been proposed in a wide range on application due to their very interesting electronic, mechanical as well as structural properties. For this project, four GDY precursors will be explored. The high chemical reactivity of the precursors will allow the *sp-sp* carbon formation, leading to an extended 2D material. The synthesis of the GDY 2D materials, will be based on APCVD reactions at relatively low temperatures (> 200 °)C. Moreover, I will employed copper foil as catalyst and substrate for the GDY growth. This chapter also aims to structurally and physically characterise the obtained films through several techniques.

Chapter 2

Direct Conversion of CO_2 to Graphene: Merging Two Fields

The results presented in this section of the thesis were obtained in collaboration with two research groups at INT: the Nanostructure Materials's group from Prof. Horst Hahn, which was involved in the preparation of the metallic substrates, and the Electron Microscopy and Spectroscopy laboratory from Prof. Christian Kübel, involved in the TEM characterisation.

The high levels of CO_2 in the environment have positioned it as one of the major greenhouse gases, hence, there is an important and undoubted contribution of this gas to climate change[114–116]. Therefore, an active area has emerged comprising the conversion of CO_2 to highly valuable products[117–119]. Nevertheless, the re-utilisation of this renewable gas source requires a series of complex processes to generate chemical systems, fuels or technological materials[120]. In this regard, some approaches targeting the capture, reduction and conversion of CO_2 into added-value products have been developed, which include techniques ranging from chemical[121], electrochemical[122,123], thermochemical[124], biochemical[125] to photochemical[126] procedures.

Amid the many carbon materials, graphene has become one of the most promising due to its extraordinary properties such as high intrinsic mobility, thermal conductivity and optical transmittance, making the synthesis of this material an active field of investigation[1,44,127]. Up to now, graphene can be obtained by different methodologies that can be classified as top-down and bottom-up approaches[49,128]. An example of a top-down approach is the exfoliation of multi-layer graphite by overcoming the van der Waals forces. Unfortunately, this procedure presents several issues such as defects caused by the re-agglomeration of the graphene sheets during the separation process, low yields and limited size patches of graphene[39]. Conversely, bottom-up approaches involve the synthesis of graphene from a molecular carbon source (e.g. methane, ethylene), a reducing agent and substrate[11]. Examples of these are Chemical Vapour Deposition (CVD)[129], epitaxial growth or electrochemical methods[130]. Amongst these, CVD synthesis is one of the most advantageous due to the possibility of obtaining large areas of high-quality graphene[131].

Until today researchers have turned their attention to develop methodologies for the reduction of CO_2 to graphitic materials. For example, an approach developed by Birong and co-workers, showed a methodology comprising a two-step process for conversion of CO_2 to graphene[132]. In the first step the CO_2 is activated by passing it through a nickel (Ni) catalyst, with a stream of hydrogen (H_2) leading to the production of more reactive carbon-based species. The second step involves the reduction of the more reactive carbon species to graphene on Cu foil at high temperature. Additionally, few experiments based on electrochemical methodologies using heterogeneous catalysts have been also developed[133,134]. For example, Hu L. and co-workers reported the graphitisation of CO_2 through an electrochemical approach *via* molten salts[133]. However, while the authors obtained some graphene-like material, most of the product resulted in amorphous carbon. More recently, it was shown that CO_2 can be electrochemically reduced to carbonaceous species at room temperature employing ceria catalysts[134]. In the frame of green chemistry, herein, we present a direct synthesis of multilayer graphene using CO_2 gas, as carbon feedstock, copper-palladium (Cu-Pd) as the substrates, and an Atmospheric Pressure Chemical Vapour Deposition (APCVD) reactor. Our results show that the Cu-Pd alloy acts not just as the catalyst for the CO_2 conversion, but also as the substrate for the graphene growth. Through this approach, we demonstrate that the stable molecule of CO_2 can be completely reduced to carbon material, by overcoming its activation energy when the high temperature of a CVD furnace is combined with the catalytic ability of the metals, Cu Pd and the reductive power of H_2 (Fig. 2.1).[135]

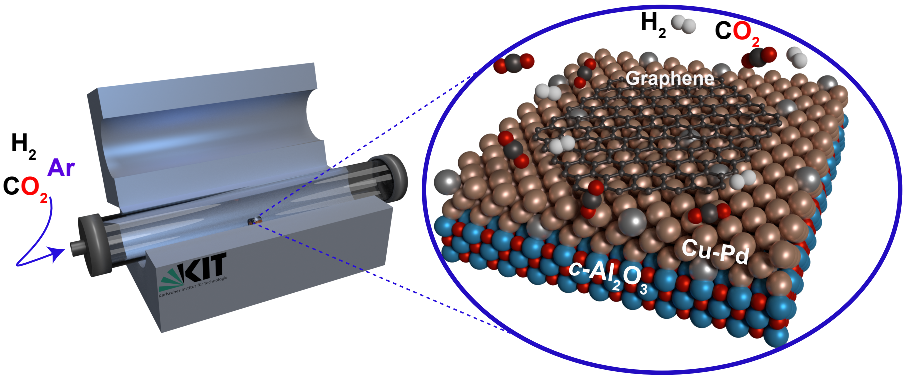

Figure 2.1: Merging CO_2 and Graphene. Schematic representation of the direct conversion of CO_2 into Graphene using Cu-Pd alloys, H_2 as reducing agent and Ar as dilutant. Reproduced from Ref. [135]. Copyrights 2019, Wiley-VCH Verlag GmbH &. KGaA Weinheim.

2.1 Substrate Preparation

The metallic substrates were prepared using copper and palladium metals. These two metals were chosen due to their valuable properties shown in the activation of CO$_2$ and graphene growth[44,136]. For the direct conversion of CO$_2$ into graphene first we focused on the study of the right metal, or combination of metals, which can act as catalytic agent and at the same time as the substrate in the process. The fabrication of the metallic substrates was carried out in an electro-sputtering set up by depositing Cu or/and Pd metals on the top of a 5×5 mm 0001-sapphire (c-Al$_2$O$_3$) chip. To study the role of Cu and Pd in the reaction four substrates were prepared with the following compositions: (*i*) Substrate 1 (**Sub1**): this substrate was prepared by depositing on c-Al$_2$O$_3$ 900 nm of Cu. Following, on the top of the previously sputtered Cu film, four islands of Pd (1 mm^2 each) were deposited with a thickness of 150 nm (Fig. 2.2a); (*ii*) Substrate 2 (**Sub2**): was prepared by sputtering only 900 nm of Cu on the c-Al$_2$O$_3$ chip (Fig. 2.2b). (*iii*) Substrate 3 (**Sub3**): this substrate consists in 900 nm layer of Pd on c-Al$_2$O$_3$ chip (Fig. 2.2c); and (*iv*) Substrate 4 (**Sub4**): for the preparation of this substrate, half side of c-Al$_2$O$_3$ was sputtered with 900 nm of Cu and on the other half with 900 nm of Pd. A separation of 1 mm was kept to avoid any direct contact between the metals (Fig. 2.2d).

Sub1 was prepared to determine the relation between Cu and Pd in the activation and conversion of CO$_2$. Additionally, **Sub1** allows us to establish the relation between the metals in the reaction, that is, whether both metals, Cu and Pd, act together in the conversion of CO$_2$ to graphene. **Sub2** and **Sub3** were prepared to study the possibility of the CO$_2$ conversion is feasible only by one of the metals, i.e. Cu or Pd, respectively; the design of **Sub4** allow us to study the possibility of one metal, such palladium, could act as the catalyst alone, whilst Cu would have the role of the substrate for the graphene growth or *vice-versa*.

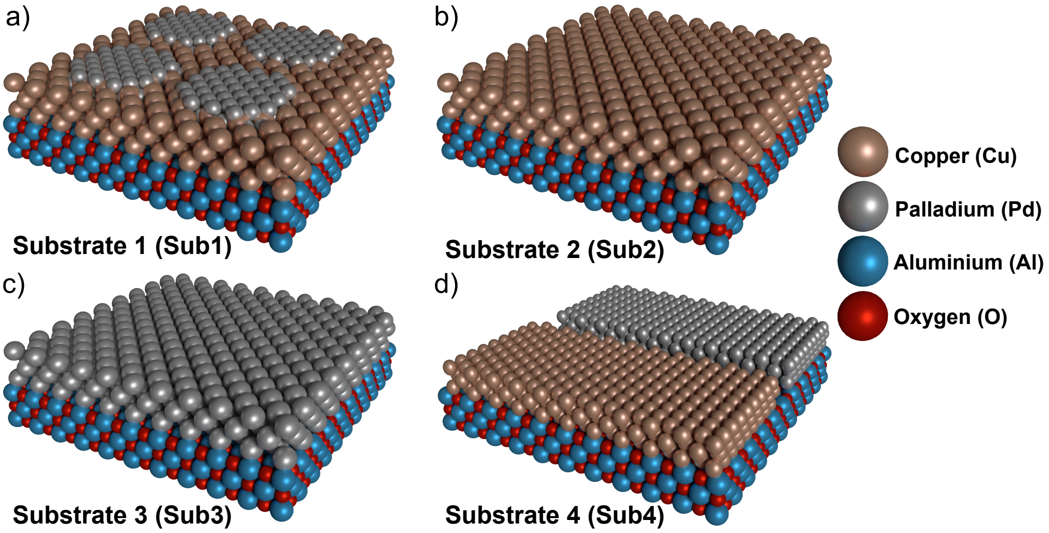

Figure 2.2: Metallic Substrates. Schematic view of the substrates employed to investigate the direct growth of graphene from CO$_2$: (a) **Sub1**: Cu sputtered on c-Al$_2$O$_3$ with 4 islands of Pd sputtered over the Cu film; (b) **Sub2**: Cu sputtered on c-Al$_2$O$_3$ chip; (c) **Sub3**: Pd sputtered on c-Al$_2$O$_3$; (d) **Sub4**: half of the c-Al$_2$O$_3$ substrate with Cu and the other half with Pd sputtered on c-Al$_2$O$_3$.

2.2 Graphene Growth

An APCVD reactor was employed to study the growth of graphene, utilising CO_2 as carbon source, hydrogen (H_2) as the reductant agent and argon (Ar) to maintain an inert atmosphere. A procedure involving 4 steps was employed in the graphene growth, as follows: (*i*) the metallic substrate was placed inside of a quartz tube and positioned in the heat zone of the CVD furnace, following by the increase of the temperature of the furnace up to 1000 °C under and Ar stream; (*ii*) the second step involved the annealing of the substrate employing a mixture of Ar and H_2 (1.4:1) for 30 min (*iii*) after the annealing immediately, the growth process was started utilising a mixture of Ar, H_2 and CO_2 with an 8:5:3.5 ratio at 1000 °C for 40 minutes; (*iv*) the last step consisted in the cooling of the sample, the metallic substrate was kept under an Ar stream until it reached the room temperature (see Fig. 5.1, section 5.2).

2.3 Characterisation of the Metallic Substrates After Growth Procedure

All the metallic substrates were characterised firstly by Raman spectroscopy, due to its important role as characterisation technique for the study of graphitic materials. Moreover, its non-invasive feature can provide a large amount of information such as thickness, grain boundaries, disorder, strain, amongst others[65,137].

Raman studies revealed that only **Sub1** presented the characteristic bands of graphitic material i.e. D (1347 cm^{-1}), G (1582 cm^{-1}) and 2D (2689 cm^{-1}) bands (Fig. 2.3). The presence of graphene along the whole substrate was examined by Raman mapping analysis, leading to the observation of characteristics D, G and 2D bands of graphene (Fig. 2.3a).

Moreover, the ratios of the 2D and G peak (I_{2D}/I_G) were obtained in the Raman mapping; the I_{2D}/I_G ratio is directly related to the number of layers of graphene, where large I_{2D}/I_G ratios indicate the presence of mono- to few-layer graphene, while low values indicate the presence of multi-layer graphene[138] (Fig. 2.3c). The values found in **Sub1** varied between 0.55 to 2.65, indicating that in this substrate there are regions containing few-layers graphene, as well as there are region with multi-layer graphene.

Note that the high temperature employed (1000 °C) for the whole growth process, triggered a diffusion of the Pd islands into Cu, thus, during the growth there is a more homogeneous Cu-Pd mixture. Nevertheless, the temperature can also lead to irregularities in the metal film structures and the height of the graphene, which could contribute to a non-homogenous intensity of the Raman peaks. This phenomenon is well known to occur in metals at high temperature and is known as de-wetting, being observable in the optical and Scanning Electron Microscopy (SEM) images (Fig. 2.3b and Fig. 2.3c). This structure has been observed in a different approach where graphene was grown employing Cu films deposited on dielectric surfaces[139].

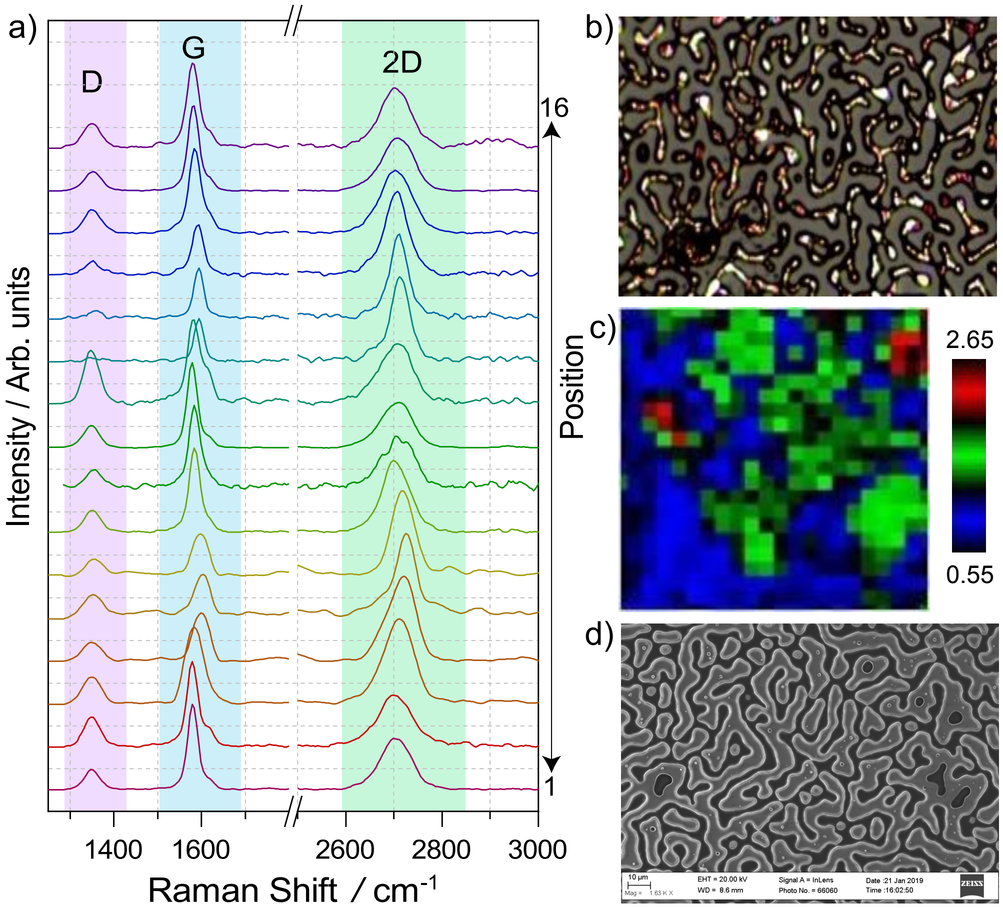

Figure 2.3: Characterisation of Graphene on Sub1. (a) Raman of 16 positions of graphene on **Sub1**. Coloured bands show the D (pink), G (pale blue) and 2D (pale green) peaks characteristics of graphene; (b) OM images of a cross-section of the Pd island on Cu; (c) Raman mapping showing the I_{2D}/I_G ratio of graphene; (d) SEM images of a cross-section of the Pd island on Cu.

The thickness of the grown graphene was further probed by Atomic Force Microscopy. For this purpose, the graphene obtained from **Sub1** was first transferred onto a silicon (Si) substrate and subsequently characterised (Fig. 2.4). AFM height profiles indicated the formation of graphene sheets with thicknesses ranging from 6 to 10 nm, denoting the number of graphene layers between 17 to 28 layers (Fig. 2.4b-c).

Furthermore, the other three substrates, i.e. **Sub2**, **Sub3** and **Sub4**, were also analysed *via* Raman spectroscopy. Interestingly, none of these metallic substrates exhibited any signal corresponding to a carbonaceous species (Fig. 2.5a-c), which indicates that the metals do not act alone in the conversion of CO$_2$ to graphene. It is important to highlight that the graphene growth was achieved solely in **Sub1**, being the only substrate where both metals, Cu and Pd, are in direct contact.

To exclude the presence of contaminants being responsible for the formation of graphene, blank experiments were performed. For this, **Sub1** was subjected to the same procedure previously described, without the inclusion of the stream of CO$_2$ as a carbon source. Raman analysis after this proce-

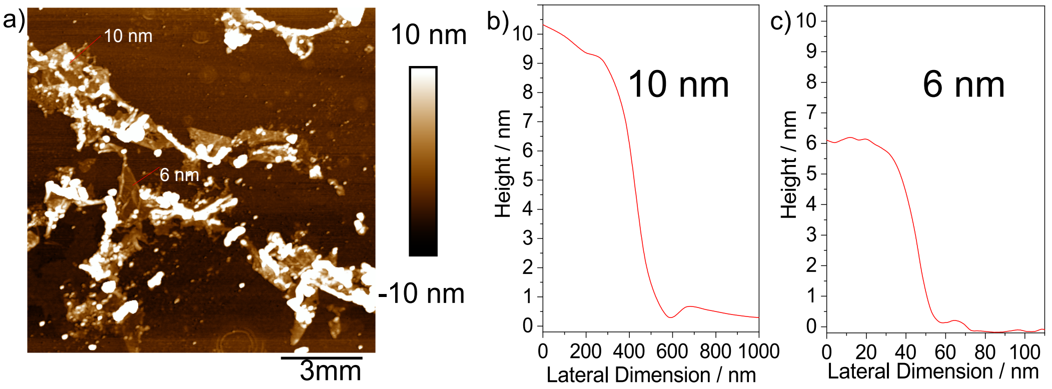

Figure 2.4: AFM of graphene on Sub1. (a) AFM image of the grown graphene transferred to a Si substrate; (b) Height profile of the graphene on Si substrate along the lines shown in the image (c), exhibiting thickness from 6 nm and 10 nm.

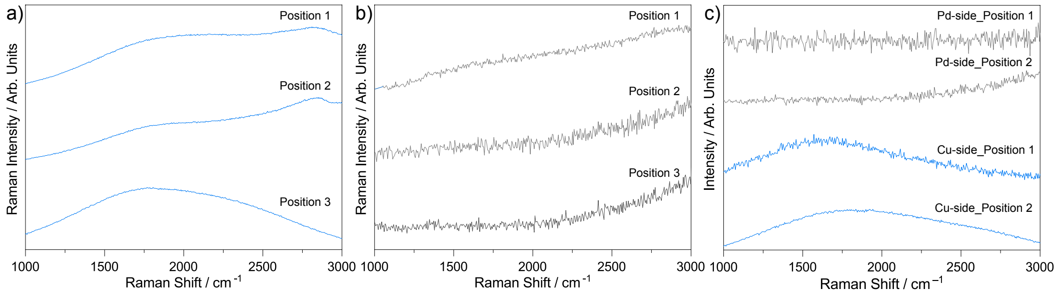

Figure 2.5: Raman analysis of Sub2, Sub3 and Sub4. (a) Raman spectrum of **Sub2**, (b) Raman spectrum of **Sub3**, (c) Raman spectrum of **Sub4**. P_i = Position.

dure, revealed no graphene formation, therefore, confirming that the source of carbon in our approach is CO$_2$ (Fig. 2.6).

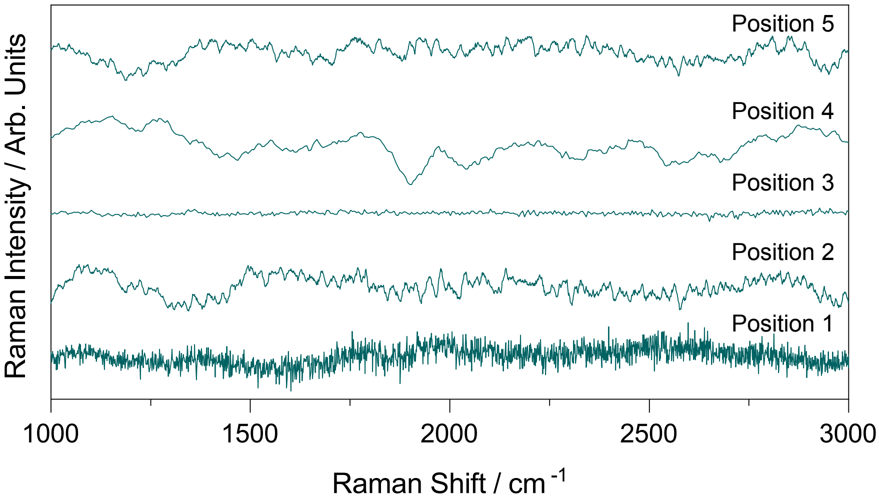

Figure 2.6: Blank Experiment. Raman analysis of the blank experiment utilising **Sub1**.

In addition, the concentration of Cu-Pd of **Sub1** was examined *via* Energy Dispersive X-ray Spectroscopy (EDS). The analysis was carried out after the growth process on the Pd island site, resulting in a concentration of Cu of 93at.% (atomic percentage) and 7at.% of Pd (Fig. 2.7a-b). Interestingly, as observed, the concentration of Cu is higher than Pd, which made us wonder whether actually any Pd/Cu metal mixture plays an important role in the conversion of CO$_2$ to graphene.

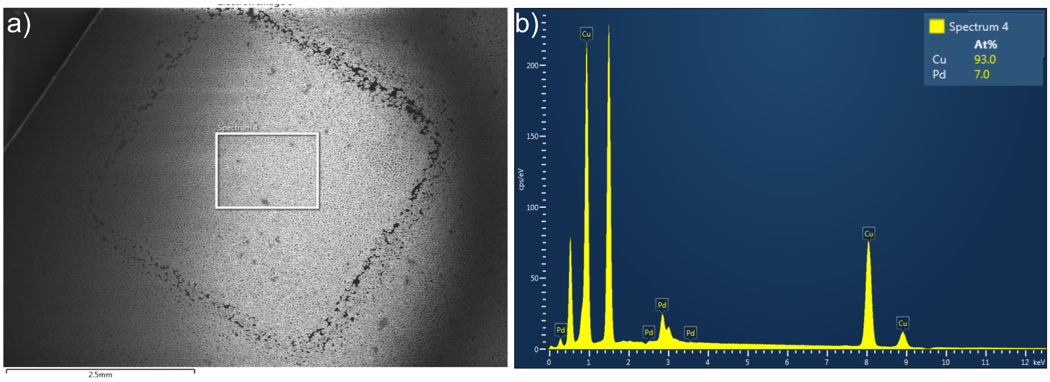

Figure 2.7: SEM and EDS of Sub1. (a) SEM of island on **Sub1** where EDS was performed; (b) EDS composition spectrum of Cu-Pd.

2.4 Preparation of Cu-Pd alloy Metallic Substrates

The experiment described in the previous section, employing different metallic substrates with different composition of metals, demonstrated that the only substrate suitable for the conversion of CO$_2$ to graphene was **Sub1**, where the Cu-Pd metals were in direct contact. This result suggested that both metals act together to promote the activation and conversion of CO$_2$ into graphene. However, an emerging question arises concerning the right Cu-Pd ratio for the direct conversion of CO$_2$ into graphene. EDS experiments revealed that the concentration in **Sub1** was 93at.% of Cu and 7 at.% of Pd (*vide supra*). Therefore, we designed two new experiments with the main goal of determining whether at any Cu-Pd ratio the one-step process would occur. To accomplish our goal, a set of two new substrates, with different Cu-Pd compositions, were prepared. The new substrates were fabricated by co-sputtering different amounts of Cu and Pd on a 5×5 mm *c*-Al$_2$O$_3$ chip.

The composition of the two new substrates is given as follows: Substrate 5 (**Sub5**) was achieved by first depositing an initial layer of 900 nm of Cu on *c*-Al$_2$O$_3$ and subsequently the co-sputtering of both metals, Cu and Pd, on the top of the pre-deposited Cu film (Fig. 2.8a). Substrate 6 (**Sub6**) was fabricated *via* a co-deposition of Cu and Pd directly on the bare *c*-Al$_2$O$_3$ chip (Fig. 2.8b). During the annealing process occurring at high temperatures, it is expected that a more homogenous mixture of Cu-Pd alloy would occur, due to diffusion of the Pd atoms into the Cu structure. From the design of the substrate and the preparation procedure, we could anticipate that **Sub5** contains a higher Cu concentration than **Sub6**. To determine the exact composition of

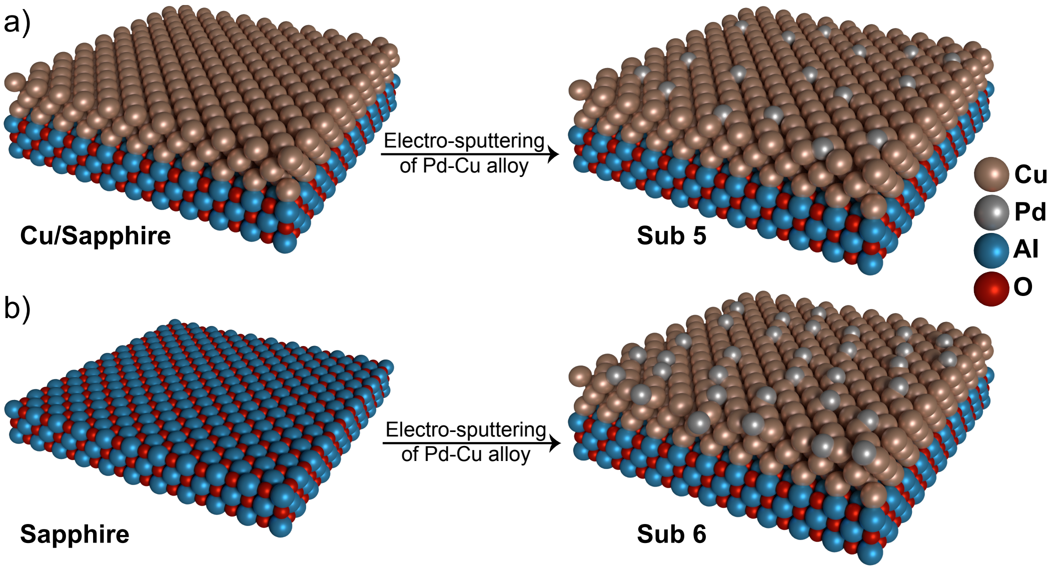

Figure 2.8: Cu-Pd alloy on *c*-Al_2O_3 chip. (a) **Sub5** using a *c*-Al_2O_3 chip pre-sputtered with 900 nm of Cu; (b) **Sub6** preparation employing a bare *c*-Al_2O_3 chip.

both substrates, EDS analysis was performed showing the expected results (Fig. 2.9a-b).

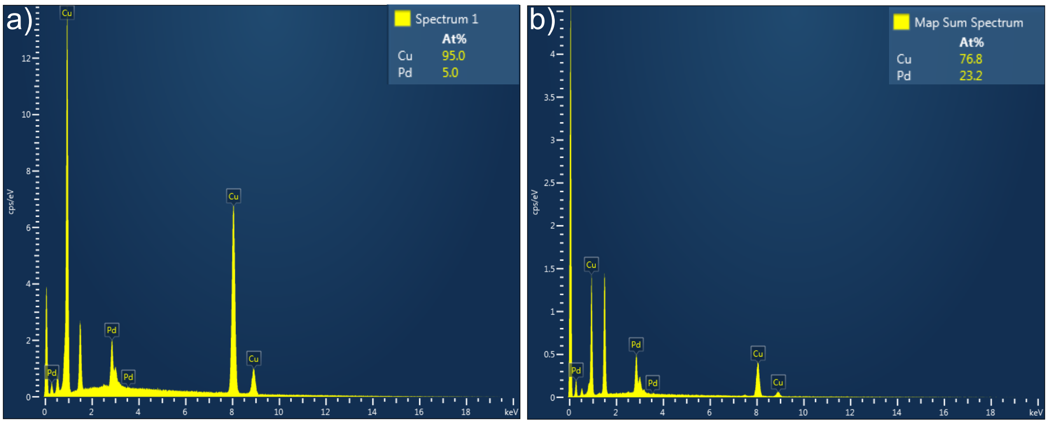

Figure 2.9: EDS analysis of Sub5 and Sub6. (a) EDS spectrum of **Sub5** showing a composition of 95at.% Cu and 5at.% Pd; (b) EDS spectrum of **Sub6** exhibiting a composition of 76.8at.% Cu and 23.2at.% Pd.

The synthesis of graphene was performed utilising the two new substrates, i.e. **Sub5** and **Sub6**, employing the same previously employed procedure (*vide supra*). Raman analysis of **Sub5** after the growing step with CO_2 revealed the characteristic D, G and 2D bands of graphene (Fig. 2.10a). As in **Sub1**, we performed a Raman mapping revealing graphene growth on the whole substrate. Furthermore, EDS was employed to quantify the exact Cu-Pd composition of **Sub5** before and after the graphene growth step (Fig. 2.10b-c). As expected, we find a high average Cu concentration (95at.%) in **Sub5**. Additionally, we find a similar de-wetting pattern in **Sub5** as the observed in **Sub1** (Fig. 2.10c).

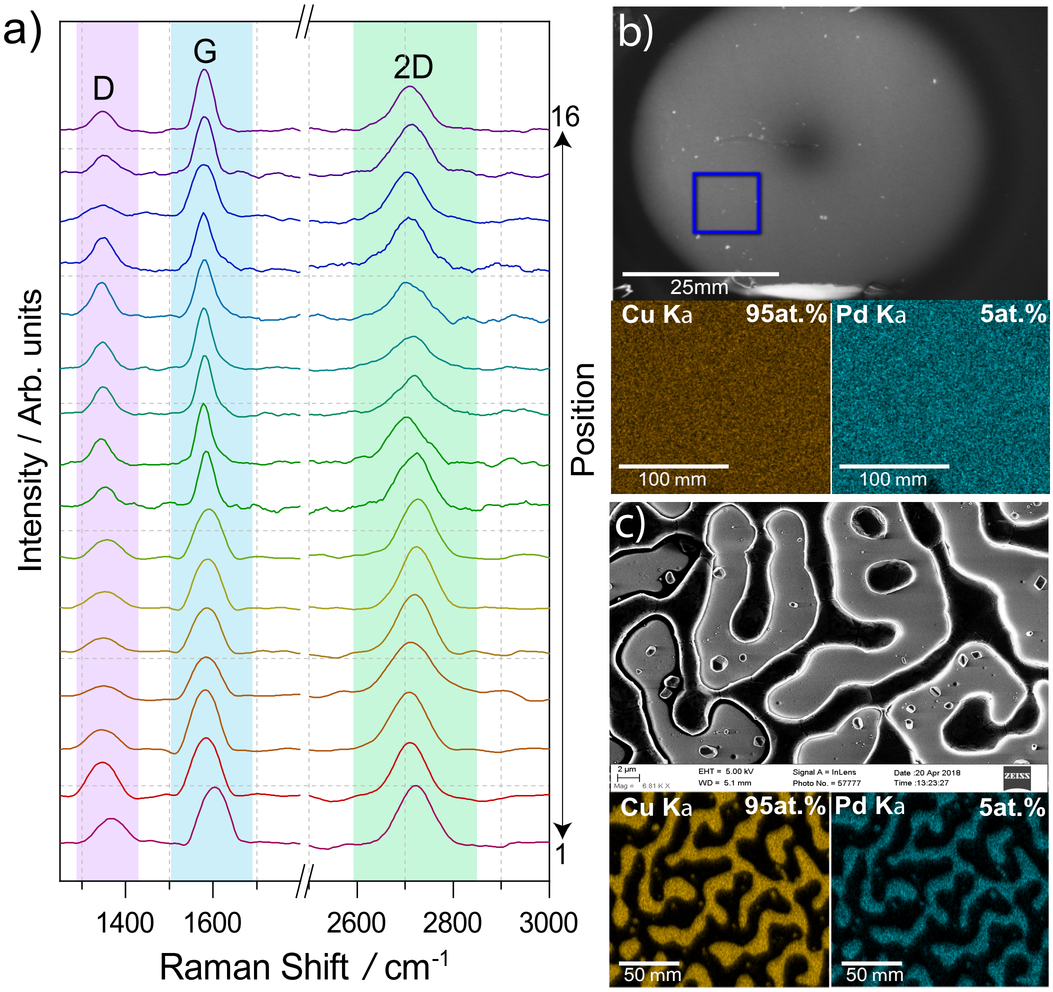

Figure 2.10: Characterisation of Graphene obtained on Sub5. (a) Raman mapping of **Sub5** showing the D (pink), G (pale blue) and 2D (pale green) peaks; (b) SEM image of **Sub5** before the growth procedure with its respective EDS analysis revealing a concentration of 95at.% Cu and 5at.%Pd; (c) SEM image of **Sub5** after growth procedure with its EDS showing the fingerprint of the metals diffusion after growing step and the sample ratio of metals.

Sub6 was employed for the synthesis of graphene under the same condition than **Sub5**, surprisingly no graphene formation was found, as confirmed by Raman spectroscopy (Fig. 2.11). It is very important to highlight that the EDS analysis of **Sub6** revealed a lower average quantity of Cu (77at.%) compared to **Sub5** (96at.%).

Furthermore, a series of experiments were carried out employing different composition of metals of the alloy substrates. Previous experiments revealed that 100% of Cu or Pd did not lead to graphene growth. Furthermore, it was also demonstrated that 77at.% of Cu in **Sub6** did not show any graphene growth. Interestingly, when the amount of Cu was increased to 85at.% we find graphene growth, whilst quantities of Cu as low as 82at.%, render the graphene growth inoperable (Fig. 2.12b-c). We also noted that

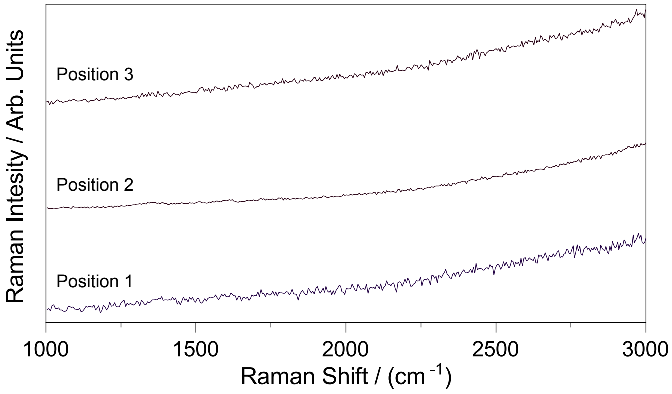

Figure 2.11: Growth Experiment. Raman of **Sub6** after growth procedure.

when the concentration of Cu is as high as 96at.% there is still a growth of graphene but with lower quality, due to the lack of 2D peak in some areas (Fig. 2.12). Our results demonstrate that when the Cu concentration in the metallic substrate is 82at.%, or lower the growth of graphene is suppressed.

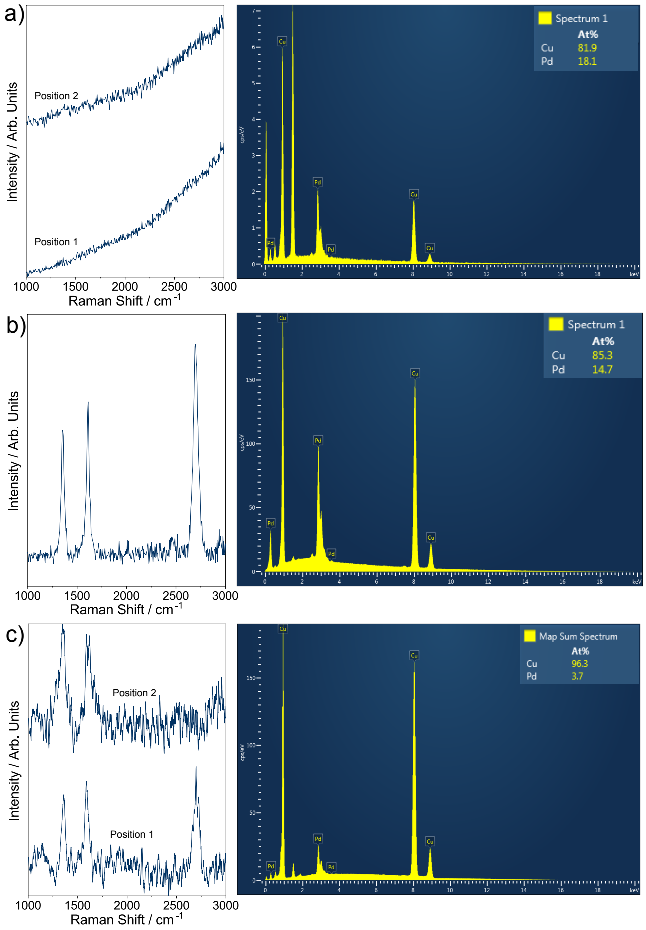

Figure 2.12: Raman spectra and EDS alloys substrates. (a) Raman spectrum of alloy with a composition of 81.9at.% Cu and 18.1at.% Pd with no growth of graphene; (b) with a composition of 85.3at.% Cu and 14.7at.% Pd exhibiting graphene growth; (c) Rwith a composition of 96.3at.% Cu and 3.7at.% Pd showing partial growth of graphene.

Note that, a more quantitative study, with a larger spectrum of alloys at different concentrations was not feasible in the present study, due to the lack of control over the concentration of the Cu and Pd metals during the sputtering process.

2.5 Structural Aspect of the Grown-Graphene: TEM Analysis

The structural aspects of the grown graphene such as the number of layers and crystallinity, as well as the quality of the obtained graphene in **Sub5**, were explored through Transmission Electron Microscopy. A piece of graphene from **Sub5** was transferred into a holey carbon grid. Afterwards, Raman analysis was conducted to confirm the transfer of the graphene films. Fig. 2.13a shows the Raman spectrum of the film of graphene on the TEM grid, which presented the characteristic peaks of graphene materials (D, G and 2D). TEM images of the film have confirmed the formation of crystalline graphene layers.

Low magnification image exhibited the film of the grown graphene with an inset exposing the Selected Area Electron Diffraction (SAED) pattern of the area framed in red (Fig. 2.13b). The SAED pattern shows two sets of diffraction spots attributed to the plane of diffraction [100] and [110] in a single crystalline area of the graphitic carbon. Additionally, there is an absence of the strong reflections from the [002] planes, which indicates a dominant in-plane growth of graphene and high crystallinity of the film. In Fig. 2.13c is presented the folded-up edges of the film, where the stacking of the layers of graphene can be clearly visible. The inset on the upper left side exhibits the local Fast Fourier Transform (FFT) applied to the red box region with the characteristic stacking of graphene at [002] with an average interlayer distance of 0.357 nm[140]. Furthermore, the inset shown at the upper-right of Fig. 2.13c, displays a local FFT from the blue section, which exhibits a diffraction pattern that does not have any [002] reflections corresponding to the in-plane growth of the grown graphene. The number of layers were counted by employing the intensity profile from the stacked region (Fig. 2.13d), which revealed a number of 10 to 20 graphene layers, in agreement with the results observed from the AFM height profile of the transferred graphene grown on **Sub1**. The TEM analysis has confirmed the direct formation of a multi-layer graphene from CO_2.

The results presented in all the experiments have demonstrated the direct formation of multi-layer graphene from CO_2, utilising Cu-Pd mixtures which acts as not only as the catalyst but also as the substrate. Previous studies have revealed that a relatively strong carbon-metal (C-M) interaction between CO_2 and Cu-Pd metals improve the efficiency of the activation and conversion of CO_2 into more reactive chemical species[141,142]. Additionally, the Cu-Pd phase has been demonstrated that it is important in the capture and conversion of CO_2. From the Cu-Pd phase diagrams it is expected that a Face Centred Cubic (FCC) phase prevails in our substrates due to the working temperatures employed in our experiments[143], there-

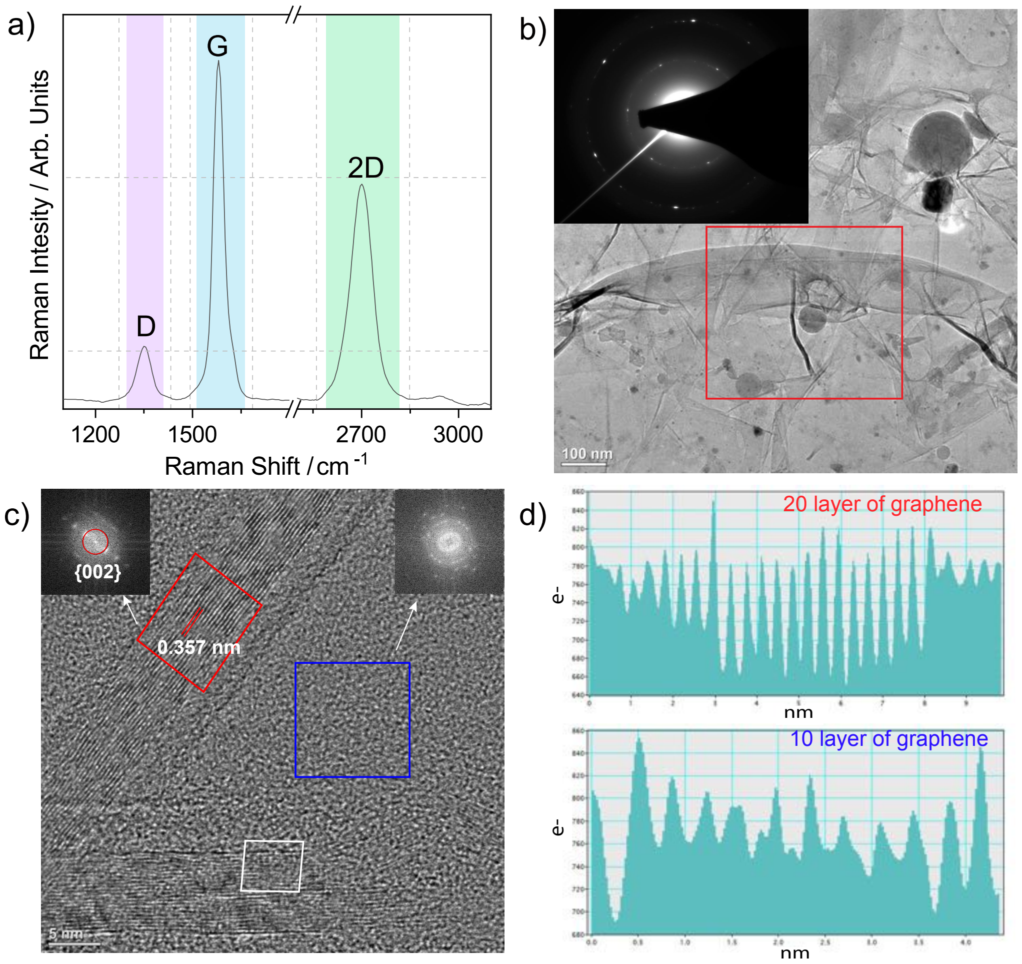

Figure 2.13: TEM Characterisation of Graphene obtained in Sub5. (a) Raman of the graphene on the TEM grid; (b) Low magnification TEM image and SAED diffraction pattern (inset) of the graphene revealing a high crystallinity; (c) Low resolution image of the staking of graphene layers; (d) High Resolution TEM image showing the graphene interlayer of 0.357 nm. The inset at the upper-left corner shows the local FFT of the [002] reflections of the stacking of graphene (red square). The upper-left inset (corresponds to the blue square) shows no reflection from the staking of graphene.

fore, a homogeneous substrate is expected when the growth of graphene occurs[144]. In addition, some approaches employing electrochemical procedures have shown that a mixture of Cu with noble metals, such as Pd, platinum (Pt) and gold (Au), can yield an efficient system for the reduction of CO_2 into more reactive species[122,141,145].

Keeping this in mind, we are able to propose a possible mechanism for the capture, reduction and conversion of CO_2 to graphene utilising Cu-Pd substrate, as follows: (*i*) the carbon of the CO_2 interacts with the Cu-Pd metal substrate, debilitating one of the oxygen bonds of the CO_2; (*ii*) subsequently, H_2 reacts with the labile oxygen of the CO_2 leading to the formation of H_2O and generation of CO[146], or other molecules such as methane[124], methanol[136], amongst others; (*iii*) the precursors obtained are rapidly converted to graphene. In fact, although other small hydrocarbons can also be produced, it has been suggested that by mixing Cu (with a high ΔH_{CO}) and Pd (with lower ΔH_{CO}) a better evolution of CO can be achieved. In Fig. 2.14 the proposed mechanism is depicted together with the reaction that describes the whole process of reaction and convention of CO$_2$ to multi-layer graphene[147].

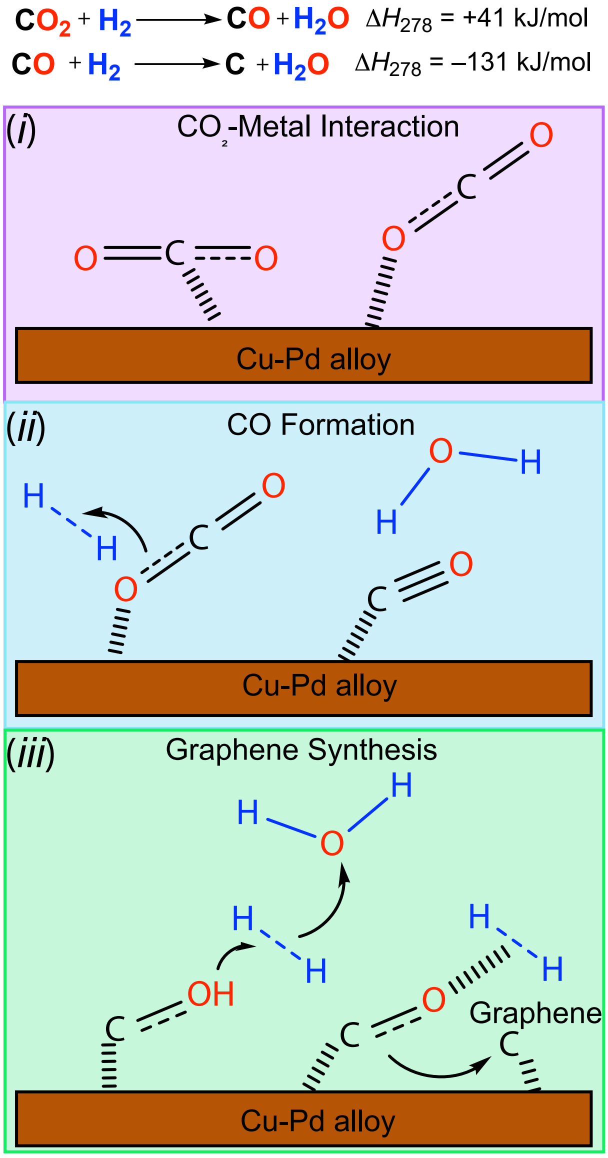

Figure 2.14: Schematic representation of capture, reduction and conversion of CO$_2$ to graphene. (*i*) Capture of CO$_2$ by interacting with the Cu-Pd metal substrate and, therefore, the oxygen bonds of the CO$_2$ are debilitated; (*ii*) the molecules of hydrogen react with the labile oxygen of the CO$_2$ leading to the formation of water and generation of CO; (*iii*) the CO molecule formed in the previous step, is rapidly converted to graphene.

It is important to highlight that graphene growth was achieved only in alloys with a Cu content higher than 82at.%, while at lower concentrations of Cu (larger of Pd) the formation of graphene was inhibited. Cu has been proposed by some reports as the promoter of a larger absorption of CO$_2$

and on the other hand, Pd enhances the desorption at the Pd reactive site, thus, large quantities of Pd preclude the reduction of CO_2. This is due to the strong affinity between Pd and CO, which binds firmly to Pd, making the Pd sites inaccessible to further CO_2 reduction steps.

2.6 Conclusions

The large quantities of CO_2 generated by industrial processes, along with the active utilisation of fossil fuels, such as coal and petrol derivates, to generate different forms of energy, has positioned CO_2 as one of the major environmentally problematic green-house gases. The obvious global warming has consequently motivated scientists to quest for methodologies to reduce the CO_2 levels. One of such possibilities is the utilisation of CO_2 as feedstock for the synthesis of carbon-based materials and fuels. In this chapter, the development of a one-step method to convert gaseous CO_2 to carbon-based materials, utilising Cu-Pd alloys as catalyst and hydrogen as reductant agent, was presented. The aim of this work was to find the right conditions for the conversion of CO_2 to graphitic material employing a one-step procedure. Firstly, the study was commenced by the design of a series of metallic substrates, where single metals, such as copper or palladium were tested to probe the catalytic power for the conversion of CO_2 to graphene. Moreover, two other metals substrates were designed, with the goal of establishing whether both metals were required for the synthesis of graphene, either separately or in direct contact. This first study resulted in the formation of graphene solely in the substrate where both metals, Cu and Pd, were in direct contact.

Further studies employing Cu/Pd alloys demonstrated that by utilising the right mixture of Cu and Pd it was possible to achieve a multi-layer graphene. Additionally, we find that the Cu-Pd alloys definitely act simultaneously as catalyst and substrates in the conversion of CO_2. It is important to stress that hydrogen was used as the reducing agent in the reaction, otherwise, the complete process would not occur. The study of the catalyst composition that the conversion of CO_2 to graphene was only achieved on substrates with a content of Cu above 82at.%. Moreover, experiments on substrates with a content of 100at.% of Cu revealed that the reaction did not proceed, demonstrating that a small amount of Pd is always required. Note that large quantities of Pd metal precludes the formation of graphene, which can be rationalised by the enhancement of the desorption of CO_2 by the Pd metal, while larger quantities of Cu have been shown to promote a larger CO_2 absorption. It is worth noticing that although Cu has been shown to promote an increased CO_2 absorption, we do not find any graphene formation employing solely Cu as substrate, demonstrating that the CO_2 conversion to graphene is a synergistic effect.

Characterisation techniques such Raman and AFM showed that the graphene obtained has 10-20 layers, which was confirmed by TEM analysis. Unfortunately, the quality of graphene was affected by the de-wetting of the metals due to the high temperature employed in this approach (T = 1000 °). This process is not possible to avoid due to the considerable amount of energy required for the activation of CO_2; a thermodynamically stable molecule. However, this study will serve as foundation for further studies in the conversion of CO_2 to graphene employing a one-step approach. There are few problems to solve such as, de-wetting of metals and the formation of several layers of graphene. We are sure that by overcoming these problems a better quality of few-layer graphene can be achieved. Note that although graphene has been earlier obtained using CO_2 as feedstock, the synthetic methodology consisted in a two-steps process, contrary to the one-step procedure herein described.

In summary, we have created a procedure where a problematic environmental gas such CO_2 can be re-utilised as carbon source in the synthesis of graphitic materials. The green house problem will not be solved using this approach, but we are sure that this will be an important step for the use of an environmentally problematic molecule to produce high asset carbon-based systems, e.g. batteries, spin-valves, etc.

Chapter 3

Nanocrystalline Graphene from an Organic Molecule

The results presented in this section were obtained in collaboration with two groups at INT: the Charge Transport and Light-matter interaction in carbon nanosystems led by Prof. Ralph Krupke, and the Electron Microscopy and Spectroscopy laboratory from Prof. Kübel, for TEM characterisation.

Monocrystalline pristine graphene has been presented as the strongest 2D carbon-based material with extraordinary mechanical and electrical properties[148]. Nevertheless, the synthesised graphene for scalable fabrication techniques has a polycrystalline nature, which also contains inherent nanoscales defects such as: lines, points grain boundaries, etc[149]. Although there are many studies about the scalability of graphene synthesis, its properties, its implementation in electronics, etc., recently, scientists have turned their attention to an interesting 2D graphene-liked material[91]. The synthesis of this 2D material has been achieved by graphitisation of polymers thin films through pyrolysis reaction. The resulting film is known as nanocrystalline graphene (NCG) owing to the domain sizes in the film has just few nanometres and as well as it presents a high-density of defects. Additionally, NCG has shown properties comparable to graphene such as electrical and optical. Moreover, the crystal structure of NCG is what makes this material very different to graphene, since NCG may contain large areas, of the the order of micrometre up to few millimetres, with high concentration of nano-crystalline domains. Few studies have been developed to address the characterisation of NCG, one of the most important technique utilised nowadays is Raman spectroscopy[79]. The major difference in Raman between graphene and NCG is that, graphene possesses a narrow and big G and 2D peak and not D peak, while NCG has as fingerprint an intense D peak, which increases when the domain size decreases. Therefore, the electrical properties of NCG are different, for instance its conductivity is lower and the resistance can be of the orders of magnitudes of 10^3 Ω/m^2, which can lead to a gate dependent behaviour[73,150].

In this section, the thesis is focused on the synthesis of NCG from the organic molecule hexaethynylbenzene (**2**). Usually, NCG is synthesised utilising very explosive or toxic gases such as CH_4, C_2H_2 and CO, that requires specialised systems and handling. Additionally, NCG has been synthesised utilising polymers as the carbon source, but the time employed for the growth is long, from 2 to 10 hours and requires high vacuums. Keeping this in mind, we proposed an alternative approach utilising as the carbon source for the NCG growth a non explosive and relative non-toxic molecule such hexaethynylbenzene. The synthesis was carried out in an atmospheric pressure chemical vapour deposition reactor, using Cu foil as the substrate and catalyst. The NCG is grown by first depositing on the surface of Cu foil at room temperature and soon after it is heated to 850 °C under a stream of Ar (Fig. 3.1). The grown-NCG is characterised *via* different surfaces techniques: Raman spectroscopy, SEM, AFM, TEM, OM and XPS.

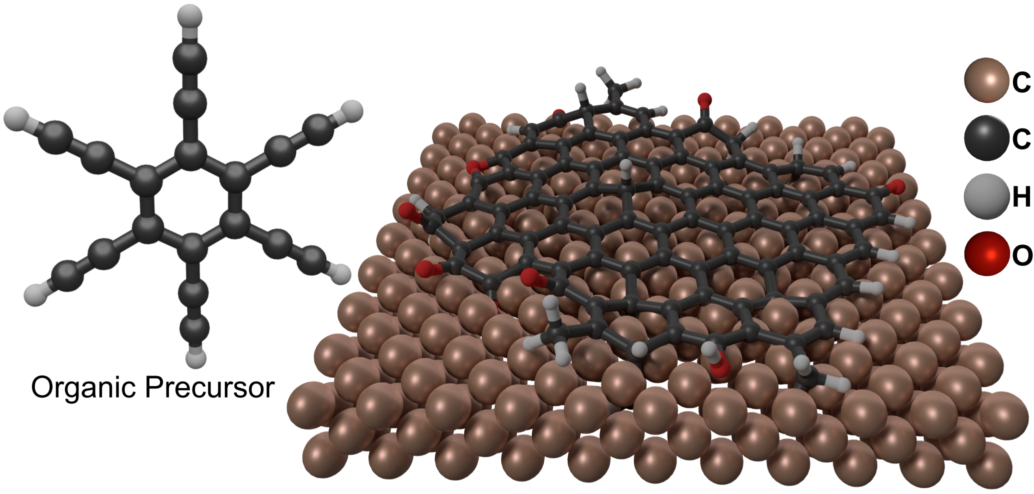

Figure 3.1: NCG from Organic Molecules. Schematic representation of the Nanocrystalline graphene growth on Cu foil from the organic molecule hexaethynylbenzene (**2**).

3.1 Synthesis of Nanocrystalline Graphene *via* APCVD

NCG synthesis was performed using compound hexaethynylbenzene (**2**) as the carbon source. A foil of Cu 1×2 cm was employed as the substrate for the growth of NCG, previously cleaned by soaking it in isopropanol under sonication. The molecule **2** was employed as the source of carbon for the synthesis of NCG under a mixture of Ar and H_2 gases. A nebuliser was employed to deposit 5 mg of **2** dissolved in acetone, on the surface of the pre-cleaned Cu foil at room temperature. The deposition of **2** was performed under a stream of Ar (2.8 sscm), applying 27.5 V to the nebuliser membrane for 10 min. Soon after, the deposition was stopped by switching off the power supply of the nebuliser, and the Cu foil was held under the Ar stream for 30 more min. Afterwards, the temperature of the CVD furnace was increased to 850 °C, which is the growth temperature, at a rate of 30 °C per min. When the growth temperature is reached, a stream of H_2 (2.5 sccm) was introduced to the CVD system, the Ar stream was held to 2.8 sccm and the growth of

NCG took place for 30 min. The role of H_2 was to reduce the oxidised **2** and to remove the unreacted compound. Posteriorly, the H_2 stream was halted and the system was cooled down to room temperature.

The grown NCG was characterised first by Raman spectroscopy and subsequently it was transferred to a Si, SiO_2 and quartz substrates, for further surface characterisation. The transfer of the grown NCG was conducted following a procedure described in section 5.4.2.

3.2 Characterisation of NCG

As mention earlier, Raman spectroscopy has become a powerful tool in the characterisation of graphic materials. The Raman analysis of the grown NCG was performed directly on Cu foil after the growth procedure. The grown-NCG exhibited the characteristic peaks of a graphitic material[76]. Fig. 3.2 shows the spectra of obtained grown-NCG, where a very large D band highlighted in sky-blue, is observed at 1354 cm^{-1} corresponding to the defective nature of NCG, at 1595 cm^{-1} is exhibited a broad G peak (marked in yellow) and a small 2D peak (in pale red) at 2706 cm^{-1} (Fig. 3.2). The analysis of several position along the whole Cu foil was performed finding almost the same Raman spectrum in all positions.

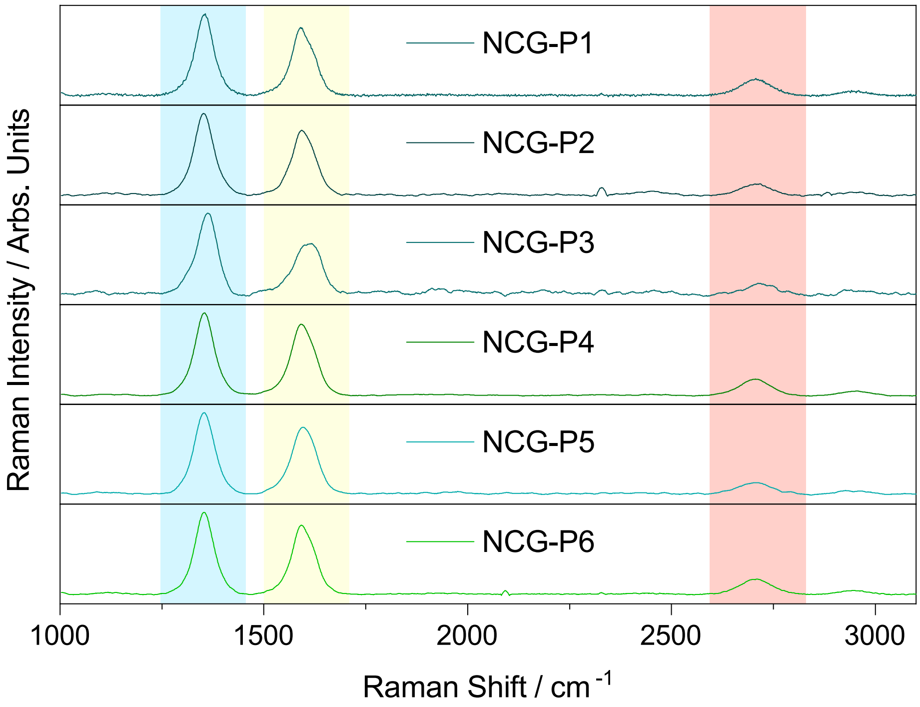

Figure 3.2: Raman of NCG. Raman Spectra of different positions along the Cu foil containing the grown-NCG, D (sky blue), G (yellow) and 2D (red) bands. P_i = position.

Moreover, the crystal size of the grown-NCG can be obtained from the Raman spectrum employing the Cancado et al. formula[79]. Cancado et al. formulated an equation to calculate the crystal size of crystalline graphene based on the full width at half maximum (FWHM) of the three peaks of graphene in Raman, which are independent of the excitation laser energy. The resulting formula is:

$$\Gamma_{FWHM} = A + BL^{-1} \tag{3.1}$$

The values of A and B are tabulated and the FWHM were obtained from a Gaussian analysis performed to Raman spectrum. The analysis of the NCG film resulted in crystals size ranging from 8 to 12 nm approximately, when the FWHM of D-bands were emplpyed for the calculation. Furthermore, when the FWHM of G band are employed to calculate the crystal size of the 6 different positions examined with Raman in Fig. 3.3, the size varies from 7 to 10 nm. This is due to the D peak is better defined than the G peak.

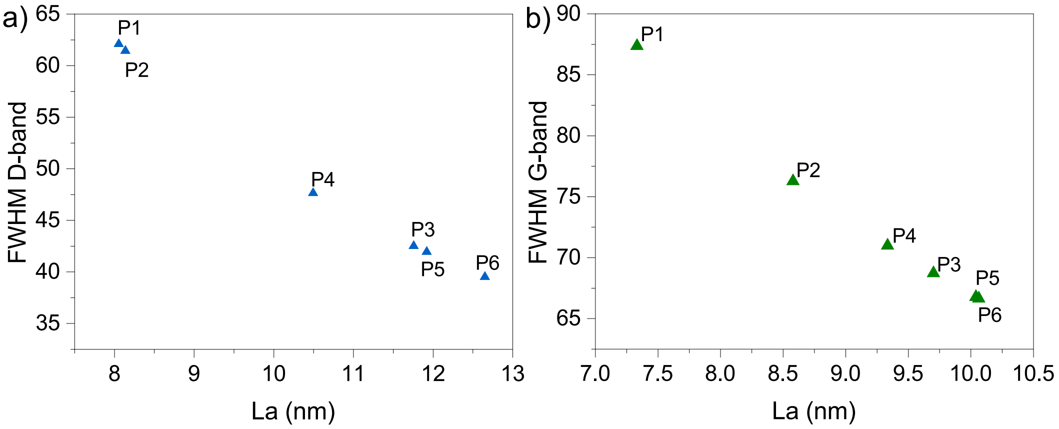

Figure 3.3: Crystal size distribution along the whole substrate. (a) FWHM of D band vs. crystal size (L_a) of different position along the whole substrate; (b) FWHM of G band vs. crystal size (L_a) of different position along the whole substrate.

Fig. 3.3 shows the distribution of the FWHM of D and G bands versus the crystal size along different position in the grown-NCG on Cu foil.

Further characterisation as XPS was performed on the grown-NCG to determine the chemical composition of the NCG. A survey spectrum of NCG exhibited two prominent peaks, the biggest peak corresponds to C1s contribution while the second peak is the contribution of O1s (Fig. 3.4). This analysis has shown the defective nature of the obtained NCG, due to the important contribution of oxygen presented in the film.

The analysis of C1s of this film on a Si substrate showed that the larger peak corresponds to the C-C sp^2 bonds displayed at 284.5 eV, which is expected due to graphene material content is mainly sp^2 carbon (Fig. 3.5). The C1S spectrum also exhibited others peaks at 285 eV corresponding to C-H bonds, C-O at 286.4 eV and C≡O at 288.7 eV. Those peaks revealed the defective nature of the NCG, which is in agreement with the Raman analysis, where the D band has an important intensity. The high contribution of C-O bonds is due to the exposure of the precursor to ambient condition prior deposition and growth of NCG.

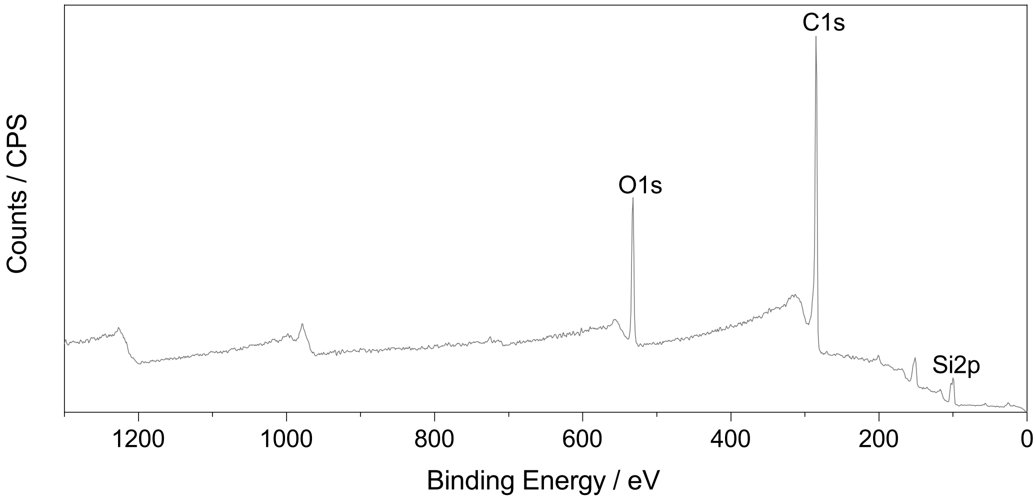

Figure 3.4: XPS Spectrum. Survey spectrum of the grown-NCG film on Si substrate.

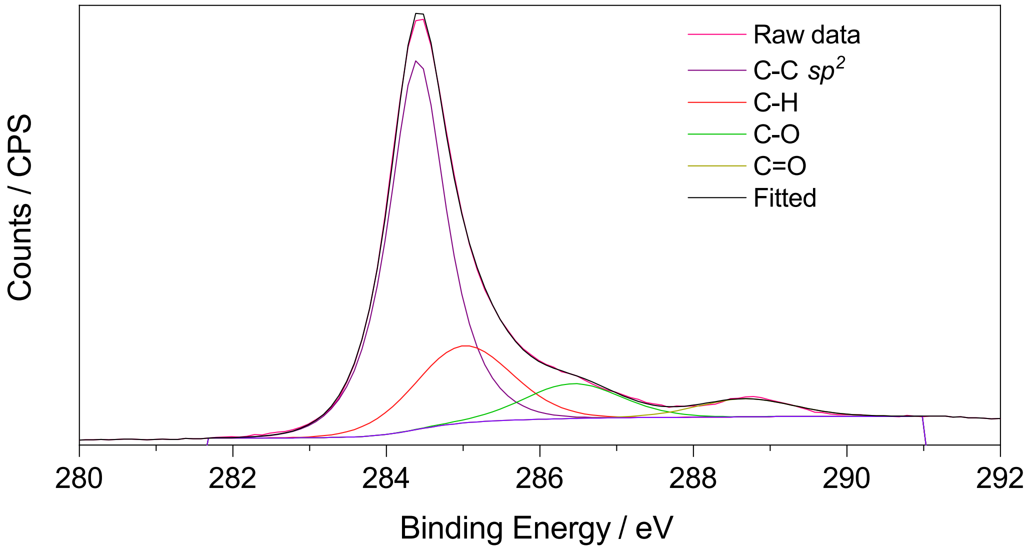

Figure 3.5: XPS Analysis. XPS of the grown NCG on Si substrate showing the C and O composition.

NCG films were examined by OM and SEM showing a continuous and inhomogeneous network. In Fig. 3.6a and c are displayed the OM images of NCG where it is possible to observe the nucleation pattern in the film on Cu foil (Fig. 3.6a) as well as after transfer to a SiO_2 substrate (Fig. 3.6c). Moreover, in the SEM image in Fig. 3.6b are shown the grain boundary of the Cu foil and the nucleation site displayed in white colour.

The SEM images presented in Fig. 3.6d shows the wrinkles formed during the CVD growth of the NCG, which are very common when high temperatures are employed during the CVD synthesis of 2D network.

AFM was employed to determine the thickness and morphology of the grown NCG. The grown film has shown to be continuous with some white spots that can be attributed to nucleation site or small areas where the num-

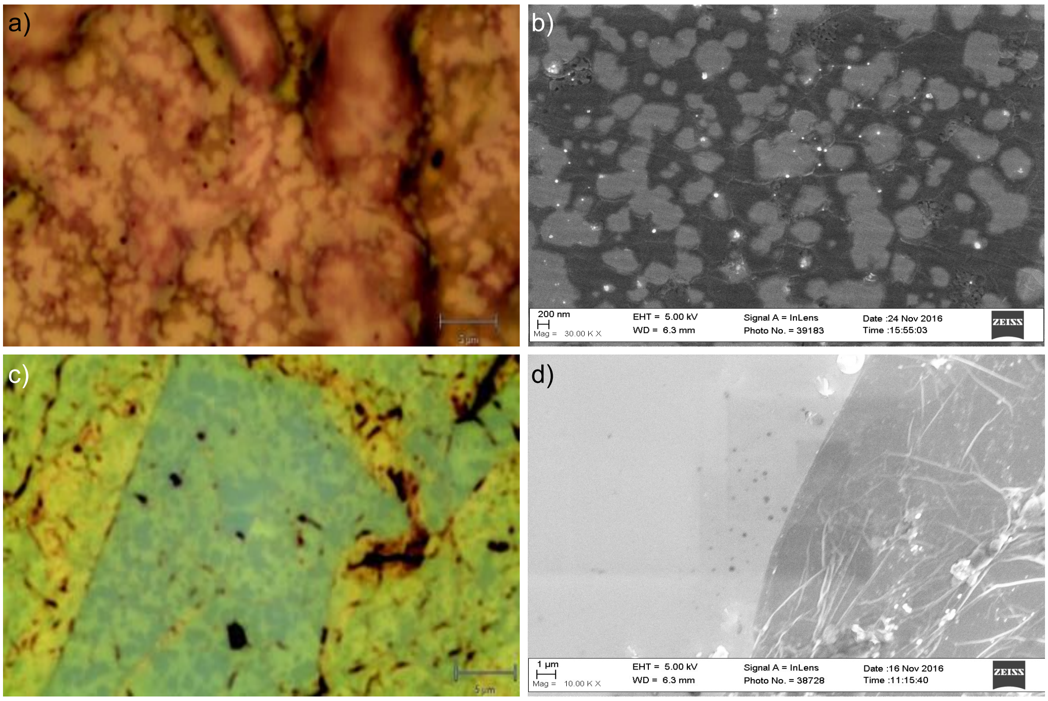

Figure 3.6: Optical and SEM images of NCG on Cu and on a Si or SiO_2 substrate. (a) NCG on Cu foil after the growth procedure; (b) SEM image of the grown NCG; (c) OM image of NCG transferred to a SiO_2 substrate; (d) SEM image of a cross section of NCG on Si substrate.

bers of layers is expected to be several. In Fig. 3.7a-b are shown cross sections of the NCG film, where two different morphologies are presented with a higher area. This could be due to nucleation during the growth, which lead to a thicker area with a considerable number of layers. Moreover, there is a smoother area showing a continuous film with a thinner thickness compared to the nucleation sites. Fig. 3.7a exhibits the nucleation sites a smoother film and also a small crack due to the transfer process, that allows the measurement of the thickness of the two morphologies presented in the NCG film. The height profile of the green line in Fig. 3.7a has shown the difference in height in the NCG film, the total thickness of the grown NCG is about 7 nm, whereby 2 nm is the thickness of the smoother morphology and about 5 nm is the height of the nucleation sites (Fig. 3.7c). Additionally, the height of a different nucleation sites in the film was measured showing a value around 4 nm (Fig. 3.7d), which lead to draw the conclusion that the height of those nucleation sites in the films is between 4 to 5 nm or 11 to 14 layers, while the smoother film has approximately 6 layers.

TEM was employed to explore others features of the grown-NCG such as quality and structural aspects. For this measurement, a small piece of NCG film was transferred to an empty Cu grid for TEM and afterwards the experiment was conducted employing 80 kV electron beam. In Fig. 3.8a-f is shown images of the NCG film. In Fig. 3.8a is shown a low resolution images of the film and an inset of the selected area electron diffraction (SAED) of the area framed in a red box, that exhibited a very crystalline pattern. Several layers of NCG are seen in Fig. 3.8c and the interlayer spacing was measured giving

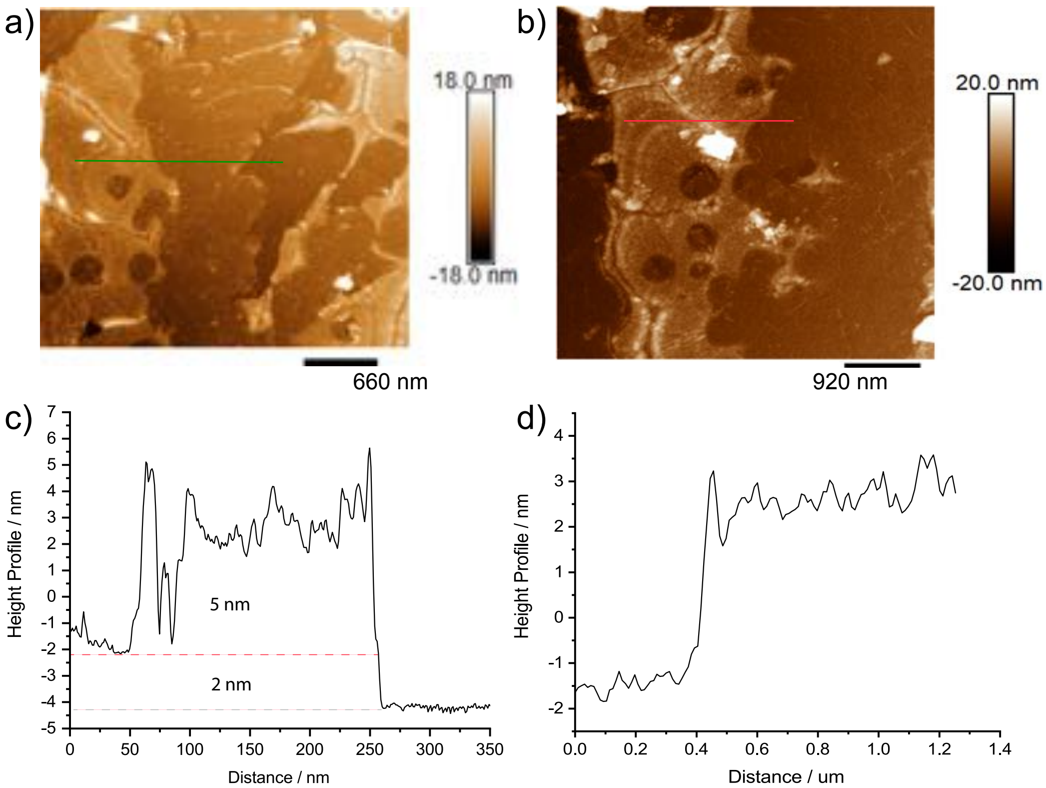

Figure 3.7: AFM images of the transferred NCG film to Si substrate. (a) Image of a cross section of NCG film on Si substrate where is possible to observe a crack owing to the transfer process; (b) Image of a cross section of NCG film on Si substrate where the nucleation part is shown; (c) Height profile of a cross section of the nucleation site and the continues film; (d) Height profile of a cross section of a nucleation site of NCG.

a value of 0.35 which correspond to the interlayer spacing of graphitic materials. In most of the images it is possible to observe some amorphous carbon around the crystal size. In Fig. 3.8c is presented an inset of the area frame in red, which is a local fast Fourier transform (FFT) that shows a hexagonal shape corresponding to the honey-comb graphene pattern and in the same image is possible to count 7 layers of NCG, which is in good agreement with the previously presented AFM data.

An *in-situ* heating was performed in the TEM microscope to examine the amorphisation trajectory of the grown-NCG. In this experiment a small section of NCG film was transferred to a SiC substrate and afterwards placed in the TEM microscope. The sample was heated to 1200 °C at a rate of 40 °C per minute and was held for others 30 min. Subsequently a series of images were taken after heating. We have to highlight that some images were recorded before heating to compare them to the ones obtained after the treatment. In Fig. 3.10a-c are shown the images of the film before heating treatment and in Fig. 3.10d-f after the heating treatment. The images before the heat treatment presented a very disordered network with a lot of amorphous carbon, nevertheless, the images after the heating exhibit a more ordered network with well-defined grains. This experiment has demonstrated that the grain size of our NCG quality can be enhanced by heating treatment.

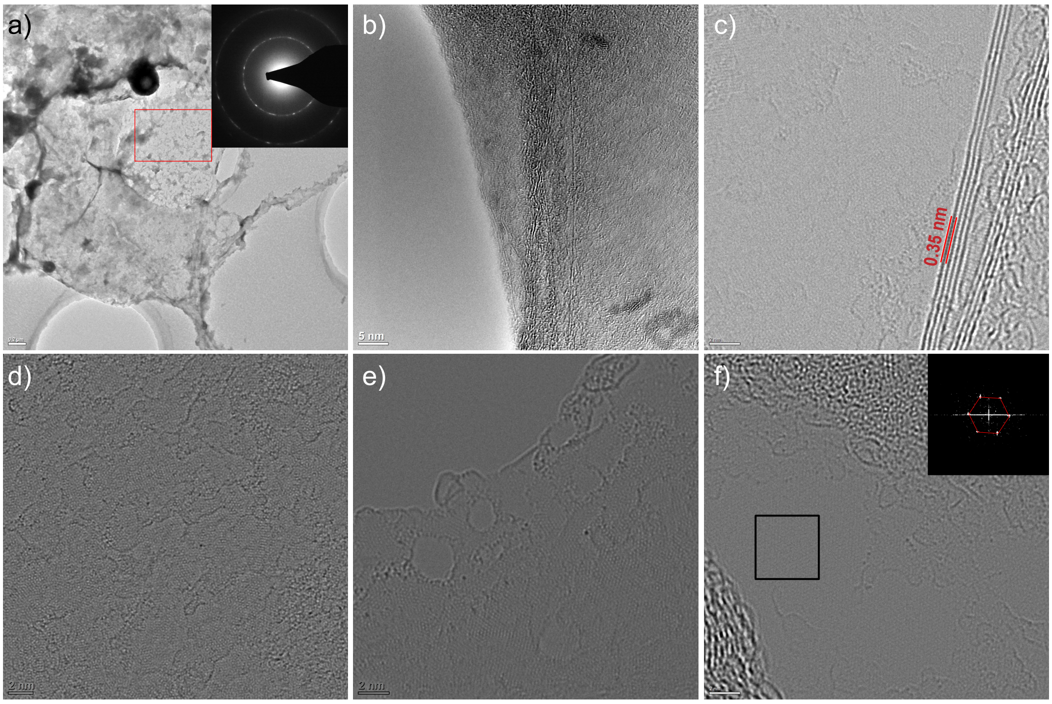

Figure 3.8: Transition electron microscopy (TEM) images. (a) NCG film on the TEM Cu grid with an inset of the SAED of the red box; (b) Low resolution image of a cross-section of NCG; (c) Layers of NCG with the interlayer spacing; (d) High resolution image of NCG; (e) High resolution image of a cross-section of NCG; (f) Low resolution image of a cross-section of NCG with a FFT displayed as an inset of the box framed in black.

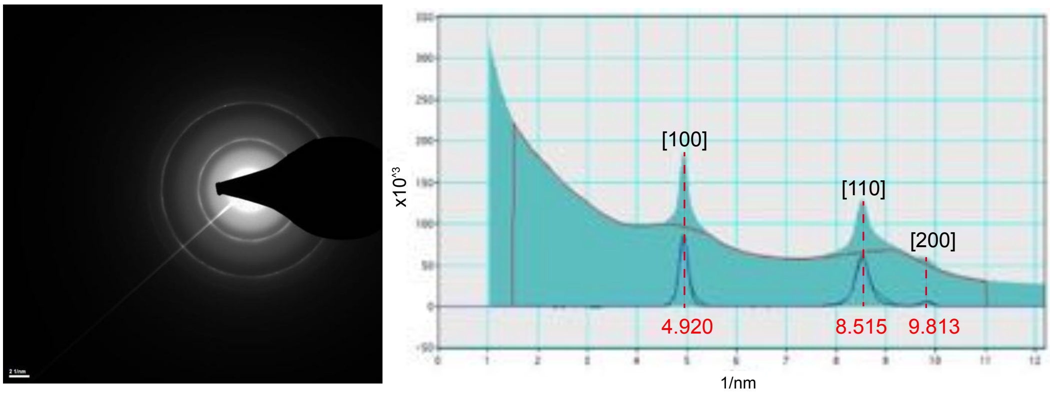

Figure 3.9: TEM Characterisation. SAED pattern with its respective reciprocal lattice.

The crystallographic planes of NCG were carefully studied by TEMs showing three prominent peaks. In Fig. 3.9 is exhibited these three planes which are [100], [110] and [200], corresponding to graphitic materials[151]. The SAED pattern presents two sets of diffraction spots, which is indicative of the polycrystalline nature of the NCG.

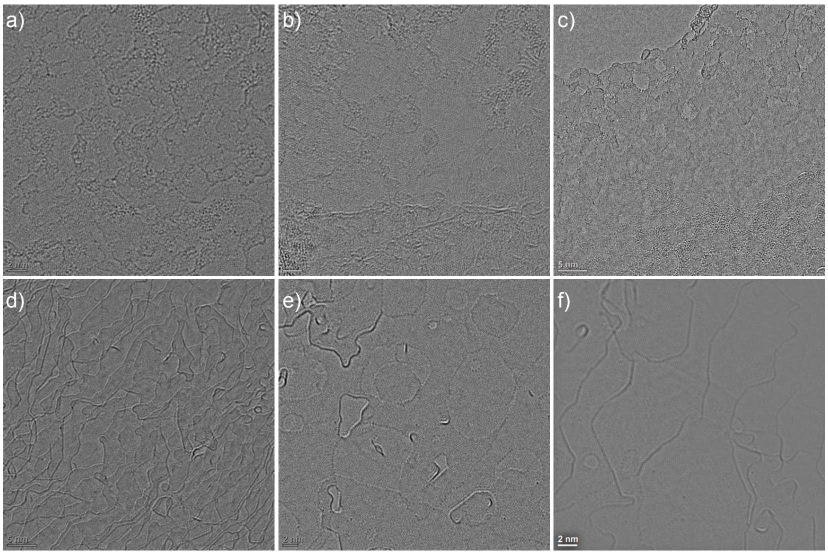

Figure 3.10: TEM Images. (a-c) TEM images of a cross-section of the NCG film before heating treatment; (d-f) TEM images of a cross-section of the NCG film after heating treatment

The heating experiment was followed by Raman spectroscopy. The Raman spectrum before and after heating is shown in Fig. 3.11, which exhibits a very important difference. It can be seen that the G peak became higher in intensity and sharp and also there is a blue Raman shift of 19 cm^{-1} for D peak and 12 cm^{-1} for G peak.

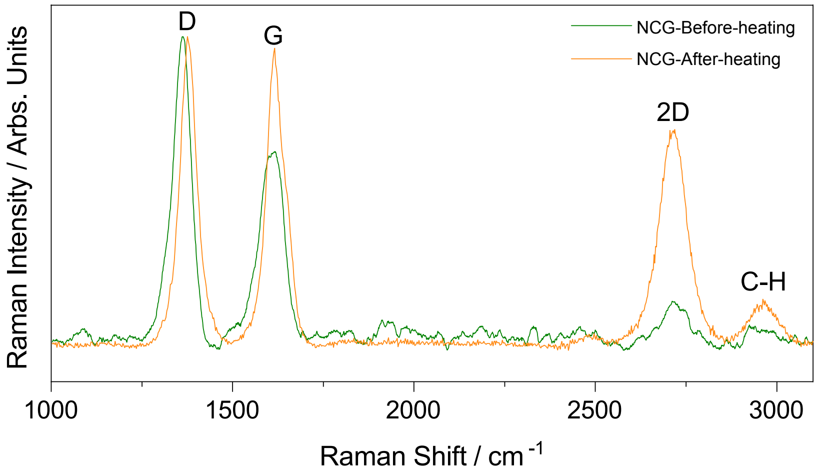

Figure 3.11: In-situ heating of NCG. Raman spectrum of the grown NCG before and after heating treatment showing the increase in the ordering of the NCG, as reflected by the height of the G and 2D peaks.

It is interesting that by following the amorphitisation trajectory proposed by Ferrari et al. we observed the formation of more sp^3 carbon, although when the crystal size was calculated using the FWHM obtained from Raman spectrum, the values reflected a change in the size. For the non-heated NCG film the value of FWHM of D peak was 61 cm^{-1} and for the heated one was

56 cm^{-1}, resulting in crystal size of 11.9 nm before heating the film and 13.2 nm for the heated film. We can conclude that even though the film has more sp^3 carbons, the crystal size grew 1 nm.

Future experiments varying the nature of the different films with different crystal sizes will give us a better understanding of the amorphisitation of this kind of materials.

3.3 Transport Measurements

The electrical properties of the NCG film were explored to determine the resistivity and conductivity of the NCG films. The measurements were carried out employing a transfer length methodology, which consists in the design of a set of metal-semiconductor contacts that are separated with various distances (length). For our device, a set of four metal-semiconductor contacts were prepared with different width of the metal contacts. The device was prepared by transferring the film to a SiO_2/Si chip coated with 1 µm of oxide and afterwards the four set of Au electrodes were deposited and shaped with the electron beam lithography technique, which is one of the most used methodology to fabricate devices. In the whole chip of the device there are two important parameters, one is the width (W) of the metal contact which vary in the 4 devices being for device labelled as A_W = 8 µm, for B_W = 16 µm, for C_W = 24 µm, for D_W = 48 µm. The other parameter is the length (L) between the metal contacts, for instance from contact A_1 to A_2 there is a L = 1 µm, A_2 to A_3 L = 2 µm, A_3 to A_4 L = 4 µm, A_4 to A_5 L = 10 µm and A_5 to A_6 L = 20 µm. These values are constants in the four devices but the values of width vary among the devices, as shown in Fig. 3.12a-e.

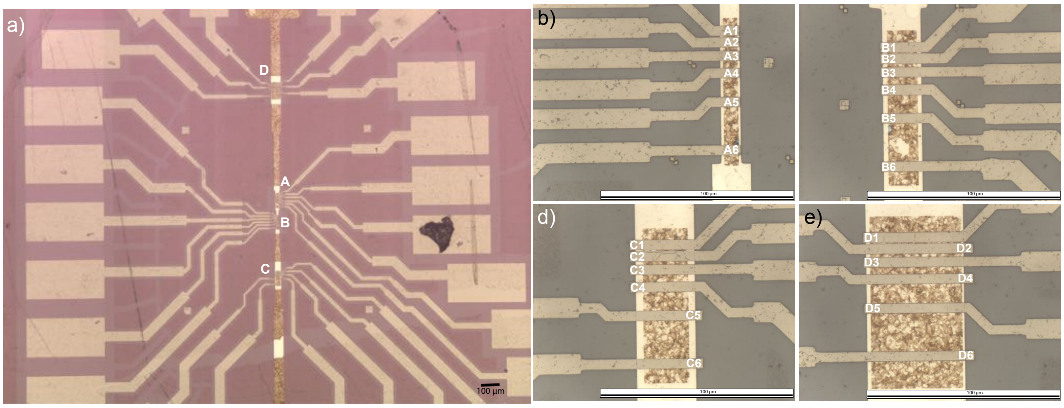

Figure 3.12: Device design Device created using transferred length methodology with four different widths and five length distance among the metal-semiconductor contacts. (a) OM image of the whole metal-semiconductor contacts; (b) Device A with a width of 8 mm and six contacts.

The height profile of the film was obtained by AFM measurement showing a film of 10 nm thickness, which is important parameter to obtain the total resistance of the film.

A four probes station was used for the measurement of the resistance of NCG, where two probes were employed, one as the source and the other

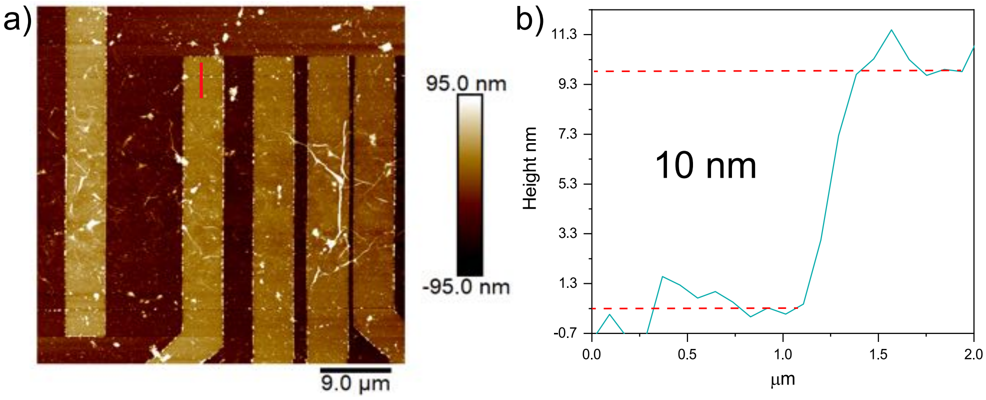

Figure 3.13: Device Characterisation. (a) Device made of NCG for conductivity measurements and (b) AFM image and height profile of the film on the device, with a thickness of 10 nm.

one as the drain. Afterwards, voltages ranging from -0.1 to 0.1 V was applied and subsequently the *I*-*V* curves of all the devices (A, B, C, D) were plotted to calculate the resistance of the system. The *I*-*V* curves showed a metallic behaviour that is possible to observe in Fig. 3.14a-d.

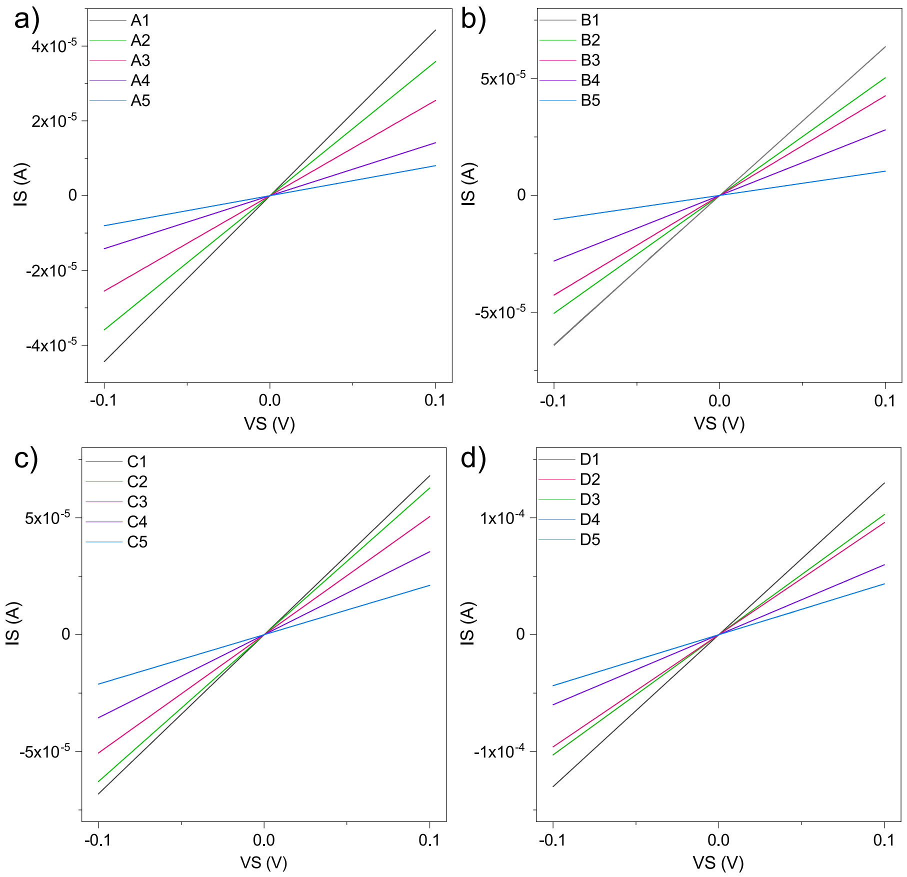

Figure 3.14: Resistance of NCG. *I* vs *V* curves of the 4 devices prepared (A, B, C, D), keeping constant the width (*W*).

The resistance of the system is the slope of the line corresponding to the measurement between two contacts, for instance in device A five slopes are obtained due to there are six contacts in the device labelled as A_1, A_2, A_3, A_4, A_5 and A_6, therefore, there are five possible measurements for the device A and all the others three devices in the chip. Subsequently, the resistance of the system (R) was plotted versus L to obtain the contact resistance (R_c), which is the intercept at the Y axis.

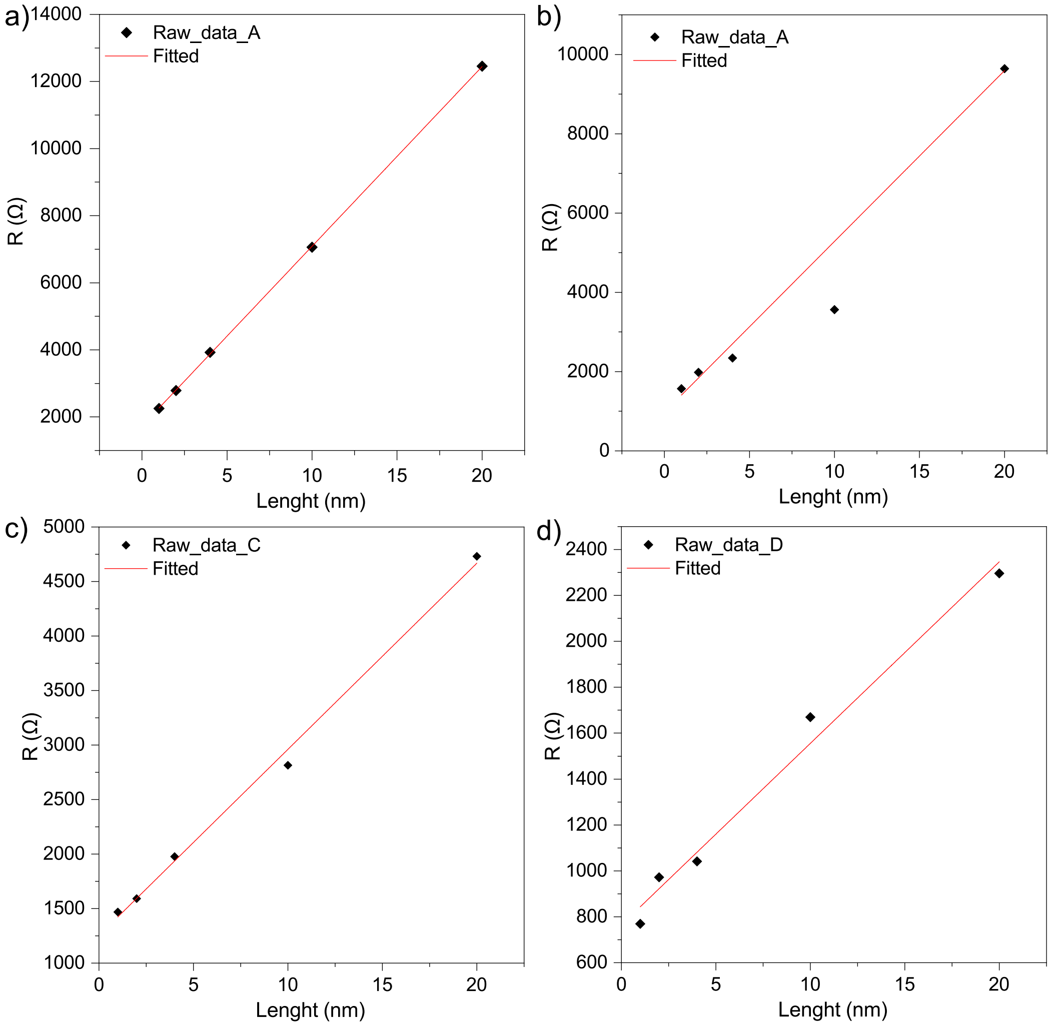

Figure 3.15: Resistivity of NCG. Resistivity plot of the 4 different devices (R vs L).

Finally, the resistance or resistivity (ρ) of the film can be calculated with the following formula:

$$\rho = (R - R_c) \times W/L \tag{3.2}$$

Where R is the resistance of the system, R_c is the resistance of the metal contact, W is the width of the device and L is the length. The results of the measurements showed values in the other of 10^3 Ω, while the mean value calculated for the four devices is $4.2\text{x}10^3 \pm 725$ Ω. Since our NCG films are not a single sheet, it is necessary to consider the contribution of the all the sheets that are part of those 10 nm thickness of the film. For this, the measured resistance has to be multiplied by the thickness of the film, then the value becomes 4.2x10^{-5} Ωm. The conductivity is the inverse of the resistivity, therefore, the equation becomes:

$$\sigma = 1/\rho \tag{3.3}$$

The NCG film exhibited value of conductivity of 2.3x10^4 S/m, which corresponds to a semiconductor behaviour.

3.4 Conclusion

In this work we presented an alternative synthetic methodology for the synthesis of NCG graphene utilising the molecule hexaethynyl benzene. In contrast to established procedure, where the synthesis of NCG is achieved *via* thermal treatment of a photoresist or the use of SAMs annealed at very high temperatures ($\approx$ 1200 °) for long annealing times, our methodology exploits an organic precursor molecule, such as hexaethynyl benzene, to prepare NCG employing lower temperatures (<900 °C) in shorter periods of time.

Our results have demonstrated that the growth of NCG employing an organic molecule yields large areas of continuous films, demonstrating an advantage over conventional synthesis of NCG, as confirmed by Raman spectroscopy. Raman spectroscopy has shown films with crystal sizes between 8 to 12 nm. In addition, XPS spectroscopy confirmed the low level of defects in the films, discriminating clearly from amorphous or glassy carbon, an important aspect for the tuning of the electrical properties.

TEM experiments have revealed a very crystalline NCG with a clear crystalline pattern, which has shown the characteristic planes of a graphene-like material. Additionally, *in-situ* TEM heating studies allowed us to observe the amorphisitation trajectory according to Ferrari et al., which has revealed a transition to a more order network. Raman studies before and after the thermal treatment showed that the G and 2D peaks increase upon annealing at high temperature. This is a direct consequence of the thermally induced ordering of the NCG network, increasing more the 2D peak, which is better related to ordering near the Brillouin zone. By this methodology, it was possible to increase the average domain size of the NCG from 11.9 to 13.2 nm. It is important to stress that in the synthetic method here described, the domain size of the NCG is larger than in those obtained by employing common methods, cf. 5 nm (conventional methods) to 8-12 nm (this work).

Furthermore, the electrical properties of the NCG films exhibited the expected semiconductor behaviour with a sheet resistance in the order of the kΩ. Additionally, the conductivity of the grown NCG showed values in the order of 10^5 S/m, which is in the typical range for this type of materials.

Summing up, we proved that by employing an organic molecule it was possible to synthesise NCG, with larger domain sizes, employing (*i*) lower temperatures and (*ii*) shorter growing times than the observed in previous methods. The methodology herein developed presents an alternative for a simpler synthesis of NCG, which should be further explored.

Chapter 4

CVD Synthesis of Graphdiyne from Organic Molecules

The results presented in this section were obtained in collaboration at INT with the Electron Microscopy and Spectroscopy laboratory from Prof. Kübel, for TEM characterisation (INT). IRRAS data collection was performed by Mr. Stefan Heißler, from the Institute of Functional Interfaces (IFG).

Over the past twenty years a large amount of research has been focused on the search of new carbon allotropes, resulting in novel forms of carbon-based materials such as fullerene[152], carbon nanotubes[53], graphene[5], amongst others. Recently, the physical properties of these systems have encouraged scientists to develop new synthetic methodologies for their preparation, characterisation and their possible implementation in applications[154−156]. Carbon has three different hybridisation states (*sp*, sp^2, sp^3), that can lead to numerous structural combinations resulting in a wide variety of allotropes, which have been foreseen as potential materials in new technologies[157−158]. For example, the optoelectronic properties of organic molecules rich Chapter3 in carbon have been predicted as promising in new generation of electronics and optoelectronics devices, due to the highly conjugated properties and their tuneable structural motifs[107,159].

In this regard, a new carbon allotrope known as graphdiyne, containing *sp* and sp^2 hybridised carbon atoms extended in a two-dimensional plane (2D), has been synthesised *via* cross-coupling reaction on a copper surface using hexaethynylbenzene (HEB), and it has been predicted to be the most stable of the non-natural carbon allotropes[160]. Graphdyine has been foreseen to be a promising material for applications in gas storage and separation, semiconducting devices, amongst others[161,162]. These characteristics span the need to create new pathways for its synthesis. Nevertheless, obtaining not only graphdyine with a well-defined and stable structure, but also a single layer, represents still one of the biggest challenges in this field.

Keeping this in mind, it is the scope of this section to focus on the synthesis and characterisation of graphdyine films employing organic molecules (See Fig. 4.1). The synthesis was performed by cross-coupling reaction employing a chemical vapour deposition reactor. The synthesis is performed on a CVD furnace, utilising as substrates copper; given that these have shown high catalytic activities towards C-C coupling. The graphdiyne preparation was carried out employing four different organic molecules and their characterisation was achieved through a variety of analytics techniques such as: scanning electron microscopy (SEM), atomic force microscopy (AFM), Raman spectroscopy, transmission electron microscopy (TEM) and X-ray photoelectron spectroscopy (XPS).

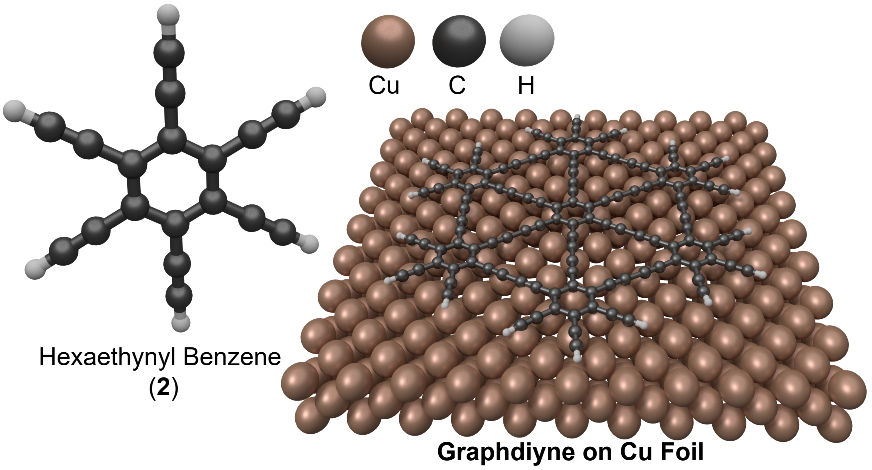

Figure 4.1: Graphdiyne made from Organic Molecules. Desired graphdiyne formation on Cu, employing as precursor an organic molecule e.g. hexaethynyl benzene (**2**).

4.1 Synthesis of Starting Materials

For the synthesis of the graphydiyne materials, four acetylene-containing molecules were chosen and prepared, as follows: hexaethynylbenzene (**2**), hexakis[4-(ethynyl)phenyl]benzene (**4**), 1,3,5-tris[4-(ethynyl)phenyl]benzene (**6**), and 1,3,6,8-tetrakis(ethynyl)pyrene (**6**), with six, six, three and four acetylene groups, respectively. The starting material molecules were synthesised as described in the following sections.

4.1.1 Hexaethynyl benzene (2)

Hexaethynylbenzene (**2**) was synthesised employing a Negishi reaction[163], which consists in the coupling of organic halides or triflates with organo-zinc compounds with Pd or Ni as the catalyst. The synthesis affords C-C coupling with *sp*, sp^2 and sp^3 carbon hybridisation. For this reaction, it was first prepared the organo-zinc compound utilising butyl lithium and tri(methylsylyl)acetylene to produce the [tri(methylsilyl)ethynyl] zinc chloride salt in solution. Afterwards, the [tri(methylsilyl)ethynyl] zinc chloride solution was transferred to a clean three-necked round bottom flask containing hexabromobenzene, tetrakis(triphenylphosphine)palladium(0) ($Pd(PPh_3)_4$) and dry toluene. It is important to mention that the during the synthesis of (**1**) an inert argon atmosphere was maintained due to the high sensitivity of the reaction towards water and oxygen. The reaction was completed after three days. Two major products were obtained, with major products being hexakis[(trimethylsilyl)ethynyl)]benzene and the pentakis[(trimethylsilyl)ethynyl)]benzene (scheme 4.1). Both materials were separated by chromatographic column with the major product being **1** (See Experimental section, section 5.4 for more details).

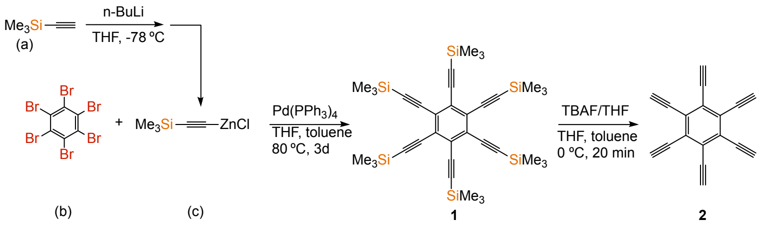

Scheme 4.1: Hexaethynylbenzene (2). Tri(methylsylyl)acetylene (a) is converted to [tri(methylsilyl)ethynyl] zinc chloride (c), and reacted with hexabromobenzene (b) to yield **1**. **1** is then reacted with TBAF to yield **2**.

Compound **1** is highly soluble in dichloromethane (DCM) and chloroform, while it is insoluble in hexane. Colourless block-shaped single crystals of this compound can be obtained from slow evaporation of a mixture of DMC and hexane after two weeks. X-ray single crystal analysis of this compound confirms the formation of hexakis[(trimethylsilyl)ethynyl)]benzene as revealed by single crystals X-ray analysis. The compound crystallises in the trigonal $R\bar{3}$ space group with solely one sixth of the molecule in the asymmetric unit (Fig. 4.2). As can be observed in Fig. 4.2b,c, all hexakis[(trimethylsilyl)ethynyl)]benzene molecules are packed in a co-planar fashion.

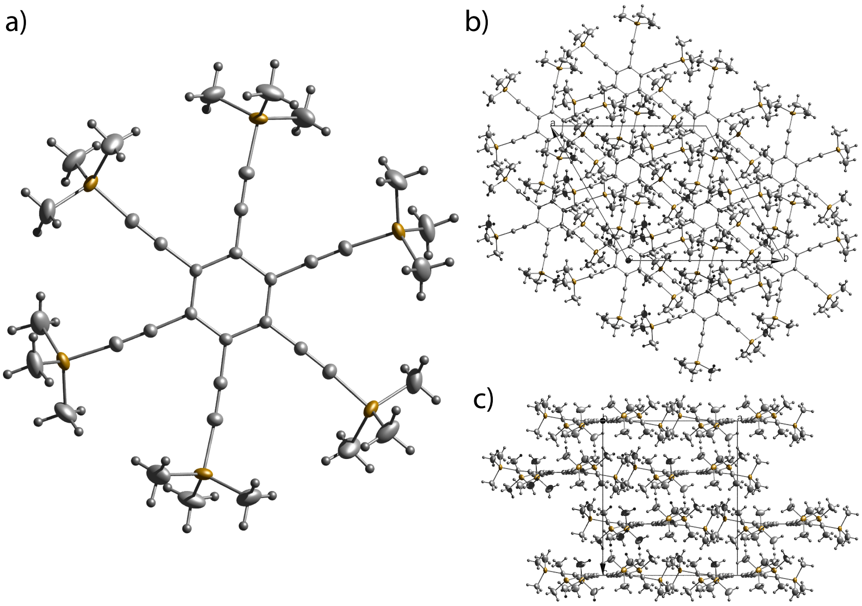

Figure 4.2: Single Crystal XRD studies of 1. Crystals structure of hexakis[(trimethylsilyl)ethynyl)]benzene (**1**). (b) and (c) (view along b-axis and c-axis, respectively) showing the packing of the **1**.

The desired product, hexaethynylbenzene (**2**), can finally be obtained by de-protection of the acetylene groups in **2** by reacting it with 1 M solution of tetrabutylamonium fluoride (TBAF) in THF at 0 °C for 20 min, under an Ar atmosphere. Compound **2** was extracted from the reaction mixture with dichloromethane and subsequently, the solvent was evaporated under reduced pressure. It is important to highlight that due to the high reactive nature of **2**, it was immediately dissolved in acetone and used for the synthesis of GDY just after the de-protection procedure. Compound **2** is highly reactive and after few minutes to exposition to the air, it turns yellow to brown which is indicative of decomposition or oxidation. Unfortunately, a full characterisation of the compound **2** was not possible due to oxidation, thus the de-protection process was followed by TLC.

4.1.2 Hexakis[4-(ethynyl)phenyl]benzene (4)

The synthesis of hexakis[4-(ethynyl)phenyl]benzene (**4**) was obtained in a three steps reaction as follows. First, the iodination of hexaphenylbenzene was performed *via* a reaction of this compound with bis[trifluoroacetoxy)iodo]benzene to obtain hexakis[(4-iodophenyl)]benzene[164]. Note that, due to the higher reactivity of hexakis[(4-iodophenyl)]benzene, the iodo atoms should be easier to cross-couple with acetylene groups of the tri(methylsylyl)acetylene than bromides. The yield of this reaction is high and the product, hexakis[(4-iodophenyl)]benzene, can be precipitated with hexane as a white powder, therefore, a separation with a chromatographic column was not required.

Subsequently, a Sonogashira reaction took place to introduce the acetylene groups to hexakis[(4-iodophenyl)]benzene employing tri(methylsylyl)acetylene. For this, dry hexakis[(4-iodophenyl)]benzene was poured into a two-necklet flask with the catalyst bis(triphenylphosphine)palladium(II) dichloride ($Pd(PPh_3)_2Cl_2$) and copper iodine (CuI); tri(methylsylyl)acetylene and all reagents were dissolved in a 1:1 mixture of THF and diphenylamine (DPA). The reaction was stirred for 18 hours at 80 °C (scheme 4.2). The product, hexakis[4-(trimethylsylylethynyl) phenyl]benzene (**3**), was extracted with dichloromethane (DCM) and purified through a chromatographic column.

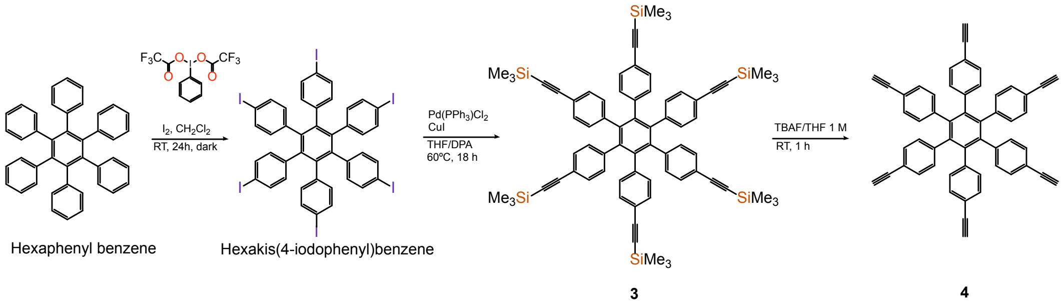

Scheme 4.2: Hexakis[4-(ethynyl)phenyl]benzene (4). Hexaphenylbenzene is iodinated and cross-coupled with tri(methylsylyl)acetylene to yield hexakis[4-(trimethylsylylethynyl)phenyl]benzene (**3**). **3** is deprotected to produce hexakis[4-(ethynyl)phenyl]benzene (**4**).[165]

Hexakis[4-(ethtynyl)phenyl)]benzene (**4**) was obtained by removing the trimethylsilyl (TMS) groups of the HEPB-TMS with TBAF[165]. For this, a reaction with a solution of TBAF (1 M) dissolved in THF was employed at room temperature. The reaction mixture was stirred for 1 h (scheme 4.2) and afterwards, the reaction was quenched with distilled water. **4** was extracted with diethyl ether and purified *via* column chromatography (see Experimental Section, section 5.4.1). A white powder was obtained and stored at 4 °C. **4** is very stable compared to **2**, but it should be kept in the fridge for a longer use. Due to the stability and good solubility of **4**, it was possible to grow single crystals from a solution of DCM and acetone. Large block-shaped colourless crystals were obtained after 1 week. Single crystal X-ray analysis shows **4** to be the desired compound (Fig. 4.3). The molecule crystallises in the triclinic $P\bar{1}$ space group with the entire molecule residing the asymmetric unit and two molecules in the unit cell. Similarly to **1**, compound **4** also shows a packing with all hexakis[4-(ethtynyl)phenyl)]benzene being parallel to each other (See Fig. 4.3b,c).

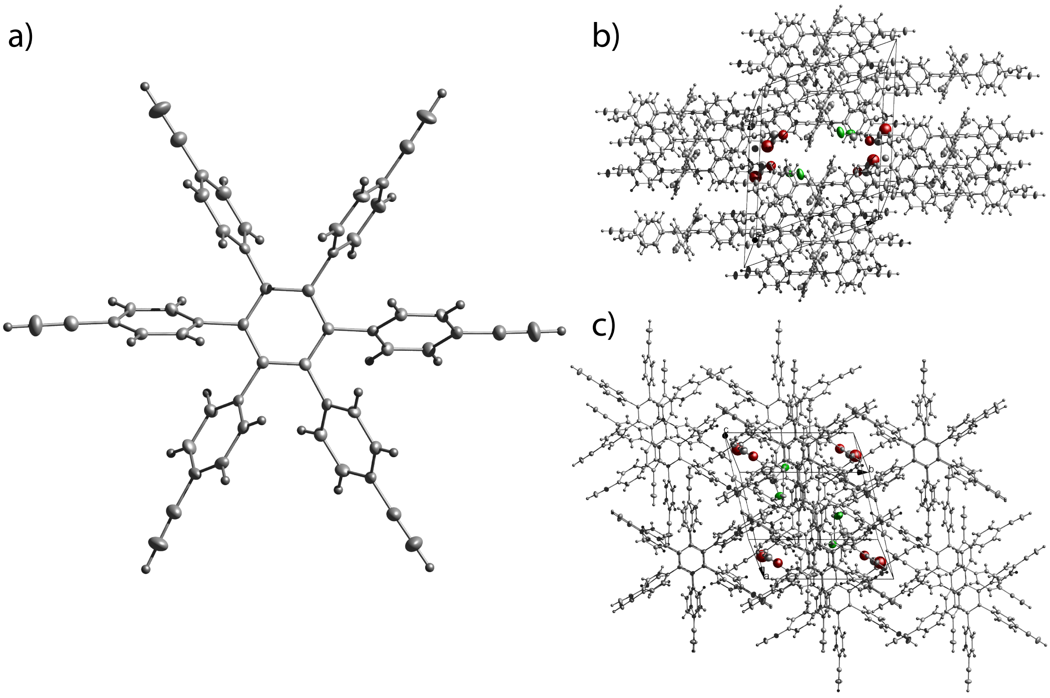

Figure 4.3: Single Crystal XRD studies of 4. (a) Crystals structure of hexakis[4-(ethtynyl)phenyl)]benzene (**4**). (b) (c) show the co-planar packing of the hexakis[4-(ethtynyl)phenyl)]benzene molecules in the unit cell.

4.1.3 1,3,5-tris[4-(ethynyl)phenyl]benzene (6)

The preparation of compound **6** was performed using a Sonogashira reaction to obtain the intermediary 1,3,5-tris[4-(methylethylsylyl)phenyl)]benzene (**3**). The Sonogashira reaction involved the introduction of acetylene groups in the 1,3,5-tris[(4-bromo)phenyl]benzene compound, utilising $Pd(PPh_3)_2Cl_2$ and CuI as catalyst, and tri(methylsylyl)acetylene as precursor of the acetylene group, in a 1:1 mixture of THF and DPA. The mixture was allowed to react for 24 h at room temperature under an Ar atmosphere. The reaction was stopped with dilute HCl and subsequently, purified through chromatographic column (see Experimental Section, section 5.4.1 for details). The compound **5** was obtained as a white powder[166].

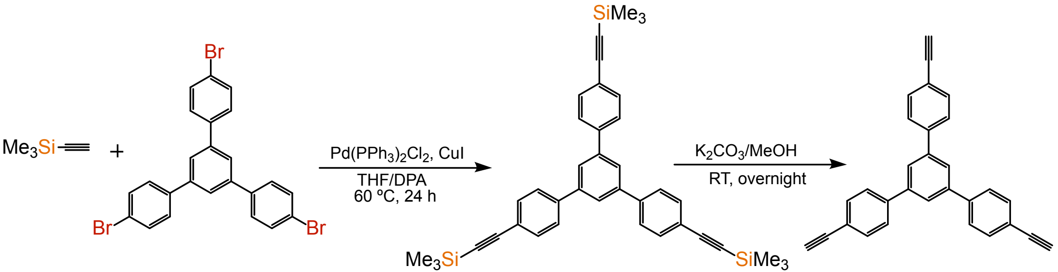

1,3,5-tris(4-bromophenyl)benzene **5** **6**

Scheme 4.3: 1,3,5-tris[4-(ethynyl)phenyl]benzene (6). Reaction of 1,3,5-tris[(4-bromo]phenyl)benzene and tri(methylsylyl)acetylene gives 1,3,5-tris[4-(methylethylsylyl)phenyl)]benzene (**5**). Deprotection of **5** gives 1,3,5-tris[4-(ethynyl)phenyl]benzene (**6**).

The solubility of compound **5** is high in DCM and chloroform, while it is insoluble in hexane. Taking advantage of the soluble character of **5** in DCM, it was possible to obtain colourless block-shaped single crystals of this compound from slow evaporation of a mixture of DMC and hexane after one week.

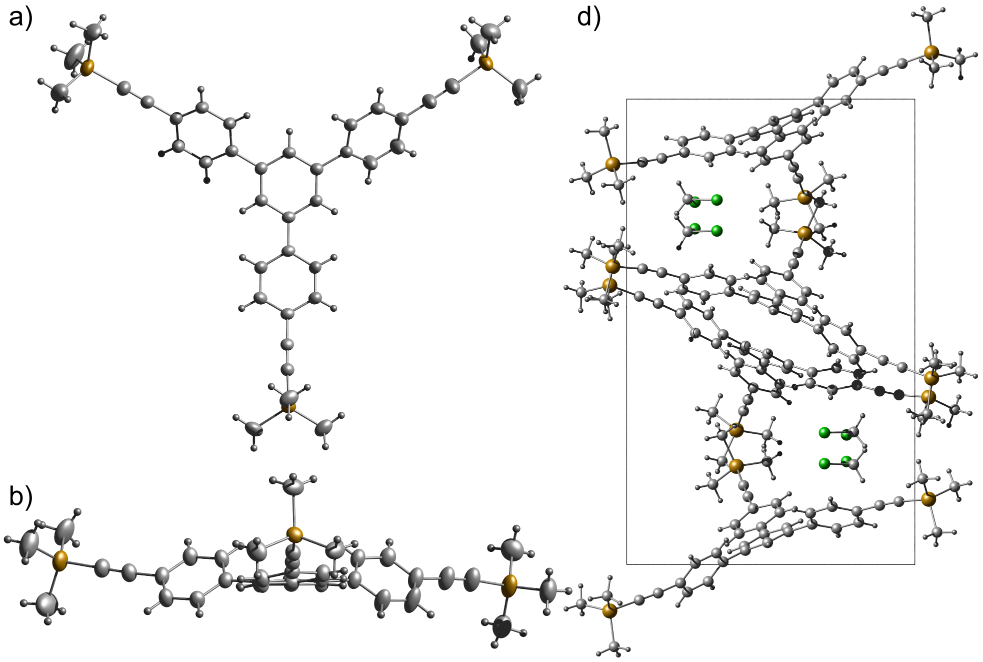

Figure 4.4: Single Crystal XRD studies of 5. Crystal structure of 1,3,5-tris[4-(methylethylsylyl)phenyl)]benzene (**5**) perpendicular to the benzene plane (a) and (b) parallel to the benzene plane. (c) shows the packing of the **5** in the unit cell (view along c-axis).

X-ray single crystal analysis of this compound confirms the formation of 1,3,5-tris[4-(methylethylsylyl)phenyl)]benzene. The compound crystallises in the orthorhombic *Pca2*$_1$ space group with the whole molecule in the asymmetric unit (Fig. 4.4), in a highly distorted fashion. As can be observed in Fig. 4.4d the molecules of all 1,3,5-tris[4-(methylethylsylyl)phenyl)]benzene show a quite distorted packing arrangement.

Compound **6** can be obtained by a de-protection process of compound **5**. The reaction was performed in a two-neck round bottom flask, which consisted on a methanolic solution of K_2CO_3 where compound **5** was added. The reaction mixture was stirred overnight under an Ar atmosphere at room temperature (scheme 4.3). After this period, the reaction was quenched with distilled water, triggering to the precipitation of compound **6** as a white powder. The powder was dried under vacuum and stored in the fridge at 4 °C.

4.1.4 Synthesis of 1,3,6,8-tetrakis(ethynyl)pyrene (8)

Compound 1,3,6,8-tetrakis(trimethylsilanylethynyl)pyrene (**7**) was synthesised through a Sonogashira reaction, as well as compound (**5**). For this, tetrabromopyrane was poured into a round bottom flask and dissolved in a toluene/trimethylamine (TEA) mixture (1:1). The catalyst, $Pd(PPh_3)_4$/CuI, were added and the mixture was heated to 60 °C and when this temperature is reached the TMS solution was added (scheme 4.4). The reaction mixture was stirred overnight at 80 °C and subsequently, was quenched by addition of distilled water. Compound **7** was obtained by extracting the reaction mixture with DCM. It was purified utilising chromatographic column, yielding an orange powder, which exhibited fluorescence at the UV light[167].

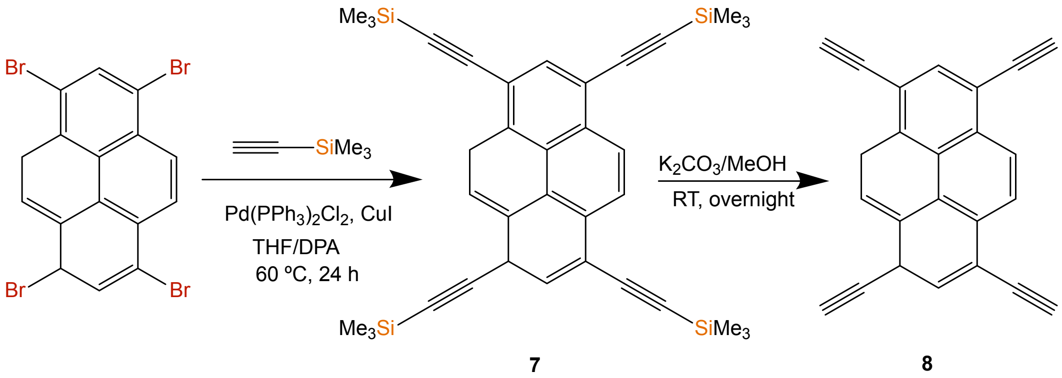

Scheme 4.4: 1,3,6,8-tetrakis(ethynyl)pyrene 8. To obtain the 1,3,6,8-tetrakis(trimethylsilanylethynyl)pyrene (**7**), a Sonogashira coupling is carried out with tri(methylsylyl)acetylene. **7** is then deprotected to afford **8** as a bright organge product.

De-protection of the compound **7** was carried out using the same procedure employed for compound **5** de-protection. Compound **8** was obtained as a yellow powder and was storage at 4 °C. **7** is highly soluble in DCM while it is insoluble in hexane. It was possible to obtain plates-like crystals of this compound; however, the crystals were too brittle and diffract poorly, therefore, it was not possible to obtain the single crystal X-ray structure of this compound. In contrast, **8** is highly insoluble, thus, precluding the crystallisation of this material. Upon completion of the synthesis of the precursors, we proceeded with the implementation of all of them to grow GDY, as described in the following sections.

4.2 Substrate Preparation

The synthesis of GDY materials was performed employing an Atmospheric Pressure Chemical Vapour Deposition reactor. Before the growth process, it is of utmost importance to treat the substrate, in this case Cu foil, to obtain a good quality of GDY material. Cu substrate is easily oxidised under ambient conditions by reacting with atmospheric oxygen. Therefore, removal of such species from the Cu foil is of high importance to prevent nucleation and an inhomogeneous growth in the synthesis of 2D materials employing CVD conditions. This has been shown to affect the morphology and quality of the desire material[168].

To eliminate oxidised species from the Cu foil and to clean the surface of the substrate, the first layer of Cu in the foil was removed through an electropolishing technique. Two different protocols for the electropolishing of Cu were used. The first one involves a steel electrode as an anode and the Cu foil in the cathode side. Then, both electrodes are dipped into a solution of isopropanol and phosphoric acid (H_3PO_4), and subsequently a power of 3.5 V is applied for 35 secs to remove the first layer of Cu in the foil. Subsequently, the Cu foil is washed with DCM, isopropanol and water, to remove traces of Cu and solution on the foil[169]. When the Cu foil was examined under the optical microscope, it presented several deformations (See Fig. 4.5a). These defects can be attributed to the relatively high voltage applied to remove the first layer of Cu, therefore, we realised that this procedure was not optimal to treat the Cu foil for our growth conditions, because the defects on the surface of Cu foil might lead to an inhomogeneous growth of GYD.

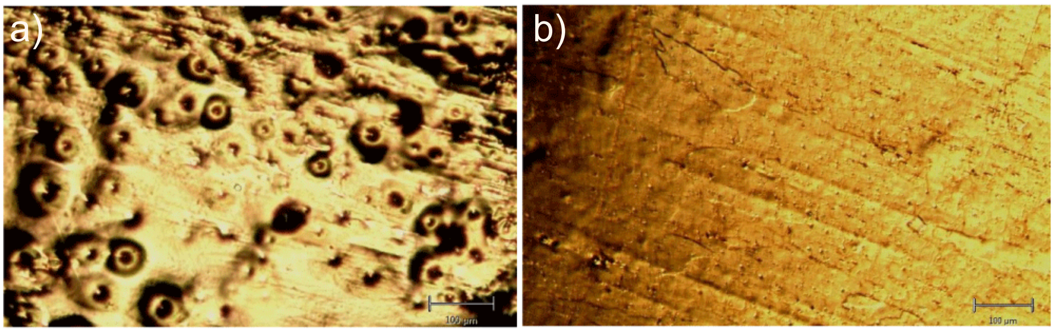

Figure 4.5: Optical Microscopy of the Cu foil treated with 2 different electropolishing procedures. (a) OM images of the Cu foil treated with the first procedure; (b) OM images of the Cu foil treated with the second approach.

An alternative procedure to clean the Cu substrate consisted in utilisation of a thicker Cu foil as anode (thickness = 1 µm) and the Cu foil for GDY growth is placed in the cathode side. A solution containing H_3PO_4, acetic acid and glycerol was used for the electropolishing. A power of 1.5 V was applied for 20 min and after this time the Cu foil was washed with copious amount of distilled water. In Figure 4.5 it can be observed the Cu foil treated employing the second approach, where the Cu foil is flatter and cleaner and it does not have any defects, as the obtained in the Cu foil treated with the first approach.

Due to our observations employing the two different substrate cleaning approaches, all substrates employed for the graphdiyne growth in the following sections were treated with the second approach, with the aim of obtaining the best quality possible of graphdiyine films.

4.3 Synthesis of Graphdiyne *via* an Atmospheric Pressure Chemical Vapour Reactor

The synthesis of graphdiyne was performed employing four different precursors (**2**, **4**, **6** and **8**), whose synthesis were previously described (*vide supra*), in an APCVD reactor. The deposition of the precursors was carried out by employing a homemade nebuliser. The nebuliser consists in a glass container assembled to the nebuliser membrane, with two connections, one for the entry of Ar and the other one connected directly to the quartz tube reactor, where the Cu foil is placed. The system has a septum on the top of the glass container, to add the solution of the precursor in acetone when the furnace has reached the growth temperature. The nebuliser membrane is connected to an AC power supply, which allows the control of the speed of deposition by controlling the applied power.

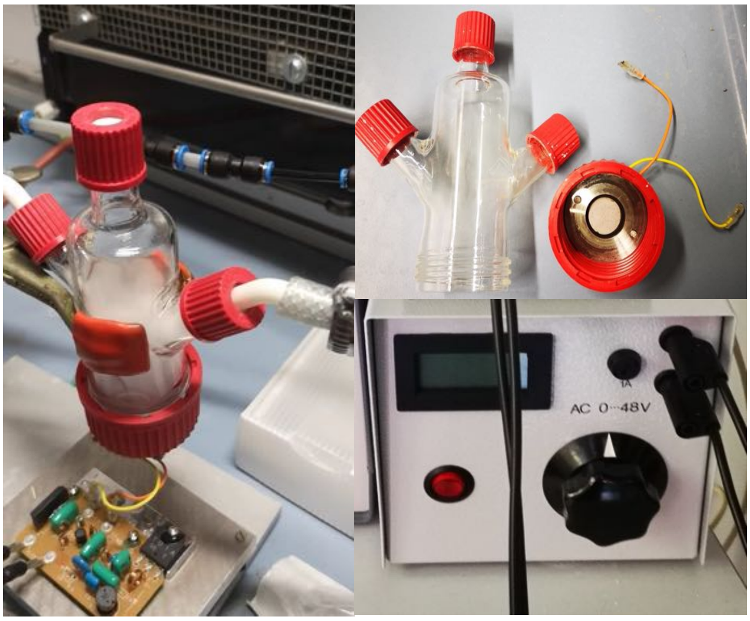

Figure 4.6: Graphdiyne Growth. Photo of the homemade Nebuliser employed for the deposition of the precursors (organic molecules), and the AC power supply adapted to the nebuliser membrane.

GDY growth starts with the de-protection of the precursor, in the case of **2** this step was performed right before the growth step, due to the high reactivity of the molecule. The deprotection for the others three precursors, which are more stable, can take place even a week prior the graphdyne growth experiments. The general description for the graphdiyne growth is given as follow: The synthesis of GDY begins after the deprotection of the organic molecules and the electropolishing of the Cu foil. The procedure involves a series of steps to achieve GDY films. The first step is to place the treated Cu foil inside of a quartz cuvette holder, which is then introduced in the CVD furnace. It is very important that the Cu foil is positioned at the heat zone of the furnace. Furthermore, the furnace is heated to 150 °C with a rate of 20 °C per minute, which takes 7.5 minutes, under an Ar stream of 2.8 sccm. When the growth temperature is reached, the precursor, dissolved in a minimum quantity of acetone, i.e. 15 mL, and is added to the nebuliser container employing a syringe and needle, to maintain the materials under Ar atmosphere. A 27.5 V of power is then applied the nebuliser membrane and a mist containing the precursor is formed, which is carried into the quartz tube by the stream of Ar. The synthesis of GDY is conducted for a period of 2 h, keeping constants all the conditions earlier mentioned. After the 2 h the nebuliser and furnace are turned off and the Cu foil with the grown-GDY is allowed to cool down for the posterior characterisation. Four graphdiyne films were grown on Cu foil each of them from different organic compound as follows:

1. **GDY-1**: Films grown from hexaethynylbenzene (**2**).
2. **GDY-2**: Films grown from hexakis[4-(ethynyl)phenyl]benzene (**4**)
3. **GDY-3**: Films grown from 1,3,5-tris[4-(ethynyl)phenyl]benzene (**6**)
4. **GDY-4**: Films grown from 1,3,6,8-tetrakis(ethynyl)pyrene (**8**)

4.4 Raman Characterisation of the Grown-GDY

Raman spectroscopy has been used in the characterisation of vibrational, rotational and others low-frequency modes in 2D systems. For our system, it is a powerful technique to observe the -C≡C-C≡C- vibrations. We made used of this technique to characterise the grown-GDY obtained from the four different precursors previously synthesised. After the growth procedure, the Cu foil containing GDY film was examined by Raman and all the spectra are shown below.

GDY-1 grown from **2** exhibited four peaks in the Raman spectra. The Raman spectrum of **GDY-1** is shown in Figure 4.7a, in which the peaks framed in green colour are the signals corresponding to the vibrations of the aromatic rings. The breathing mode of the sp^2 carbon domains of aromatic ring is seen at 1407 cm^{-1}, as well as the in-plane stretching vibration of sp^2 carbon in aromatic ring is shown at 1583 cm^{-1}, this correspond to the first order scattering E_{2g} mode. Additionally, two small peaks highlighted in yellow colour correspond to the butadiene vibrations, which are observed at 2179 cm^{-1} and 1936 cm^{-1}, indicating the GDY linkage.

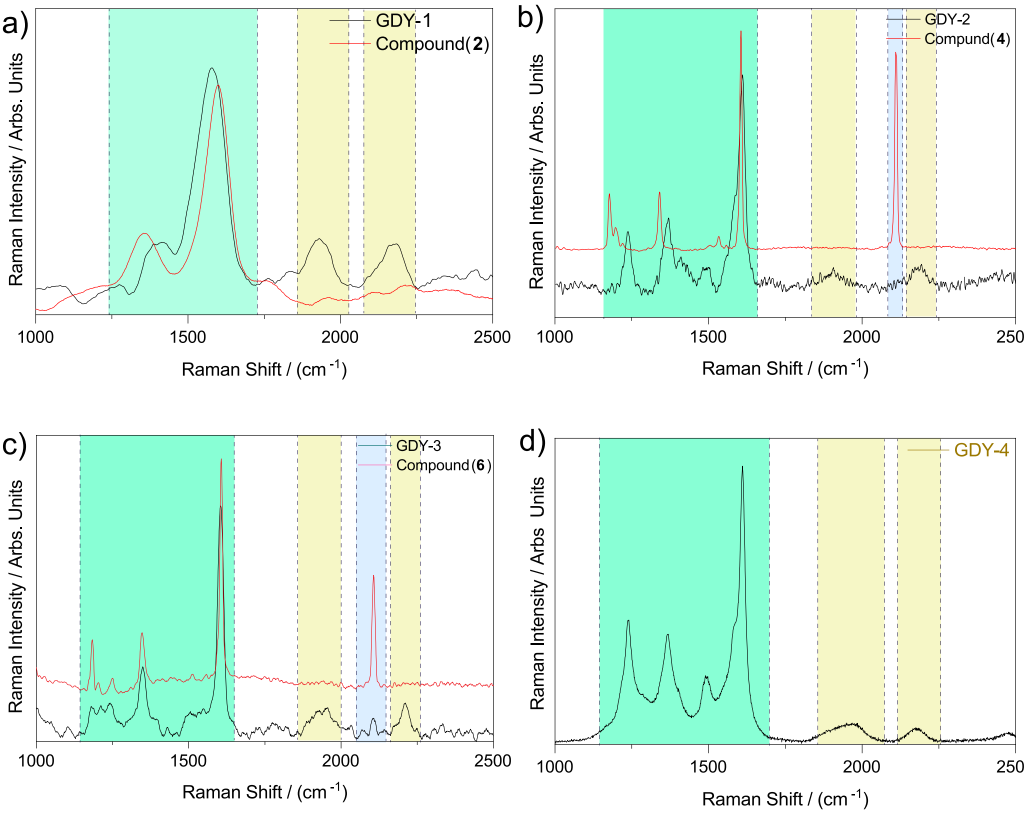

Figure 4.7: Raman Spectra of Graphdiyne. Raman spectra of (a) **GDY-1** and its precursor (**2**); (b) **GDY-2** and its precursor (**4**); **GDY-3** and its precursor (**6**); (d) **GDY-4**.

The signal of **GDY-2** was compared to **2** resulting in a shift of the breathing and stretching vibrations of the aromatic rings. Unfortunately, this compound is very reactive, therefore, the vibrations of the acetylene groups are no present in the Raman spectrum of **2**, which could be due to the fast oxidation of the triple-bonds in contact with air.

GDY-2 grown from compound **4** exhibited five peaks in Raman analysis (Fig. 4.7b). The peaks at 1235 cm^{-1}, 1368.5 cm^{-1} and 1611 cm^{-1}, are attributed to CH in-plane bending, C-C breathing and C-C stretching of aromatic rings, respectively (marked in green colour). Moreover, two peaks related to the di-acetylene linkage are presented at 1906.7 cm^{-1} and 2189 cm^{-1}. The precursor Raman spectrum is also shown in Fig. 4.7b, and it also shows a blue shift in all the peaks. For our study the most important shift seen is the signal of the acetylene groups at higher energy, which presents a blue shift when the binding of the acetylene groups occurs. As observed, there is an increased in energy of 76.8 cm^{-1} (from 2112.2 to 2189 cm^{-1}, indicative that graphdiyne bonds have been formed.

GDY-3 grown from **6** also shows five peaks in Raman analysis, as well as the **GDY-2**, owing to the aromatic nature of both precursors (Fig. 4.7c). We can see also the C-C stretching and breathing of aromatic rings, as well as the in-plane bending of the CH groups (1605 cm^{-1} 1349 cm^{-1} and 1184 cm^{-1}, respectively). Interestingly, with this precursor just the peak related to the acetylene group (at higher energy) showed a blue shift, when compared to the Raman of the precursor. We can see the two peaks related to the di-acetylene linkage at 1946 cm^{-1} and 2209 cm^{-1}, where the acetylene group peak has an increased of energy of 103 cm^{-1}, i.e. from 2106 to 2209 cm^{-1}.

In Figure 4.7d is shown the Raman spectrum of the **GDY-4** grown from compound **8**. **GDY-4** shows different bands, some of them attributed to the pyrene structure and others two that are related to GDY linkage. The peak at 1240 cm^{-1} represent the in-plane bending of CH, furthermore, at 1364 cm^{-1} is shown the C=C-H breathing vibration in the aromatic ring and at 1604 cm^{-1} appears the C=C stretching, which is characteristic in aromatic rings.

It is important to highlight that **GDY-4** has stronger signals of the butadiene linkage shown at 1959 cm^{-1} and 2177.7 cm^{-1}. Unfortunately, we could not collect the Raman spectrum of the precursor of **GDY-4**, due to its fluorescence. The fluorescent signal of **8** in the Raman spectra overlapped all the signals in the Raman spectrum.

Raman spectroscopy was used as a preliminary tool to confirmed the formation of GDY employing the four different synthesised precursors. The presence of the two peaks attributed to the di-acetylene linkage was the most important information obtained by Raman, given that this is a strong proof that the homo-coupling of the precursor occurs during the synthetic process.

4.5 X-ray Photoelectron Spectroscopy (XPS) Analysis of Graphdiyne Films

One of the most widely used technique in surface analysis is the X-ray Photoelectron Spectroscopy (XPS), also known as electron spectroscopy for chemical analysis (ESCA). Due to its applicability in a wide range of materials, which provide important information regarding the surface chemistry of the material under study. The XPS analysis can also provide the chemical composition, chemical state, empirical formula and electronic state of the elements of the material examined. The application of this technique is very important in industry and in some research fields such as: photovoltaics, catalysis, nanomaterials, corrosion, adhesion, electronics devices and packing, surfaces treatment, thin films, among others.

To continue our characterisation, we turned to XPS spectroscopy to determine the contents of *sp* and sp^2 carbons in the graphdiyne films. For this, the films were studied directly on Cu foil after the GDY growth procedure.

The C1s XPS analysis of **GDY-1** revealed a high C-C binding peak and also an important intensity of C-O bonds (Fig. 4.8a). The *sp* C-C bonds has the highest intensity at 285.2 eV, confirming the di-acetylene binding of GDY. Moreover, at 284.5 eV the C-C sp^2 carbon bonds appears, owing to the aromatic ring of the precursor. There is a peak at 286 eV related to the C-O bonds and also at 289 eV, which is the intensity of C=O bonds. The high content of C-O bonds is expected due to the highly reactivity of the precursor (compound **2**).

The analysis of **GDY-2** also showed an important oxidation in the grown GDY film (Fig. 4.8b). The C-C *sp* peak appears at 285.2 eV and the C-C sp^2

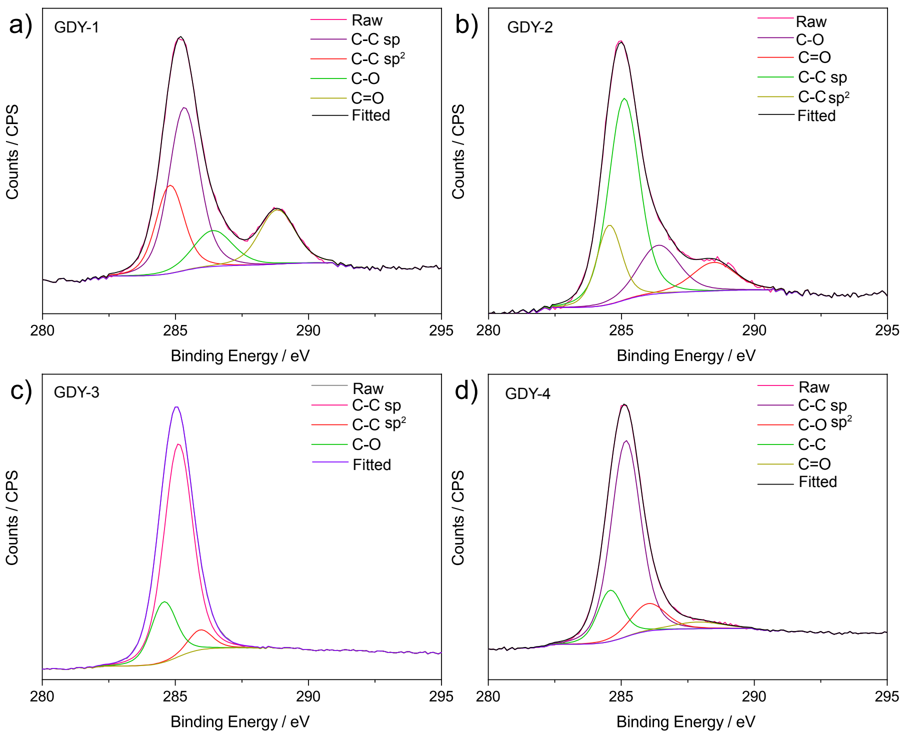

Figure 4.8: C1s XPS Spectrum of all Graphdiyne films. (a) **GDY-1**; (b) **GDY-2**; (c) **GDY-3** and (d) **GDY-4**.

carbon peak is at 284.5 eV. Moreover, the peak at 286 eV is related to C-O binding and the one at 289 eV is the C=O bonds.

GDY-3 has mostly C-C *sp* and C-C sp^2, as we can see in Figure 4.8c, where it is shown the high peak at 285.2 ev (C-C *sp*) and the peak at 284.5 eV (C-C *sp*). This GDY has a very small C-O peak at 286 eV, which indicates a good stability of the precursor **GDY-4** similar to **GDY-3**. The C-C *sp* binding is at 285.2 eV and the contribution of the C-C sp^2 is displayed at 284.5 eV (Fig. 4.8d). There is a small oxidation peak at 286 eV which related to C-O bonds.

XPS definitely shows that from the four obtained films, **GDY-3** and **GDY-4** had more stability during the synthesis of GDY than the others two films, which indicates that the stability of the precursor does affect the oxidation state of GDY films and also the amount of di-acetylene linkage in GDY network.

4.6 Transfer of the GDYs to a Silicon and SiO_2 substrate for Surface Characterisation

Raman analysis confirmed growth of GDY fims on Cu foil, thus, to proceed with our characterisation, the transfer of GDY to a Si or SiO_2 substrate was followed. This step is important, not just for the characterisation, but also for the possible applicability of GDY films in device applications[170]. The transfer step involved the etching of the Cu foil using a $(NH_4)_2S_8O_2$ solution. The Cu foil containing the grown-GDY was coated with Poly(methyl methacrylate) (PMMA) through a spin coating process. Afterwards, the $(NH_4)_2S_8O_2$

solution was heated for 5 min at 70 °C and subsequently the PMMA/Cu-foil was placed carefully on the top of the warm solution (Fig. 4.9).

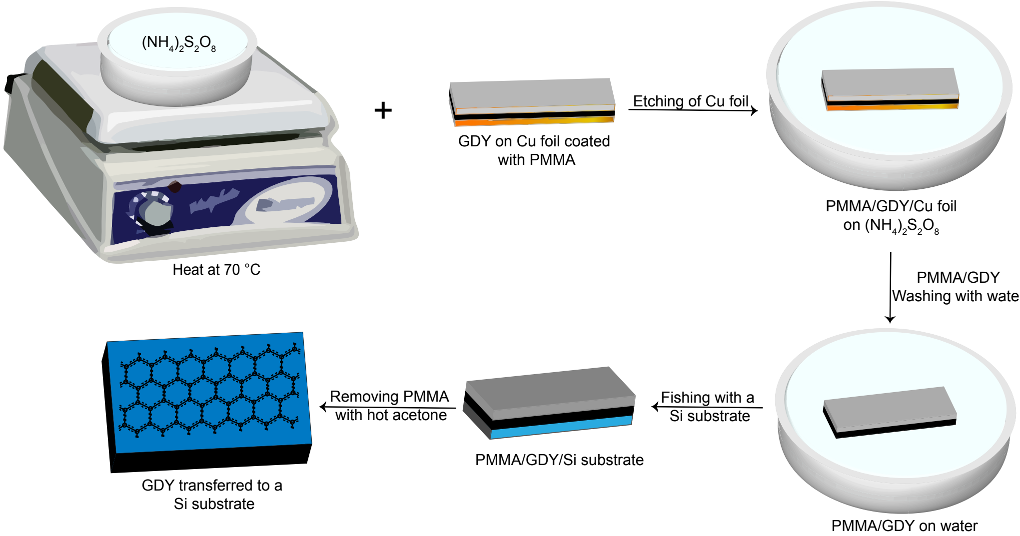

Figure 4.9: GDY Transfer. Schematic representation of the transference of GDY on a Si or SiO_2 substrate.

The etching of Cu foil takes about 4-5 h and when it was completely removed, the PMMA/GDY was washed with water as it is shown in the Fig. 4.9. Subsequently, PMMA/GDY was placed on a Si or SiO_2 substrate and PMMA was removed by dissolving it with hot acetone. Finally, the characterisation of morphology and thickness of GDY was performed on the Si or SiO_2 substrate.

4.7 Characterisation of GDY after Transfer

4.7.1 Optical Images

GDY-1 grows on the surface of the Cu as it is shown in Fig. 4.10a-b. The continuity of the GDY depends mostly on the quality of the Cu foil. When the Cu foil is smooth and contains low oxidation, GDY can grow continuously and smooth without nucleation sites, which can be seen as black spots. In the optical image (OM) of **GDY-1** it is possible to observe few black spots in the film on Cu foil. While transferring the film to a Si or SiO_2 substrate, caution must be taken, since too much distortion of the solution, where the film is contained, can lead to disintegration of the films. In Fig. 4.10c-d it is shown the **GDY-1** on SiO_2. As can be seen, the film is very continuous and flat, although it is also possible to observe some wrinkles attributable to the CVD growth and small scratches due to the transfer process.

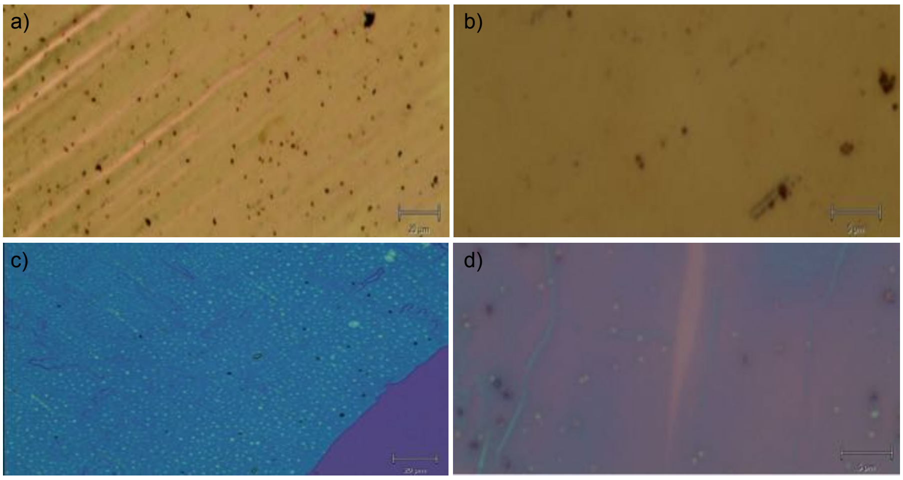

Figure 4.10: Optical microscopy of GDY-1. (a) with 20× lens on Cu foil; (b) using a 100× lens on Cu foil; (c) **GDY-1** transferred to SiO_2 substrate using a 20× lens; (d) **GDY-1** transferred to SiO_2 substrate using a 100× lens.

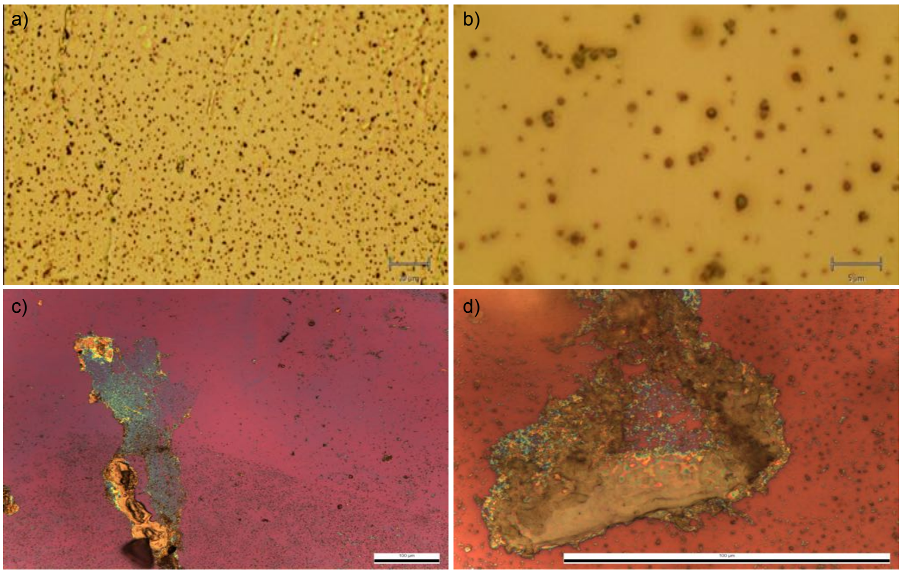

Figure 4.11: Optical microscopy of GDY-2. (a) with 20× lens on Cu foil; (b) using a 100× lens on Cu foil; (c) **GDY-2** transferred to SiO_2 substrate using a 20× lens; (d) **GDY-2** transferred to SiO_2 substrate using a 100× lens.

Furthermore, the **GDY-2** was transferred to a SiO_2 substrate, but unfortunately, we could not succeed with this process. The film grown on Cu foil presented many black spots, indicating a large quantities of defects (Fig. 4.11a-b). Although Cu foil can be the cause of inhomogeneous growth and bad quality of the film, in this particular case we do not consider the Cu foil to be responsible for the quality of **GDY-2**, since the Cu foil for this experiment was also treated under the same cleaning conditions for all the other three precursors. Instead, we consider that the bad quality of the film can be attributed to the non-planar arrangement of the precursor and the dynamic process of growth, where the precursor is passed through continuously for a period of time (see experimental section).

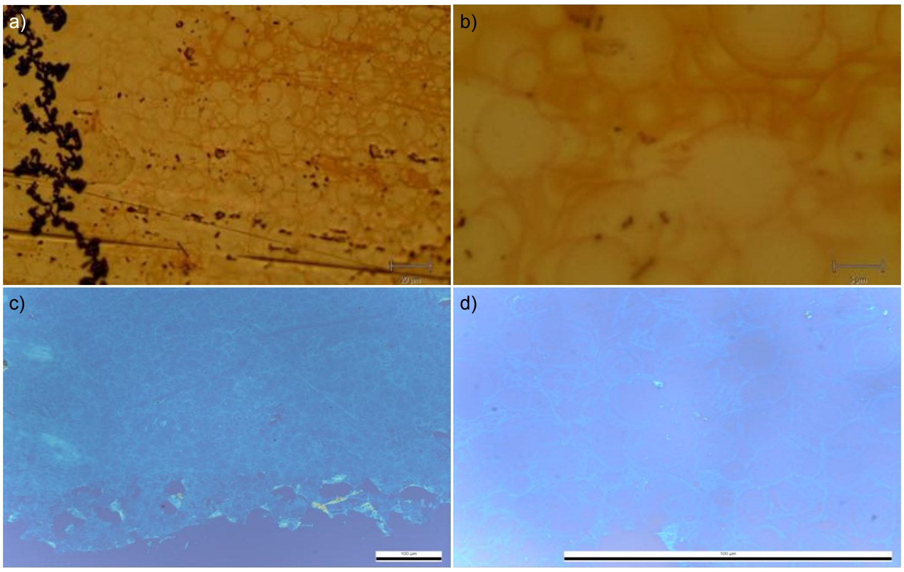

Figure 4.12: Optical microscopy of GDY-3. (a) with 20× lens on Cu foil; (b) using a 100× lens on Cu foil; (c) **GDY-3** transferred to SiO_2 substrate using a 20× lens; (d) **GDY-3** transferred to SiO_2 substrate using a 100× lens.

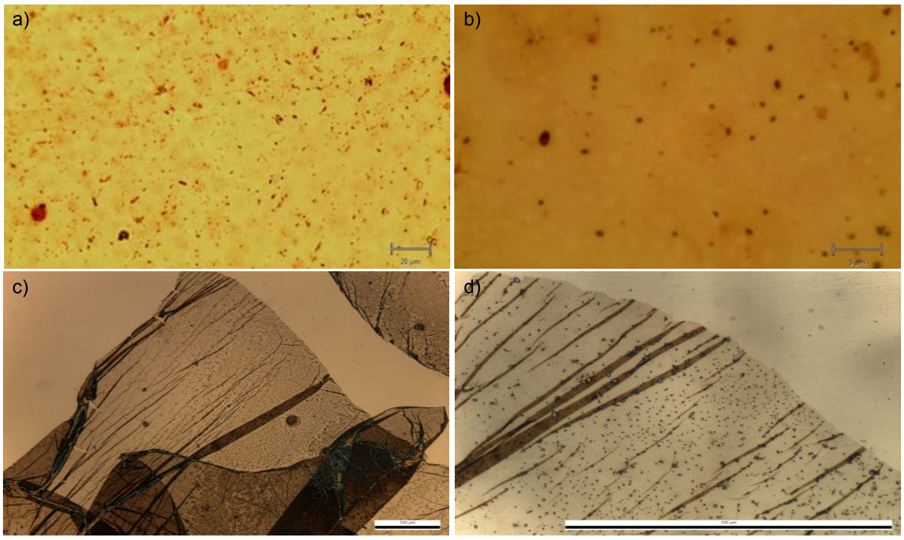

Figure 4.13: Optical microscopy of GDY-4. (a) with 20× lens on Cu foil; (b) using a 100× lens on Cu foil; (c) **GDY-4** transferred to SiO_2 substrate using a 20× lens; (d) **GDY-4** transferred to SiO_2 substrate using a 100× lens.

The linkage of acetylene groups is more difficult with **4**, leading to discontinuity and hence, during the transfer process, the film breaks in very small pieces of GDY that are very difficult to handle. In Fig. 4.11c-d it is shown the OM images of one of the small pieces of **GDY-2** after transfer.

The synthesis of **GDY-3** resulted in a very interesting growth pattern observed on the Cu foil (Fig. 4.12a-b), where is possible to see a circular form in the grown GDY. When **GDY-3** is transferred to a SiO_2 substrate the OM images (Fig. 4.12c-d) show this circular shapes along the whole film, as well as small breaks at the edge of the film, due to the transfer process.

GDY-4 was examined by OM exhibiting a continuous film grown on Cu foil (Fig. 4.13a-b). Moreover, the film was transferred to a Si substrate and posteriorly, observed under the optical microscope revealing the wrinkles in the film due to the CVD growth. **GDY-4** film looks very large and flat (Fig. 4.13c-d).

4.7.2 Infrared Reflection Absorption Spectroscopy

Infrared Reflection Absorption Spectroscopy (IRRAs) is a vibrational IR spectroscopy that has been employed in the characterisation of thin films on highly reflecting metal substrate, as well as for non-metals and even liquid surfaces. Using the surface selection rules, it is possible to derive the structure and composition of the thin film on the metal substrates, since the obtained data is a conventional spectrum of absorption[171]. For the non-metals substrates simulations are required to interpret the spectrum, due to the complex nature of this type of substrates, leading to a derivative-shape absorption profile.

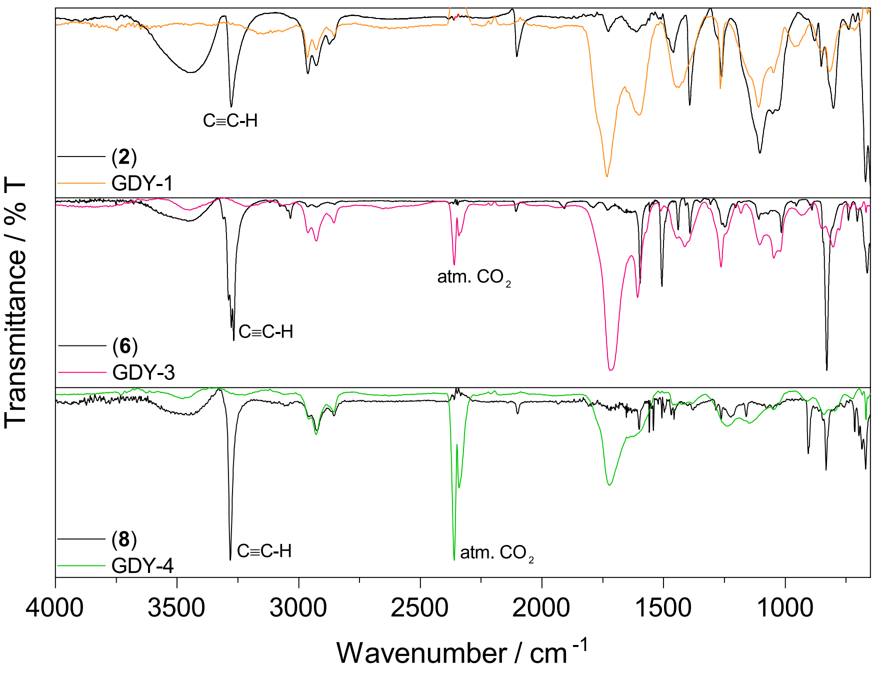

Figure 4.14: IRRAS and IR for GDY films and precursors. Colour code: precursors **2**, **6** and **8** (black traces); **GDY-1** (orange); **GDY-3** (pink) and **GDY-4** (green).

For this measurement, it was necessary to transfer the GDYs films to a reflecting metal substrate such gold (Au), due to the high scattering power of Si and SiO_2 substrates. The film transfer was carried out employing the same transfer procedure described above (*vide supra*). In Figure 4.14 are shown the IRRAS spectra for all transferred graphdyine films, while the FT-IR for all precursors are shown in black.

All the precursor presented an important peak at 3200 cm^{-1} corresponding to the C-H aliphatic terminal of the C≡C-H bonds. This vibration disappears completely when the GDY network is formed. The absence of this vibration may be attributed to the formation of the di-acetylene bonds. The first part of the IR spectra from 700 to 1600 cm^{-1} corresponds to the aromatic vibration owing to all the precursor presents an aromatic structure. The peaks become broader between 1600 and 1700 cm^{-1} corresponding the aromatic structures in the GDY network, and a small shift to high wavenumber, which was also observed in Raman, indicating a higher energy vibrational mode.

4.7.3 Scanning Electron Microscopy

Scanning electron microscopy (SEM) was used to examine more in detail the morphology of the GDY films that cannot be seen in a conventional optical microscope. **GDY-1** films show several wrinkles that were not visible in the OM images. In Figure 4.15a is possible to observe a very flat and continuous film, but when zooming in it is possible to visualise the wrinkles mentioned before (Fig. 4.15b).

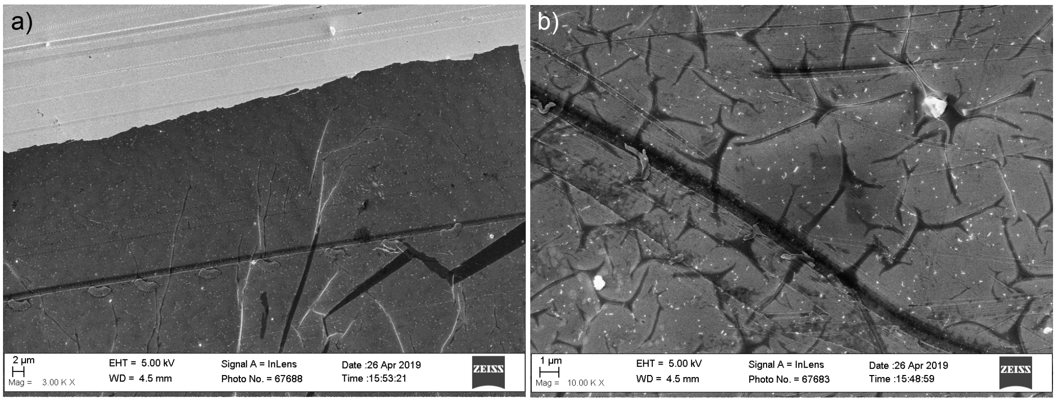

Figure 4.15: SEM images of GDY-1. (a) Cross section of edge of **GDY-1** film on Si; (b) Zoom in the **GDY-1** film on Si.

SEM images of **GDY-3** revealed a flat film with a good continuity. In Fig. 4.16a one of the edges of the **GDY-3** film, which is slightly bended and, as we mentioned before, presents few scratches owing to the transfer process. Furthermore, in a high magnification SEM images, Fig. 4.16b, exhibits the circular pattern seen in the OM as shown previously (*vide supra*).

The Figure 4.17a shows the **GDY-4** film obtained from precursor **7**, which presents the wrinkles in the films and as well as some darker spots which we attribute to nucleation sites. When zooming in (Fig. 4.17b), the film presented some random shapes inside its network. Similarly to **GDY-3**, **GDY-4** also has some shapes in the film, although in **GDY-3** there is a very defined shape of circles, in **GDY-3** more randomly oriented.

4.7.4 Atomic Force Microscopy

Atomic Force Microscopy was employed to examine the morphology of the obtained GDY, as well as to determine the thickness of GDY films grown with different precursors. **GDY-1** exhibited the wrinkles seen in the SEM images, which according to the scale bar of height are a bit higher than the

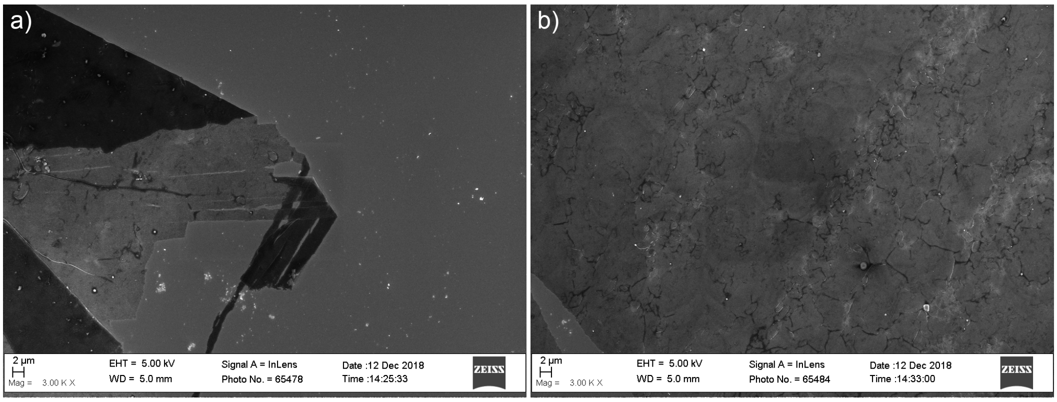

Figure 4.16: SEM images of GDY-3. (a) Cross section of edge of **GDY-3** film on Si; (b) Zoom in the **GDY-3** film on Si.

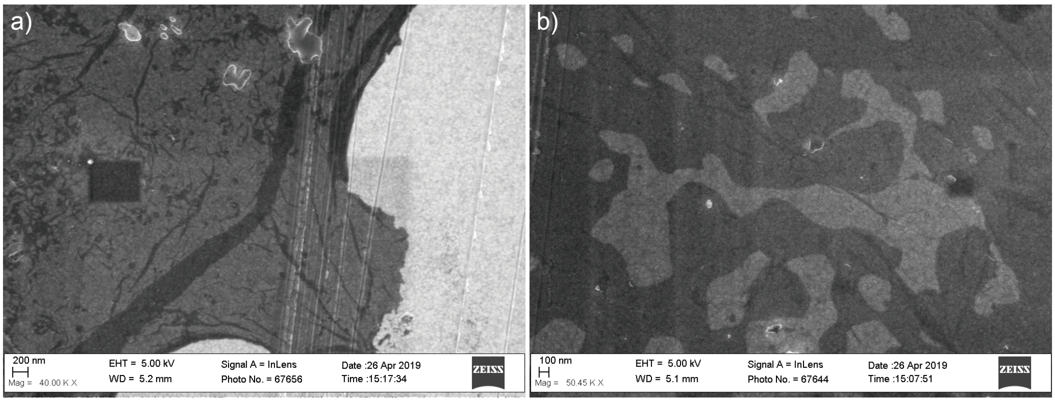

Figure 4.17: SEM images of GDY-4. (a) Cross section of edge of **GDY-4** film on Si; (b) Zoom in the **GDY-4** film on Si.

film itself (Fig. 4.18a). The height profile of **GDY-1** film revealed a thickness of 32 nm approximate or 97 layers of GDY (inset Fig. 4.18b). Even though the film looks flat and homogenous; the wrinkles make the film uneven (Fig. 4.18b).

The circular pattern of **GDY-3** is exhibited in the AFM images in Fig. 4.18. In the inset of Fig. 4.18c is shown the height profile which displayed a thickness about 8 nm, corresponding to 22 layers of GDY. When zooming in, it is possible to observe more clearly the circular pattern (Fig. 4.18d), which looks like small islands of the precursor have been formed on the film. **GDY-4** presents a smoother film, very continuous with few wrinkles. Compared to **GDY-1** and **GDY-3**, the **GDY-4** film looks flatter and larger. The inset in Fig. 4.18e shows the height profile which displays a thickness about 14 nm, corresponding to 38 layers of GDY, slightly thicker than **GDY-3** but thinner than **GDY-1**.

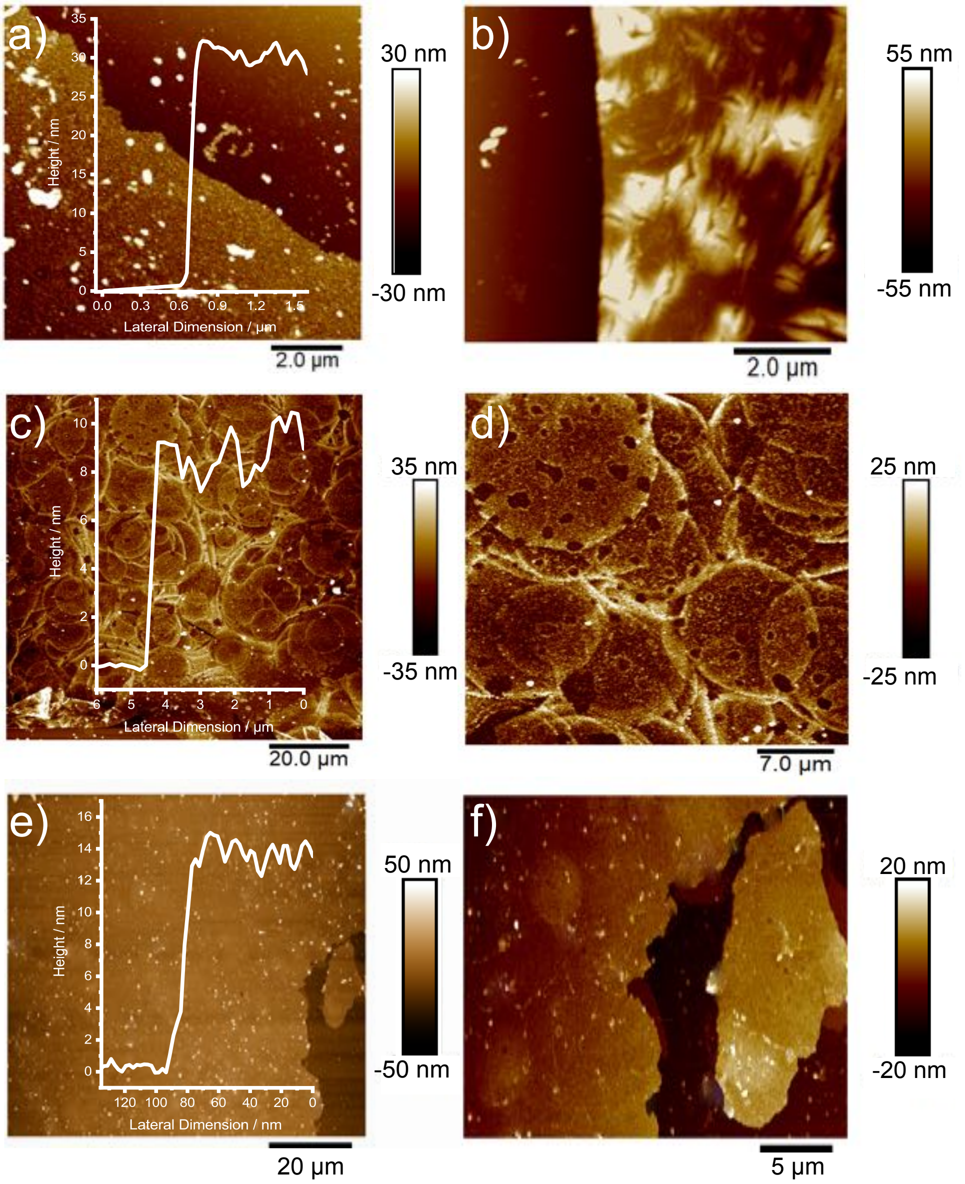

Figure 4.18: AFM images of GDYs (a) Cross section of **GDY-1** film and inset showing height profile with thickness of 32 nm; (b) Zoom-in of cross section of **GDY-1**; (c) Cross section of **GDY-3** film and inset showing height profile with thickness of 8 nm; (d) Zoom-in of cross section of **GDY-3**; (e) Cross section of **GDY-4** film and inset showing height profile with thickness of 14 nm; (f) Zoom-in of cross section of **GDY-4**.

From the AFM analysis of all GDY films, we can observe the formation of thick films for all precursors, with more than 10 layers of GDYs. The morphology of all films is different, while in **GDY-1** a film with several wrinkles is seen, in **GDY-3** we observed a circular pattern and in **GDY-4** a flatter film is obtained. In this regard we can clearly claim that the precursor is playing an important role in the structure and morphology of the grown GDY, as well as in the thickness of the film, given that all films were grown utilising the same conditions.

4.7.5 Transmission Electron Microscopy

To have an insight of the crystallinity of the formed GDYs films, we turned our attention towards Transmission electron microscopy. By examining the crystallinity of **GDY-1** *via* TEM we find an amorphous morphology (Fig. 4.19a-d) for this film. The selected area electron diffraction (SAED) profile did not present any crystalline pattern (See Fig. 4.19b). This observation can attributed to the large thickness of the film, which did not allow to find any domain in the films.

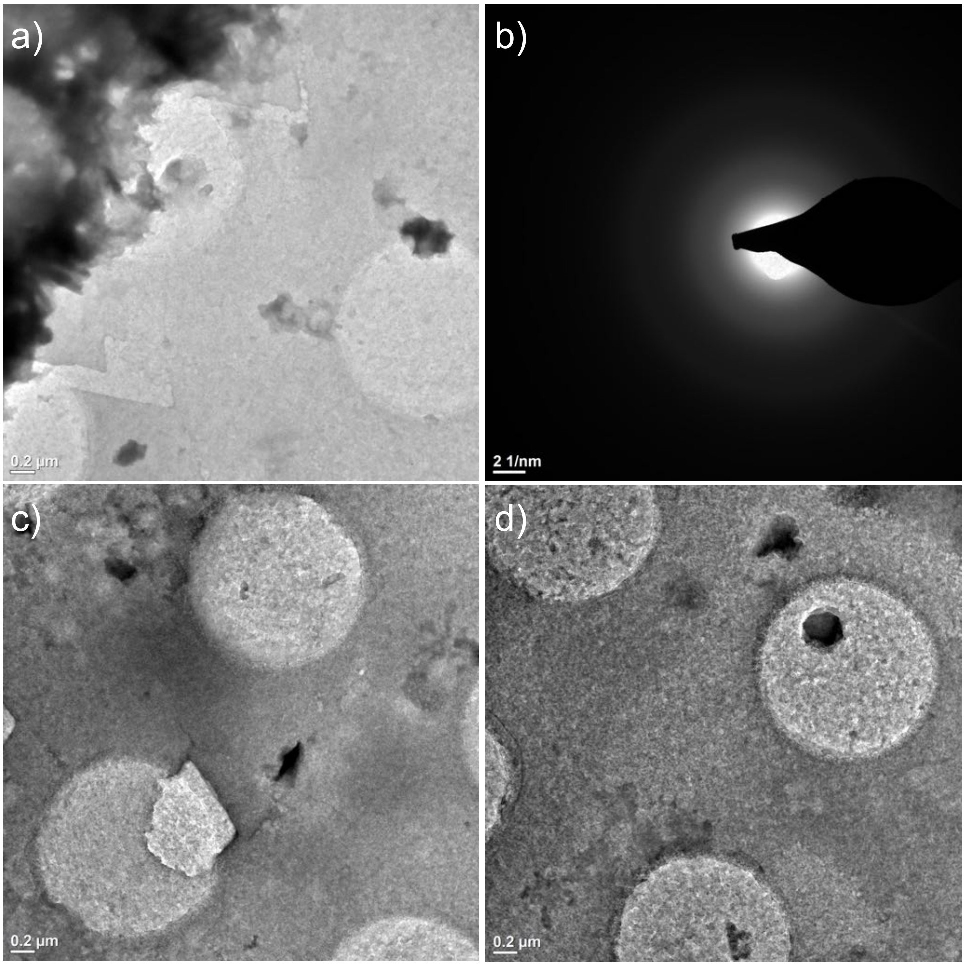

Figure 4.19: TEM images of GDY-1. (a) High magnification image of **GDY-1** film; (b) SAED pattern of **GDY-1** film; (c) and (d) High magnification image of **GDY-1** film.

Similarly, TEM images of **GDY-3** shown in Figure 4.20a-d exhibits mostly amorphous carbon similar to **GDY-1**. Moreover, the SAED pattern in Figure 4.20b did not show a crystalline domain, which suggested that this kind of materials is too amorphous or the domain sizes are too small.

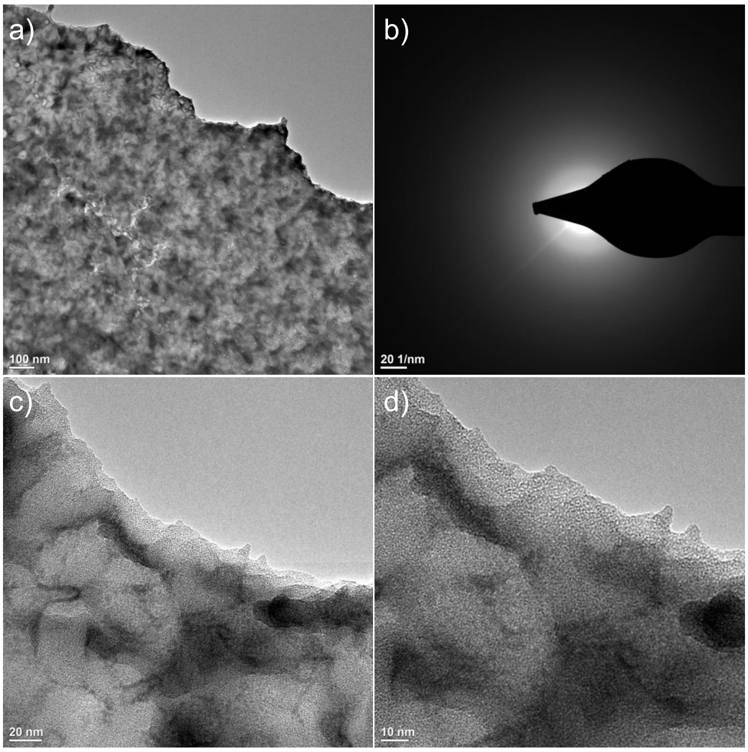

Figure 4.20: TEM images of GDY-3. (a) Low magnification image of **GDY-3**; (b) SAED pattern of **GDY-3** film; (c) High magnification of a cross section of **GDY-3**; (d) High magnification of a cross section of **GDY-3**.

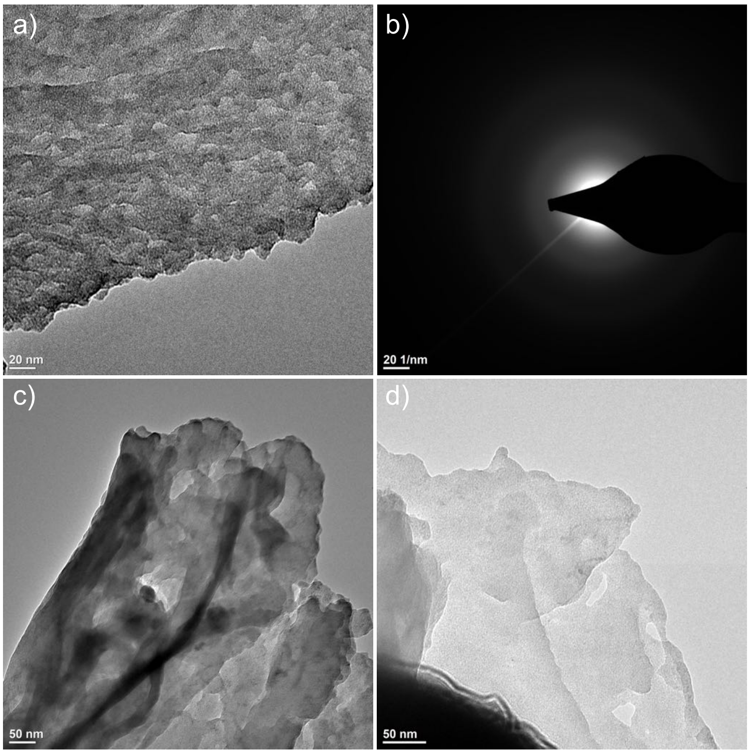

Figure 4.21: TEM images of GDY-4. (a) high magnification image of **GDY-4**; (b) SAED pattern of **GDY-4** film; (c) Low magnification of a cross section of **GDY-4** film; (d) Low magnification of a thinner cross section of **GDY-4** film.

Lastly, we examined the **GDY-4** film, resulting in an amorphous phase, as observed for **GDY-1** and **GDY-3** films (See Fig. 4.21a-d). We also did not observe any crystallinity in the SAED pattern of **GDY-4**, where as observed in Fig. 4.21b the film is mostly amorphous carbon.

A recent review has described that the crystallinity of this kind of GDY materials has only been seen in a 3-layer films, while in thicker films it seems that there is mostly amorphous carbon[172]. The report is in agreement with our results. Additionally, most of the information concerning the crystallinity of GDY has been made only employing theoretical models. Until now, there is no report of single layer GDY, which indicates that the synthesis of this material is not well understood and requires further investigations.

4.7.6 Optical Bandgap Calculation

The band-gap of materials can indicate the degree of electrical conductivity that can be achieved in the organic film, hence, the applicability of the film in transistors devices, or other electronic applications. To have an estimate of the band-gap in **GDY-1**, **GDY-3** and **GDY-4**, the optical band-gap of the three GDY films, was determined measuring the UV-vis absorbance of all the films. For this, a small piece of GDYs film grown on Cu foil was transferred to a quartz chip (3×1 cm) as shown in Fig. 4.22. Afterwards, the absorbance of each of the GDYs was measured employing a UV spectrometer. To determine the optical band-gap the Tauc plot methodology was used to measure the UV-vis-near IR absorption of all the GDY films on the quartz glass substrate. The Tauc-plot consists in the plotting of $h\nu$ vs. $(\alpha h\nu)^{1/r}$, where $h\nu$ is the energy in eV and is the coefficient of absorption of the material. The value of r is determined by the nature of the transition in the material, that is, whether is direct or indirect. Previous studies of GDY band-gap have shown that GDY has an direct transition, which lead to a value of r = 1/2.

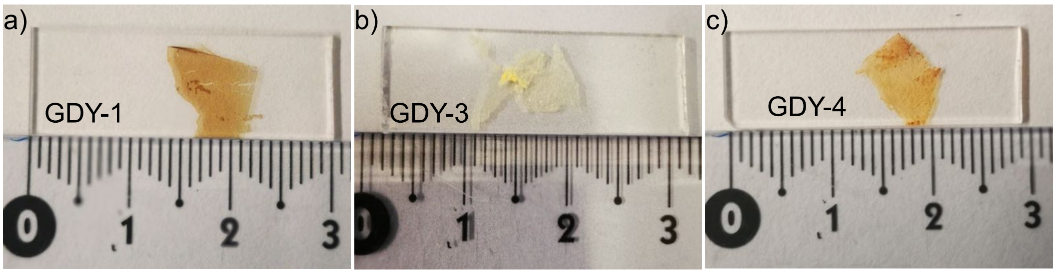

Figure 4.22: Films employed for Optical Band-gap measurements. The images show a small piece of (a) **GDY-1**, (b) **GDY-3** and (c) **GDY-4**, film transferred to a quartz glass chip.

The spectrum of **GDY-1** and the precursor **2** were measured and compared. The spectrum of the precursor presented two maxima of absorption at 304 and 323 nm, but when the precursor forms the **GDY-1** film, the absorption spectrum changes and becomes a broader peak with a wider range of absorption including the visible region. In Fig. 4.23 is clear the bathochromic shift of the **GDY-1** film respecting to the precursor **2**.

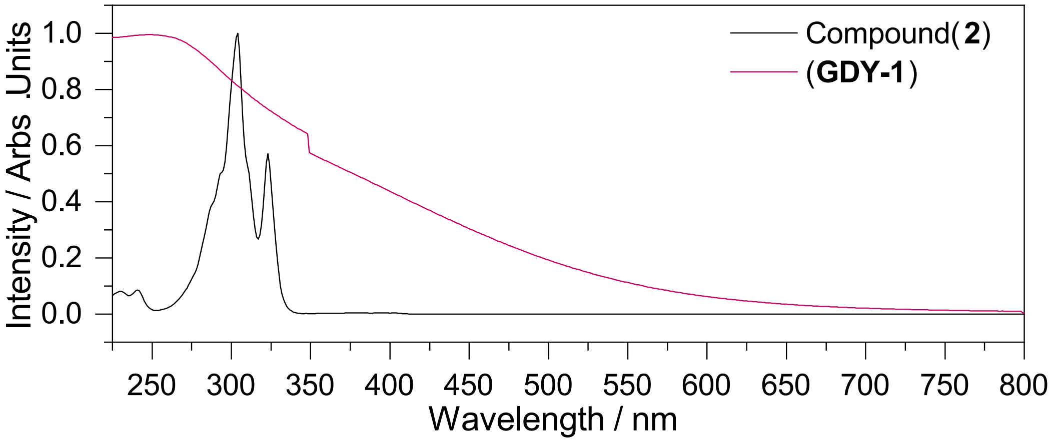

Figure 4.23: Optical Band-gap. UV-Vis spectrum of **GDY-1** (red trace) and the precursor **2** (black trace).

The absorbance at the visible region was expected due to precursor **2** is a colourless compound and when the homo-coupling occurs the film has a brown colour as shown in Fig. 4.22a, which can lead to a wider absorbance in the visible region.

A Tauc plot of **GDY-1** was employed to estimate the optical band gap resulted in a value of energy of 3.39 eV (Fig. 4.24). The optical band gap exhibited by **GDY-1** is larger compared to calculated that is in a range of 0.5 eV to 1.0 eV, indicating that this growth methodology has led to a material with properties like an insulator more than the predicted semiconductor that has been shown in several theoretical works.

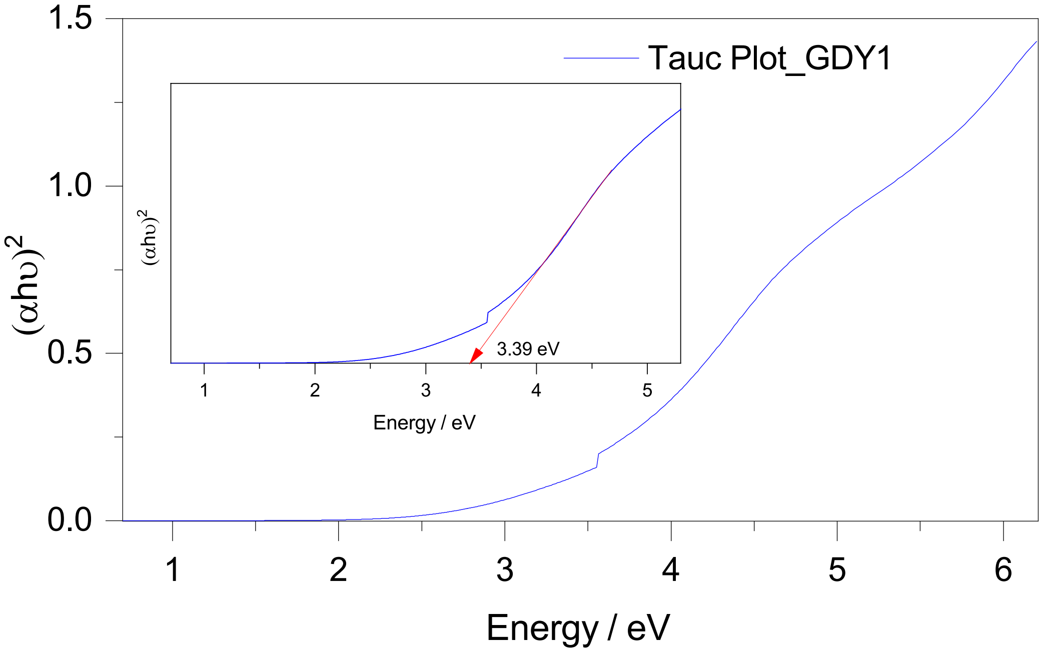

Figure 4.24: GDY-1 Tauc plot. The x-axis corresponds to energy in eV, while the y axis corresponds to $(\alpha h\nu)^{1/r}$. The band-gap obtained through this analysis is 3.39 eV.

The spectrum UV-Vis of **GDY-3** was measured using a quartz glass chip (Fig. 4.21b). The UV-Vis spectrum of **GDY-3** presented a broad peak of abortion between the UV and the visible region, being the maximum of absorption at 280 nm. In Fig. 4.25 is shown the spectrum UV-Vis of **GDY-3** and precursor **6**, there is a notable bathochromic shift in the absorption of **GDY-3** compared to the precursor **6**, complementing the differences between the precursor and the grown-GDY seen in Raman and IR analysis. This confirmed the homo-coupling due to the electronic structured has changed.

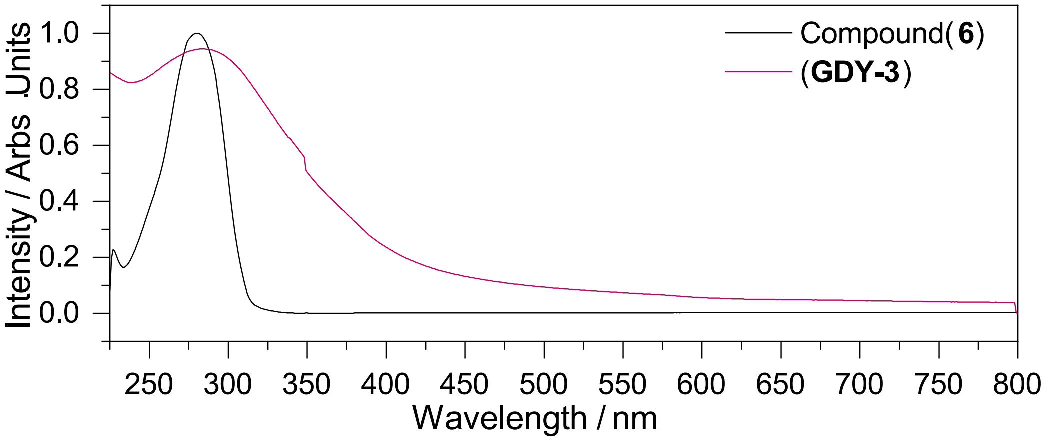

Figure 4.25: Optical Band-gap. UV-Vis spectrum of **GDY-3** (red trace) and the precursor **6** (black trace).

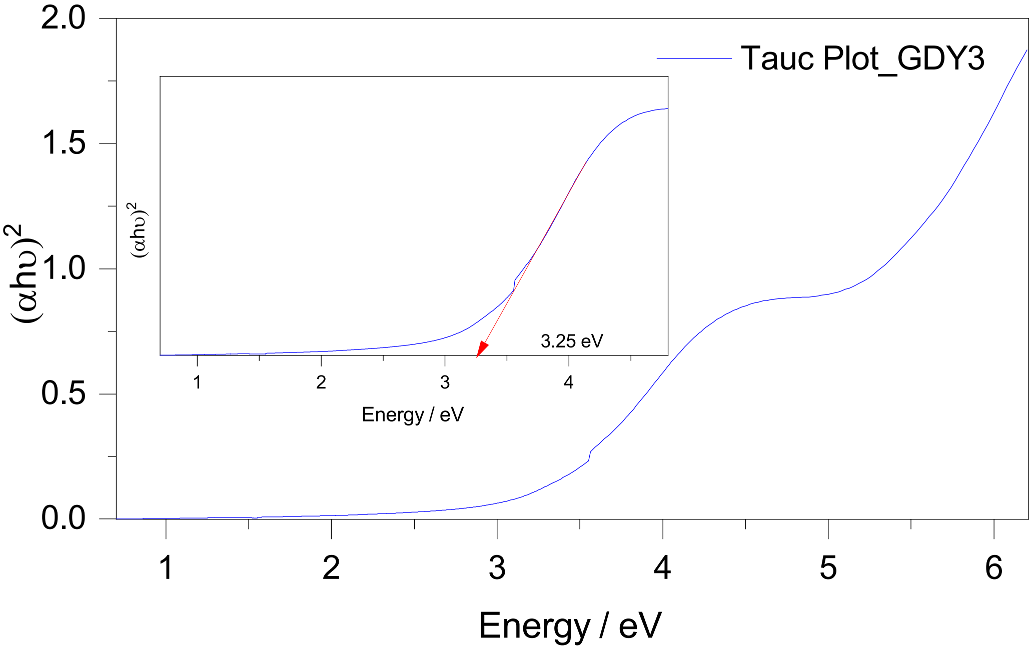

Figure 4.26: GDY-3 Tauc plot. The x-axis corresponds to energy in eV, while the y axis corresponds to $(\alpha h\nu)^{1/r}$. The band-gap obtained through this analysis is 3.25 eV.

A Tauc plot was employed to calculate the optical band-gap of **GDY-3**, we found that this band-gap is around 3.25 eV (Fig. 4.26). Compared to

GDY-1, **GDY-3** has a similar bang-gap with an insulator behaviour. This is very interesting owing to the electronic structure of the precursors are very different and can be attributed to the chemical structure of **6**, which has the triple bond far from the central aromatic rings, leading to less conjugation in the **GDY-3** electronic structure.

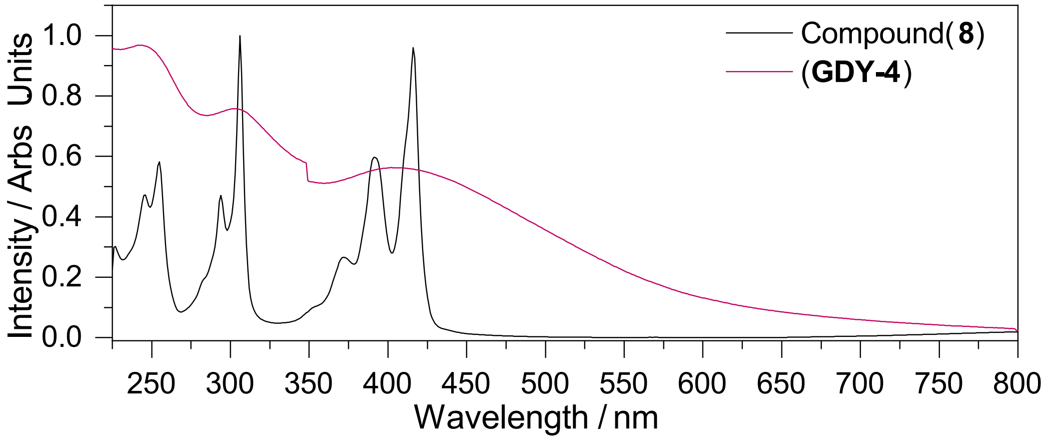

Figure 4.27: Optical Band-gap. UV-Vis spectrum of **GDY-4** (red trace) and the precursor **8** (black trace).

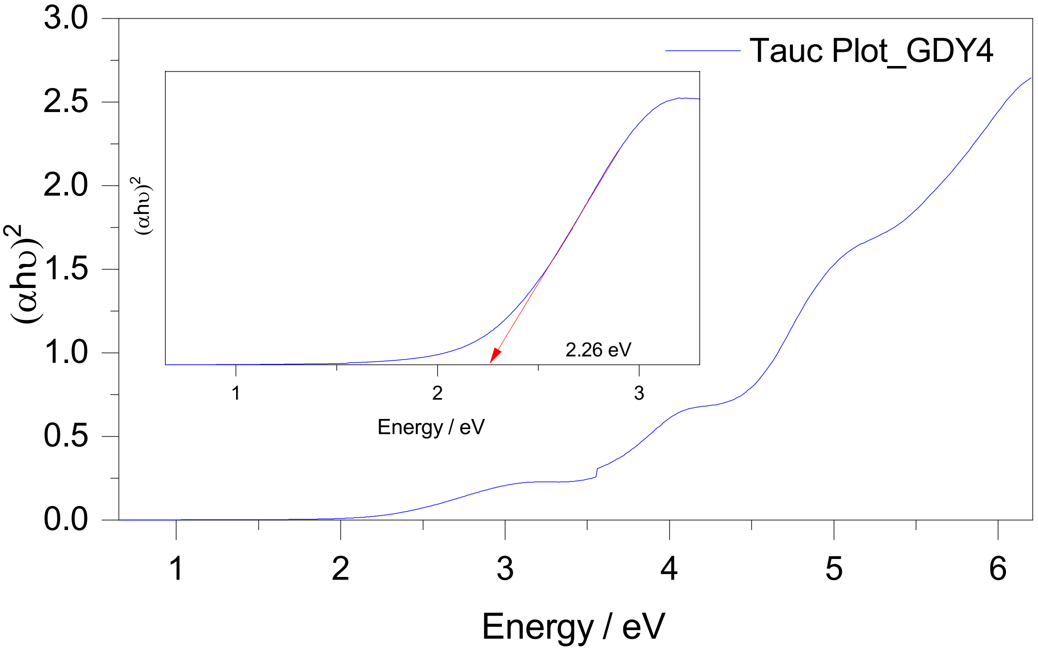

Figure 4.28: GDY-3 Tauc plot. The x-axis corresponds to energy in eV, while the y axis corresponds to $(\alpha h\nu)^{1/r}$. The band-gap obtained through this analysis is 2.26 eV.

UV-Vis absorption spectrum of **GDY-4** and its precursor **8** is shown in Fig. 4.27. The absorption of **GDY-4** presented three broad peaks at 247 nm, 306 nm, and 420 nm. Compared to the precursor, which has a yellow colour, the **GDY-4** presents a broader absorption in the visible region, indicating that the electronic structure has changed, owing to the homo-coupling within the triple bonds of the precursor.

The optical band gap of **GDY-4** obtained from a Tauc plot showed a value of 2.26 eV (Fig. 4.28). This is the smaller value exhibited by our synthesised GDY films, nevertheless, the value shown by **GDY-4** resembles more to an insulator material than a semiconductor.

The optical measurement has shown interesting results, due to the GDY network has been predicted to exhibit a semiconductor behaviour. Unfortunately, the three grown GDY films did not show this behaviour. We can attribute our observation to the thickness and the amorphous nature show in the TEM of the obtained films. The optical band gap has been predicted for ideal systems, a single layer with a perfect coupling among the molecules linked by triple bonds in the GDY network[173], our systems are very different from the ideal GDY-single-layer, as shown by our results.

4.8 Conclusions

GDY 2D networks have been predicted as the most stable non-natural allotropes of carbon. Furthermore, theoretical calculations have predicted remarkable electrical, mechanical and catalytic properties of these materials. Based on this, in this chapter, we explored an approach, using an APCVD reactor, for the synthesis of GDY films and utilising organic molecules as precursors. For this, four organic molecules were employed: hexaethynyl benzene **2**, hexakis[4-(ethynyl)phenyl]benzene **4**, 1,3,5-tris[4-(ethynyl)phenyl]benzene (**6**) and 1,3,6,8-tetrakis(ethynyl)pyrene (**8**). All precursors were prepared employing Negishi and/or Sonogashira reactions in good yield. Thorough characterisation of the starting materials confirms the successful synthesis of the desired compounds, which were subsequently employed for the GDY film synthesis.

The synthesis of the GDY films was accomplished on an APCVD reactor utilising Cu foil as metallic substrate as well as catalytic agent for the homo-coupling reaction. This substrate was chosen given the catalytic role of Cu in the solution based synthesis of GDY. The quality of the GDY films has been shown to be contingent upon the smoothness and flatness of the substrate. Therefore, before the GDY synthesis, the Cu substrates were subjected to a cleaning process to remove oxide impurities and/or traces of other metals present in it. The formation of organic films was observed for all organic precursors as revealed by surface characterisation such as Raman spectroscopy, XPS, IRRAS, OM and SEM. Furthermore, AFM of the films obtained from the precursors **2**, **6** and **8** shows film thicknesses from 8 to 35 nm. Note that it was not possible to transfer the films obtained from **4**, due to the fragility of the material during the transfer process. This can be rationalised by an discontinuous homo-coupling of **4** due to its non-planar and flexible motif.

The films obtained from **2**, **6** and **8**, which allowed the film transfer, were explored *via* TEM, leading to the observation of an amorphous diffraction pattern, due to the absence of crystalline domains of the respective GDYs. This result can be attributed to the large thickness of the films, as observed in AFM studies, which hinders the resolution of small crystalline domains. This is consistent with reports, in which crystalline domains have been observed in GDY films with rather small thicknesses. It is worth stressing that the thickness of the GDY films prepared in this doctoral work was difficult to control. Test experiments with lower concentration of the precursors, shorter growth times and smaller flows of the carrier gas led to either no formation of a continuous film or the formation of thick films. Li and co-workers have shown that by using Ag substrates for the GDY growth, the film thickness is restricted to the surface area of the Ag substrate, leading to films with thickness not larger than 1.4 nm. This can be rationalised by a catalytic reaction, where the growth is precluded once the Ag sites are covered with the GDY films. Interestingly, Li et al. also studied the GDY growth on Cu foil using a CVD reactor, however, they were not able to obtain any film, in contrast with the results presented in this thesis.

The observed large thickness of the GDY films oinf this thesis suggests that not only the presence of the Cu catalyst plays a significant role, but also the temperature at which the homo-coupling is carried out influences the outcome of the film growth. The effect of the temperature in the GDY growth has been previously observed by Zuo et al. *via* a metal-free methodology. They demonstrated that by increasing the temperature to 120 °C it was possible to grow GDY without requiring a metal catalyst for the synthesis. Our observations are also based on the fact that the thicknesses of the obtained films were very large (8 to 35 nm). This observation will certainly require further investigations.

Due to the theoretical prediction of the remarkable electronic properties of graphene, we turned our attention to the optical properties of the GDY films. The optical properties of the GDY films were characterised employing an UV spectrometer. In all cases we observed an insulating nature of the films, in contrast with the prediction of several theoretical works, in which a semiconductor behaviour has been foreseen. Nevertheless, it should be noted that all theoretical predictions are made for single-layer crystalline GDY films, which have not been achieved experimentally up to now. Conversely, the GDY films we reported herein showed a non-crystalline nature and multilayer character, which might be responsible for the insulator properties of the GDY films.

In summary, GDY films were obtained from four different organics molecules. Moreover, **GDY-1**, **GDY-3** and **GDY-4** were successfully transferred to a Si, SiO_2, gold and quartz substrates for surface characterisation that confirmed the formation of the films. In this approach we have shown that the synthesis of GDY can be achieved utilising Cu foil, a CVD reactor and a nebuliser. This work will serve as foundation for further investigations of the synthesis of GDYs employing organic molecules with different content of acetylene groups. Still, there is a lot of work to be done for the understanding of the synthesis of this new carbon-based 2D material, such as the control of the thickness of the films and the role of the Cu substrate and temperature.

Chapter 5

Experimental Section

5.1 Materials and Equipment

All solvents and reagents were obtained from commercial sources and used without further purification. Tetrahydrofuran (THF) and trimethylamine (Et_3N) were dried over sodium and CaH_2, respectively, before use, employing a distillation system under argon atmosphere. Merck silica gel 60 (230-400 mesh) were used to purify the starting materials through chromatography columns.

The separation and purification of the organic molecules was followed by thin-layer chromatography (TLC) on aluminium plates coated with Merck 5735 silica gel 60 F254. The ^{1}H-NMR and ^{13}C-NMR spectra were collected on a Bruker DRX 500 spectrometer, employing deuterated solvents. The analysis of the molecular mass for the synthesised compounds was carried out *via* matrix-assisted laser desorption/ionisation time-of-flight (MALDI-ToF), in a Voyager-DE PRO Bio spectrometry. For this, the samples were mixed in 2,5-dihydroxy-benzoic acid matrix. Infrared (IR) spectra were obtained with a MAGNA FTIR 750, Nicolet in region from 400 to 4000 cm^{-1}. The samples were prepared by grinding the organic compounds with dry potassium bromide (KBr). Subsequently, a pellet of the mixture was prepared for IR measurements. The elemental analysis (carbon, hydrogen, nitrogen) was carried out in a Vario Micro Cube machine. UV-vis spectra were acquired on an UV-vis spectrophotometer Cary 500 Scan. Thermogravimetric differential scanning calorimetry (TGA-DSC) measurements were conducted by a SETARAM SENSYS Evo thermal analyser under air flow (20 mL min^{-1}) with a heating rate of 5 °C min^{-1}.

The sapphire chips were obtained commercially from SurfaceNet with the specification such as: thickness of 0.43 mm, chip size of 5×5mm, orientation of 0001-sapphire (*c*-Al_2O_3), and one side polished. Palladium Target for electro-sputtering was purchased in Gmaterial, with purity of 99.95%, diameter of 3 inches, 1 mm thickness and an approximately weight of 54.8 g. All the gases employed for the CVD synthesis were acquired from Alphagaz with the following purity: argon (Ar) 99.9995%, Hydrogen (H_2) 99.9999%, carbon dioxide (CO_2) 99.995%. Silicon (Si) and Silicon Oxide (SiO_2) were purchased in Active Business Company GmbH. Ammonium persulfate salt ($(NH_4)_2S_2O_8$) was commercially obtained from Alpha Aesar. A solution of

4% PMMA in anisole was obtained from Sigma-Aldrich. The Copper for electro-sputtering was purchased in Gmaterials with 3 inches of diameter, 0.12 inches thickness and a purity of 99.99%.

All Chemical Vapour Deposition (CVD) reactions were carried out in a CVD furnace equipped with a quartz tube and thermo-controller operating temperature range between RT and 1100 °C. The quantities of gasses employed during the growth procedure was controlled and monitored employing four mass-flow controllers ranging from 10-1000 sccm for Ar, H_2 and CH_4 gases and a range of 1-100 sccm for CO_2 gas. The surface characterisation of the 2D materials synthesised was conducted with the following equipment: The Raman spectra was collected in a Renishaw inVia Raman Microscope with a 532 nm argon ion laser. Scanning electron microscopy (SEM) images were obtained by employing a ZEISS LEO Gemini 1530 system. Energy dispersive X-ray spectroscopy (EDS) measurements were performed in an Oxford Instruments X-MaxN 50 mm^2 Silicon Drift Detector in a Gemini LEO SEM. Atomic force microscopy (AFM) imaging was carried out with a Bruker Dimension Icon microscope in tapping mode with µmash. Transmission electron microscopy (TEM) measurements were carried out in a Titan 80-300 (FEI Company) aberration-corrected (image) microscope at 80 and 300 kV. For the infrared reflection absorption spectroscopy (IRRAS) measurement, was employed a Bruker VERTEX 80 purged with dried air and with a fixed angle of incidence of 80° in the A518 accessory. The detector used for this measurement is a narrow-band liquid-nitrogen-cooled mercury cadmium telluride. The XRD data was collected employing a D8-Advance Bruker AXS diffractometer with Cu Kα radiation (λ= 1.5418 $\AA$) in θ-θ geometry and with a position sensitive detector and variable divergence slit.

Single crystal X-ray diffraction data of the organic precursors was collected employing STOE StadiVari 25 diffractometer with a Pilatus300 K detector using GeniX 3D HF micro focus with MoKα radiation (λ = 0.71073 Å).The structures were solved using direct methods and were refined by full-matrix least-squares methods on all F^2 using SHELX-2014 implemented in Olex2. The crystals were mounted on a glass tip using crystallographic oil and placed in a cryostream. Data were collected using φ and ω scans chosen to give a complete asymmetric unit. All non-hydrogen atoms were refined anisotropically. Hydrogen atoms were calculated geometrically riding on their parent atoms.

5.2 Synthesis of graphene from CO_2

5.2.1 Metallic Substrate Preparation

All metallic substrates for the graphene growth section were prepared by sputtering copper (Cu) and palladium (Pd) metals on sapphire chips (*c*-Al_2O_3 chips) (5×5 mm^2), using a direct current magnetron sputtering at a working pressure of 5×10^{-3} mbar. The base pressure of the magnetron sputtering chamber was 10^{-8} mbar. During the sputtering process the power was kept at 110 W for the Cu target and 20 W for the Pd target. The deposition was accomplished at room temperature for 45 min, maintaining all the parameters constant. The target-substrate distance was fixed approximately at 11.5 cm. This methodology was employed to prepare all substrates.

Metallic substrates with different composition of Cu and Pd were obtained as it is described below:

1. **Substrate 1** (**Sub1**): the composition consists in an initial layer of 900 nm thick of Cu. Subsequently, 4 islands of Pd are sputtered *in-situ* on top of the Cu thin film with a thickness of 150 nm each.
2. **Substrate 2** (**Sub2**): this substrate has 900 nm of Cu sputtered on the top of sapphire, as composition.
3. **Substrate 3** (**Sub3**): the preparation involves a deposition of 900 nm of Pd on the top of c-Al_2O_3 Pd.
4. **Substrate 4** (**Sub4**): with one half of Cu (900 nm) and one half of Pd (900 nm) sputtered on the top of c-Al_2O_3 ($\approx$ 1 µm of thickness each layer).
5. **Substrate 5** (**Sub5**): preparation consisted in the deposition of 900 nm of Cu on the c-Al_2O_3 substrate and followed by the deposition of Cu and Pd metals simultaneously, above the 900 nm of Cu previously deposited ($\approx$1 µm of thickness).
6. **Substrate 6** (**Sub6**): was prepared by depositing simultaneously for 45 minutes Cu and Pd metal targets, directly on the c-Al_2O_3 substrate ($\approx$900 nm of thickness).

5.2.2 Graphene Growth

The growth of graphene was accomplished employing an atmospheric pressure CVD reactor (APCVD). For the growth procedure, the substrate was placed into a quartz tube in the heat zone of the furnace. Three main gases were used with a purity of, Ar (99.9999%), CO_2 (99.995%) and H_2 (99.9999%). Graphene was synthesised employing a 4 steps ramp which consisted in: (*i*) the substrate is heated up to 1000 °C with a rate of 30 °C per minute; (*ii*) the annealing procedure starts soon after the temperature reached 1000 °C by passing through a mixture of Ar (70 sccm) and H_2 (50.5 sccm) for 30 minutes; (*iii*) afterwards, the synthesis of graphene initiated by introducing the stream of CO_2 (25.9 sccm) into the CVD reactor, the H_2 was kept and the stream of Ar was increased to 83.5 sccm. The mixture of gases was allowed to react for 40 minutes at 1000 °C; (*iv*) finally, the system was cooled down slowly under a stream of Ar (70 sccm).

5.2.3 Transfer of Graphene to a Silicon substrate

A wet transfer was employed to place the graphene on a silicon (Si) substrate. The metallic substrate with the grown graphene was spin-coated with 4% PMMA solution. Subsequently, it was dipped in a warm solution of $(NH_4)_2S_2O_8$ 0.1 M. After 3 hours, the metals were etched and the

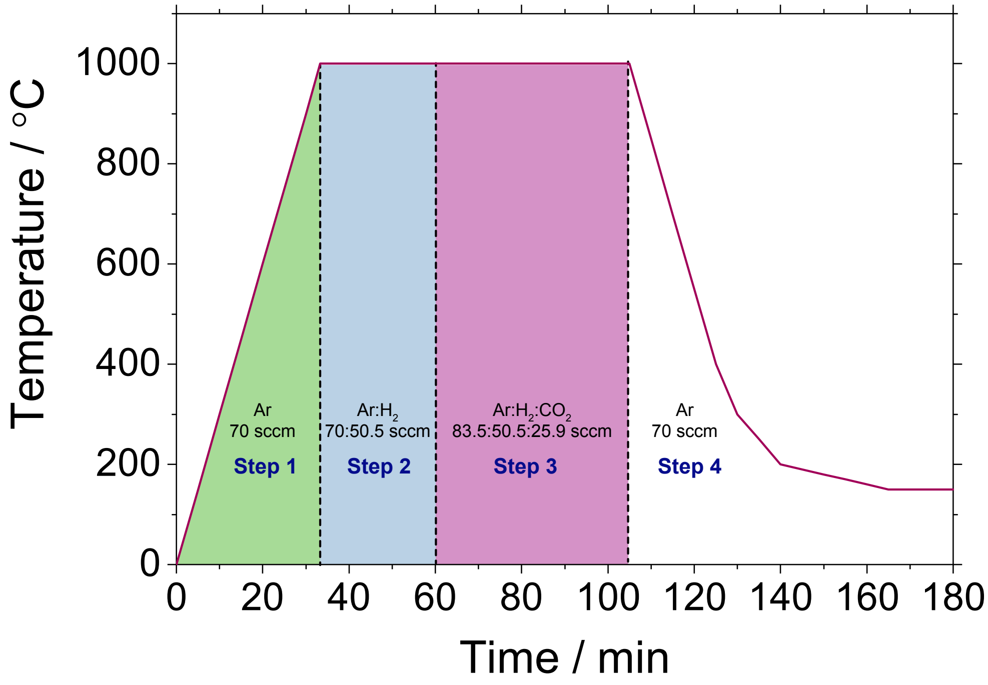

Figure 5.1: Graphene from CO_2. Heating ramp employed to grow Graphene using CO_2 as carbon source.

PMMA/graphene was washed with distilled water several times to eliminate any remaining salt. The PMMA/graphene was placed on a clean silicon wafer and then hot acetone was used to remove the PMMA. Subsequently, the Si substrate containing the graphene was dipped for 5 minutes in diluted aqua regia ($2H_2O$:$2HNO_3$:1HCl) to eliminate any remaining of metals.

5.2.4 TEM Sample Preparation

TEM samples were prepared following the procedure of W. Regan et al. with slightly modifications[174]. This procedure consists in placing a TEM Grid of molybdenum (Mo) with carbon coated on the top of the metallic substrate with the graphene, and dropping some isopropanol (IPA) on the top of the grid. When the IPA is evaporated, the carbon coated on the Mo grid is strongly attached to the graphene grown on the metallic substrate and afterwards, this sandwich is dipped into diluted aqua regia to etch the metals. The carbon filling containing the grown graphene is washed with distilled water and subsequently it is was carefully collected with a 200-mesh copper TEM grid.

5.3 Synthesis of Nanocrystalline Graphene

Nanocrystalline graphene was grown using APCVD reactor. For this, hexaethynyl benzene (**2**) was employed as precursor of graphene. The process consists first in the deposition of the precursor dissolved in acetone, utilising a nebuliser at room temperature for 30 min, with a flow of 35 sccm Ar and 27.5 V power for the nebuliser membrane. After the deposition of the precursor, the nebuliser was turned off and any remaining of acetone was purged with Ar (35 sccm) for 20 min. Subsequently, the furnace was heated to 850 °C (growth temperature) at a rate of 30 °C per min. When the growth temperature is reached, and stream of H_2 (25.3 sccm) is introduced and the growth process takes place for 30 min. As the final step, the sample is allowed to cool down.

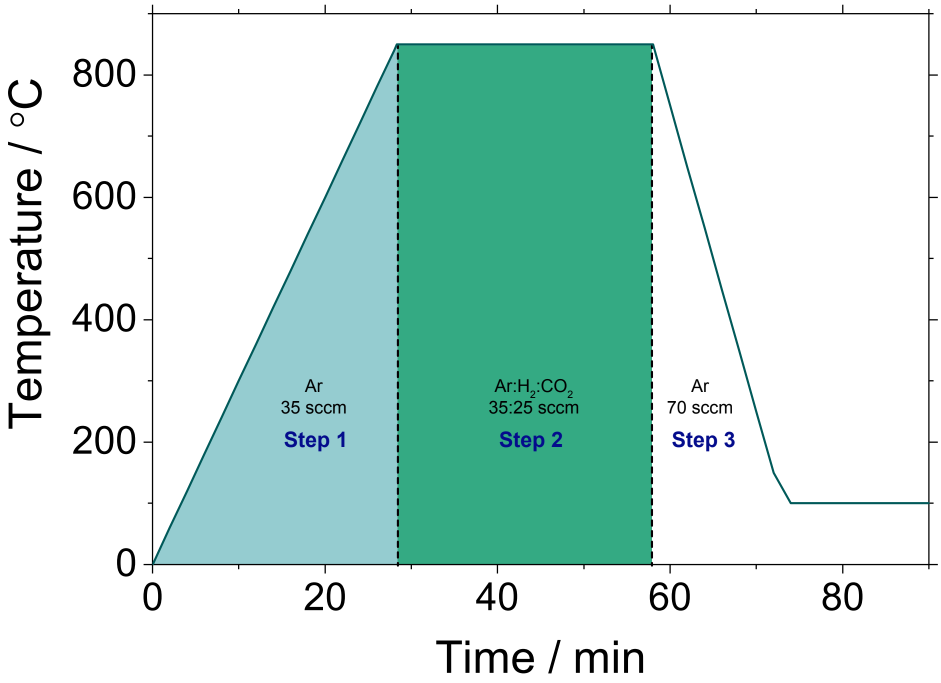

Figure 5.2: NCG from an Organic Molecule. Heating ramp for the growth of Nanocrystalline Graphene employing an organic molecule.

5.3.1 Transfer of NCG to Si and SiO_2 substrate

For the transference of NCG to Si and SiO_2 substrate, we employed a wet transference using $(NH_4)_2S_2O_8$ 0.1 M as Cu etchant. For this, the grown NCG on the Cu foil was spin coated with PMMA 4% solution and subsequently, it was placed on the top of a warm solution of $(NH_4)_2S_2O_8$ 0.1 M for 3 to 4 h. afterwards PMMA/NCG is washed several times with DI water and posteriorly, it is placed on a Si or SiO_2 substrate. PMMA was removed with hot acetone.

5.3.2 TEM Sample Preparation

TEM samples were prepared by etching the Cu foil utilising the same warm solution of $(NH_4)_2S_2O_8$ 0.1 M, that we used in the transfer of NCG into a Si or SiO_2 substrate. For this procedure, the Cu foil containing the grown NCG was placed on the etchant solution for 3 to 4 h. The grown NCG free of Cu is washed several times with DI water and afterwards, it is placed carefully on a 200-mesh copper TEM grid.

5.4 Synthesis of Graphdiyne from Organics Molecules

5.4.1 Synthesis of Starting Material

Synthesis of Hexakis[(trimethylsilyl)ethynyl)]benzene (1) and Hexaethynylbenzene (2): The synthesis of compound **1** (TMS-HEB) was carried out using Guoxing Li et al. procedure with slights modifications.[87] First of all, we synthesised [tri(methylsilyl)ethynyl] zinc chloride by following K. Shimizu et al. procedure[175].

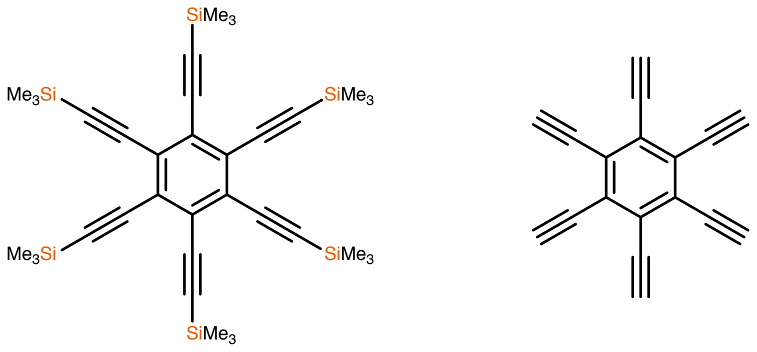

(**1**) (**2**)

Figure 5.3: Hexakis[(trimethylsilyl)ethynyl)]benzene (**1**) and Hexaethynylbenzene (**1**)

As first step, $ZnCl_2$ was dried in vacuum at 130 °C overnight. Subsequently, in a two-neck round bottom flask was added (trimethylsilyl) acetylene (27.5 mL), BuLi 2.5 M (77 mL, 192.5 mmol) and freshly dry THF (105 mL) under an argon atmosphere at -78 °C for 45 minutes, then the mixture was added to dry $ZnCl_2$ in freshly dry THF (124.3 mL). The mixture was stirred at 0 °C for 3h. The final calculated concentration of the solution was 0.92 M.

The synthesis of (**1**) was conducted by mixing hexabromobenzene (9.66 g, 17.5 mmol), tetrakis(triphenylphosphine)palladium ($Pd(PPh_3)_4$) (1.00 g, 0.865 mmol), freshly dry toluene (122.5 mL) and [tri(methylsilyl)ethynyl] zinc chloride (192 mL, 175 mmol) at 60 °C under argon atmosphere for 3 days. After completion of the reaction 500 mL of HCl 2 M were added, the organic fraction was separated and posteriorly washed with 500 mL of brine. The brine/organic mixture was extracted with 1.3 L of diethylether, followed by concentration of the organic fraction under vacuum. The obtained residue was purified by column chromatography with cyclohexane:dichloromethane as eluents. Two columns were carried out for the separation and purification of the molecule, the first one was performed on neutral Al_2O_3 active using cyclohexane:dichloromethane (95:5). The second fraction of the first column was re-chromatographed employing neutral Al_2O_3 column grade brockmann III (6% of water), with a solvent system of cyclohexane:dichloromethane (99:1). The product was obtained as a white crystalline powder. Yield: 36% (4.49 g); ^{1}H-NMR (500 MHz, $CDCl_3$)

δ/ppm: 0.28 (54H); ^{13}C-NMR (126 MHz, $CDCl_3$) δ/ppm 128.11, 105.36, 101.15, 0.16; NIR-IR (KBr, cm^{-1}): 2158 (C≡C), 2901-2964 (sp^3 C-H); ESI-MS, found (calcd.): 654.2 [M–H]$^-$, (655.3); Elemental analysis for $C_{36}H_{54}Si_6$, found (calcd.) for: C, 65.50 (65.98), H, 8.28 (8.31).

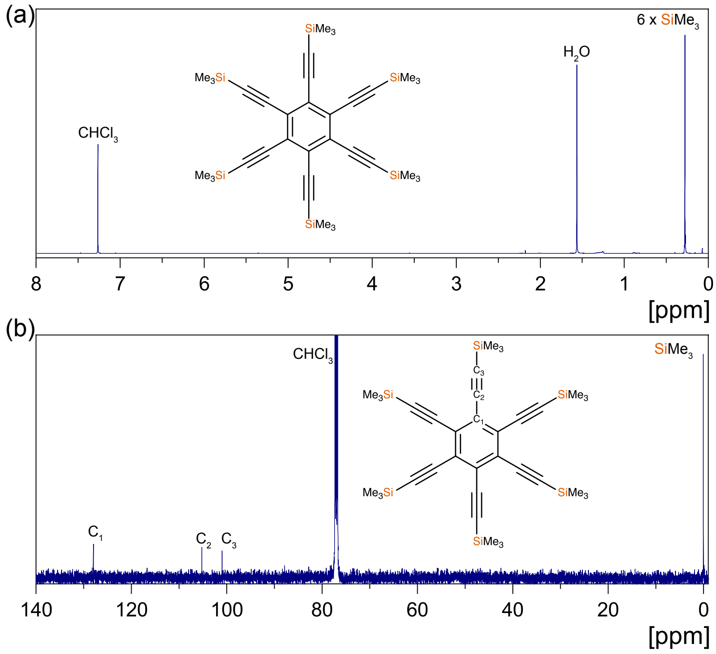

Figure 5.4: NMR spectra of compound **1**. (a) ^{1}H-NMR in $CHCl_3$ (500 MHz); ^{13}C-NMR in $CDCl_3$ (126 MHz).

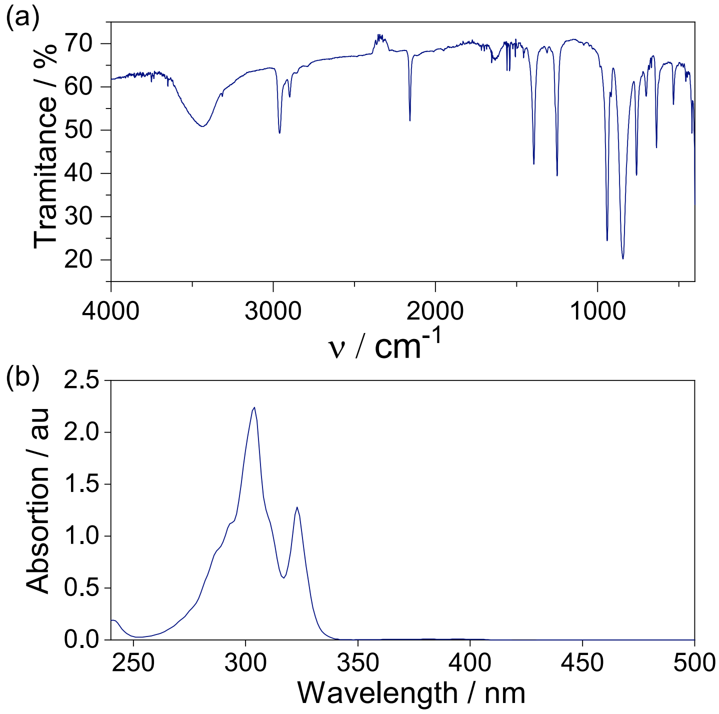

Figure 5.5: (a) IR spectrum and (b) UV spectrum of compound **1** in dry CH_2Cl_2.

Furthermore, the synthesis of **2** was carried out by de-protecting **1**. For this 100 mg of **1** was added to a solution of 0.1 M of tetrabutyl ammonium fluoride (TBAF), then the solution is stirred for 20 min at 0 °C under an Ar atmosphere. subsequently, the reaction was quenched with DI water and finally **2** was extracted with diethyl ether. Unfortunately, compound **2** is very reactive making impossible the determination of the yield of the reaction, and a full characterisation.

Synthesis of Hexakis[4-(trimethylsilylethynyl)phenyl]benzene (3) and Hexakis[4-(ethynyl)phenyl]benzene (4): The synthesis of Hexakis[4-(trimethylsilylethynyl)phenyl]benzene contains two parts as described below.

For the synthesis of **3** and **4**, it is necessary to synthesise the intermediary hexakis(4-iodophenyl)benzene, the synthesis of this intermediary is carried out employing an iodination. In a two-neck round bottom flask was mixed hexaphenylbenzene (2.14 g, 4.0 mmol), bis[trofluoroacetoxy)iodo]benzene (10.75 g, 25 mmol), iodine (6.35 g, 25 mmol) and CH_2Cl_2 (250 mL) under argon atmosphere for 24 h at room temperature in the dark. After completion, the stirring was stopped leading to a final purple colour. 5% of Na_2SO_3 was the added to the reaction to neutralise the unreacted iodine, leading to a colourless solution. Then the mixture was extracted with CH_2Cl_2 and then precipitated with cyclohexane (ca. 500 mL). The precipitated was subsequently filtered, yielding a white powder. Yield: 89.06% (4.60 g)

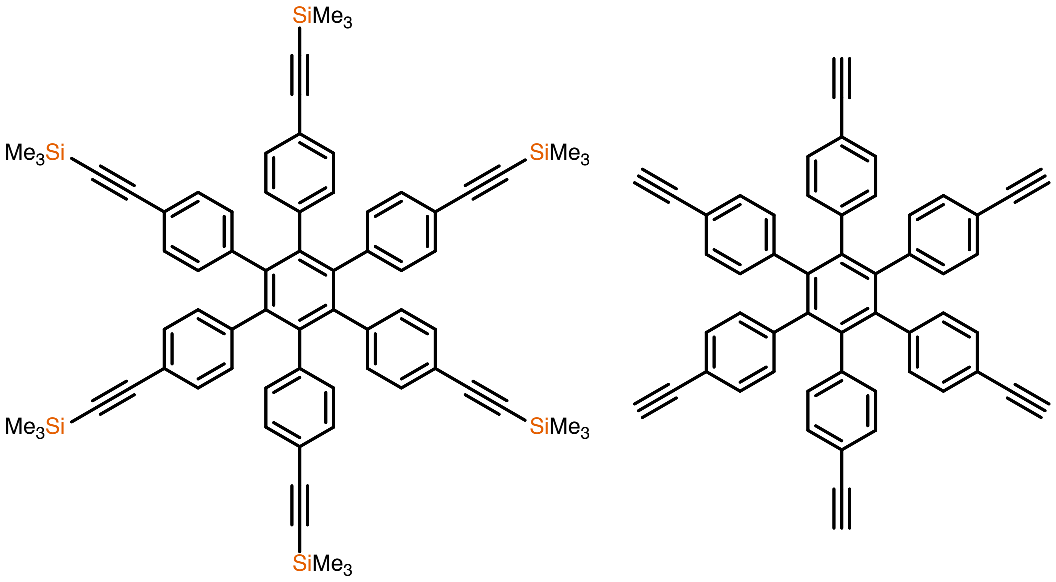

(3) **(4)**

Figure 5.6: Hexakis[4-(trimethylsilylethynyl)phenyl]benzene (**3**) and Hexakis[4-(ethynyl)phenyl]benzene (**4**)

The next step was accomplished in a two-neck round bottom flask, where hexakis(4-iodophenyl)benzene (5.43 g, 10 mmol), (trimethylsilyl)acetylene (5.5 mL, 40 mmol), $Pd(PPh_3)_2Cl_2$ (0.35 g, 0,5 mmol) and CuI (0.10 g, 0.5 mmol) were mixed with a mixture of dry THF (150 mL)/DPA(150mL) under argon atmosphere at 60 °C for 18 h. The reaction was allowed to react and upon completion the reaction was poured into a saturate solution of NH_4Cl followed by extraction with CH_2Cl_2. The solvent was evaporated under vacuum and the residue was re-dissolved with a small amount of CH_2Cl_2. The solution was passed through a flash chromatographic column using 100% CH_2Cl_2. Then, the residue was cleaned with charcoal and warm cyclohexane, to remove palladium traces. The compound was purified by chromatography column using silica gel and a mixture of cyclohexane:CH_2Cl_2 (85:15) and it was obtained as a white powder. Yield: 75% (3.33 g). ^{1}H-NMR (500 MHz, $CDCl_3$) δ/ppm: 0.20 (54H), 6.672, 6.68 (d, J = 8.3 Hz, 12H), 6.98(d, J = 8.3 Hz, 12H); ^{13}C-NMR (126 MHz, $CDCl_3$) δ/ppm: 140.23, 139.94, 131.06, 130.96, 120.47, 105.37, 94.25, 0.06: NIR-IR (KBr, cm^{-1}): 2158 (C≡C), 2963 (sp^3 C-H); ESI-MS, found (calcd.): 1111.3 $[M–H]^-$, (1111.9); Elemental analysis for $C_{72}H_{78}Si_6$, found (calcd.): C, 76.41 (77.77), H, 6.98 (7.07).

The last step, the synthesis of compound **4**, is performed by de-protecting **3**. A solution of TBAF 0.1 M is reacted with 100 mg of **3** with constant stirring under an Ar atmosphere at 0 °C for 1 h. Afterwards, the reaction was quenched with DI water and **4** was extracted with diethyl ether. Further purification employing chromatographic column was required, using silica gel and hexane and DCM as solvent. Compound **4** was obtained as a white powder with a yield of 48.7% (30 mg).

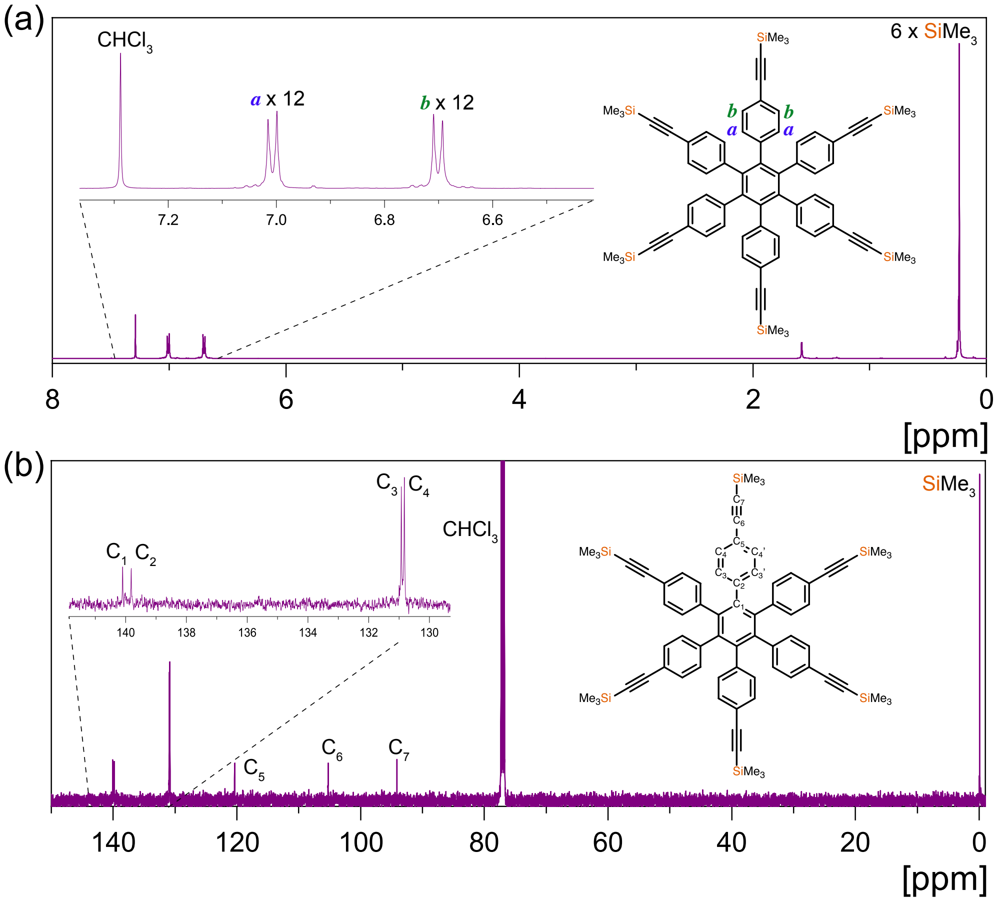

Figure 5.7: NMR spectra of compound **3**. (a) ^{1}H-NMR in $CHCl_3$ (500 MHz); ^{13}C-NMR in $CDCl_3$ (126 MHz).

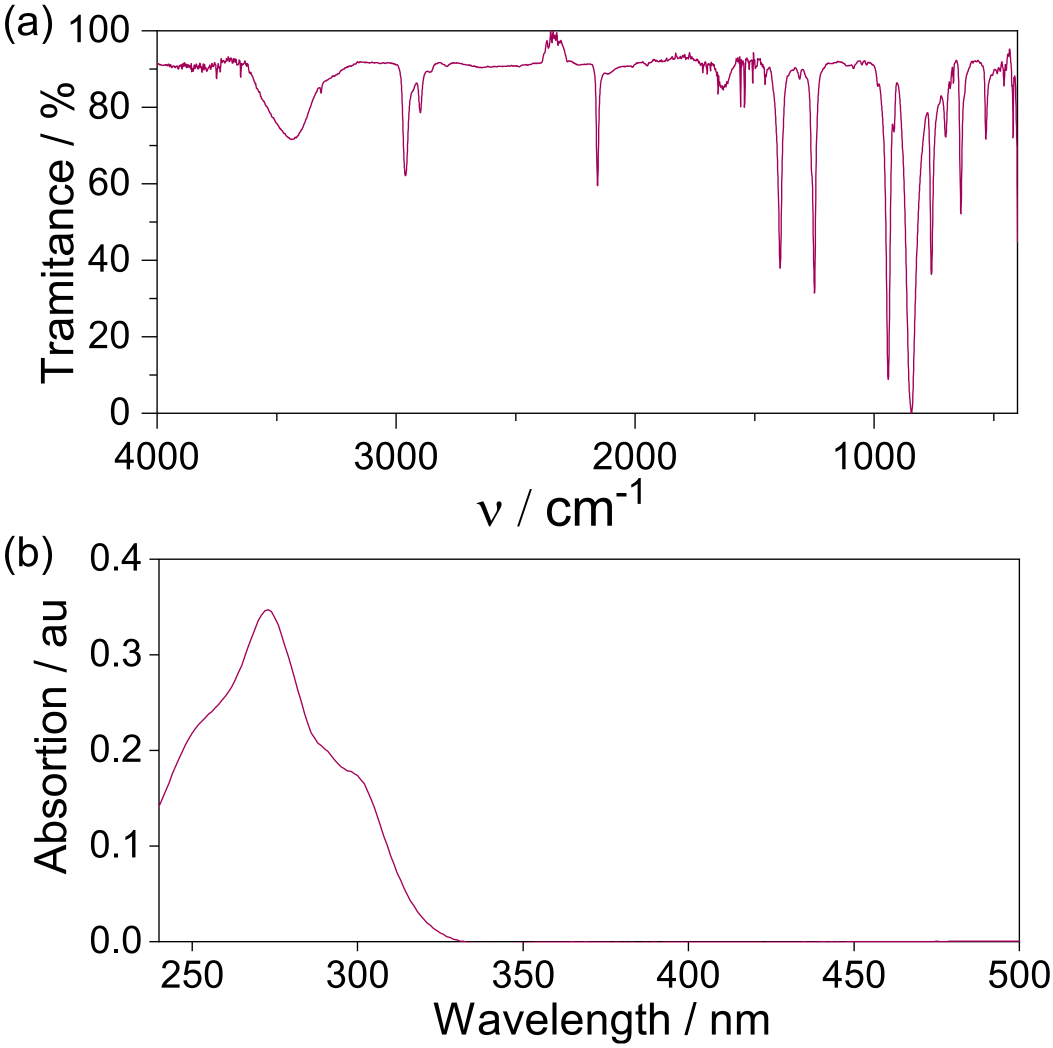

Figure 5.8: (a) IR spectrum and (b) UV spectrum of compound **3** in dry CH_2Cl_2.

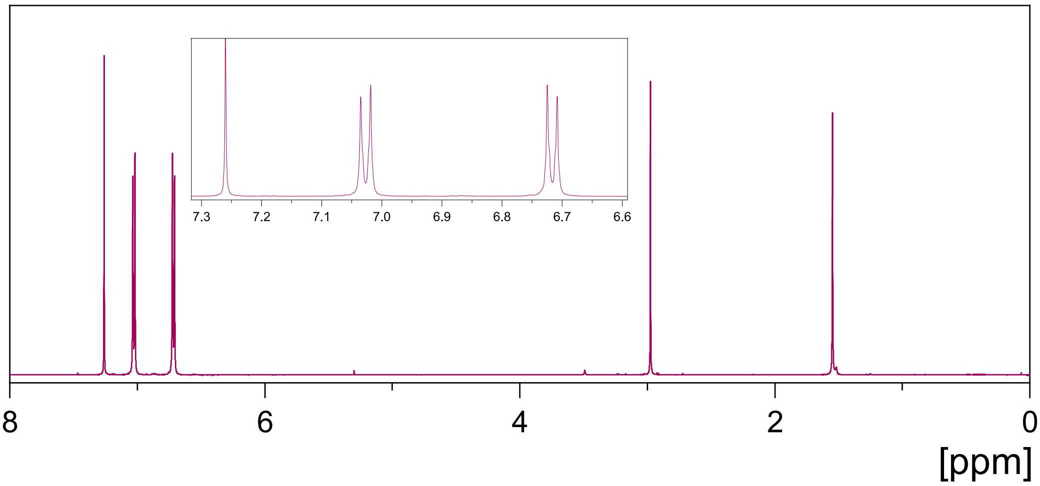

Figure 5.9: ^{1}H-NMR (500 MHz) spectra of the deprotected compound **4** in $CDCl_3$.

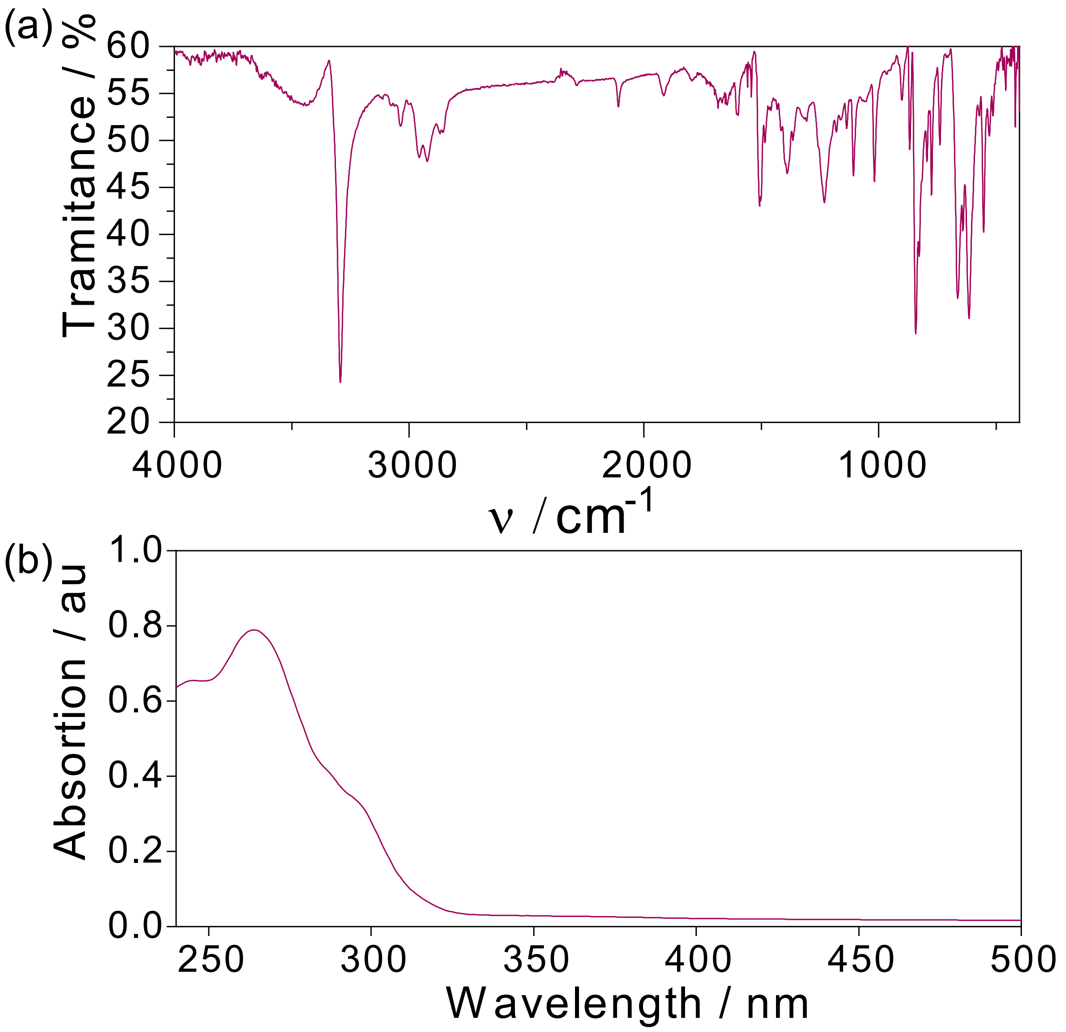

Figure 5.10: (a) IR spectrum and (b) UV spectrum of compound **4** in dry CH_2Cl_2.

Synthesis of 1,3,5-tris[4-(trimethylsilylethynyl)phenyl]Benzene (5) 1,3,5-tris[4-(ethynyl)phenyl]Benzene (6): The synthesis of compound **5** was carried out in a two-neck round bottom flask adding, 1,3,5-tris(4-bromophenyl)benzene (5.04 g, 4 mmol), (trimethylsilyl)acetylene (4.2 mL, 30 mmol), $Pd(PPh_3)_2Cl_2$ (0.56 g, 0.8 mmol) and CuI (0.4 g, 0.8 mmol) and a mixture of THF (300 mL)/DPA(300 mL) under argon atmosphere and constant stirring at 60 °C for 18 hours. Upon completion it was poured in a saturated solution of NH_4Cl and it was extracted with CH_2Cl_2. The solvent was evaporated under vacuum and the residue was re-dissolved with an amount of cyclohexane:CH_2Cl_2 (1:1) and then it was passed through a flash chromatography column using the same solvent system. Subsequently, the residue was cleaned with active carbon and warm cyclohexane, following the solution was allowed to cool down to room yielding a precipitate and subsequently it was collected by filtration as a white powder. Yield: 43% (2.54 g). ^{1}H-NMR (500 MHz, $CDCl_3$) δ/ppm: 0.27 (27H), 7.57 (d, *J* = 8.5 Hz, 6H), 7.68 (d, *J* = 8.5 Hz, 6H), 7.81 (3H); ^{13}C-NMR (126 MHz, $CDCl_3$) δ/ppm: 140.23, 139.94, 131.06, 130.96, 120.47, 105.37, 94.25, 0.06; NIR-IR (KBr, cm^{-1}): 2161 (C≡C), 2852-2960 (sp^3 C-H); ESI-MS, found (calcd.): 594.15 $[M{-}H]^-$, (595.01); Elemental analysis for $C_{39}H_{42}Si_3$, found (calcd.) for: C, 78.87 (78.72), H, 7.18 (7.11).

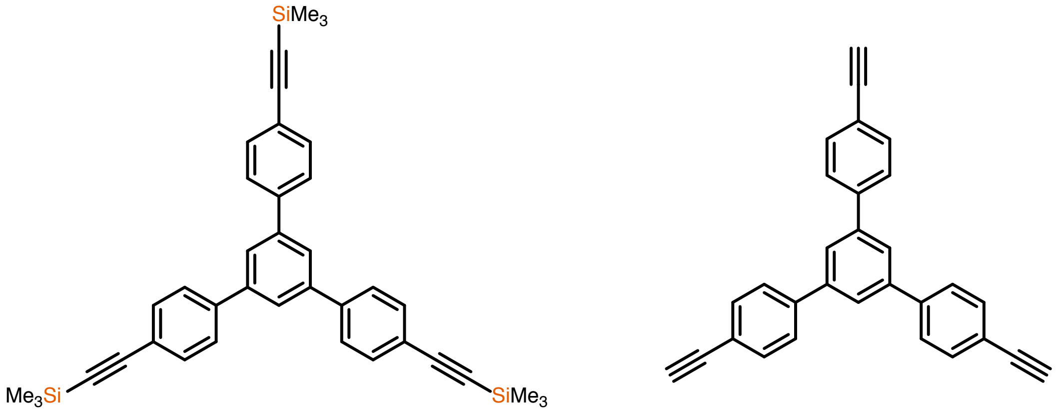

(**5**) (**6**)

Figure 5.11: 1,3,5-tris[4-(trimethylsilylethynyl)phenyl]benzene (**5**) and 1,3,5-tris[4-(ethynyl)phenyl]Benzene (**6**)

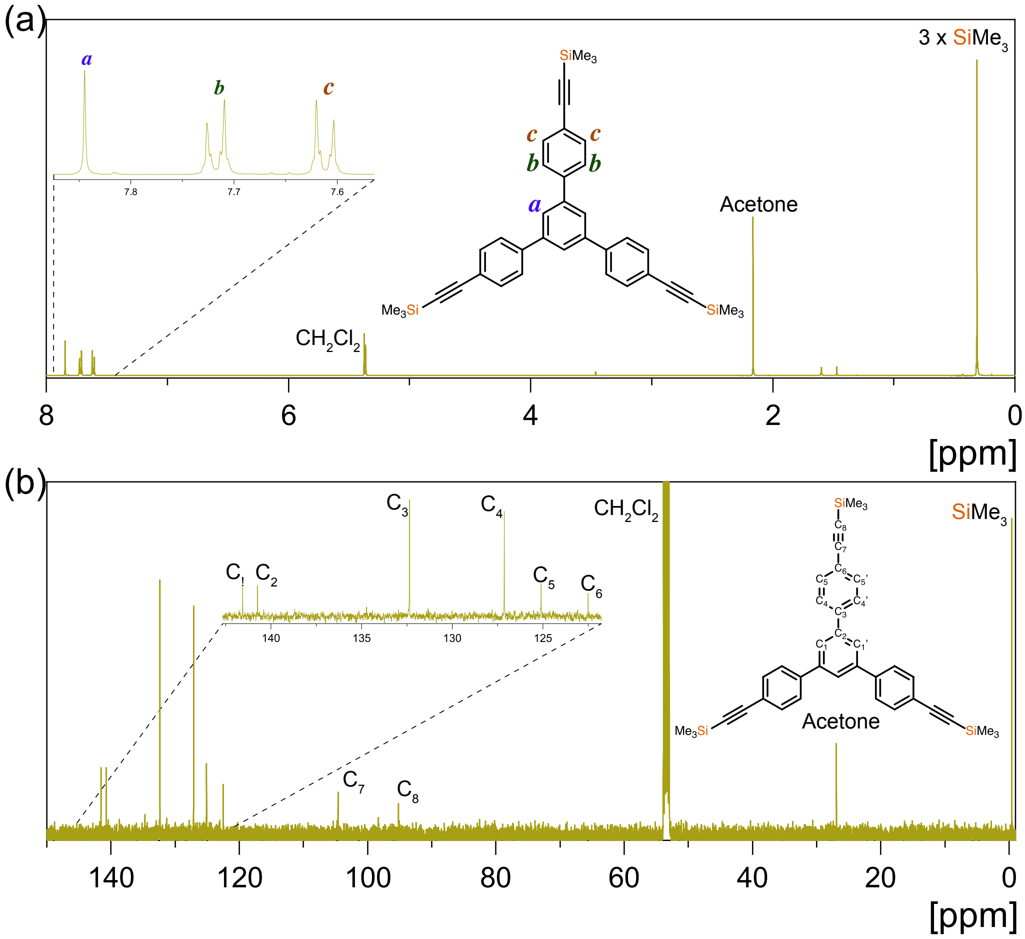

Figure 5.12: NMR spectra of compound **5**. (a) ^{1}H-NMR (500 MHz); ^{13}C-NMR in CD_2Cl_2 (126 MHz).

The synthesis of compound **6** was conducted by performing a de-

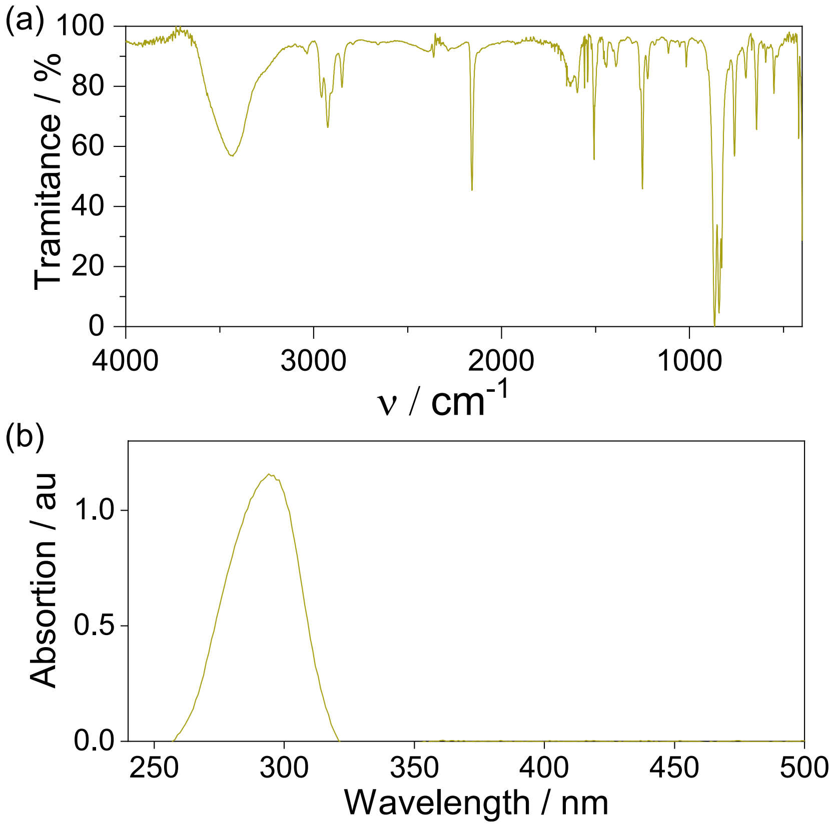

Figure 5.13: (a) IR spectrum and (b) normalised UV spectrum of compound **5** in dry CH_2Cl_2.

protection of **5**. A methanolic solution of K_2CO_3 0.1 M is employed to deprotect 200 mg of (**5**), the reaction was stirred overnight under an Ar atmosphere at room temperature. Afterwards, the reaction was stopped with DI water and the compound **6** precipitated. Furthermore, **6** was filtered and dry under vacuum obtaining a white powder with a yield of 75 % (45 mg).

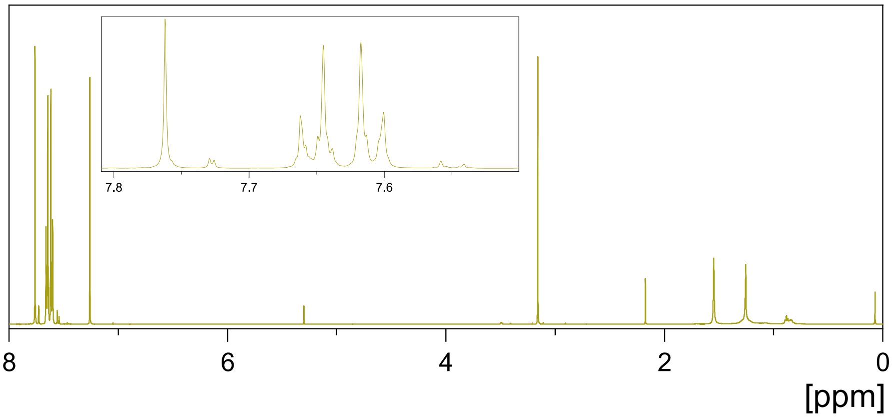

Figure 5.14: ^{1}H-NMR (500 MHz) spectra of the deprotected compound **6** in $CDCl_3$.

Synthesis of 1,3,6,8-tetrakis(trimethylsilanylethynyl)pyrene (7) and

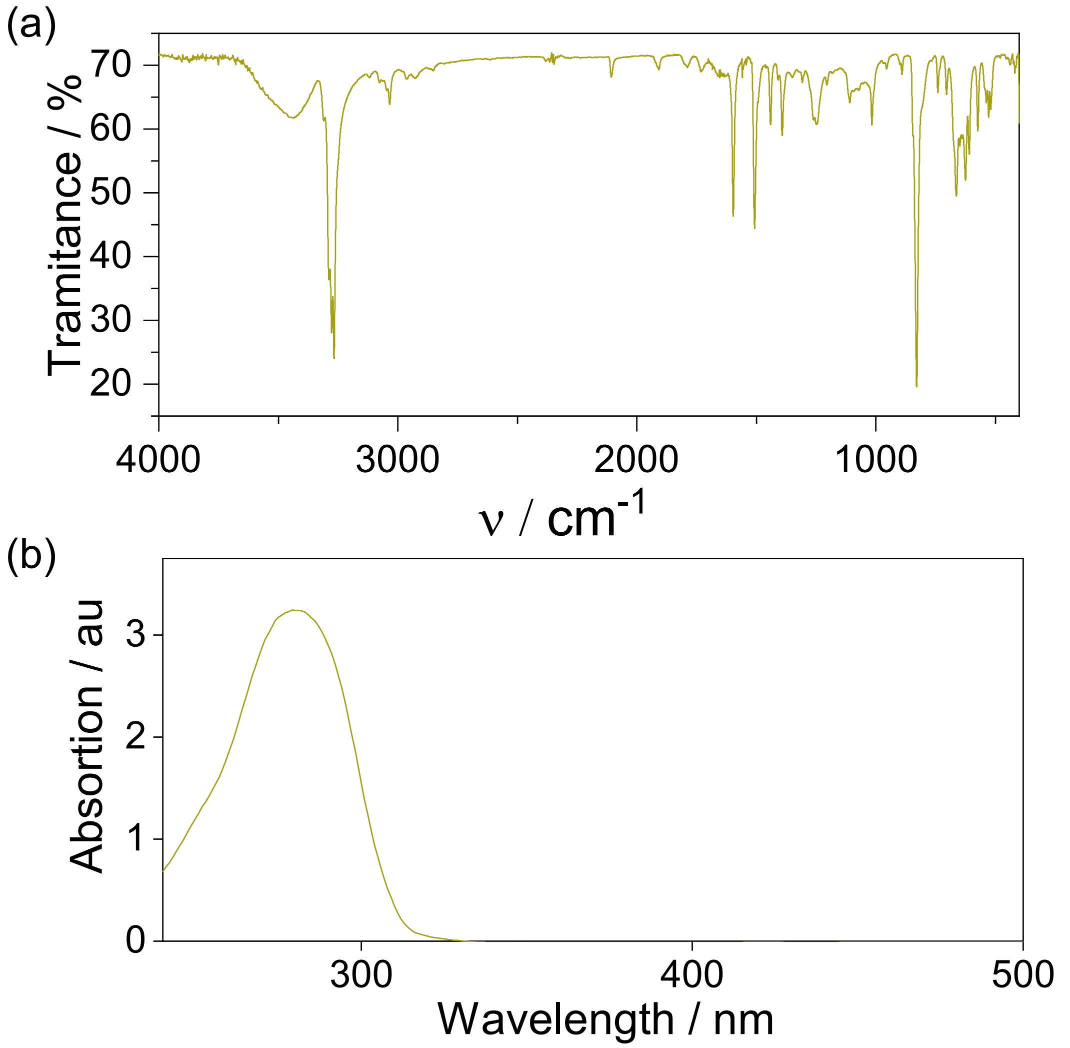

Figure 5.15: (a) IR spectrum and (b) UV spectrum of compound **6** in dry CH_2Cl_2

1,3,6,8-tetrakis(ethynyl)pyrene (8): The synthesis of compound **7** was performed in a two-neck round bottom flask, which was first purged with Ar. 1,3,6,8-tetrabromopyrene (2.07 g, 4.0 mmol) was suspended in triethylamine (TEA) (30 mL) and toluene (10 mL), and $Pd(PPh_3)_4$ (185 mg, 0.16 mmol), and copper(I) iodide (61.2 mg, 0.32 mmol) were added. The reaction mixture was heated to 60 °C, and trimethylsilylethyne (2.35 g, 24.0 mmol) was added into the solution through a septum. Afterwards, the reaction mixture was heated to 80 °C and stirred overnight under Ar atmosphere. The cooled reaction mixture was diluted with water and extracted with CH_2Cl_2. The organic phase was dried over $MgSO_4$, and the solvent was removed under reduced pressure. The crude product was purified by column chromatography (silica gel, DCM:Hx) to afford compound (**7**) as an orange solid (1.52 g, 2.5 mmol, 65%). ^{1}H-NMR (500 MHz, $CDCl_3$) δ/ppm: 0.42(12H), 8.35 (d, J = 8.5 Hz, 2H), 8.64 (d, J = 8.5 Hz, 4H), 7.81 (3H); ^{13}C-NMR (126 MHz, $CDCl_3$) δ/ppm: 140.23, 139.94, 131.06, 130.96, 120.47, 105.37, 94.25, 0.06; NIR-IR (KBr, cm^{-1}): 2161 ($C\equiv C$), 2852-2960 (sp^3 C-H); ESI-MS, found (calcd.): 594.15 $[M–H]^-$, (595.01); Elemental analysis for $C_{36}H_{44}Si_4$, found (calcd.) for: C, 73.57 (73.40), H, 7.78 (7.53).

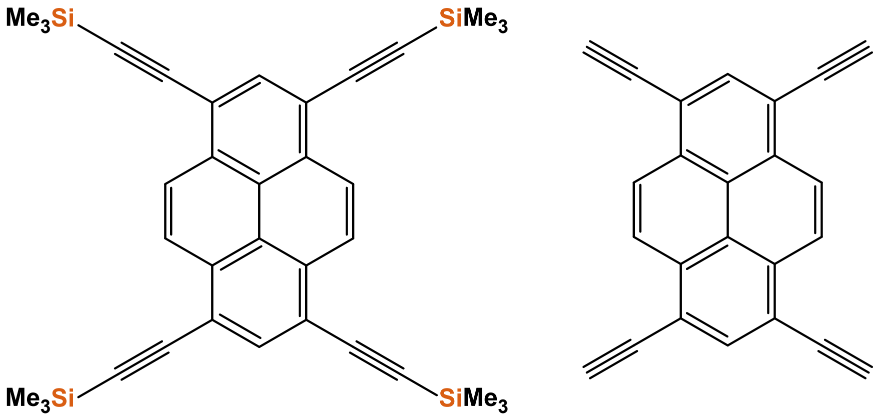

(**7**) (**8**)

Figure 5.16: 1,3,6,8-tetrakis(trimethylsilanylethynyl)pyrene (**7**) and 1,3,6,8-tetrakis(ethynyl)pyrene (**8**)

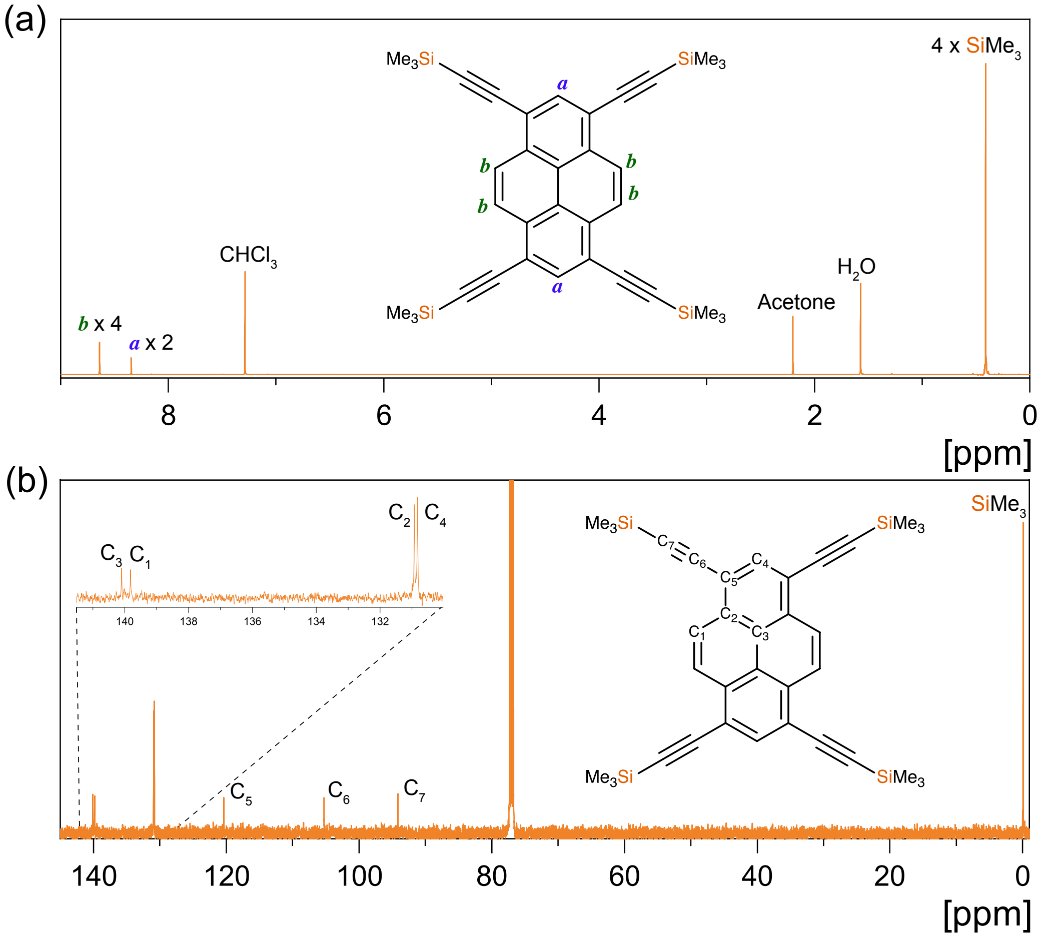

Figure 5.17: NMR spectra of compound **7**. (a) ^{1}H-NMR (500 MHz); ^{13}C-NMR in CD_2Cl_2 (126 MHz).

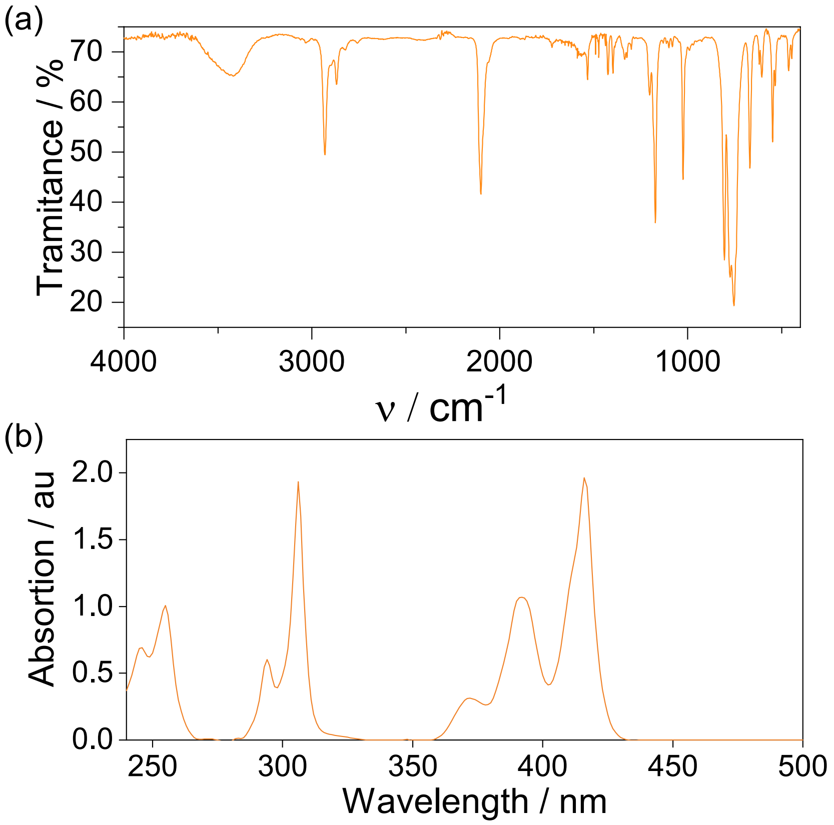

Figure 5.18: (a) IR spectrum and (b) UV spectrum of compound **7** in dry CH_2Cl_2

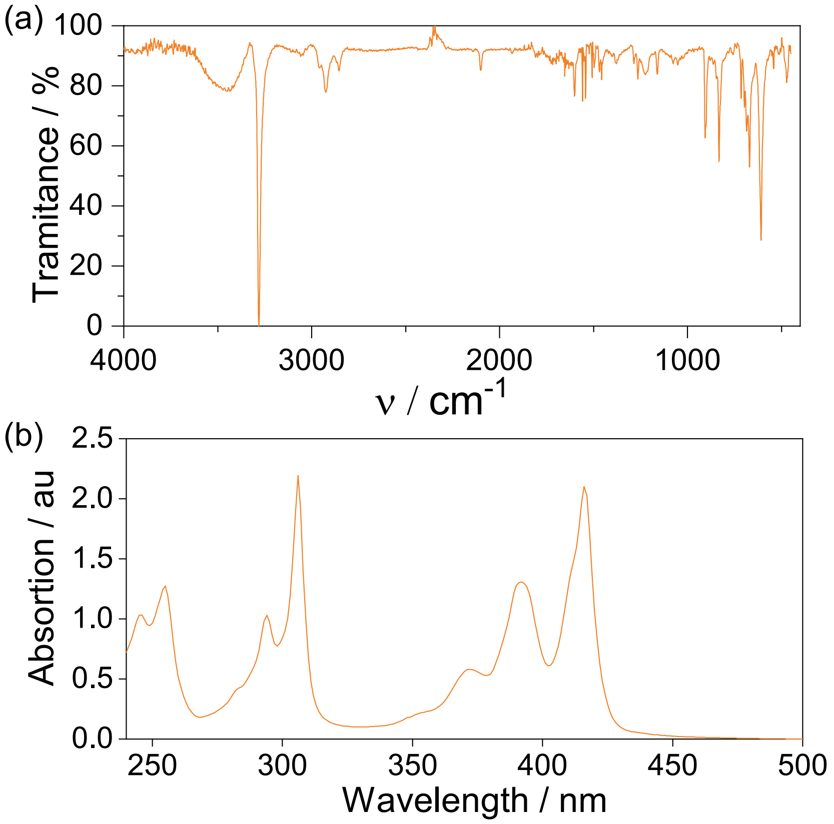

Figure 5.19: (a) IR spectrum and (b) UV spectrum of compound **8** in dry CH_2Cl_2

Compound **8** was obtained by performing a de-protection of **7**. For this, 50 mg of **5** were deprotected *via* a reaction with a methanolic solution of K_2CO_3 0.1 M. The reaction was stirred overnight under an Ar atmosphere at room temperature. As the final step, compound **8** was precipitated by adding DI water to the reaction mixture and then, **8** was filtered and dry under vacuum obtaining as a yellow powder with a yield of 84.3 % (21.5 mg).

5.4.2 Cu Foil Electro-polishing

In order to obtain a flat and smooth substrate, the copper foil commercially obtained from Alpha Aesar (99.8%, uncoated, 0.025mm thick) was treated to eliminate any impurity and oxidation. In this regard, an electro-polishing (EP) procedure was applied to the Cu foil utilising a mixture of H3PO4 85% with 2.2 mL and 1 mL of glycerol. The Cu foil was cut in pieces of 2×1 cm^2 and placed in the cathode side. Following it was dipped in the acidic solution and a thicker Cu foil was used as anode. The EP was performed for 20 minutes with a power of 1.5 volts using a DC power supply. Afterwards, the Cu foil was washed with DI water and dipped for 10 s to remove any metal impurity, and washed again with DI water and isopropyl alcohol and dried under a stream of nitrogen.

5.4.3 CVD growth of Graphdiyne Films

After the EP of Cu foil, the synthesis of graphdiyne was performed as follow: (*i*) First, the Cu foil was placed inside a quartz boat which was positioned carefully inside a quartz at the heat zone of the CVD furnace. (*ii*) The substrate was heated up to 150 °C under a stream of Ar (2.8 sccm for compounds **2** and **8**, while for compounds **4** and **6** the flow was 5.6 and 3.5 sccm, respectively). (*iii*) When the substrate reached the growth temperature, the reaction started by passing through the starting materials previously prepared (*vide supra*), for 2 h. The starting material is deposited by employing a homemade nebuliser, which consist in a NB-59S-09S-0 membrane assembled in a glass container which is connected to an AC power supply at a constant voltage of 27.5 V.

5.4.4 Transfer of the Grown GDY

For further characterisation of the obtained GDY, it was transferred to a silicon (Si) and silicon oxide (SiO_2) substrates. For this, the Cu foil was etched using $(NH_4)_2S_2O_8$ 0.1M solution. First the solution was heated at 70 °C for 5 min, then the Cu foil containing the grown GDY, is placed carefully on the top of the warm solution. The etching process takes few hours (between 3-5 hours) and when the Cu foil is completely dissolved, the free-standing film is fished with a Si or SiO_2. Afterwards the grown film is ready for further surface characterisation, which were enlisted above.

Concluding Remarks

In this thesis, we successfully synthesised three different types of carbon-based 2D materials such as graphene, nanocrystalline graphene and graphdiyne, employing an APCVD reactor. The materials obtained were structurally and physically characterised by a range of spectroscopic and surface techniques. Below are summarised the main conclusions of the three projects developed in this work:

Direct Conversion of CO_2 to Graphene: through a new concept, we were able to employ an abundant and environmentally problematic molecule as CO_2 in the synthesis of a highly technological material as graphene. The substrates, consisting of Cu and Pd, showed a catalytic activity towards the conversion of CO_2 to graphene. From the design of the metallic substrate we could observe that Cu and Pd must to be in direct contact to proceed with the hydrogenous reduction of CO_2 and graphene growth. Interestingly, the amount of Cu required in the metallic substrate for the process is more than 82at.% and less than 18at.% for Pd. We demonstrated that the reaction is precluded when the alloy has a concentration of Pd higher than 18at.%. This result is very promising for the fabrication of new metallic substrates, since Cu is a cheap and abundant metal. Moreover, Raman analyses, before and after transfer, showed the formation of graphene, while AFM studies indicated the formation of a multilayer structure. The growth of graphene films was confirmed unambiguously by TEM analysis. TEM images clearly showed the formation of a crystalline graphene film *via* an analysis of the SAED pattern. The study of the lattice space showed a value corresponding to a graphene material and the intensity profile of the stacked region exhibited around 10 to 20 layers of graphene, therefore, the formation of multilayer graphene from CO_2 was confirmed. Our results have shown a one-step synthesis producing graphene from CO_2, therefore, this study can be used as foundation for further investigation of the direct CO_2 reduction employing metallic substrates.

Nanocrystalline Graphene (NCG) from an Organic Precursor: in the quest of synthetic methodologies for the preparation of new 2D materials, it was possible to employ hexaethynylbenzene as precursor for the synthesis of NCG. The reaction was carried out at relatively low temperatures and short growth times employing an APCVD reactor. Raman studies confirmed the formation of NCG as demonstrated by the D peak being the fingerprint of NCG. Through Raman analysis we also demonstrated the formation of NCG with crystal sizes around 8-12 nm. HRTEM study showed a film with a high crystallinity and with a lattice stacking corresponding to a graphitic material. Resistivity studies of the NCG exhibited values of the order of 10^3 Ω, values that are expected due to the semiconductor behaviour of this material. Our results have demonstrated that organic molecules with aromatic systems can act as good candidates for the synthesis of NCG. Furthermore, our methodology offers the possibility to obtain NCG without employing high vacuum, explosive gases as carbon source on very long graphitisation times. In addition, with this alternative methodology it is possible to obtain enlarged crystalline domains of NCG.

CVD Synthesis of Graphdiyne from Organic Precursors Molecules: in this project a total of four organic molecules were prepared, which was subsequently employed as precursors for the synthesis of 2D graphdiyne materials. APCVD synthesis for all molecules yielded GDY films, as confirmed by Raman analysis performed on the GDY directly grown on the Cu substrates. The transfer of the grown films onto Si and SiO_2 substrates is possible for three of the four GDY films. The impossibility of transferring **GDY-2** is thought to be due to the inflexible backbone of the molecular precursors, which does not allow a uniform -C≡C- coupling. AFM analysis of the films reveals the formation of multilayer structures, while HRTEM shows that none of the GDY films is crystalline. The amorphous character of the GDY films highlights the difficulties for the successful synthesis of mono- to few layers GDY. Also, the thick characteristics of the films indicates that the reaction is not entirely catalysed by the copper substrate and hints to a possible thermal influence in the reaction. Finally, optical band-gap studies reveal that the films behave as insulators, which might be a consequence of the amorphous character of the films.

Bibliography

1. A. K. Geim, K. S. Novoselov, *Nat. Mater.*, **2007**, *6*, 183-191.
2. P. Miró, M. Audiffred, T. Heine, *Chem. Soc. Rev.*, **2014**, *43*, 6537-6554.
3. A. B. Kaul, *J. Mater. Res.*, **2014**, *29*, 348-361.
4. G. Yang, L. Li, W. B. Lee, M. C. Ng, *Sci. Technol. Adv. Mater.*, **2018**, *19*, 613-648.
5. K. S. Novoselov, A. K. Geim, S. V Morozov, D. Jiang, *Sience*, **2004**, *306*, 666-669.
6. G. Fiori, F. Bonaccorso, G. Iannaccone, T. Palacios, D. Neumaier, A. Seabaugh, S. K. Banerjee, L. Colombo, *Nat. Commun.*, **2014**, *9*, 768-779.
7. J. H. Jeong, J. H. Kim, R. Joshi, N. Kim, G.-H. Lee, *J. Phys. D.*, **2018**, *52*, 083001.
8. R. Mas-Ballesté, C. Gómez-Navarro, J. Gómez-Herrero, F. Zamora, *Nanoscale*, **2011**, *3*, 20-30.
9. Y. Wang, J. Mao, X. Meng, L. Yu, D. Deng, X. Bao, *Chem. Rev* , **2018**, *119*, 1806-1854.
10. M. R.-E. Tanjil, Y. Jeong, Z. Yin, W. Panaccione, M. C. Wang, *Coatings*, **2019**, *9*, 133.
11. Y. I. Zhang, L. Zhang, C. Zhou, *Acc. Chem. Res.*, **2013**, *46*, 2329-2339.
12. T. Heine, *Acc. Chem. Res.*, **2015**, *48*, 65-72.
13. W. Choi, I. Lahiri, R. Seelaboyina, Y. S. Kang, *Crit. Rev. Solid State*, **2010**, *35*, 52-71.
14. Z. Cai, B. Liu, X. Zou, H. M. Cheng, *Chem. Rev.*, **2018**, *118*, 6091-6133.
15. J. Kang, W. Cao, X. Xie, D. Sarkar, W. Liu, K. Banerjee, *Micro- and Nanotechnol. Sensors, Sys. Appl. VI*, **2014**, *9083*, 908305.
16. A. H. Castro Neto, F. Guinea, N. M. R. Peres, K. S. Novoselov, A. K. Geim, *Rev. Mod. Phys*, **2009**, *81*, 109-162.
17. Y. Zhang, A. Rubio, G. Le Lay, *J. Phys. D*, **2017**, *50*, aa4e8b.

18. G. Zhang and Y.-W. Zhang, *Mechanical Properties and Applications of Two-Dimensional Materials*; Intech; Rijeka, Croatia, **2016**; *Chapter 10*.
19. P. Solís-Fernández, M. Bissett, H. Ago, *Chem. Soc. Rev.*, **2017**, *46*, 4572-4613.
20. B. Dubertret, T. Heine, M. Terrones, *Acc. Chem. Res.*, **2015**, *48*, 1-2.
21. I. V. Vlassiouk, Y. Stehle, P. R. Pudasaini, R. R. Unocic, P. D. Rack, A. P. Baddorf, I. N. Ivanov, N. V. Lavrik, F. List, N. Gupta, et al., *Nat. Mateer.*, **2018**, *17*, 318-322.
22. N. J. Borys, M. C. Hersam, S. Subramanian, M. Drndić, J. Robinson, N. Briggs, S. McDonnell, A. M. Lindenberg, H. Yuan, J. C. M. Hwang, et al., *2D Mater.*, **2016**, *3*, 042001.
23. S. Das, J. A. Robinson, M. Dubey, H. Terrones, M. Terrones, *Annu. Rev. Mater. Sci.*, **2015**, *45*, 1-27.
24. D. Geng, H. Y. Yang, *Adv. Mater.*, **2018**, *30*, 1-23.
25. R. Pilot, R. Signorini, C. Durante, L. Orian, M. Bhamidipati, L. Fabris, *Biosensors*, **2019**, *9*, 48-99.
26. B. Schrader, *Infrared and Raman Spectroscopy: Methods and Applications*; Wiley VCH, Weinheim, Germany **1995**.
27. G. D. Rostron Paul, Gaber Safa, *IJETR*, **2018**, *392*, 1-10.
28. J. Hodkiewicz, *Prog. Mater. Sci.* **2010**, *50*, 929-961.
29. E. Cordero, *J. Biomed. Opt.*, **2018**, *23*, 071210-1.
30. J. H. Hibben, *Chem. Rev.*, **1936**, *18*, 1-232.
31. J. Legleiter, *Nanotechnology*, **2009**, *20*, 1-10.
32. Y. Seo, W. Jhe, *Rep. Prog. Phys*, **2008**, *71*, 016101
33. J. A. Last, P. Russell, P. F. Nealey, C. J. Murphy, *Investig. Ophthalmol. Vis. Sci.*, **2010**, *51*, 6083-6094.
34. N. Jalili, K. Laxminarayana, *Mechatronics*, **2004**, *14*, 907-945.
35. S. Liu, Y. Wang, *Advances in Food and Nutrition Research*; Elsevier Inc., Burlington, USA, **2011**, vol. 62, *Chapter 6*.
36. D. R. Clarke, *J. Mater. Sci.*, **1973**, *8*, 279-285.
37. M. Winey, J. B. Meehl, E. T. O'Toole, T. H. Giddings, *Mol. Biol. Cell*, **2014**, *25*, 319-323.
38. E. P. Randviir, D. A. C. Brownson, C. E. Banks, *Mater. Today*, **2014**, *17*, 426-432.

39. M. S. A. Bhuyan, M. N. Uddin, M. M. Islam, F. A. Bipasha, S. S. Hossain, *Int. Nano. Lett.*, **2016**, *6*, 65-83.

40. H. C. Lee, W. Liu, S. Chai, R. Mohamed, *RSC Adv.*, **2017**, *7*, 15644-15693.

41. D. Gray, A. Mccaughan, B. Mookerji, *Physics for Solid State Applications*, **2009**, 1-20.

42. Y. Zhong, Z. Zhen, H. Zhu, *FlatChem.*, **2017**, *4*, 20-32.

43. D. Fathi, *J. Nanotech.* **2011**, *3*, 471241.

44. W. Choi, I. Lahiri, R. Seelaboyina, Y. S. Kang, *Crit. Rev. Solid State* **2010**, *35*, 52–71.

45. M. Buzaglo, E. Ruse, I. Levy, R. Nadiv, G. Reuveni, M. Shtein, O. Regev, *Chem. Mater.* **2017**, *29*, 9998–10006.

46. A. J. Hong, E. B. Song, H. S. Yu, M. J. Allen, J. Kim, J. D. Fowler, J. K. Wassei, Y. Park, Y. Wang, J. Zou, et al., *ACS Nano* **2011**, *5*, 7812–7817.

47. G. Zhang, *Nanofabrication and Its Application in Renewable Energy*; The Royal Society of Chemistry, Cambridge, UK, **2014**, vol. 32, *Chapter 1*.

48. Z. Tehrani, G. Burwell, M. A. Mohd Azmi, A. Castaing, R. Rickman, J. Almarashi, P. Dunstan, A. Miran Beigi, S. H. Doak, O. J. Guy, *2D Mater.* **2014**, *1*, 025004.

49. J. M. Tour, *Chem. Mater.* **2014**, *26*, 163–171.

50. F. Cataldo, O. Ursini, G. Angelini, S. Iglesias-Groth, *Fuller. Nanotub. Car. N.* **2011**, *19*, 713–725.

51. D. Jariwala, A. Srivastava, P. M. Ajayan, *J. Nanosci. Nanotechnol.* **2011**, *11*, 6621–6641.

52. M. Yi, Z. Shen, *J. Mater. Chem. A* **2015**, *3*, 11700–11715.

53. M. Coroş, F. Pogăcean, L. Măgeruşan, C. Socaci, S. Pruneanu, *Front. Mater. Sci.* **2019**, *13*, 23–32.

54. J. H. Ding, H. R. Zhao, H. Bin Yu, *Sci. Rep.* **2018**, *8*, 1–8.

55. J. M. Munuera, J. I. Paredes, M. Enterría, A. Pagán, S. Villar-Rodil, M. F. R. Pereira, J. I. Martins, J. L. Figueiredo, J. L. Cenis, A. Martínez-Alonso, et al., *ACS Appl. Mater. Interfaces* **2017**, *9*, 24085–24099.

56. K. Parvez, Z. S. Wu, R. Li, X. Liu, R. Graf, X. Feng, K. Müllen, *J. Am. Chem. Soc.* **2014**, *136*, 6083–6091.

57. P. Yu, S. E. Lowe, G. P. Simon, Y. L. Zhong, *Curr. Opin. Colloid.* **2015**, *20*, 329–338.

58. G. Yazdi, T. Iakimov, R. Yakimova, *Crystals* **2016**, *6*, 53.

59. M. H. Ani, M. A. Kamarudin, A. H. Ramlan, E. Ismail, M. S. Sirat, M. A. Mohamed, M. A. Azam, *J. Mater. Sci.* **2018**, *53*, 7095–7111.

60. H. Tan, D. Wang, Y. Guo, *Coatings* **2018**, *8*, 40.

61. B. R. Muõoz, C. Gómez-Aleixandre, *Chem. Vap. Deposition* **2013**, *19*, 297–322.

62. K. Matsumoto, *Frontiers of Graphene and Carbon Nanotubes: Devices and Applications*; Springer Tokyo Heidelberg New York Dordrecht London, **2015**, *Chapter 1*.

63. Y. M. Manawi, M. A. Atieh, n.d., *Materials* **2018**, *11*, 822.

64. A. Merlen, J. G. Buijnsters, C. Pardanaud, *Coatings*, **2017**, *7*, 153.

65. A. C. Ferrari, J. C. Meyer, V. Scardaci, C. Casiraghi, M. Lazzeri, F. Mauri, S. Piscanec, D. Jiang, K. S. Novoselov, S. Roth, et al., *Phys. Rev. Lett.* **2006**, *97*, 1–4.

66. A. Bianco, H. M. Cheng, T. Enoki, Y. Gogotsi, R. H. Hurt, N. Koratkar, T. Kyotani, M. Monthioux, C. R. Park, J. M. D. Tascon, et al., *Carbon* **2013**, *65*, 1–6.

67. A. Riaz, F. Pyatkov, A. Alam, S. Dehm, A. Felten, V. S. K. Chakravadhanula, B. S. Flavel, C. Kübel, U. Lemmer, R. Krupke, *Nanotechnology* **2015**, *26*, 325202.

68. C. T. Nottbohm, A. Turchanin, A. Beyer, R. Stosch, A. Gölzhäuser, *Small* **2011**, *7*, 874–883.

69. A. Turchanin, D. Weber, M. Büenfeld, C. Kisielowski, M. V. Fistul, K. B. Efetov, T. Weimann, R. Stosch, J. Mayer, A. G”olzhäuser, *ACS Nano* **2011**, *5*, 3896–3904.

70. F. Zhao, N. Wang, M. Zhang, A. Sápi, J. Yu, X. Li, W. Cui, Z. Yang, C. Huang, *Chem. Commun.* **2018**, *54*, 6004–6007.

71. C. N. S. Kumar, V. S. K. Chakravadhanula, A. Riaz, S. Dehm, D. Wang, X. Mu, B. Flavel, R. Krupke, C. Kübel, *Nanoscale* **2017**, *9*, 12835–12842.

72. C. N. S. Kumar, M. Konrad, V. S. K. Chakravadhanula, S. Dehm, D. Wang, W. Wenzel, R. Krupke, C. Kübel, *Nanoscale Adv.* **2019**, *1*, 2485-2494.

73. M. S. Dresselhaus, A. Jorio, A. G. Souza Filho and R. Saito, *Phil. Trans. R. Soc. A* **2010**, *368*, 5355–5377.

74. L. M. Malard, M. A. Pimenta, G. Dresselhaus, M. S. Dresselhaus, *Phys. Rep.* **2009**, *473*, 51–87.

75. A. C. Ferrari, *J. Solid State Commun.* **2007**, *143*, 47–57.

76. F. Tuinstra, J. L. Koenig, *J. Chem. Phys.* **1970**, *53*, 1126–1130.

77. M. M. Lucchese, F. Stavale, E. H. M. Ferreira, C. Vilani, M. V. O. Moutinho, R. B. Capaz, C. A. Achete, A. Jorio, *Carbon* **2010**, *48*, 1592–1597.

78. L. G. Caņado, K. Takai, T. Enoki, M. Endo, Y. A. Kim, H. Mizusaki, A. Jorio, L. N. Coelho, R. Magalhñes-Paniago, M. A. Pimenta, *Appl. Phys. Lett.* **2006**, *88*, 1–4.

79. L. G. Cançado, A. Jorio, M. A. Pimenta, *Phys. Rev. B* **2007**, *76*, 1–7.

80. A. C. Ferrari, J. Robertson, *Phil. Trans. R. Soc. Lond. A* **2004**, *362*, 2477–2512.

81. C. Huang, Y. Li, N. Wang, Y. Xue, Z. Zuo, H. Liu, Y. Li, *Chem. Rev.* **2018**, *118*, 7744–7803.

82. M. M. Haley, *Pure App. Chem.* **2008**, *80*, 519–532.

83. X. Gao, H. Liu, D. Wang, J. Zhang, *Chem. Soc. Rev.* **2019**, *48*, 908–936.

84. Y. Zhao, H. Tang, N. Yang, D. Wang, *Adv. Sci.* **2018**, *5*, 1800959.

85. Z. Meng, X. Zhang, Y. Zhang, H. Gao, Y. Wang, Q. Shi, D. Rao, Y. Liu, K. Deng, R. Lu, *ACS Appl. Mater. Interfaces* **2016**, *8*, 28166–28170.

86. G. Venkataramana, S. Sankararaman, *Eur. J. Org. Chem.* **2005**, *xxx*, 4162–4166.

87. G. Li, Y. Li, H. Liu, Y. Guo, Y. Li, D. Zhu, *Chem. Commun.* **2010**, *46*, 3256–3258.

88. M. Long, L. Tang, D. Wang, Y. Li, Z. Shuai, *ACS Nano* **2011**, *5*, 2593–2600.

89. J. Zhou, J. Zhang, Z. Liu, Wuli Huaxue Xuebao *Acta Phys-Chim. Sin.* **2018**, *34*, 977–991.

90. Q. Peng, J. Crean, L. Han, S. Liu, X. Wen, S. De, A. Dearden, *Nanotechnol. Sci. Appl.* **2014**, , 1.

91. A. N. Enyashin, A. L. Ivanovskii, *Phys. Status Solidi B Basic Res.* **2011**, *248*, 1879–1883.

92. C. Li, X. Lu, Y. Han, S. Tang, Y. Ding, R. Liu, H. Bao, Y. Li, J. Luo, T. Lu, *Nano Res.* **2018**, *11*, 1714–1721.

93. X. Gao, Y. Zhu, D. Yi, J. Zhou, S. Zhang, C. Yin, F. Ding, S. Zhang, X. Yi, J. Wang, et al., *Sci. Adv.* **2018**, *4*, 1–8.

94. X. Qian, H. Liu, C. Huang, S. Chen, L. Zhang, Y. Li, J. Wang, Y. Li, *Sci. Rep.* **2015**, *5*, 1–7.

95. F. Klappenberger, Y.-Q. Zhang, J. Bjoörk, S. Klyatskaya, M. Ruben, and J. V. Barth, *Acc. Chem. Res.* **2015**, *48*, 2140-2150.

96. Y.-Q. Zhang, N. Kepčija, M. Kleinschrodt, K. Diller, S. Fischer, A. C. Papageorgiou, F. Allegretti, J. Bjoörk, S. Klyatskaya, F. Klappenberger, ; M. Ruben, and J. V. Barth, *Nat. Commun.* **2012**, *3*, 1286-1-8.

97. J. Liu, P. Ruffieux, X. L. Feng, K. Muüllen, R. Fasel, *Chem. Commun.* **2014**, *50*, 11200-11203.

98. J. Zhou, X. Gao, R. Liu, Z. Xie, J. Yang, S. Zhang, G. Zhang, H. Liu, Y. Li, J. Zhang, et al., *J. Am. Chem. Soc.* **2015**, *137*, 7596–7599.

99. X. Qian, Z. Ning, Y. Li, H. Liu, C. Ouyang, Q. Chen, Y. Li, *Dalton Trans.* **2012**, *41*, 730–733.

100. B. C. Salinas, Y.–Q. Zhang, J. Björk, S. Klyatskaya, Z. Chen, M. Ruben, J. V. Barth and F. Klappenberger, *Nano Lett.* **2014**, *14*, 1891-7.

101. F. Klappenberger, R. Hellwig, P. Du, T. Paintner, M. Uphoff, L. Zhang, T. Lin, B.A. Moghanaki, M. Paszkiewicz, I. Vobornik, J. Fujii, O. Fuhr, Y.-Q. Zhang, F. Allegretti, M. Ruben, J. V. Barth, *Small* **2018**, *14*, 1704321.

102. G. Li, Y. Li, X. Qian, H. Liu, H. Lin, N. Chen, Y. Li, *J. Phys. Chem. C* **2011**, *115*, 2611–2615.

103. R. Matsuoka, R. Sakamoto, K. Hoshiko, S. Sasaki, H. Masunaga, K. Nagashio, H. Nishihara, *J. Am. Chem. Soc.* **2017**, *139*, 3145–3152.

104. R. Liu, X. Gao, J. Zhou, H. Xu, Z. Li, S. Zhang, Z. Xie, J. Zhang, Z. Liu, *Adv. Mater.* **2017**, *29*, 1604665.

105. J. He, N. Wang, Z. Cui, H. Du, L. Fu, C. Huang, Z. Yang, X. Shen, Y. Yi, Z. Tu, et al., *Nat. Commun.* **2017**, *8*, 1–11.

106. C. Wang, P. Yu, S. Guo, L. Mao, H. Liu, Y. Li, *Chem. Commun.* **2016**, *52*, 5629–5632.

107. T. Lin, J. Wang, *ACS Appl. Mater. Interfaces* **2019**, *11*, 2638–2646.

108. M. Bartolomei, E. Carmona-Novillo, M. I. Hernández, J. Campos-Martínez, F. Pirani, G. Giorgi, *J. Phys. Chem. C* **2014**, *118*, 29966–29972.

109. Z. Zuo, H. Shang, Y. Chen, J. Li, H. Liu, Y. Li, Y. Li, *Chem. Commun.* **2017**, *53*, 8074–8077.

110. S. Gong, S. Wang, J. Liu, Y. Guo, Q. Wang, *J. Mater. Chem. A* **2018**, *6*, 12630–12636.

111. R. Liu, H. Liu, Y. Li, Y. Yi, X. Shang, S. Zhang, X. Yu, S. Zhang, H. Cao, G. Zhang, *Nanoscale* **2014**, *6*, 11336–11343.

112. Y. Jiao, A. Du, M. Hankel, Z. Zhu, V. Rudolph, S. C. Smith, *Chem. Commun.* **2011**, *47*, 11843–11845.

113. S. W. Cranford, M. J. Buehler, *Nanoscale* **2012**, *4*, 4587–4593.

114. F. Calaza, C. Stiehler, Y. Fujimori, M. Sterrer, S. Beeg, M. Ruiz-Oses, N. Nilius, M. Heyde, T. Parviainen, K. Honkala, et al., *Angew. Chem. Int. Ed.* **2015**, *54*, 12484–12487.

115. C. J. Yang, M. Oppenheimer, *Clim. Change* **2007**, *80*, 199–204.

116. J. Summers, C. Smith, E. Vetter, P. Bergman, E. Adams, M. Akai, E.S. Rubin, D.W. Keith, C.F. Gilboy, M. Wilson, T. Morris, J. Gale, K. Thambimuthu, *Greenhouse Gas Control Technologies, 7, Elsevier Science Ltd, Oxford* **2005**, *2*, 1475–1480.

117. R. Dorner, D. Hardy, F. Williams, *Energ. Fuels* **2009**, *23*, 4190–4195.

118. D. Walther, M. Ruben, S. Rau, *Coord. Chem. Rev.* **1999**, *182*, 67-100.

119. Q. Liu, L. Wu, R. Jackstell, M. Beller, *Nat. Commun.* **2015**, *6*, 1–15.

120. Q. Xiang, B. Cheng, J. Yu, *Angew. Chem. Int. Ed.* **2015**, *54*, 11350–11366.

121. A. S. Agarwal, E. Rode, N. Sridhar and D. Hill, *Conversion of CO_2 to Value-Added Chemicals: Opportunities and Challenges. In Handbook of Climate Change Mitigation and Adaptation*; Springer New York: New York, NY, **2016**, pp 1-29.

122. S. Liu, H. Tao, L. Zeng, Q. Liu, Z. Xu, Q. Liu, J. L. Luo, *J. Am. Chem. Soc.* **2017**, *139*, 2160–2163.

123. J. Choi, J. Kim, P. Wagner, S. Gambhir, R. Jalili, S. Byun, S. Sayyar, Y. M. Lee, D. R. MacFarlane, G. G. Wallace and D. L. Officer, *Energy Environ. Sci.*, **2019**, *12*, 747—755.

124. V. Vaiano, D. Sannino, P. Ciambelli, *Photoch. Photobio. Sci.* **2015**, *14*, 550–555.

125. S. Sultana, P. Chandra Sahoo, S. Martha, K. Parida, *RSC Adv.* **2016**, *6*, 44170–44194.

126. X. Meng, T. Wang, L. Liu, S. Ouyang, P. Li, H. Hu, T. Kako, H. Iwai, A. Tanaka, J. Ye, *Angew. Chem., Int. Ed.* **2014**, *4*, 11662–11666.

127. C. D. Reddy, A. Ramasubramaniam, V. B. Shenoy, Y. W. Zhang, *Appl. Phys. Lett.* **2009**, *94*, 2007–2010.

128. S. S. Shams, R. Zhang, J. Zhu, *Mater. Sci.- Poland* **2015**, *33*, 566–578.

129. M. I. Kairi, M. K. N. M. Zuhan, M. Khavarian, B. Vigolo, S. A. Bakar, A. R. Mohamed, *Mater.* **2018**, *227*, 132–135.

130. H. Ago, Y. Ito, N. Mizuta, K. Yoshida, B. Hu, C. M. Orofeo, M. Tsuji, K. I. Ikeda, S. Mizuno, *ACS Nano* **2010**, *4*, 7407–7414.

131. I. Vlassiouk, P. Fulvio, H. Meyer, N. Lavrik, S. Dai, P. Datskos, S. Smirnov, *Carbon* **2013**, *54*, 58–67.

132. B. Luo, H. Liu, L. Jiang, L. Jiang, D. Geng, B. Wu, W. Hu, Y. Liu, G. Yu, *J. Mater. Chem. C* **2013**, *1*, 2990–2995.

133. L. Hu, Y. Song, S. Jiao, Y. Liu, J. Ge, H. Jiao, J. Zhu, J. Wang, H. Zhu, D. J. Fray, *ChemSusChem* **2016**, *9*, 588–594.

134. D. Esrafilzadeh, A. Zavabeti, R. Jalili, P. Atkin, J. Choi, B. J. Carey, R. Brkljacča, A. P. O'Mullane, M. D. Dickey, D. L. Officer, et al., *Nat. Commun.* **2019**, *10*, 865.

135. C. Molina-Jirón, M. R. Chellali, S. K. C. Neelakandhan, C. Kübel, L. Velasco, H. Hahn, E. Moreno-Pineda and M. Ruben, *ChemSusChem*, **2019**, *12*, 3509.

136. L. Lu, X. Sun, J. Ma, D. Yang, H. Wu, B. Zhang, J. Zhang, B. Han, *Angew. Chem., Int. Ed.* **2018**, *57*, 14149–14153.

137. J. Bin Wu, M. L. Lin, X. Cong, H. N. Liu, P. H. Tan, *Chem. Soc. Rev.* **2018**, *47*, 1822–1873.

138. N. M. Phan, V. T. Nguyen, T. T. Tam Ngo, H. D. Le, X. N. Nguyen, D. Q. Le, V. C. Nguyen, *Adv. Nat. Sci.-Nanosci.* **2013**, *4*, 035012.

139. A. Ismach, C. Druzgalski, S. Penwell, A. Schwartzberg, M. Zheng, A. Javey, J. Bokor, Y. Zhang, *Nano Lett.* **2010**, *10*, 1542–1548.

140. M. Koshino, *Phys. Rev. B* **2013**, *88*, 115409.

141. J. He, N. J. J. Johnson, A. Huang, C. P. Berlinguette, *ChemSusChem* **2018**, *11*, 48–57.

142. J. Artz, T. E. Müller, K. Thenert, J. Kleinekorte, R. Meys, A. Sternberg, A. Bardow, W. Leitner, *Chem. Rev.* **2018**, *118*, 434–504.

143. F. Geng, J. R. Boes, J. R. Kitchin, *Calphad: Compt. Coupling Phase Diagrams Thermochem.* **2017**, *56*, 224–229.

144. S. Bärthlein, G L W Hart, A. Zunger and S .Müller, *J. Phys.: Condens. Matter*, **2007**, *19*, 032201.

145. M. Li, J. Wang, P. Li, K. Chang, C. Li, T. Wang, B. Jiang, H. Zhang, H. Liu, Y. Yamauchi, et al., *J. Mater. Chem. A* **2016**, *4*, 4776–4782.

146. D. Kim, J. Resasco, Y. Yu, A. M. Asiri, P. Yang, *Nat. Commun.* **2014**, *2014*, 4948.

147. S.Vilekar, K. Hawley, C. Junaedi, D. Walsh, S. Roychoudhury, M. Abney, J. Mansell, *AIAA, 42^{nd} International Conference on Environmental Systems, San Diego, CA*, **2012**, DOI: 10.2514/6.2012-3555K.

148. H. C. Lee, W.-W. Liu, S.-P. Chai, A. R. Mohamed, C. W. Lai, C.-S. Khe, C. H. Voon, U. Hashim, N. M. S. Hidayah, *Procedia Chem.* **2016**, *19*, 916–921.

149. A. Isacsson, A. W. Cummings, L. Colombo, L. Colombo, J. M. Kinaret, S. Roche, *2D Mater.* **2017**, *4*, 012002.

150. A. Shekhawat, R. O. Ritchie, *Nat. Commun.* **2016**, *7*, 1–8.

151. T. B. Shiell, D. G. McCulloch, J. E. Bradby, B. Haberl, R. Boehler, D. R. McKenzie, *Sci. Rep.* **2016**, *6*, 1–8.

152. R. E. Smalley, *Nature* **1985**, *318*, 162–163.

153. S. Iijima, *Nature* **1991**, *354*, 56–58.

154. S. Sanvito, *Chem. Soc. Rev.* **2011**, *40*, 3336–3355.

155. G. Salvan, D. R. T. Zahn, *Beilstein J. Nanotechnol.* **2017**, *8*, 2464–2466.

156. D. Akinwande, C. J. Brennan, J. S. Bunch, P. Egberts, J. R. Felts, H. Gao, R. Huang, J. S. Kim, T. Li, Y. Li, et al., *Extreme Mech. Lett.* **2017**, *13*, 42–77.

157. H. Lu, S. D. Li, *J. Mater. Chem. C* **2013**, *1*, 3677–3680.

158. W. B. Wan, S. C. Brand, J. J. Pak, M. M. Haley, *Chem. Eur. J* **2000**, *6*, 2044–2052.

159. F. Diederich, *Chem. Commun.* **2001**, *3* , 219–227.

160. G. Li, Y. Li, H. Liu, Y. Guo, Y. Li, D. Zhu, *Chem. Commun.* **2010**, *46*, 3256–3258.

161. K. Srinivasu, S. K. Ghosh, *J. Phys. Chem. C* **2012**, *116*, 5951–5956.

162. X. Chen, P. Gao, L. Guo, S. Zhang, *Sci. Rep.* **2015**, *5*, 1–9.

163. M. Sonoda, A. Inaba, K. Itahashi, Y. Tobe, *Org. Lett.* **2001**, *3*, 2419–2421.

164. K. Kobayashi, N. Kobayashi, M. Ikuta, B. Therrien, S. Sakamoto, K. Yamaguchi, *J. Org. Chem.* **2005**, *70*, 749–752.

165. S. Ito, M. Wehmeier, J. D. Brand, C. Kübel, R. Epsch, J. P. Rabe, K. Müllen, *Chem. Eur. J.* **2000**, *6*, 4327–4342.

166. Y. Q. Zhang, T. Paintner, R. Hellwig, F. Haag, F. Allegretti, P. Feulner, S. Klyatskaya, M. Ruben, A. P. Seitsonen, J. V. Barth, et al., *J. Am. Chem. Soc.* **2019**, *141*, 5087–5091.

167. M. Zhang, X. X. Wang, H. Sun, N. Wang, Q. Lv, W. Cui, Y. Long, C. Huang, J. Zhou, X. Gao, et al., *Carbon* **2017**, *40*, 908–936.

168. J. Pang, A. Bachmatiuk, L. Fu, C. Yan, M. Zeng, J. Wang, *J. Phys. Chem. C.*, **2015**, *119*, 13363-13368

169. H.-C. Wang, C.-C. Ting, Y.-P. Hsieh, K.-Y. Chen, C.-C. Yang, Y.-W. Wang, *J. Nanomater.* **2013**, 1–6.

170. M. Wang, E. H. Yang, R. Vajtai, J. Kono, P. M. Ajayan, *J. Appl. Phys.* **2018**, *123*, 195103 .

171. J. Fan, M. Trenary, *Langmuir* **1994**, *10*, 3649–3657.

172. H. Bu, M. Zhao, A. Wang, X. Wang, *Carbon* **2013**, *65*, 341–348.

173. G. Luo, X. Qian, H. Liu, R. Qin, J. Zhou, L. Li, Z. Gao, E. Wang, W. N. Mei, J. Lu, et al., *Phys. Rev. B* **2011**, *84*, 1–5.

174. W. Regan, N. Alem, B. Alemáán, B. Geng, Ç. Girit, L. Maserati, F. Wang, M. Crommie, and A. Zettl, *Appl. Phys. Lett.* **2010**, *96*, 113102.

175. S. Motohiro, I. Akiko, I. Kayo and T. Yoshito, *Org. Lett.* **2001**, *3*, 241.